

# **Lorentz microscopy of MFM tips and related structures**

by Lin Zhou

submitted for the degree of PhD at the University of Glasgow



This work is conducted at

Solid State Physics Group  
Department of Physics and Astronomy  
University of Glasgow  
UK

© August 1996 Lin Zhou

ProQuest Number: 13818906

All rights reserved

INFORMATION TO ALL USERS

The quality of this reproduction is dependent upon the quality of the copy submitted.

In the unlikely event that the author did not send a complete manuscript and there are missing pages, these will be noted. Also, if material had to be removed, a note will indicate the deletion.



ProQuest 13818906

Published by ProQuest LLC (2018). Copyright of the Dissertation is held by the Author.

All rights reserved.

This work is protected against unauthorized copying under Title 17, United States Code  
Microform Edition © ProQuest LLC.

ProQuest LLC.  
789 East Eisenhower Parkway  
P.O. Box 1346  
Ann Arbor, MI 48106 – 1346

Heris  
10622  
Copy 1



**TO MY BELOVED YONG**

**AND**

**WITH LOVE AND GRATITUDE TO MY PARENTS**

## **Acknowledgements**

First of all, I would like to thank my supervisor Dr S McVitie and Professor J N Chapman for their continuous guidance, invaluable discussions and critical proof reading of the manuscript. The imaging processing and data storage would not be possible without the provision of RISC6000 workstation by Professor R P Ferrier. I also want to thank them for providing electron microscope facilities in the Solid State Physics Group at University of Glasgow.

I must thank Professor C D W Wilkinson for permitting me to use the electron beam lithography and plasma etching facilities in the Department of Electrical Engineering. Thanks are also due to Dr A N Farley of Manchester Metropolitan University for discussion and suggestions on MFM tip work.

For maintenance of the electron microscope and evaporation facilities, I would like to thank Dr W A P Nicholson, Mr J Simms, Miss M Low, Mr. A Howie, Mr. A Yong and Mr D McDonald. Since the imaging processing and data analysis are performed in computers, I am especially indebted to Mr A Howie for his excellent management of computers in the Solid State Physics Group. Preparation of images in this thesis would not have been possible without the help of Mr G Kirkland and Ms. L Adam at the Media Services of Glasgow University.

Finally, I would like to thank Overseas Research Awards (ORS) Scheme and Glasgow University for financial support.

## **Declaration**

This thesis is a record of the work carried out by me in the Solid State Physics Group of Department of Physics and Astronomy at the University of Glasgow. The work discussed herein is my own with the exception of the fabrication of needle MFM tip and Nanoprobe™ MFM tip which were provided by Dr M Rührig at Twente University and Dr K Babcock at Digital Instrument Inc. respectively. Some of the work given in this thesis can be found in the following papers:

'Magnetic imaging of magnetic force microscope tips', 1994, Zhou L, McVitie S and Chapman J N, *J. Magn. Magn. Mater.*, 148, P237

'In-situ magnetising experiments using coherent magnetic imaging in TEM', 1994, McVitie S, Chapman J N and Zhou L, *J. Magn. Magn. Mater.*, 148, P232.

'Imaging domains in Co/Pt multilayers by magnetic force microscopy', 1995, Valera M S, Farley A N, Hoon S R, Zhou L, McVitie S and Chapman J N, *Appl. Phys. Lett.*, 67, (17), P2566.

'Magnetic force microscopy of soft magnetic materials', 1996, Valera, Tomlinson S L, Heydon G P, Farley A N, Hoon S R, Zhou L, McVitie S and Chapman J N, *J. Magn. Magn. Mater.*, 7251.

This thesis has not previously been submitted for a higher degree.

Lin Zhou

August 1996

## Summary

The work described in this thesis is focused on the fabrication and understanding of the characteristics of small magnetic thin film elements and ferromagnetic thin film magnetic force microscope (MFM) tips so as to optimise the performance of the MFM used in our collaboration with a group at Manchester Metropolitan University. The small elements which have similar geometry as the magnetic film on the tip are studied in this thesis not only because some properties they exhibit are beneficial for quantitative MFM imaging but also because they enable the domain structure in the MFM tip to be observed directly. The basic concepts of ferromagnetism are given in Chapter 1, which serve as a starting point for further discussions.

Magnetic characterisations are performed using Lorentz microscopy in the modified JEOL 2000FX CTEM/STEM and VG HB5 STEM. The imaging formation of the Fresnel, Foucault and Differential Phase Contrast (DPC) modes of Lorentz microscopies are discussed in Chapter 2. The principle of MFM imaging technique and its basic instrumentation are also discussed there.

Chapter 3 gives a detailed description of the specimen fabrication process and some devices assisting the characterisations. The  $\text{Si}_3\text{N}_4$  membrane is discussed along with the photolithography technique. Electron beam lithography as a major technique employed to define small element patterns on  $\text{Si}_3\text{N}_4$  membrane is described. The oblique thermal evaporation produces MFM tips suitable for the MFM equipped with an interferometric detecting system. The preparation of such tips for observation in the VG HB5 STEM also forms a part of this chapter.

The main body of results is presented in Chapter 4 - 7. Chapter 4 focuses on the anisotropy induced by oblique thermal evaporation in the rectangular permalloy thin film elements. The nature of this anisotropy is investigated in various magnetic states as well as through in-situ magnetising experiments. In chapter 5, the stray field of the MFM tip is characterised experimentally using MDPC imaging and compared with the computer simulated MDPC images of a uniformly magnetised MFM tip. In chapter 6, magnetic structures of permalloy and cobalt thin film elements fabricated on the  $\text{Si}_3\text{N}_4$  membranes to simulated the magnetic films on MFM tips are described.

Direct imaging of the domain structure in various states is presented along with in-situ magnetising experiment. The characterisations of Nanoprobe™ and needle tips are presented in Chapter 7. The conclusions drawn from the above projects and future work are given in Chapter 8.

# Contents

## Acknowledgements

## Declaration

## Summary

<b>Chapter 1</b>	<b>Ferromagnetism</b>	<b>1</b>
	1.1 Ferromagnetism and ferromagnetic materials	1
	1.2 Energy of a magnetic body	3
	1.2.1 Exchange energy	3
	1.2.2 Magnetostatic energy	3
	1.2.3 Anisotropy energy	5
	1.3 Domain and domain walls in ferromagnetic thin films	5
	1.3.1 Review of domain structure research	5
	1.3.2 Domain theory	6
	1.3.3 Categories of domain walls in magnetic thin films	8
	1.3.4 Bloch wall	8
	1.3.5 Neel wall	9
	1.3.6 Cross-tie wall	10
	1.3.7 Vortex wall	11
	1.4 Hysteresis	11
<b>Chapter 2</b>	<b>Magnetic imaging of thin film specimens</b>	<b>13</b>
	2.1 Introduction	13
	2.1.1 Optical techniques	13
	2.1.2 Electron microscopy	14
	2.1.3 MFM technique	15
	2.2 Electron-specimen interaction	16
	2.2.1 Lorentz deflection - a classical approach	16
	2.2.2 Aharonov and Bohm theory - a quantum mechanical approach	17

2.3 Lorentz microscopy in a CTEM	18
2.3.1 General principle of magnetic image formation of a CTEM	18
2.3.2 Fresnel mode of Lorentz microscopy	21
2.3.3 Foucault mode of Lorentz microscopy	23
2.3.4 JEOL 2000FX CTEM/STEM	24
2.4 Lorentz microscopy technique in STEM - DPC imaging mode	25
2.4.1 Image forming in a STEM	25
2.4.2 Classical description of the DPC mode of Lorentz microscopy	27
2.4.3 MDPC mode of Lorentz microscopy	29
2.4.4 VG HB5 STEM and eXL acquisition system	31
2.5 Magnetic force microscope (MFM)	32
2.5.1 Introduction	32
2.5.2 Basic principle and instrumentation of MFM imaging	32
2.5.3 Instrumentation of MFM	33
2.5.4 Evolution of MFM tips	34
<b>Chapter 3 Specimen Preparation and characterisation</b>	<b>36</b>
3.1 Introduction	36
3.2 Materials studied in this work	37
3.3 Si <sub>3</sub> N <sub>4</sub> membrane substrate	38
3.4 Thermal evaporation of magnetic thin films	39
3.5 Electron beam lithography	40
3.6 Fabrication of small element samples	41
3.6.1 Elements used in the investigation of induced anisotropy by oblique evaporation	41
3.6.2 Simulated MFM tip elements	43

3.7	Fabrication of MFM tips	45
3.7.1	Microlever™	45
3.7.2	Cleaning Microlevers™ and coating with magnetic films	46
3.7.3	Preparation of MFM tip samples for examination in the VG HB5 STEM	47
3.7.4	Preparation of MFM tip samples for examination in the JEOL 2000FX CTEM/STEM	48
3.8	Equipment used in magnetic characterisation	49
3.8.1	Magnetising stage	49
3.8.2	In-plane ac-demagnetising stage	51
<b>Chapter 4</b>	<b>Induced Anisotropy in permalloy thin film elements by oblique incidence evaporation</b>	<b>53</b>
4.1	Introduction	53
4.2	Physical characteristics of the elements	54
4.2.1	Elements evaporated at normal incidence	54
4.2.2	Elements evaporated at 30° incidence	55
4.3	Schematic diagrams of some domain structures	55
4.4	Magnetic study of elements evaporated at normal incidence	58
4.4.1	As-grown state	58
4.4.2	Ac-demagnetised state	59
4.4.3	In-situ magnetising experiments	61
4.5	Magnetic study of AN2, AN4 and AN6 elements evaporated at oblique incidence	63
4.5.1	As-grown State	63
4.5.2	Ac-demagnetised State	64
4.5.3	In-situ magnetising experiments	66
4.6	Magnetic study of AN1, AN3 and AN5 elements evaporated at oblique incidence	67
4.6.1	As-grown State	67
4.6.2	Ac-demagnetised State	68
4.6.3	In-situ magnetising experiments	69
4.7	Comparison and conclusion	71

<b>Chapter 5</b>	<b>Characterisation of MFM tips using the MDPC mode of Lorentz microscopy and computer simulation</b>	<b>80</b>
	5.1 Introduction	80
	5.2 Fabrication of MFM tip	81
	5.3. Experimental study of physical characteristics of tips	83
	5.3.1 CTEM observation of whole-surface coated tip	83
	5.3.2 SEM observation of one-face coated cobalt tip	84
	5.4 Experimental MDPC imaging of one-face coated tip	84
	5.4.1 MDPC images of one-face coated tip	84
	5.4.2 Analysis of the MDPC images using arrow mapping method	85
	5.4.3 Analysis of experimental MDPC images using line tracing method	86
	5.5 Models used in computer simulation	90
	5.5.1 One-face coated models	90
	5.5.2 Whole-surface coated tip	92
	5.6 Details of the simulation	94
	5.6.1 Brief description of the simulation	94
	5.6.2 Calculation of components of the stray field perpendicular to the electron beam	95
	5.6.3 Calculation of Lorentz deflection angles	97
	5.6.4 Conversion of Lorentz deflection angle data to an image format	97
	5.7 Simulation of MDPC images using the one-face coated models	98
	5.7.1 Simulated MDPC images	98
	5.7.2 Analysis of the simulated MDPC images using arrow mapping method	98
	5.7.3 Analysis of simulated MDPC images using line tracing method	99
	5.7.4 Comparison between experiment and simulations	103

5.8	Simulation of MDPC images using whole-surface coated models	106
5.8.1	Simulated MDPC images	106
5.8.2	Analysis of MDPC images using arrow mapping method	107
5.8.3	Analysis of MDPC images using line tracing method	107
5.8.4	Comparison between whole-surface coated models and one-face coated models	110
5.9	Conclusion	111
<b>Chapter 6</b>	<b>Characterisation of elements simulating thin films on MFM tips</b>	<b>112</b>
6.1	Introduction	112
6.2	Cobalt elements	113
6.2.1	Physical characteristics of elements	113
6.2.2	Magnetic study of SIM1 element	113
6.2.3	Magnetic study of SIM2 element	116
6.2.4	Magnetic study of SIM3 element	119
6.2.5	Magnetic study of SIM4 element	120
6.3	Permalloy elements	122
6.3.1	Physical characteristics of elements	122
6.3.2	Magnetic study of SIM1 element	122
6.3.3	Magnetic study of SIM2 element	125
6.3.4	Magnetic study of SIM3 element	126
6.3.5	Magnetic study of SIM4 element	127
6.4	Conclusion and discussion	127
<b>Chapter 7</b>	<b>Characterisation of other types of MFM tip</b>	<b>130</b>
7.1	Introduction	130
7.2	Investigation of Nanoprobe™ thin film tip	130
7.2.1	Tip fabrication	130
7.2.2	Physical characteristics	131
7.2.3	Magnetic study of as-grown state	131
7.2.4	Magnetic study of remanent state	131

	7.3 Investigation of needle tips	132
	7.3.1 Tip fabrication	132
	7.3.2 Characterisation of the needle tip	132
	7.4 Conclusion	133
<b>Chapter 8</b>	<b>Conclusion and Future Work</b>	<b>135</b>
	8.1 Conclusion	135
	8.2 Future work	138
<b>Appendix 1</b>	<b>Conversion of 16 bit grey scale image to 8 bit grey scale image</b>	<b>141</b>
<b>Appendix 2</b>	<b>BASIC program used to display electron beam lithography patterns</b>	<b>143</b>
<b>Appendix 3</b>	<b>BASIC program used to display results of electron beam lithography</b>	<b>146</b>
<b>Appendix 4</b>	<b>FORTRAN 77 program converting Lorentz deflection angle data to 8-bit grey scale raw data format image</b>	<b>151</b>
<b>References</b>		<b>153</b>

# Chapter 1

## Ferromagnetism

### 1.1 Ferromagnetism and ferromagnetic materials

Ferromagnetic materials possess a temperature dependent spontaneous magnetisation below the Curie temperature  $\theta_f$ . One of their important properties in practical applications is that they have large susceptibilities (about 50 to 10,000) which enable high magnetic induction to be obtained with only modest magnetic fields.

The behaviour of magnetic insulators can be understood by the Heisenberg model (Heisenberg 1928) of quantum mechanics in terms of the interaction of the magnetic moments associated with the spin and orbital motion of electrons (Dirac 1929). The following four assumptions are usually used so as to simplify the calculation.

(1) the exchange interaction  $J$  between electrons of the same atom is omitted.  $J$  is also termed the exchange integral as expressed in (1.1).

(2) the form of the exchange interaction between any two electrons of different atoms is the same over the whole system (Li 1985), i.e.

$$J_{ij} = \int \varphi_i^*(\mathbf{r}_i) \varphi_j^*(\mathbf{r}_j) V(\mathbf{r}_{ij}) \varphi_i(\mathbf{r}_j) \varphi_j(\mathbf{r}_i) d\mathbf{r}_i d\mathbf{r}_j \quad (1.1)$$

where  $V(\mathbf{r}_{ij})$  is the Coulomb potential between electrons  $i$  and  $j$ ,  $\varphi$  is the wave function of the electrons.  $\mathbf{r}_i$ ,  $\mathbf{r}_j$  are the position vector of electrons  $i$  and  $j$  respectively.  $\mathbf{r}_{ij}$  is the relative position of electron  $i$  and  $j$  and it is defined as  $\mathbf{r}_{ij} = \mathbf{r}_i - \mathbf{r}_j$ .

(3) As  $J_{ij}$  depends on the overlay of the electron waves, it is a short-range interaction. Therefore,  $J_{ij}$  can be approximated to the interaction between the nearest neighbouring atoms.

(4)  $J_{ij}$  is uniform in the system, i.e.  $J_{ij} = J$

Thus, the total interaction energy  $E_{\text{ex}}$  can be expressed as

$$E_{\text{ex}} = -\frac{J}{2} \sum_{i \neq j} \mathbf{S}_i \cdot \mathbf{S}_j \quad (1.2)$$

where  $1/2$  is due to the fact that the energy is shared by two electrons and double counting must be avoided when summing over all the nearest neighbour atoms.

Using this equation, magnetic materials are categorised into several groups and two of them will be discussed here.

When  $J > 0$  and  $S_i = S_j$ , the system is ferromagnetic and all the spins align along the same direction so as to minimise the exchange energy. This will give rise to spontaneous magnetisation. The spin configuration in this class of material is shown in Fig. 1.1.

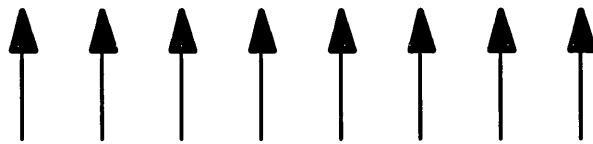


*Fig. 1.1 Schematic drawing of the 1-D spin configuration in a ferromagnetic material.*

When  $J < 0$  and  $S_i = S_j$  the system is antiferromagnetic and therefore each spin moment is antiparallel to the neighbouring spins to reduce the exchange energy. The spin configuration is displayed in Fig. 1.2.

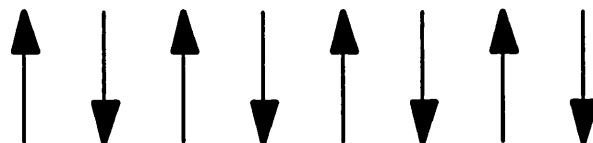


*Fig. 1.2 Schematic drawing of the 1-D spin configuration in an antiferromagnetic material.*

In spite of the presence of spontaneous magnetisation, a block of ferromagnetic material is usually not uniformly magnetised. This is due to the fact that the interior of the block is divided into many magnetic domains (discussed later in this chapter) each of which is spontaneously magnetised. Since the direction of domain magnetisation varies from domain to domain, the resultant magnetisation can be changed from zero to the value of spontaneous magnetisation by applying an external magnetic field.

## 1.2 Energy of a magnetic body

### 1.2.1 Exchange energy

The exchange energy expressed by (1.2) describes the interaction between neighbouring spin moments  $S_i$  and  $S_j$ . Bethe-Peierls-Weiss statistical physics theory described the relation between the exchange integral  $J$  and Curie temperature  $\theta_f$  (Weiss 1948)

$$J = 0.54K\theta_f \text{ (simple cubic lattice structure, } S = 1/2 \text{)} \quad (1.3)$$

$$J = 0.34K\theta_f \text{ (body centred cubic lattice structure, } S = 1/2 \text{)} \quad (1.4)$$

$$J = 0.15K\theta_f \text{ (face centred cubic lattice structure, } S = 1 \text{)} \quad (1.5)$$

where  $K$  is Boltzmann's constant ( $1.38 \times 10^{-23}$  J/K). Hence the exchange integral  $J$  could be determined experimentally by measuring the Curie temperature of a magnetic material.

### 1.2.2 Magnetostatic energy

This energy arises from the interaction between the magnetic moment and magnetic fields. The magnetic fields can be external ( $H_{ext}$ ) or arise from volume magnetic poles due to non-zero divergence of magnetisation and surface magnetic poles due to a discontinuity of the magnetisation.

In the case of external field, the magnetostatic energy is

$$E_H = -\mu_o \int \mathbf{M} \cdot \mathbf{H}_{ext} dv \quad (1.6)$$

In the case of demagnetising fields, the magnetostatic energy is

$$E_m = -\frac{1}{2} \mu_o \int \mathbf{M} \cdot \mathbf{H}_d dv \quad (1.7)$$

where 1/2 arises due to the fact that this is the energy shared by two poles and the integral is performed over both of them.  $\mathbf{H}_d$  is the demagnetisation field which originates from the contributions of the volume and the surface poles. These contributions are expressed as the 1st and 2nd terms respectively in the equation below

$$\begin{aligned} \mathbf{H}_d(\mathbf{r}) = & -\frac{1}{4\pi} \iiint_{\text{magnetic body}} \frac{(\mathbf{r}-\mathbf{r}')}{|\mathbf{r}-\mathbf{r}'|^3} [\nabla_{\mathbf{r}'} \cdot \mathbf{M}(\mathbf{r}')] dv \\ & + \frac{1}{4\pi} \iint_{\text{magnetic body}} \frac{(\mathbf{r}-\mathbf{r}'')}{|\mathbf{r}-\mathbf{r}''|^3} [\mathbf{M}(\mathbf{r}'') \cdot \mathbf{n}(\mathbf{r}'')] ds \end{aligned} \quad (1.8)$$

$\mathbf{r}$  is the position vector of the point where the field is calculated,  $\mathbf{r}'$  and  $\mathbf{r}''$  are the position vector of points inside and on the surface of the magnetic body respectively.  $\mathbf{n}$  is the unit vector normal to the surface of the body. This is illustrated in Figure 1.3.

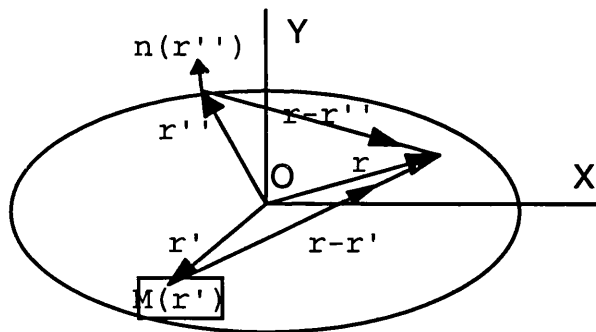


Fig. 1.3 Schematic diagram illustrating the definition of the terms used in the calculation of  $H_d(\mathbf{r})$

### 1.2.3 Anisotropy energy

Another contribution to the total magnetic energy of a ferromagnetic body is the anisotropy energy. This energy term is highly dependent on the orientation of magnetisation with respect to certain preferred directions. Such directions are normally termed the easy axes. The presence of the easy axis can arise from a number of sources. Spin-orbit coupling results in magnetocrystalline anisotropy while the growth condition of a sample may give rise to texturing and thus induce an easy axis. More details of this topic will be given in Chapter 5.

The mathematical expression of an uniaxial anisotropy energy to the 1st order is

$$E_a = K_u \sin^2 \gamma \quad (1.9)$$

where  $K_u$  is the anisotropy constant of the material and  $\gamma$  is the angle which the magnetisation makes with the easy axis.

Cubic anisotropy may also occur in a material of cubic crystalline structure. The magnitude of this energy term is dependent on the angles which the magnetisation makes relative to the three crystal axes.

## 1.3 Domain and domain walls in ferromagnetic thin films

### 1.3.1 Review of domain structure research

A magnetic domain is a region of material within which the magnetisation is uniform and a magnetic sample usually comprises several domains. The presence of ferromagnetic domain structures was first predicted by Weiss (1907) in his famous paper on the hypothesis of the molecular field. The energy stored in domain walls, which separate domains, was calculated by Bloch (1932). This model will be discussed later in section 1.3.4. The theoretical treatment of ferromagnetic domain structures was first tried by Landau and Lifshitz (1935) and Lifshitz (1944) using energy minimisation methods to predict domain structures. Domain structure was first indirectly confirmed experimentally by Barkhausen (1919). His experiment was

performed by studying the noise in the magnetisation process of a ferromagnetic specimen and thus proved that the magnetisation process consisted of many small discontinuous flux changes. The direct observation of ferromagnetic domain structure was attempted by Bitter (1931 and 1932) and independently by Hamos and Thiessen (1932). These researchers applied a drop of ferromagnetic colloidal suspension, containing many fine ferromagnetic particles, to the surface of a magnetic specimen and observed the locations of the domain walls where the particles accumulated. More recent domain structure studies and the techniques used will be given in Chapter 2.

### 1.3.2 Domain theory

The energy of a magnetic body is the summation of the energy terms given in section 1.2, i.e.

$$E_{\text{total}} = E_{\text{ex}} + E_{\text{m}} + E_{\text{H}} + E_{\text{a}} \quad (1.10)$$

The magnitude of these energy terms depends on the orientation of the magnetic moment at each point in the body as well as external magnetic fields. The presence of domains is the result of the minimisation of the total energy. The minimisation of exchange energy (1.2) favours a single domain structure (Fig. 1.4) although this gives rise to a large magnetostatic energy. Such a domain structure is one of the non-solenoidal domain structures where the magnetisation distribution does not result in flux closure. By contrast the minimisation of the magnetostatic energy (1.8) favours a multidomain structure so as to form a solenoidal magnetisation configuration (Fig. 1.5). The minimisation of anisotropy energy (1.9) simply favours a magnetisation parallel to the easy axis (Fig. 1.6).

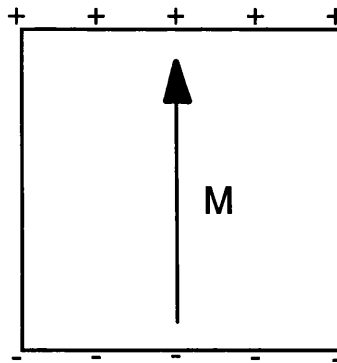


Fig. 1.4 Single domain structure favoured by the minimisation of the exchange energy. The symbols "+" and "-" on the surface indicate positive and negative magnetic poles respectively.

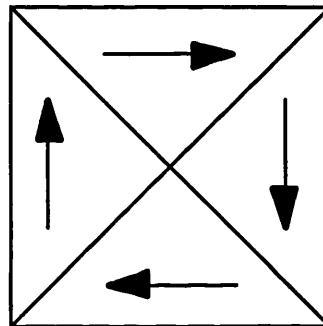


Fig. 1.5 Solenoidal domain structure favoured by the minimisation of the magnetostatic energy due to the surface poles  $M \cdot n$ .

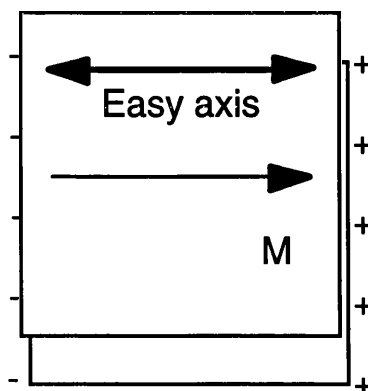


Fig. 1.6 Domain structure favoured by the minimisation of anisotropy energy.

### 1.3.3 Categories of domain walls in magnetic thin films

The transition region between adjacent domains is called the magnetic domain wall. One of the reasons that domain walls occur in thin films is that they reduce the magnetostatic energy associated with surface poles. Domain walls can be categorised according to the angle between the magnetisation of the adjacent domains (e.g.  $180^\circ$  wall and  $90^\circ$  wall, etc.). On the other hand, they also can be categorised according to the form of magnetisation variation across the wall. The magnetisation within the wall may vary along one direction such as in Bloch wall or Néel wall. They are therefore termed 1-D (1 dimension) walls. In some other walls, such as the cross-tie wall and vortex wall, the magnetisation varies along two directions and they are termed 2-D walls. These walls are described in the following sections.

#### 1.3.4 Bloch wall

Schematic drawings of Bloch walls are shown in Fig. 1.7. In diagram (a), the magnetisation rotates around the negative X axis whereas in diagram (b) it rotates around the positive X axis. However, as these cases give rise to equal wall energy, they have equal chance to occur.

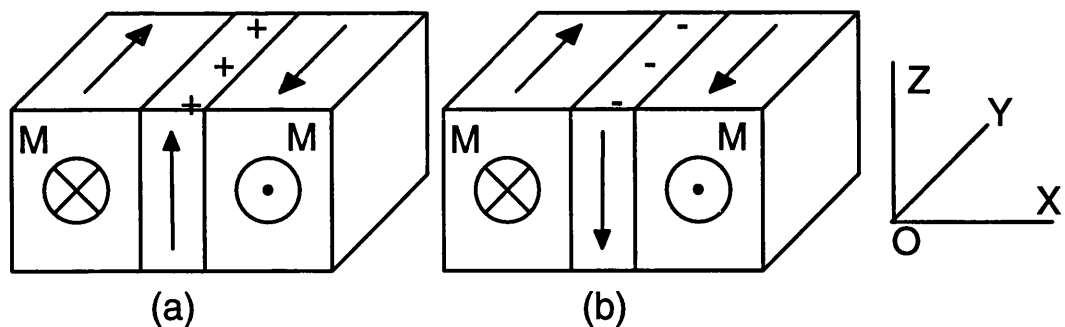


Fig. 1.7 Schematic drawing of Bloch walls.

This type of domain wall has three important features:

(1) The magnetic moments rotate gradually about the X axis in the YZ plane, i.e. the magnetisation varies only along the X direction. Therefore it is divergence free in the volume of the sample and the magnetic moments are parallel to the Z axis in the centre of the wall.

(2) Magnetic free poles are present on both of the top and bottom surfaces of the sample since the magnetisation is not parallel to the plane of the film there, i.e.  $\mathbf{M} \cdot \mathbf{n}$  is not zero.

(3) Bloch walls usually occur in thick films as the relative importance of the magnetostatic energy associated with the free poles on the Bloch wall surface intersection decreases as the thickness increases.

### 1.3.5 Néel wall

Another type of domain wall was proposed by Néel (1955) and named after him. A schematic drawing of the Néel wall is shown in Fig. 1.8. The magnetisation in the configuration (a) rotates around the negative Z direction whereas it rotates around the positive Z direction in the configuration (b). Both structures are equivalent and have equal chance to occur. This will be mentioned again in the discussion of cross-tie wall.

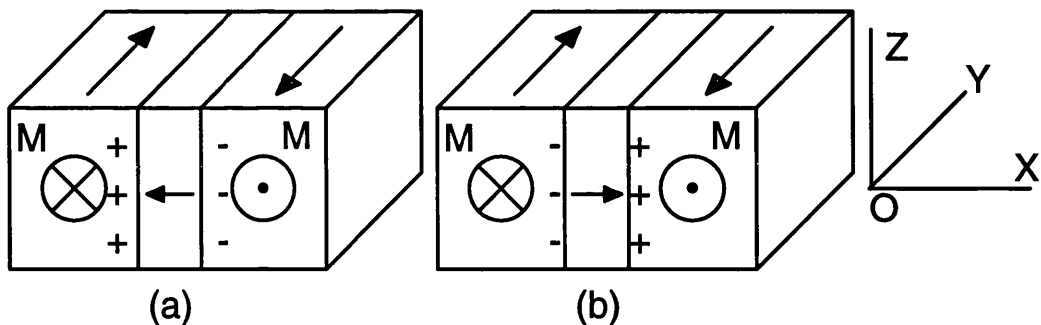


Fig. 1.8 Schematic drawing of Néel walls.

In this model, magnetic moments rotate in the plane of the film (the XY plane) about the Z axis. The magnetisation is parallel to the X axis in the centre of the wall. Although no free poles are generated on the surface, the

wall has non-zero divergence of magnetisation in the volume. Therefore, Néel walls usually occur in thin films and are generally quite wide so as to reduce the magnetostatic energy associated with the magnetic poles within the wall.

### 1.3.6 Cross-tie wall

This type of domain wall was first observed by Huber et. al. (1958). The wall is essentially a  $180^\circ$  wall with regions of alternately polarised Néel walls separated by Bloch walls. The polarities of the Bloch walls are not defined as it has been stated in section 1.3.4 that both polarities get an equal chance to occur. The cross-tie line occurs at positions where non-closure magnetisation is present whereas the circular Bloch lines occur in regions where closure magnetisation is present. In the Néel wall, the magnetisation varies along the Y axis while the magnetisation varies along the X axis in the Bloch wall. Therefore, this is a 2-D wall. For permalloy, cross-tie walls usually occur in 20 nm to 80 nm thick films as the result of the magnetostatic energy associated with both volume poles in the Néel walls and surface poles on Bloch walls. The schematic drawing of this type of wall is shown in Fig. 1.9. More details of the theoretical treatment of the cross-tie domain walls can be found in the work accomplished by Middelhoek (1963) and Kosinski (1977).

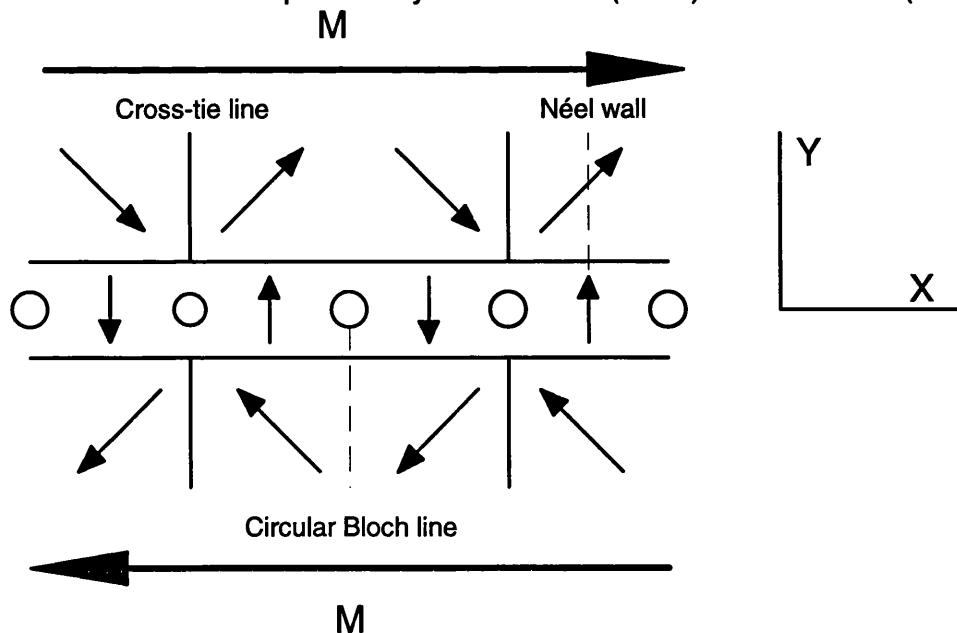


Fig. 1.9 Schematic diagram of cross-tie wall.

### 1.3.7 Vortex wall

Another type of 2D domain wall is the Vortex wall which was proposed by LaBonte (1969). A schematic diagram of the domain wall is given in Fig. 1.10. On the top and the bottom of the wall, the magnetisation is in the plane of the specimen and rotates around the Z axis (Néel variation) whereas the magnetisation rotates around the X axis along the X axis (Bloch variation). The variation of the magnetisation at anywhere else is between the Bloch variation and the Néel variation. The essence of such structure is that there is little or no stray field (Hubert 1969).

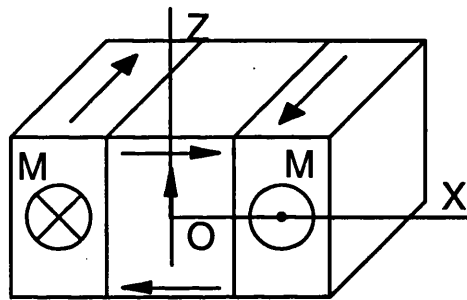


Fig. 1. 10 Schematic diagram of Vortex wall.

### 1.4 Hysteresis

When an external field  $H_{\text{ext}}$  is applied to a ferromagnetic sample, the magnetisation of the sample  $M$  is changed and finally reaches the saturation magnetisation  $M_{\text{sat}}$ , which is equal to the spontaneous magnetisation. If the field is reduced, the magnetisation may again decrease, but usually does not come back to the original value. Such an irreversible process of magnetisation is called hysteresis. This phenomenon was first observed by Warburg (1881). The presence of saturation magnetisation and hysteresis are important features of ferromagnetic materials. A plot of the external field against the magnetisation  $M$  of the sample is termed the hysteresis loop and some essential characteristics of a sample can be deduced from its hysteresis loop.

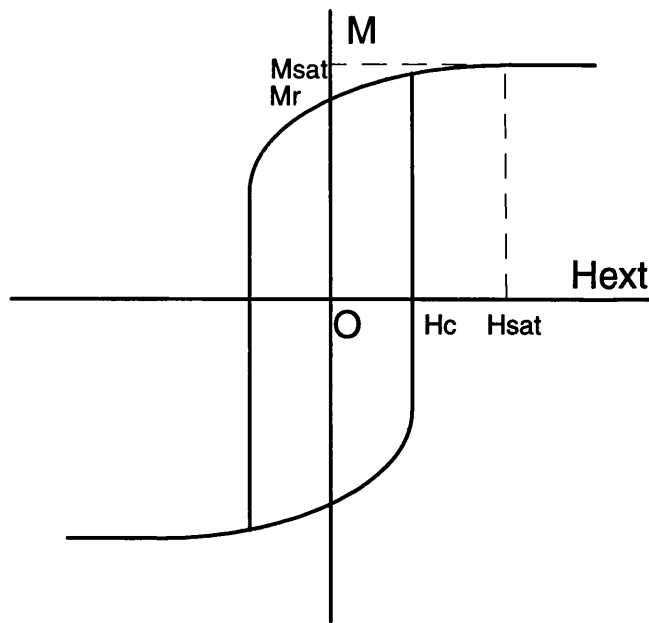


Fig. 1.11 Schematic diagram of a hysteresis loop.

A hysteresis loop is shown schematically in Fig. 1.11. The sample is initially saturated at a field which is equal to or bigger than  $H_{\text{sat}}$ . While the external field  $H_{\text{ext}}$  is decreased to zero the magnetisation also decreases but only to a positive value of  $M_r$  rather than zero. If a negative field is applied from this point, the magnetisation will be further reduced but still maintains a positive value until  $H_{\text{ext}}$  reaches  $-H_c$  where the magnetisation switches to the negative direction. Applying an external field to  $-H_{\text{sat}}$  will saturate the sample along the negative direction. Conventionally,  $H_c$  and  $M_r$  are termed coercivity and remanent magnetisation respectively. The higher the  $H_c$  is, the magnetically harder a material is.

The hysteresis loops of a bulk sample, a thin film sample and a thin film element may be different although they are the same material. This reflects the complex nature of the magnetisation process. There have been a few techniques which can be applied to investigate the magnetic characteristics of a sample and they will be discussed in Chapter 2.

## **Chapter 2**

### **Magnetic imaging of thin film specimens**

#### **2.1 Introduction**

The domain structure of a magnetic material provides important information in the understanding of its magnetic properties. Any technique which can extract such information is therefore of great utility and in this chapter the principal techniques used to investigate magnetic domain structures are discussed.

##### **2.1.1 Optical techniques**

Magnetic domain structures were first observed directly by Bitter (1931). In his method, fine magnetic particles in the form of a colloidal suspension are spread on the surface of a specimen and these accumulate at the regions with strong magnetic field gradient such as Bloch domain walls. This is due to the attractive force associated with the field gradient above these walls. The resolution of this method is limited by the wavelength of the illumination. Normally samples are required to have a flat polished surface for ease of observation.

Two other techniques of light microscopy are based on Faraday and Kerr magneto-optic (M-O) effects (Chikazumi 1964). Both detect the rotation of the polarisation of plane polarised light upon interaction with a magnetic specimen. The Faraday microscope utilises the transmitted light and therefore the Faraday microscope can only be applied to optically transparent specimens. The Kerr microscope utilises the reflected light and the rotation of its polarisation. Thus Kerr microscopy is a surface technique revealing only the surface domain structure of the specimen. The rotation of the polarisation is usually smaller than 20 minutes of arc for the Kerr effect and therefore a highly sensitive detection system is required.

The merits of these two sets of techniques are:

(1) They are linear techniques, i.e. the change in the polarisation of the light is a linear function of the specimen's magnetisation.

(2) They are capable of being used in in-situ magnetising experiments with a large field applied (Rührig et al. 1990, Rave and Hubert 1990).

Nevertheless, the resolution of the M-O techniques are still limited by the wavelength of the light used although a 0.3  $\mu\text{m}$  resolution has been obtained by Schmidt et al. (1985). Therefore these techniques are suitable for domain observation where the domains are substantially larger than 1  $\mu\text{m}$ .

Early studies using the Kerr microscope were successfully performed by Robert and Bean (1954) in the observation of the domain pattern on the c plane of a thin MnBi single crystal specimen. It was developed later by Rave et al. (1987) using a digital image processing method based on a combination of longitudinal Kerr effect (the magnetisation is in the plane of the incident light as well as the plane of the specimen) and transverse Kerr effect (the magnetisation is perpendicular to the incident light but in the plane of the specimen). This enables quantitative determination of the magnetisation on the surface of the specimen. Faraday microscopy was performed by Dillion (1958) and revealed the domain structure of a transparent ferromagnetic garnet specimen. The interference contrast colloid technique combining Kerr and Faraday effects with the Bitter pattern technique has been performed by Hartmann (1987), which provides high contrast images of the surface domain pattern and is suitable for both transparent and opaque specimens. A laser magneto-optic microscope (LAMOM) has been developed by Argyle and Herman (1986) and been applied for domain studies in read/write heads for magnetic recording devices (Herman and Argyle 1987). Clegg et al. (1990) also built a LAMOM which can be used for either Faraday or Kerr microscopy and obtained high quality domain patterns from a  $(\text{YSmBi})_3(\text{FeGa})_5\text{O}_{12}$  specimen.

### **2.1.2 Electron microscopy**

Since Hale et al (1959) first performed the Fresnel mode of Lorentz microscopy on a conventional transmission electron microscope (CTEM),

other modes of Lorentz microscopy have been developed to investigate different aspects of micromagnetic structures in thin film specimens (Jakubovics 1975 & 1978). The principal merits of Lorentz microscopy performed on a transmission electron microscope (TEM) or a scanning transmission electron microscope (STEM) are that it has very high spatial resolution and may be used for in-situ experiments (Hefferman et al. 1991). In section 2.2, the basic magnetic interaction between electron and specimen is described and serves as a starting point for further discussion of the Fresnel mode of Lorentz microscopy in section 2.3.2, the Foucault mode of Lorentz microscopy in section 2.3.3 and the modified differential phase contrast (MDPC) mode of Lorentz microscope in section 2.4.

Another electron microscopy technique involves a scanning electron microscope and a polarisation analysis detector (SEMPA) which can also be used to investigate magnetic domain structure (Koike and Hayakawa 1984). The basic principle of this technique is that the polarisation of the secondary electrons generated in the SEM depends on the surface magnetisation of the specimen and therefore the domain image is formed by detecting the polarisation. This technique provides lateral resolution as high as 20 nm (Allenspach 1994) and can be used in the characterisation of thick samples. The disadvantages include its requirement for ultrahigh vacuum.

The electron holographic method devised in 1949 by Gabor is another magnetic electron microscopy technique. Its basic principle is that a magnetic specimen is illuminated by electron beams in an electron microscope and the beams are modified in their phase on passing through the specimen due to the Aharonov and Bohm effect (refer section 2.2.2). This instrument also allows a reference beam to reach the detector plane from free space. The resulting interference pattern is recorded and analysed. A recent application of this technique to the observation of magnetic flux lines was performed by Tonomura (1993) and the review of this technique can also be found there.

### **2.1.3 MFM technique**

The magnetic force microscope (MFM) built by Martin and Wickramasinghe (1987) provides a powerful tool for high lateral resolution magnetic

observations of surface domain structures. MFM images reflect the interaction between the MFM tip and the stray field projecting from the surface of the specimen. More details of the MFM technique can be found in section 2.5. The advantages of the MFM is that no complex specimen preparation is needed. However, the MFM technique today is not quantitative.

## 2.2 Electron-specimen interaction

In this section, the basic principles underlying the interaction between moving electrons and magnetic induction in a thin magnetic film are discussed.

### 2.2.1 Lorentz deflection - a classical approach

An electron moving with velocity  $\mathbf{v}$  in a magnetic induction  $\mathbf{B}$  experiences a force  $\mathbf{F}$  and is therefore deflected from its original path. Such a phenomenon is termed Lorentz deflection and  $\mathbf{F}$  is termed the Lorentz force. The mathematical expression for  $\mathbf{F}$  is

$$\mathbf{F} = -e\mathbf{v} \times \mathbf{B} \quad (2.1)$$

Fig. 2.1 shows schematically this effect on electrons passing through a thin film containing a  $180^\circ$  wall. In the region where the magnetisation is constant, for a specimen of thickness  $t$  and saturation induction  $B_0$ , the Lorentz deflection angle  $\beta_L$  due to the magnetisation in the specimen is given by

$$\beta_L = eB_0\lambda t / h \quad (2.2)$$

where  $\lambda$  is the wavelength of the electron and  $h$  is Planck's constant.

Thus for a 50 nm thick specimen with saturation induction of 1.0 T, 200 keV electrons suffer 0.03 mrad deflection. Such a Lorentz deflection angle is very small compared to the 1st order Bragg diffraction angle, which is typically 10 mrad for a ferromagnetic crystal specimen.

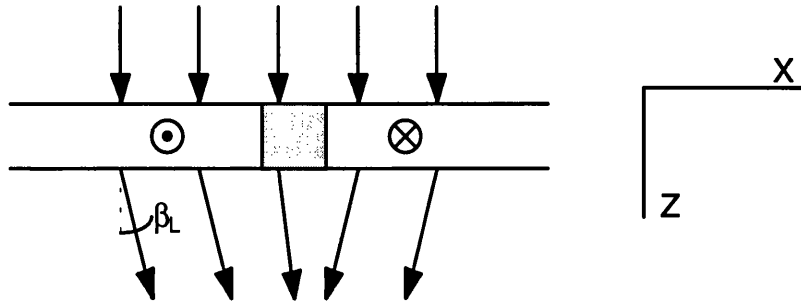


Fig. 2.1 Schematic diagram showing the Lorentz deflection when electrons pass through a magnetic specimen containing an  $180^\circ$  wall.

As a general case, if the magnetic induction perpendicular to the electron trajectory is  $B_y(x,z)$ , the local Lorentz deflection angle can be calculated using

$$\beta_L(x) = \frac{e\lambda}{h} \int_{z_1}^{z_2} B_y(x,z) dz = \frac{e\lambda B_a(x)t}{h} \quad (2.3)$$

Where the integral is performed along the whole electron path which starts from  $Z_1$  and finishes at  $Z_2$ .  $B_a(x)$  is the average magnetic induction along the electron trajectory.

$$B_a(x) = \frac{1}{t} \int_{z_1}^{z_2} B_y(x,z) dz \quad (2.4)$$

$B_y(x,z)$  arises not only from the foil's magnetisation but also from any magnetic stray field components perpendicular to the electron path. This may arise from regions of non-zero  $\nabla \cdot \mathbf{M}$  and  $\mathbf{M} \cdot \mathbf{n}$  where  $\mathbf{n}$  is the unit vector of the specimen surface.

### 2.2.2 Aharonov and Bohm theory - a quantum mechanical approach

Aharonov and Bohm (1959) postulated that two electrons originating from the same point have a phase difference in addition to the one arising from a

difference in their paths when they are brought together again after travelling paths enclosing non-zero magnetic flux  $N$  (Fig. 2.2). This phase difference is

$$\varphi = 2\pi eN/h \quad (2.5)$$

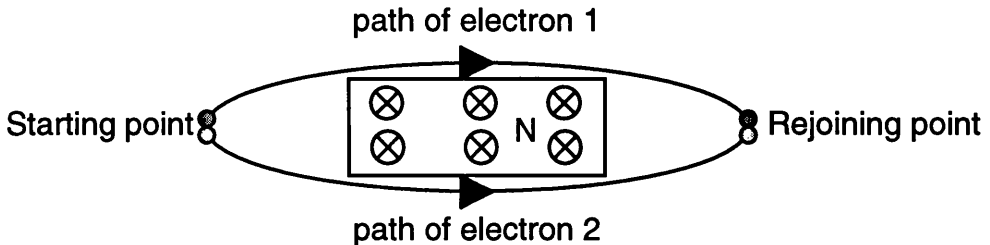


*Fig. 2.2 Schematic diagram showing the Aharonov and Bohm effect. Electron 1 and Electron 2 suffer a phase difference when their paths enclose a non-zero magnetic flux  $N$ .*

Applying this to the case shown in Fig. 2.1, after passing through the film, the electrons at two points with the  $x$  coordinates  $x_1$  and  $x_2$  have a phase difference

$$\varphi(x_2 - x_1) = \frac{2\pi e t}{h} \int_{x_1}^{x_2} B_o(x) dx \quad (2.6)$$

As far as magnetic imaging is concerned, a magnetic specimen is considered as a pure phase modulator of the electron beam. Any amplitude modulation which is due to the physical structure of the specimen is neglected. The fundamental principle of all modes of Lorentz microscopy is that they attempt to recover this modulated phase information. In the next few sections, this theory is applied to explain the techniques of Lorentz microscopy.

## 2.3 Lorentz microscopy in a CTEM

### 2.3.1 General principle of magnetic image formation of a CTEM

A schematic diagram of a CTEM is given in Fig. 2.3, indicating the important

instrumental components for magnetic imaging. The electron gun is the source which generates and accelerates electrons to a certain energy. These electrons are then brought to a selected area on the specimen by the condenser lenses and upper objective lens. The lower objective lens is the image forming lens and the intermediate lens is used to magnify this image.

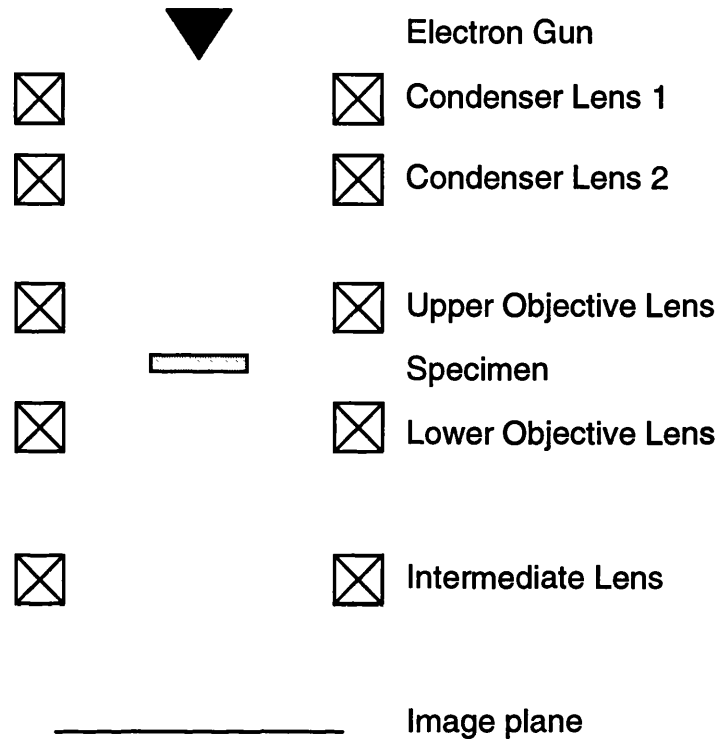


*Fig. 2.3 Schematic diagram of a CTEM illustrating the essential instrumentation components.*

As the electron source (filament) is usually very small in dimension and is situated far from the specimen, the electron wave incident on the specimen can be approximately treated as a plane wave  $\exp(i2\pi kz)$  with the wave number  $k$  defined as  $1/\lambda$ . On leaving the specimen, the electron wave function  $\Psi$  is

$$\Psi(x, y) = \exp[i\phi(x, y)] \exp[i2\pi kz_0] \quad (2.7)$$

The first part of the equation is termed specimen transmittance  $f(x, y)$  with  $\phi(x, y)$  defined by equation (2.6).  $z_0$  is the  $z$  axis coordinate of the specimen.

In the back focal plane of the image forming lens (objective lens), the electron disturbance  $g(k_x, k_y)$  can be described as the Fourier transform of the specimen transmittance

$$g(k_x, k_y) = FT[f(x, y)] = \iint f(x, y) \exp[-2\pi i(k_x x + k_y y)] dx dy \quad (2.8)$$

where FT indicates taking a Fourier transform of the function in brackets.

As all electron lenses suffer from aberrations and there may be a finite defocus present, the electron wave expressed in the above equation is further modified by a factor of  $t(k_x, k_y)$

$$t(k_x, k_y) = A(k_x, k_y) \zeta_a \zeta_d \quad (2.9)$$

$$\zeta_a = \exp\left[\frac{\pi i (C_s \lambda^3 (k_x^2 + k_y^2)^2)}{2}\right] \quad (2.10)$$

$$\zeta_d = \exp\left[\pi i \Delta z \lambda (k_x^2 + k_y^2)\right] \quad (2.11)$$

$A(k_x, k_y)$  is the pupil function which is uniform within the objective aperture and zero elsewhere,  $\zeta_a$  is the contribution of the spherical aberration of the objective Lens,  $\zeta_d$  is the contribution of the defocus,  $C_s$  is the spherical aberration coefficient and  $\Delta z$  is the defocus.

For magnetic imaging the spherical aberration usually makes negligible contribution to the final image (Chapman 1984). Hence (2.9) becomes

$$t(k_x, k_y) = A(k_x, k_y) \zeta_d \quad (2.12)$$

Therefore, in the image plane the wave function is the inverse Fourier transform  $FT^+$  of  $g(k_x, k_y)t(k_x, k_y)$

$$\begin{aligned} \Psi_i(x, y) &= FT^+ \left[ g(k_x, k_y) t(k_x, k_y) \right] \\ &= \iint g(k_x, k_y) t(k_x, k_y) \exp[2\pi i(k_x x + k_y y)] dk_x dk_y \end{aligned} \quad (2.13)$$

The intensity of the image  $I(x, y)$  is related to the wave function by the following equation

$$I(x, y) = |\Psi_i(x, y)|^2 \quad (2.14)$$

Thus, the image is formed in the image plane. The above calculation contains all the necessary information to discuss the principle of Lorentz microscopy in a CTEM.

It is obvious that if  $t(k_x, k_y)$  is a constant, then  $\Psi_i(x, y) = f(x, y) = \exp[i\phi(x, y)]$  so that  $I(x, y) = 1$  and there would be no contrast in the image plane. Magnetic contrast is generated when  $t(k_x, k_y)$  is not a constant, e.g. the defocus  $\Delta z \neq 0$  or objective aperture is used to modify the electron distribution in the back focal plane ( $A(k_x, k_y)$  is not constant). These two cases give rise to the Fresnel and Foucault modes of Lorentz microscopy respectively and they are detailed through the next two sections.

### 2.3.2 Fresnel mode of Lorentz microscopy

A classical description of the Fresnel mode of Lorentz microscopy is illustrated in Fig. (2.4). Electrons are deflected through an angle  $\beta_L$  due to the Lorentz force. The objective lens is focused on a plane either below or above the specimen rather than on the specimen. Thus domain walls are revealed as bright and dark bands due to the convergence or divergence of the electron beam respectively whereas the domains appear as a uniform background. Interference fringes can be observed in the bright band if the electron beam is sufficiently coherent.

As the Fresnel image is formed by introducing a non-zero defocus  $\Delta z$ ,  $\zeta_d$  is not zero. Moreover, usually the objective aperture is not introduced in the Fresnel mode ( $A(k_x, k_y) = 1$  effectively). Hence, the electron intensity in the image plane is

$$\begin{aligned} I(x, y) &= \left| \text{FT}^+ \left[ g(k_x, k_y) \zeta_d(k_x, k_y) \right] \right|^2 \\ &= \left| f(x, y) \otimes \exp \left[ \pi i (x^2 + y^2) / \lambda \Delta z \right] \right|^2 \end{aligned} \quad (2.15)$$

here  $\otimes$  represents a convolution integral of two functions.

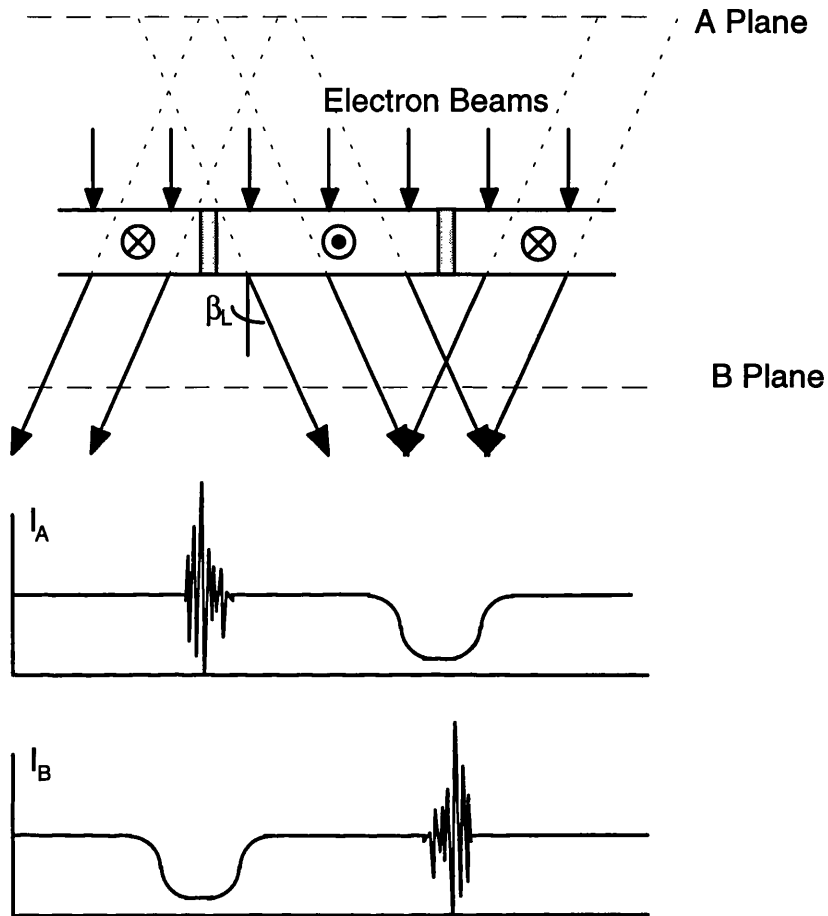


*Fig. 2.4 Schematic diagram of the Fresnel mode of Lorentz microscopy. Domain patterns are obtained by focusing on either A or B planes.  $I_A$  and  $I_B$  in the bottom diagrams represent the intensities of electron wave in A and B planes respectively.*

It is obvious that (2.15) is a complicated expression and the relation between  $I(x, y)$  and the deflection angle  $\beta_L$  is usually not linear. The merit of the Fresnel mode of Lorentz microscopy is its operational simplicity. The drawbacks of this mode are that there is no information on the direction of the magnetisation. Therefore, this imaging mode is usually used in the study of domain walls and domain geometry.

### 2.3.3 Foucault mode of Lorentz microscopy

The Foucault mode of Lorentz microscopy relies on the deliberate off-centring of the objective aperture in the back focal plane of the image forming lens to generate magnetic contrast. The classical explanation of this imaging mode is given in Fig. 2.5. For such a specimen containing domains with antiparallel magnetisations, two spots are observed in the back focal plane due to the Lorentz interaction. By introducing the aperture as shown with one spot obscured, only the electron beams with positive  $\beta_L$  contribute to the final image. Therefore, the domains with the  $\odot$  magnetisation appear bright whereas domains with the  $\otimes$  magnetisation appear dark.

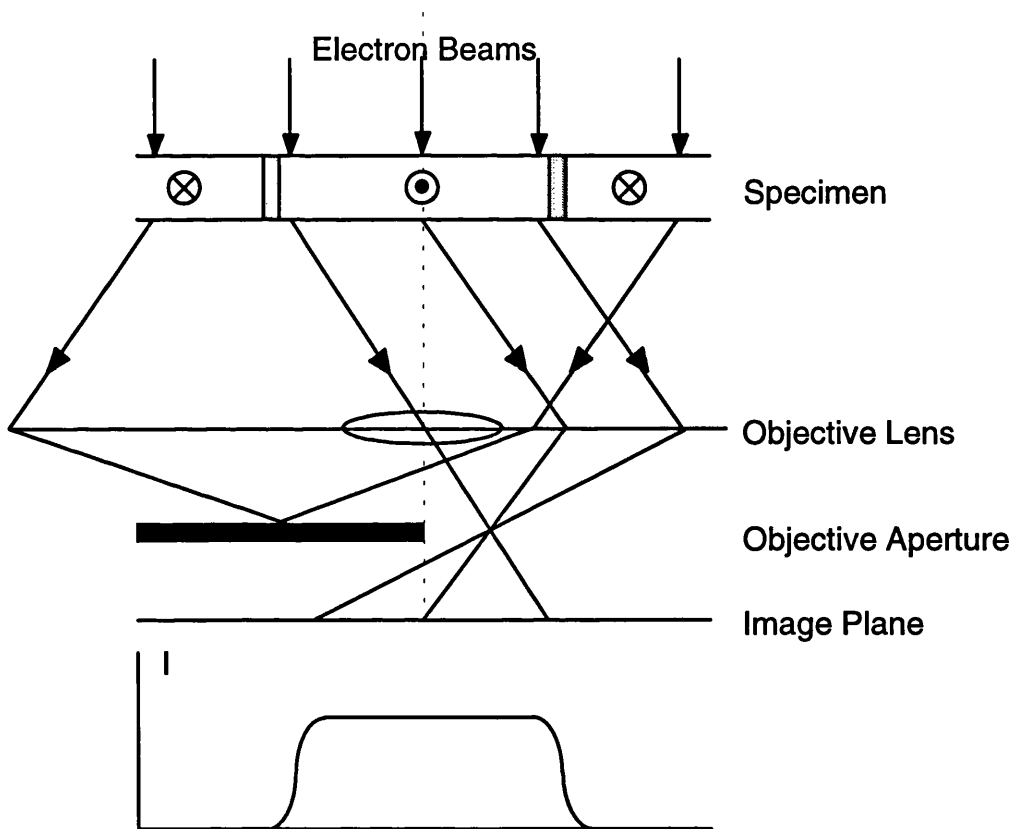


*Fig. 2.5 Schematic diagram of image forming in the Foucault mode Lorentz microscopy. The objective aperture is off-centred to obscure electrons coming through from  $\otimes$  domains so that they appear dark in the image plane, whereas the electrons coming through from  $\odot$  domains can pass through the objective aperture and give rise to bright regions in the image.*

In terms of wave theory, the pupil function used  $A(k_x, k_y)$  is not uniform in the back focal plane. Moreover as the Foucault imaging mode is an in-focus technique,  $\Delta z = 0$ . Hence the expression for the intensity in the imaging plane is

$$I(x,y) = |f(x,y) \otimes A(x,y)|^2 \quad (2.16)$$

where  $A(x,y)$  is the expression of the pupil function in real space, i.e.

$$A(x,y) = FT^+ [A(k_x, k_y)] \quad (2.17)$$

The advantages of the Foucault mode over the Fresnel mode are that it can provide the information on the orientation of the induction within specific domains and additionally it is operated with the specimen in focus. However this mode also suffers from the fact that there is no simple relationship between the intensity in the image plane and the induction in the specimen. Therefore, it is not a linear technique either.

### 2.3.4 JEOL 2000FX CTEM/STEM

In an ordinary CTEM, the objective lens is usually switched off while imaging a magnetic specimen. The focusing function is performed by using a mini objective lens which has weak field and is far below the specimen. This is due to the fact that the field of the objective lens will usually affect the domain structure of the sample. The drawback of switching off the objective lens is that the resolution is decreased. The schematic diagram shown in Fig. 2.3 is actually based on the JEOL 2000FX CTEM/STEM. In this microscope, the objective lens has been modified so that the stray field in the specimen area is very small (Tsuno and Taoka 1983). Thus the objective lens may still be used in the investigation of the magnetic specimen so as to achieve better resolution.

This CTEM/STEM is one of the major characterisation instruments used in this work. In order to get a good resolution, specimens are characterised using an accelerating voltage of 200 kV. A condenser aperture with a diameter of 120  $\mu\text{m}$  is used to help define electron beams. An objective

aperture is built into the back focal plane of the objective lens to allow the performance of the Foucault mode of Lorentz microscopy. Usually this aperture is set in such a way that its diameter is 80  $\mu\text{m}$ .

## 2.4 Lorentz microscopy technique in STEM - DPC imaging mode

### 2.4.1 Image forming in a STEM

A schematic diagram of a STEM is given in Fig. 2.6 with the electron gun on the bottom of the diagram. The beam spray aperture prevents scattered electrons from entering the probe forming lens. The probe forming lens focuses electrons on the surface of the specimen and the position of the probe is varied by exciting the scan coils. In this case, the angle of the probe is defined by the size of the probe forming aperture. The electron wave is modified by the specimen and then projected onto the detector where the signal is acquired. The function of the descans coils is that in the absence of the specimen, the bright field cone falls centrally on the detector. An image is formed by collecting signals sequentially while the probe is rastering over the specimen.

Supposing that the wave function of the electrons in the beam spray aperture is  $\Psi_0(k_x, k_y)$ , the wave function on the specimen  $\Psi_0[x, y, x_0, y_0]$  can be expressed as the inverse Fourier transform of  $\Psi_0(k_x, k_y)$ .

$$\Psi_0[x, y, x_0, y_0] = \text{FT}^+[\Psi(k_x, k_y)] \quad (2.18)$$

Where  $(x_0, y_0)$  is the central position of the electron probe on the specimen. The specimen modifies the wave by a factor of the transmittance  $f(x, y)$  so that after passing through the specimen the wave function becomes

$$\Psi(x, y, x_0, y_0) = \Psi_0(x, y, x_0, y_0)f(x, y) \quad (2.19)$$

In the detector plane the wave function is the Fourier transform of  $\Psi(x, y, x_0, y_0)$ , i.e.

$$\Psi(k_x, k_y, \tilde{x}_0, \tilde{y}_0) \equiv \text{FT}[\Psi(x, y, \tilde{x}_0, \tilde{y}_0)] \quad (2.20)$$

If the detector has a response function  $R(k_x, k_y)$  which depends on the acquisition mode operated, the intensity of the detected signal is the integral of  $|\Psi(k_x, k_y, x_o, y_o)|^2$  in reciprocal space.

$$I(x_o, y_o) = \iint |\Psi(k_x, k_y, x_o, y_o)|^2 R(k_x, k_y) dk_x dk_y \quad (2.21)$$

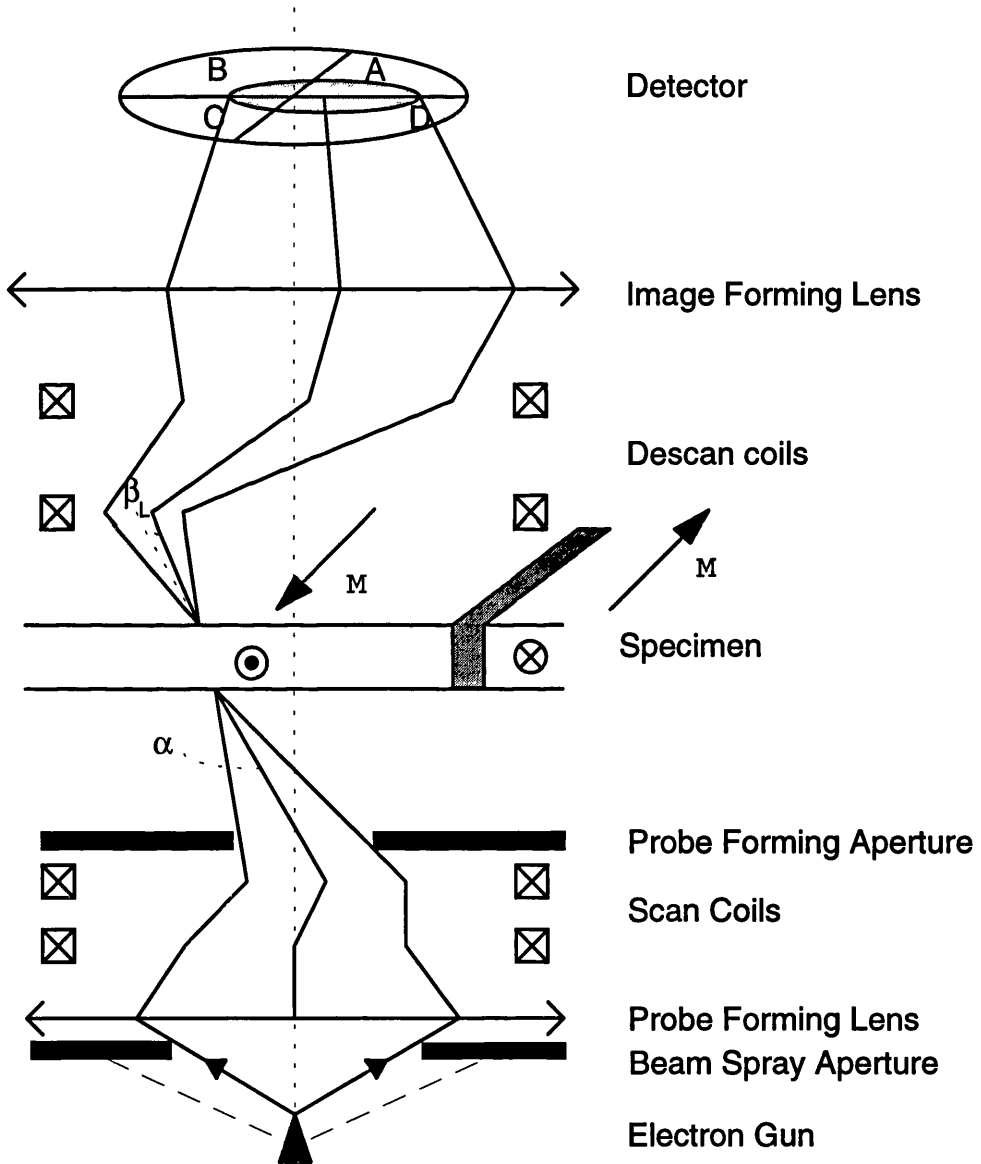
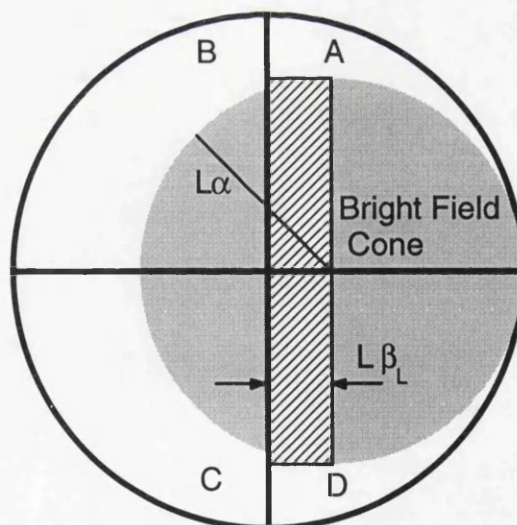


Fig. 2.6 Schematic diagram illustrating the image forming in a STEM.

### 2.4.2 Classical description of the DPC mode of Lorentz microscopy

The differential phase contrast (DPC) mode of Lorentz microscopy was introduced by Dekkers and de Lang (1974) and subsequently applied to the study of magnetic thin film specimens by Chapman et al. (1978). Unlike the Fresnel and Foucault mode of Lorentz microscopy, the DPC mode of Lorentz microscopy can only be operated on a STEM. The comparison of computer simulated and experimental DPC images of magnetic force microscope tips has been performed (McVitie et al. 1991) and their good agreement proved that the DPC technique is a powerful tool for high resolution magnetic studies.

In the schematic diagram of STEM (Fig. 2.6), electrons are focused to a small probe with a probe angle  $2\alpha$  onto the specimen. Assuming that the effective camera length of the image forming lens is  $L$ , the radius of the bright field cone in the detector plane is  $L\alpha$ . Due to the Lorentz deflection, this bright field cone is deflected a distance  $L\beta_L$  to the right, resulting in an asymmetry in the recorded signals of different quadrants. The detector is highlighted in Fig. 2.7 along with the bright field cone on it.



*Fig. 2.7 Highlight of the four quadrant detector and the deflected bright field cone. The radius of the cone is  $L\alpha$  and it is deflected a distance  $L\beta_L$  to the right.*

We can choose  $\alpha$  by varying the STEM set up. For DPC imaging,  $\alpha$  is chosen to be much bigger than  $\beta_L$  so that the signal on the detector plane is

$$I_A = I_D = \left[ \frac{\pi(L\alpha)^2}{4} + \frac{S_{hatch}}{2} \right] p \quad (2.22)$$

$$I_B = I_C = \left[ \frac{\pi(L\alpha)^2}{4} - \frac{S_{hatch}}{2} \right] p \quad (2.23)$$

where  $p$  is the intensity of the electron beam and  $S_{hatch}$  is the area of the hatched region in Fig. 2.7, which can be approximately expressed as

$$S_{hatch} = 2\alpha\beta_L L^2 \quad (2.24)$$

Therefore the signal difference between the quadrants (A+D) and (B+C) can be expressed as

$$(I_A + I_D) - (I_B + I_C) = 4\alpha\beta_L L^2 p \quad (2.25)$$

The essence of this equation is that it indicates the DPC signal is proportional to the Lorentz diffraction angle  $\beta_L$ , i.e. DPC Lorentz microscopy is a linear technique.

In terms of wave-optic theory, the image formation of the DPC Lorentz microscopy is explained using the equation (2.21). If  $R(k_x, k_y)$  is set to a constant 1, then the sum signal is acquired. In this case, a bright field image is obtained. On the other hand, if  $R(k_x, k_y)$  is set to be

$$R(k_x, k_y) = \begin{cases} 1 & k_x > 0 \\ -1 & k_x < 0 \end{cases} \quad (2.26)$$

then a DPC image is acquired.  $R(k_x, k_y)$  can be chosen in many other ways and thus the resulting DPC images can be used to map the magnetic induction along a certain direction (mapping direction). This is shown in Fig. 2.8 for the example of a simple solenoidal domain structure. Using this 4 quadrant detector, 4 independent mapping directions can be obtained at  $45^\circ$  intervals. Usually the magnetic structure of a specimen is determined by

recording DPC images along two orthogonal mapping directions.

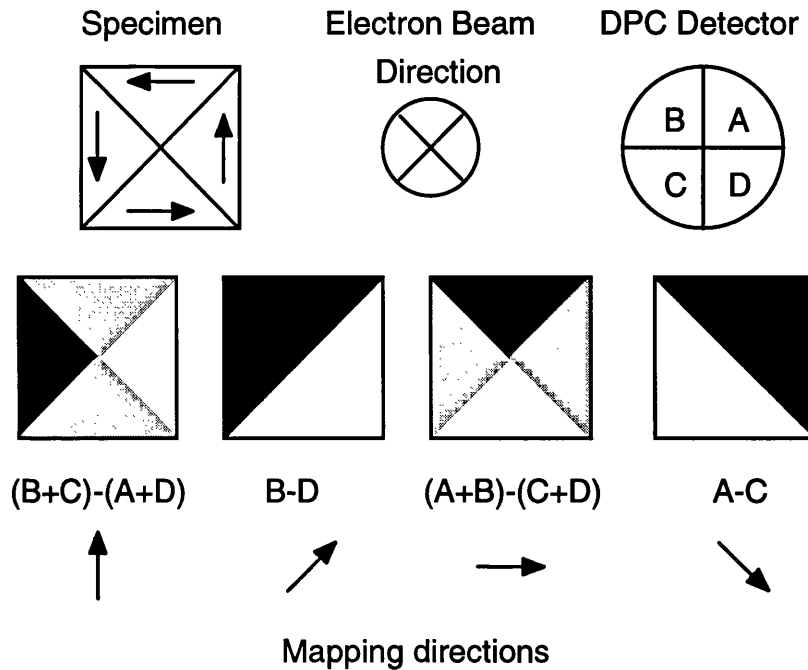


*Fig. 2.8 Schematic diagram of the DPC images of a solenoidal domain structure as shown in the top left corner using different signal combinations (mapping directions).*

### 2.4.3 MDPC mode of Lorentz microscopy

The theoretical explanation of the DPC imaging mode has been given by Dekkers and de Lang (1974) in terms of the phase modification of the electron wave. Their major conclusions are that the DPC image only presents the phase modification information and the intensity is proportional to the gradient of the phase modulation. Since the crystalline structure of a specimen can also modify the phase of the wave, the acquired DPC images comprise both the magnetic and crystalline information. The crystalline contrast is "noise" from the view point of magnetic imaging and it is important to reduce it so as to obtain a high quality magnetic DPC image. This is accomplished using the modified differential phase contrast (MDPC) mode of Lorentz microscopy.

Fig. 2.9 is a schematic diagram of a MDPC detector, which comprises a four-

quadrant DPC detector surrounded by an annular detector. Chapman et al. (1990) demonstrated that by acquiring MDPC images using the annular detector, signals with medium band spatial frequencies can be significantly suppressed while signals with low band spatial frequencies are almost unaffected. Due to the fact that the crystalline signal has a medium band spatial frequency and the magnetic domain structure has a low band spatial frequency, the MDPC images achieve high signal to noise ratio (SNR).

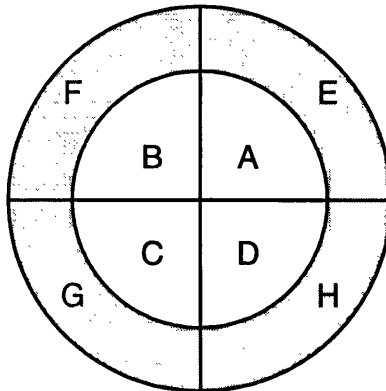


*Fig. 2.9 Schematic diagram of an 8 segment MDPC detector. Only the E, F, G and H segments are used in the MDPC imaging mode.*

The merits of DPC/MDPC imaging mode are:

- (1) It provides quantitative information on induction components of each domain perpendicular to the electron trajectory.
- (2) The bright field image can be acquired simultaneously by collecting the sum signal.
- (3) To an excellent approximation, the contrast of the (M)DPC images is a linear function of the Lorentz deflection angle  $\beta_L$ .
- (4) In the MDPC imaging mode, the SNR is improved for low band spatial frequency signals compared to DPC imaging.

#### **2.4.4 VG HB5 STEM and eXL acquisition system**

In the Solid State Physics group at the University of Glasgow, the MDPC imaging mode is implemented on a VG HB5 STEM equipped with a field emission gun and is usually performed with the acceleration voltage set at 100 kV. Illumination of the specimen in the STEM is normally controlled by the two condenser lenses C1 and C2 and the objective lens. However, as the field of the objective lens is strong (about 0.8T) which may affect the magnetic configurations of the specimens investigated in this work, it is switched off during the MDPC imaging. The magnification of the C1 lens is bigger than 1 while the magnification of the C2 lens is 1, thus, in order to obtain a small probe C2 is used as the probe forming lens. The probe angle is defined by the selected area aperture and in this work it is set at 100  $\mu\text{m}$  (diameter). Three post specimen lenses (P1, P2 and P3) are fitted in this STEM which allow a wide range of camera lengths to be used. Such an arrangement is extremely advantageous as it means that the size of the bright field cone in the detector plane may be matched to the physical dimensions of the detector. For the specimens investigated in this work, we found by setting P1=6, P3=6 and P2 is switched off, high quality MDPC images can be obtained. An Oxford Instruments eXL computer system is linked to the STEM to collect signals from the MDPC detector and converts them into images. Using such an acquisition system, signals can be acquired from several channels simultaneously and usually three channels are used to collect 2 orthogonal MDPC images and a bright field image. The final images are formed normally by acquiring several frames and taking the average of them. The advantage of doing so is that the random noise level is reduced. The images can be in either 16 bit or 8 bit raw data format (Appendix 1). However, if the 8 bit format is used, the average function is disabled and therefore may result in noisy images. Hence, all MDPC images in this work are acquired in 16 bit format.

In Chapter 5, MDPC images will be analysed quantitatively using commercial software. As this software can only process 8 bit format images, it is necessary that the original 16 bit format images are converted into 8 bit format. The details about this process can be found in Appendix 1.

## 2.5 Magnetic force microscope (MFM)

### 2.5.1 Introduction

The first magnetic force microscope (MFM) images were obtained by Martin and Wickramasinghe (1987) from a magnetic recording head with the instrument operated in static mode. The success of their instrument has stimulated research in this field and MFM has been applied to study various magnetic specimens.

In this section, the basic principle of the MFM will be discussed first in section 2.5.2. This leads to the instrumentation requirement which is detailed in section 2.5.3. The evolution of MFM tip from the bulk tip to the state-of-art needle tip is given in section 2.5.4.

### 2.5.2 Basic principle and instrumentation of MFM imaging

The most important part of a MFM is the sensor, which is a flexible cantilever spring incorporating a sharp tip at the end. While the tip is scanning over a magnetic sample, it experiences a magnetostatic force  $\mathbf{F}(\mathbf{r})$  due to its interaction with the stray field of the sample. The most significant effects of this magnetostatic interaction between the tip and the specimen's stray field are

(1) The cantilever is deflected by the force. According to Hooke's law, the magnitude of the deflection is a linear function of  $\mathbf{F}(\mathbf{r})$ . Thus MFM images can be acquired by detecting the deflection of the cantilever while the cantilever is scanning over the specimen. This is so called static mode operation of a MFM.

(2) The resonance frequency of the cantilever is changed due to the force gradient. Therefore, another type of MFM image can also be acquired by detecting the amount of shift of the resonance frequency. Under such condition, the MFM is operated in dynamic mode.

### 2.5.3 Instrumentation of MFM

Fig. 2.10 illustrates the basic set up of a MFM. The sample is mounted on a piezo scanner so that it can be moved in the X, Y and Z directions. This is controlled by the voltage input  $U_x$ ,  $U_y$  and  $U_z$  respectively. The tip is set at a short distance (flying height) from the specimen and the cantilever is deflected; the resonance frequency is changed due to the tip-sample interaction. Such changes are detected by the detector above the cantilever so that output signal  $U_o$  is generated. One part of  $U_o$  is sent to the computer to form the MFM image while the other part is sent back to the piezo scanner to stabilise the imaging condition according to  $U_{set}$ .

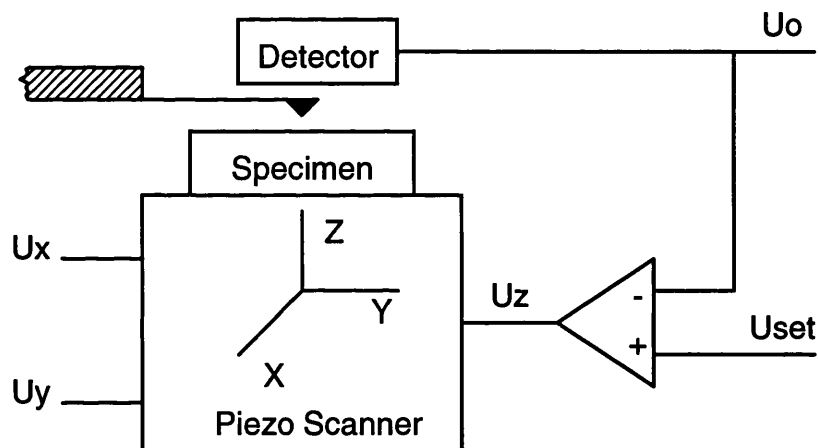


Fig. 2.10 Schematic diagram of a basic MFM set up.

Several methods have been used in MFM to detect the interaction. Tunnelling techniques utilise electron tunnelling between the cantilever and an STM (Scanning Tunnelling Microscope) tip located behind the cantilever to detect cantilever displacement; this has been used by Grütter et al. (1988). One disadvantage of the tunnelling sensor is that the cantilever must be conducting and be reasonably free of contamination so that a good tunnel junction is formed. Optical detection is currently the most prevalent sensing method for MFM and it can detect deflections in excess of 100 nm while the tunnelling technique is restricted to below 1 nm. In the MFM which has been built in our collaboration lab at the Manchester Metropolitan University, the interferometric optical detecting system is used and the details will be

discussed in chapter 5.

#### 2.5.4 Evolution of MFM tips

Since the birth of MFM, several types of MFM tips have been successfully employed. The first generation was the bulk tip which is fabricated from fine, electrochemically etched ferromagnetic wires such as iron, nickel and cobalt (Martin and Wickramasinghe, 1987), amorphous FeBSiC wires (Iijima and Yasuda 1988) and nickel foil (Saenz et al. 1987). The merit of the bulk tip is its simplicity of fabrication. The tip-sample interaction has been studied by Rugar et al. (1990), Schönenberger and Alvarado (1990), Wadas and Grütter (1989), Wadas and Guntherodt (1990) and Grütter et al. (1992). One of the main conclusions of their work is that the best achievable resolution is limited by the tip radius and the tip-sample separation (flying height of the tip). Thus the magnetic volume of the tip plays a major role in determining the resolution. As the bulk tip has a large magnetic volume, it suffers from relatively low resolution compared with other types of tip. The MFM imaging of thin film magnetic recording media was performed recently using a tungsten bulk tip and it suggests that such tip is capable of observing 50 nm details (Porthun et al. 1994).

Modern semiconductor technologies have allowed atomic force microscope (AFM) sensors with tip radii around 20 nm to be fabricated. Usually the AFM sensors are fabricated using non-magnetic materials such as  $\text{Si}_3\text{N}_4$ . By coating such AFM sensors with a thin layer of magnetic film, the second generation of MFM tip - thin film tip is obtained. The study of such type of tip will be discussed in Chapter 5. Magnetic thin film tips have substantial advantages over bulk tips and they are listed below.

(1) As the magnetic film is usually thinner than 50 nm, the magnetic volume of the tip is reduced and this is beneficial to high resolution MFM imaging. The MFM imaging performed by Valera et al (1995) indicates that such a tip has revealed domain structure with 30 nm details.

(2) The stray field of the tip is significantly reduced compared to a bulk tip (Grütter et al. 1991) so that it is expected to be more applicable to the study of soft magnetic materials.

(3) Its magnetic properties can be controlled by choosing an appropriate coating material.

The most recent development in the AFM tip fabrication is that non-magnetic needles have been obtained using an electron beam induced deposition (EBID) technique in a SEM (Fischer et al. 1993). The radius of such needles can be as small as a few nm. It is expected that most future MFM tips will be made by such tips coated with magnetic material. They are termed needle tips although the magnetic coating is also a thin film. As the needles provide an even sharper apex than the thin film tip, they have great potential for high resolution MFM imaging. Initial Lorentz microscopy studies of such tips will be detailed in Chapter 7.

## Chapter 3

# Specimen preparation and characterisation

### 3.1 Introduction

The interests in regularly shaped magnetic thin film elements are twofold. Firstly, they provide ideal systems for the theoretical investigations of magnetic phenomena on small scales. The energies of various magnetic configurations were calculated by Kittel (1946) in terms of domain boundary, magnetostatic and anisotropy energies. It was found for sufficiently small dimensions, the optimum structure consists of a single domain. More recent theoretical study of the magnetising process in micron scaled permalloy elements ( $\sim 2 \mu\text{m}$  long) was performed by Fredkin and Koehler (1990) using micromagnetics. By assuming that external fields are applied along the long in-plane axes of the elements, they determined the values of the fields where domain nucleation and reversal occur. Rectangular elements on the scale of about  $10 \mu\text{m}$  with uniaxial anisotropy were simulated by Schmidts and Kronmüller (1994). They calculated the remanent states for different ratios of the anisotropy and magnetostatic energies so that the critical dimensions for single domain elements were determined. Moreover the demagnetising curves were also obtained. Secondly, on the experimental side, the small elements have great potential to be used as magnetic storage media or sensors. Lo et al. (1985) proposed that by utilising the “Y” shaped domain wall structures in Ni-Fe thin film elements memory bits could be obtained and the data rates of 50 ns coincident current write and a 250 ns non-destructive read were achieved. In addition some thin film elements have been sandwiched into spin valve reading heads and good experimental results have been obtained (Tsang et al. 1994).

The magnetic elements are usually fabricated using lithographic techniques. Photolithography is the simplest one to implement and the magnetic elements used in early experimental studies were produced by a combination of photolithography and thermal evaporation or sputter etching techniques (Huijjer and Watson 1979). However, since the resolution of the photolithography technique is limited by the wavelength of the light used to

expose patterns, which is typically about several hundred nanometres, the sizes of the elements were usually relative large. Electron beam lithography uses accelerated electrons which have much shorter wavelength to define the patterns. Therefore it has superior resolution and enables patterns with in-plane dimensions of about 0.1  $\mu\text{m}$  (McVitie 1988) to be fabricated. In this work, all the magnetic elements are fabricated using electron beam lithography. The details of thermal evaporation, electron beam lithography and fabrication of the small elements samples used in this work will be discussed in section 3.4, 3.5 and 3.6 respectively.

It has been discussed in Chapter 2 that Lorentz microscopies performed in CTEMs or STEMs can provide superior resolution compared to optical techniques; thus they are chosen to characterise samples in this work. Since electrons can only travel a very short distance in a specimen due to the scattering effect, it is necessary that the element is fabricated on a thin support so that it can be imaged using CTEM or STEM. This is achieved by using  $\text{Si}_3\text{N}_4$  membrane substrates which will be described in section 3.3.

The magnetic force microscope (MFM) is also a powerful technique in the characterisation of magnetic samples. The principle and instrumentation of MFM has been given in Chapter 2. In this work, commercial  $\text{Si}_3\text{N}_4$  AFM Microlevers<sup>TM</sup> supplied by Park Scientific Instrument are made suitable for MFM study by coating with a thin layer of magnetic film. The coating and cleaning processes as well as the preparation of MFM tip samples for imaging in VG HB5 STEM and JEOL 2000FX CTEM/STEM will be detailed in section 3.7. An in-plane ac-demagnetising stage and an in-situ magnetising stage have been built and used in this work; they are detailed in section 3.8.

## **3.2 Materials studied in this work**

Two magnetic materials are studied in this work: permalloy ( $\text{Ni}_{82.5}\text{Fe}_{17.5}$ ) and cobalt. They are investigated in the form of continuous thin films or patterned thin films (thin film elements).

The reason for using permalloy is that it is a soft ferromagnetic material with negligible crystalline anisotropy so that the domain structure is dominantly determined by exchange energy and magnetostatic energy. Anisotropy

energy may occur due to externally induced easy axes. Such an easy axis can be induced by evaporating the sample at an oblique angle (Chapter 5) or by applying an external magnetic field in the evaporation process (Rührig 1994).

Permalloy elements with micron scale dimensions have been studied by McVitie and Chapman (1988) using Lorentz microscopy. These elements contain fully exchange coupled grains (Wong et al. 1992). They concluded that the in-plane ratio ( $R$ ) of dimensions of the element is an essential factor determining the domain structure (McVitie 1988). The behaviour of the permalloy elements in an external field was investigated by Hefferman et al. (1991) by performing in-situ magnetising experiments. They found that while  $R$  and the thickness were varied, the magnetising process could be described by three different types of hysteresis loop.

Cobalt films are studied in this work because they represent a magnetically harder ferromagnetic material. This is important for MFM application since single domain tips with high coercivity are necessary for quantitative and consistent MFM imaging (refer to Chapter 5). Previous studies of Co films suggest that by varying the evaporation conditions micron sized elements with reduced exchange coupling between grains can support a near uniform magnetisation (Wong et al. 1992). Although this is achieved by using slow-rate evaporation to degrade the deposition conditions and therefore induces impurity atoms incorporated at grain boundaries, it serves as a useful means to obtain a near uniform domain structure on the MFM tip (Chapter 5).

### 3.3 $\text{Si}_3\text{N}_4$ membrane substrate

Fig. 3.1 is the schematic diagram showing the profile (a) and top view (b) of the  $\text{Si}_3\text{N}_4$  membrane substrate. The 0.5 mm thick Si is used to support the membrane which is a 120  $\mu\text{m}$  square. The PMMA layers on the  $\text{Si}_3\text{N}_4$  membrane are the electron resists where the patterns are defined during the electron beam lithography process (Mackie 1984). In order that it can be mounted into the specimen holders of the JEOL 2000FX CTEM/STEM (Chapter 2), the in-plane dimension of the substrate is designed to be  $2 \times 2$  mm as indicated in the diagram.

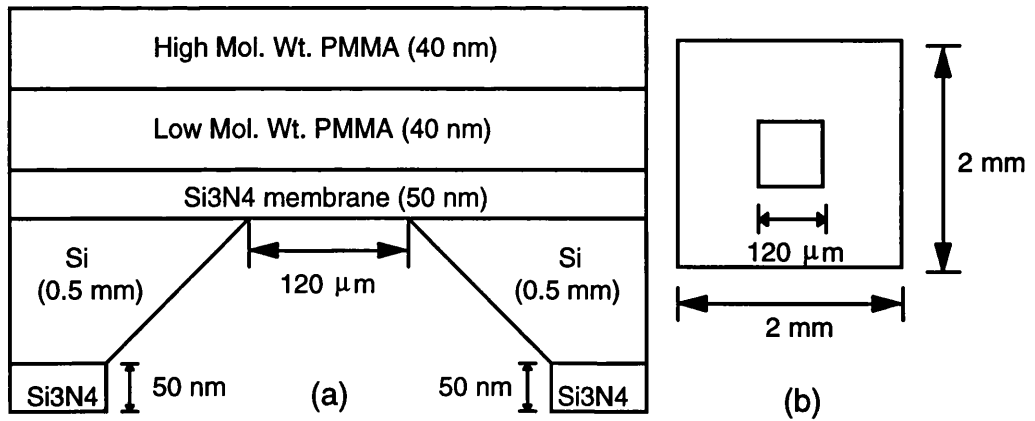


*Fig. 3.1 The schematic drawing of a Si<sub>3</sub>N<sub>4</sub> membrane substrate. (a) Profile. (b) Top view.*

### 3.4 Thermal evaporation of magnetic thin films

Thermal evaporation is a well established technique for the deposition of thin films. The instrumentation consists of essentially a material source, a thickness gauge and a vacuum system. Usually resistive heating is used to heat the material above its melting point so that atoms are emitted and deposited on a substrate placed above it. The deposition rate (evaporation rate) is controlled by adjusting the temperature, which in turn is controlled by adjusting the electric current in the heating coils. In our system, the thickness of the evaporated film is monitored dynamically by a quartz crystal during the evaporation process. The quartz crystal's resonant frequency is a linear function of the film thickness deposited on it and is calibrated preceding the experiments. All of the specimens used in this work are deposited in a vacuum of  $10^{-5}$  mbar. No magnetic field is applied during the evaporation although there are environmental magnetic fields, e.g. the earth's field.

The substrate is usually mounted with its surface at normal incidence to the source during evaporation and this is termed "normal evaporation". The other possible set up is that the surface of the substrate is not normal to the source and this is termed "oblique evaporation". The angle of incidence is defined as the angle between the evaporation beam and the direction normal to the substrate surface.

### 3.5 Electron beam lithography

Electron beam lithography is a state-of-the-art technique for defining sub-micron scaled samples. The principle of electron beam lithography is that the electron resist is exposed in the volume where electrons are incident. This exposed volume is removed while the unexposed area is kept after developing when a positive electron resist is used. The material layer is evaporated after the developing process and it covers the whole surface of the substrate. The elements are preserved on the substrate by the lift-off procedure which is usually performed by immersing samples in acetone to dissolve the electron resist. Electron beam lithography with a positive resist is illustrated in Fig. 3.2

The basic instrumentation required for electron beam lithography is a beam writer which drives electrons to write patterns on the electron resist and a computer control system. This computer control system builds an interface between the beam writer and users so that it works according to the user's commands. The commands are usually written into files to minimise input errors and allow performance of batch jobs. There are essentially two types of file: pattern file and position file. The pattern file comprises the commands which define the shape of patterns. Additionally, it also includes exposure time which the beam writer should use to write patterns. The position file comprises the commands instructing the beam writer where to write the corresponding patterns defined in the pattern file. In this work, a Philips 500 SEM was modified as the beam writer and the computer interface was built by the EBSS (Electron Beam Scanning System) software running in an IBM PC compatible computer. Patterns are defined on the  $\text{Si}_3\text{N}_4$  membrane substrates (section 3.3) using 50keV electrons. More details of this Philips 500 SEM electron beam lithography system can be found in McVitie's PhD thesis (1988).

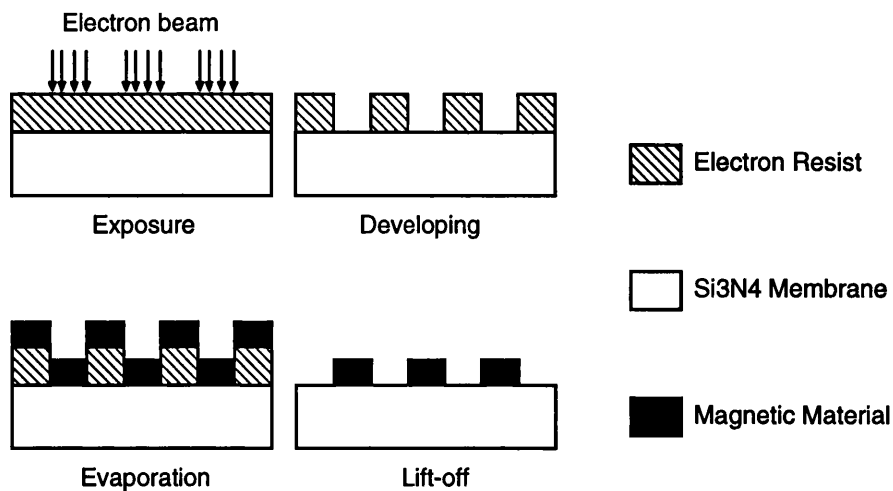


*Fig. 3.2 Schematic diagram showing electron beam lithography process with a positive resist.*

Two programmes have been developed in this work to preview the pattern design and the results of electron beam lithography. They are written in BASIC language and detailed in Appendix 2 and 3 respectively.

### 3.6 Fabrication of small element samples

#### 3.6.1 Elements used in the investigation of induced anisotropy by oblique evaporation

Patterns used in this part of the project are basically rectangles with various values of  $R$  and an anisotropy induced by the oblique evaporation termed the oblique anisotropy. The motivation for varying the  $R$  of these elements is that the shape effect is varied. Furthermore, the effect of the oblique anisotropy on the domain structure of elements with different  $R$  is investigated. As the domain structure of an element could be affected by some local mechanisms such as a pinning centre, the magnetic study results of a single element may not be identical to that of another although they are identical in dimensions. Thus for a given  $R$ , a group of geometrically identical elements (at least 8 elements in a group) are fabricated as a check for reproducibility. Six different groups of elements are fabricated and they are summarised in Table 3.1. The separation between any two elements is at least  $5 \mu\text{m}$  and previous studies (McVitie 1988) indicated that these elements are non-

interacting.

Group	Length ( $\mu\text{m}$ )	Width ( $\mu\text{m}$ )	R
AN1	3.73	1.02	3.7
AN2	4.00	0.92	4.3
AN3	3.73	0.79	4.7
AN4	4.00	0.72	5.5
AN5	3.73	0.50	7.4
AN6	4.00	0.49	8.1

*Table 3.1 The in-plane dimension of the elements used in the study of the oblique anisotropy.*

Permalloy as described in section 3.2 is used in this study. It is found that when the oblique angle exceeds  $30^\circ$ , complete lift off of the excess permalloy film may not be achieved. This is due to the fact that there is no cut-off between the evaporated film on the PMMA layer and on the  $\text{Si}_3\text{N}_4$  membrane. Fig. 3.3 demonstrates this effect schematically. Thus an angle of  $30^\circ$  is chosen for the oblique evaporation.

In order that the thickness of the normal incidence elements is the same as the oblique incidence elements, they are evaporated simultaneously. The calibration of the quartz crystal indicates that films are deposited at the rate of 0.1 nm/s and the thickness of the films is 25 nm. The orientation of the oblique incidence elements is illustrated in Fig. 3.4. It indicates that the length of the AN1, AN3 and AN5 group is normal to the evaporation beam while the width of AN2, AN4 and AN6 group is normal to the beam.

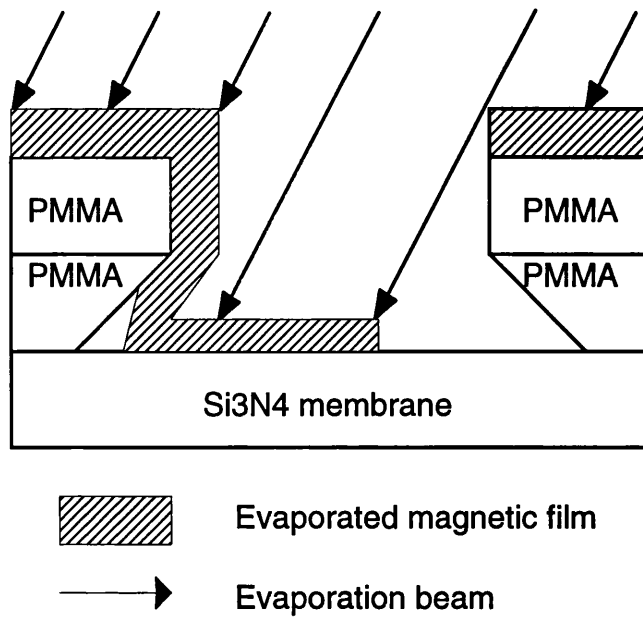


*Fig. 3.3 Obliquely evaporated magnetic thin film does not have a cut-off and therefore causes difficulty in the lift-off process.*

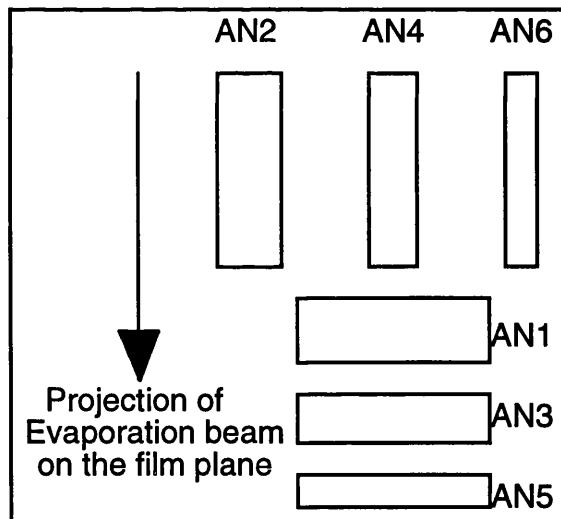


*Fig. 3.4 Schematic diagram showing the orientation of each group of elements during the oblique evaporation.*

### 3.6.2 Simulated MFM tip elements

Fig. 3.5 is the schematic diagram of the top view of a one-face coated MFM tip (section 3.7). The magnetic film is coated on a single triangular face of the

pyramid as well as the whole of the cantilever. Although this forms a near continuous film, the part nearest to the specimen during MFM imaging is triangular in shape and this is the motivation for the design of elements for comparison. By simulating the different geometries, it is hoped that we can get an insight into the properties of the magnetic thin film on the tip.

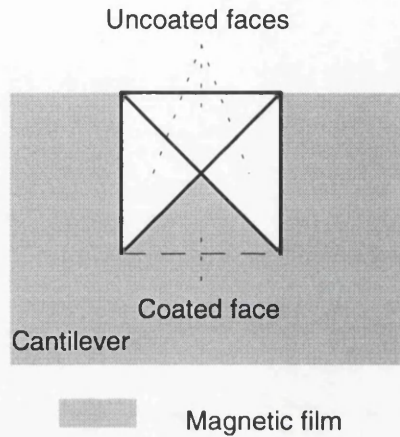


*Fig. 3.5 Schematic diagram of the top view of a one-face coated MFM tip which shows the magnetic film on the pyramid tip and the cantilever.*

Four patterns (SIM1 to SIM4) are designed for this project and they are shown schematically in Fig. 3.6. The cobalt and permalloy specimen are fabricated using normal evaporation at a rate of 0.04 nm/s and 0.1 nm/s respectively. The crystal gauge monitor indicated that 35 nm thick films were deposited. In order to obtain non-interacting elements, they are separated by 10  $\mu\text{m}$  from each other. The details of their physical structure can be found in Chapter 6.

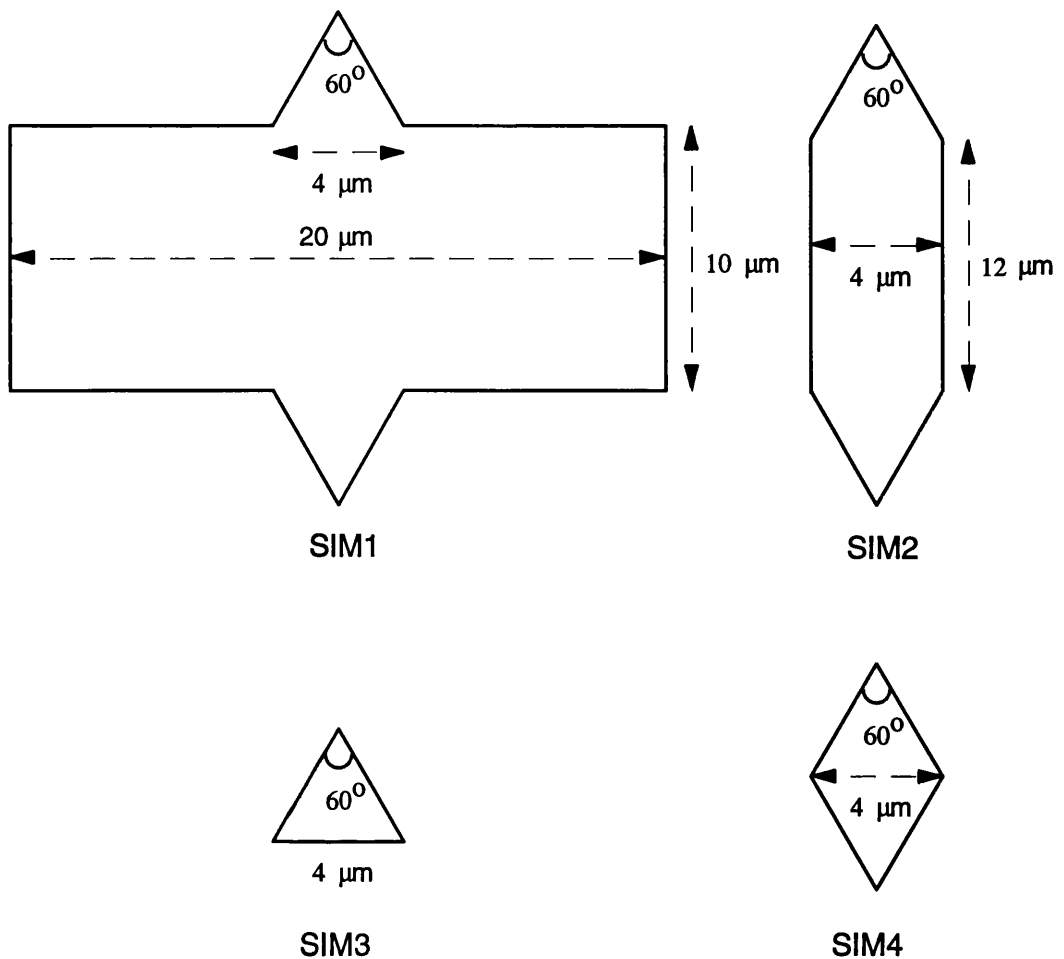


Fig. 3.6 Schematic diagram of the SIM1 to SIM4 patterns.

## 3.7 Fabrication of MFM tips

### 3.7.1 Microlever™

The MFM tips used in this work are fabricated using commercial Microlevers™ supplied by Park Scientific Instrument in California. Each comprises a  $\text{Si}_3\text{N}_4$  spring cantilever on a glass substrate with a  $\text{Si}_3\text{N}_4$  pyramid etched at the end of the cantilever. The edges of the pyramid are 4 μm and each face makes an angle of  $54.7^\circ$  with the plane of the cantilever. This Microlever™ is illustrated by the SEM image and the schematic diagram shown in Fig. 3.7 and 3.8 respectively. The triangular shadow on the cantilever is the result of the deposition of a magnetic thin film and will be discussed in chapter 5.

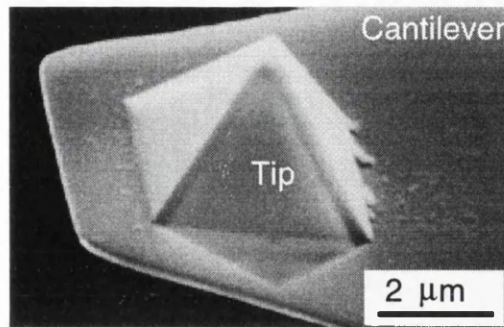


Fig. 3.7 SEM image of the pyramidal tip at the end of the Park Scientific AFM Microlever<sup>TM</sup>.

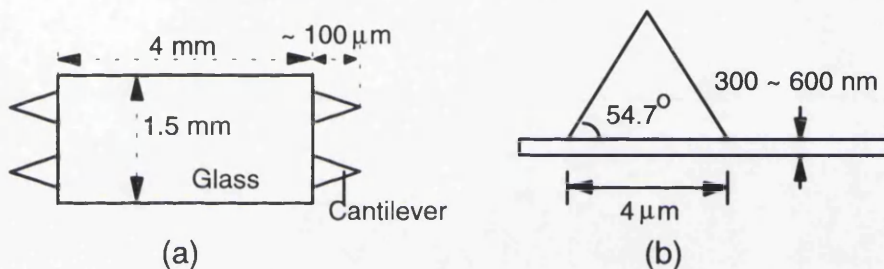
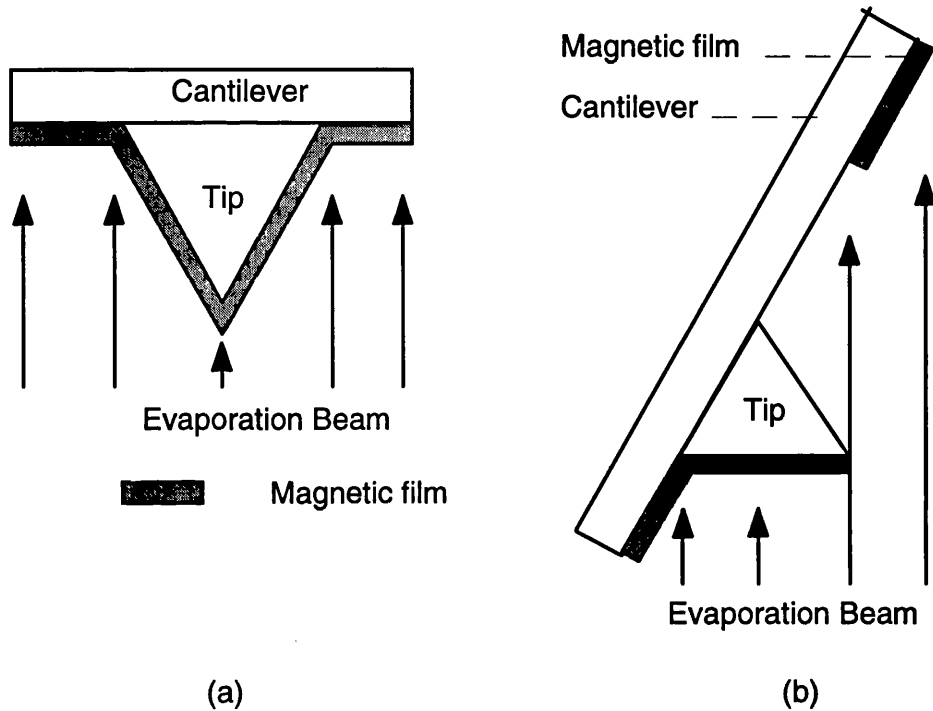


Fig. 3.8 Schematic diagram of (a) the overview of the Microlever<sup>TM</sup> and (b) the tip at the end of the cantilever.

### 3.7.2 Cleaning Microlevers<sup>TM</sup> and coating with magnetic films

The Microlever<sup>TM</sup> was initially designed for atomic force microscopes. The thin film MFM tip used in this work is obtained by coating a thin layer of magnetic material on it. The Microlever<sup>TM</sup> is cleaned before evaporation by holding the glass substrate with fine tweezers and dipping it into acetone. In this process, the surface of the substrate must be perpendicular to the surface of the acetone as the surface tension may deform the fragile cantilever. Pure alcohol is not recommended to be used to clean the Microlever<sup>TM</sup> as it leaves drying marks. The Microlever<sup>TM</sup> is then blown dry using dry N<sub>2</sub> gas to avoid the drying marks and dust contamination. The gas flow should be applied obliquely to the surface of the substrate; otherwise it will destroy the cantilever.

The magnetic material can be coated on the whole surface or one face of the pyramidal tip using normal or oblique thermal evaporation respectively as illustrated in Fig. 3.9. 35 nm thick cobalt film is deposited with an evaporation rate of 0.04 nm/s as our previous studies indicated the cobalt thin film elements of similar dimensions, are capable of supporting near uniform magnetisation (Wong et al 1992). The characterisation of such tips will be detailed in Chapter 5.



*Fig. 3.9 Schematic diagram of coating magnetic film on (a) whole surface of the pyramidal tip and (b) one face of the pyramidal tip.*

### 3.7.3 Preparation of MFM tip samples for examination in the VG HB5 STEM

Modified differential phase contrast magnetic imaging is performed on the VG HB5 STEM (Chapter 2). The specimen cartridge can only take samples with in-plane diameter less than 3 mm. The dimension of the glass substrate of the MFM tip is however 4 mm by 1.5 mm. Therefore, the substrate must be broken into two halves so that one can be mounted into the cartridge. This is accomplished by scribing the central line of the glass substrate using

a fine diamond glass cutter. To avoid the substrate moving during the scribing, it is stuck on a glass slide using a piece of double sided tape. Any debris is removed by rinsing in pure alcohol. Before being mounted into the cartridge, the sample is stuck on a 3 mm copper slot support using a small drop of Ag dag so that it can be secured by the cartridge clip. It is necessary that the sample is stuck on the side so that the cantilever does not block the electron beam during the imaging of the tip. This is demonstrated schematically in Fig. 3.10. In the normal room environment, it usually takes about 1 hour for the Ag dag to dry and therefore the sample should be left about 70 minutes before imaging to avoid contaminating the STEM.

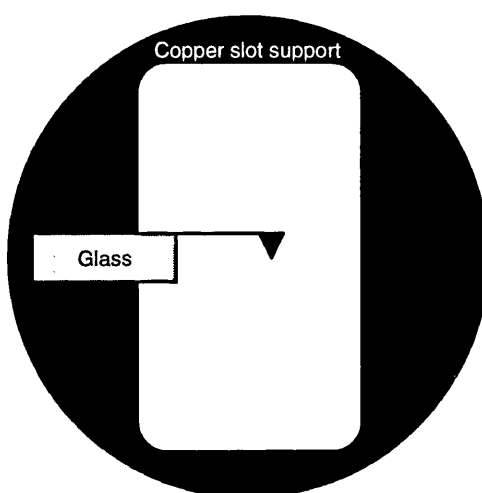


*Fig. 3.10 Schematic diagram showing how to stick an MFM tip sample on a copper slot support so that it can be imaged using the VG HB5 STEM.*

#### **3.7.4 Preparation of the MFM tip samples for examination in the JEOL 2000FX CTEM/STEM**

Foucault and Fresnel imaging are performed in the JEOL 2000FX microscope (Chapter 2). One of the commercial specimen holders can accommodate samples with in-plane dimension  $\sim 23 \times 6$  mm. This space is sufficient for the mounting of the whole of the Microlever<sup>TM</sup>. Nevertheless, the tip sample is rather awkward to secure using normal procedures. Thus, a copper piece is made to support the tip and this piece can be easily mounted in the holder. As the cantilever and tip are opaque to 200 keV electrons, the

specimen is stuck on the side so as to image the stray field projecting from the tip (Chapter 5). Fig. 3.11 shows schematically the copper support and the orientation of the sample secured with a drop of Ag dag.

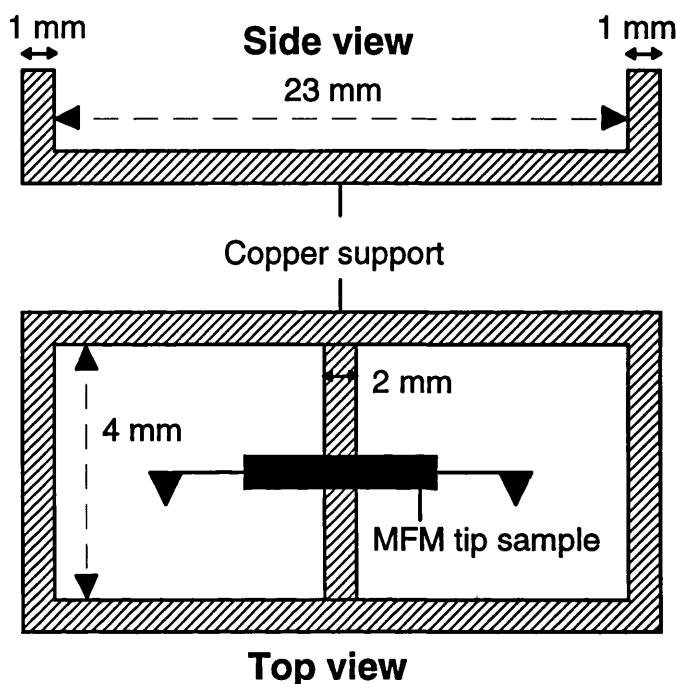


*Fig. 3.11 Schematic diagram showing how to stick an MFM tip sample on a copper support so that it can be imaged using the JEOL 2000FX CTEM/STEM.*

## 3.8 Equipment used in magnetic characterisation

### 3.8.1 Magnetising stage

The domain structure of a magnetic specimen reflects its magnetic history. In order to get a complete understanding of its magnetic properties, the domain structure at each stage of the magnetising process should be known. In the CTEM/STEM, this requires that in-situ magnetising experiments be performed. The commercial specimen holder has allowed specimen to be characterised in various states, however it is not possible to apply a magnetic field to the specimen once in the microscope. In order to overcome this, a special in-situ magnetising stage has been designed by Dr Nicholson. A photograph of this stage is shown in Fig. 3.12. The sample is mounted

between two coils made of silver wires wound round a magnetic core which generates magnetic field in the plane of the sample. The magnitude of the field is proportional to the supplied current which can be monitored and controlled outside the microscope. The relation between them has been calibrated using a Hall probe. It was found that the measurement was very sensitive to the position of the probe. Thus it was performed by setting the probe at the centre between the two coils where the specimens are mounted. This stage is capable of supplying the maximum field of 100 Oe with a step of 0.05 Oe. Moreover, it also allows the sample to be rotated through a maximum angle of about  $270^\circ$  so that the field can be applied along a chosen direction with respect to the specimen. This is especially important in the work discussed in Chapter 5 as we need the magnetic field to be precisely aligned with the edges of the small elements. The sample is first securely mounted on a specially designed copper stub as shown in Fig. 3.13 using Ag dag. This ensures that the specimen is in the centre of the stage. A pair of spring copper wire clips are built in the stage to secure the stub.

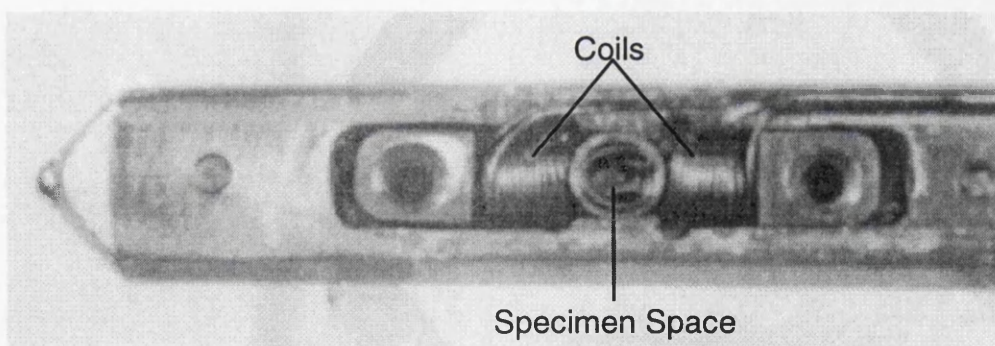


*Fig. 3.12 Photograph of the magnetising stage used in the JEOL 2000FX CTEM/STEM.*

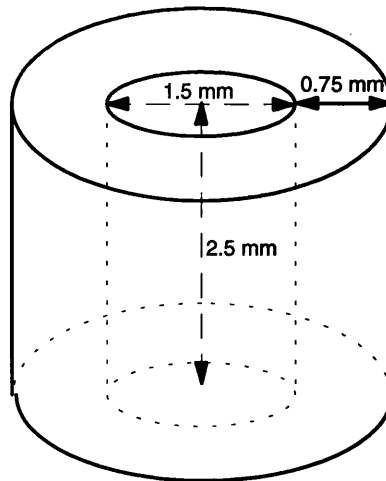


*Fig. 3.13 Schematic diagram of the copper stub used to support membrane samples.*

### 3.8.2 In-plane ac-demagnetising stage

Ac-demagnetisation experiments are performed in the manner that a specimen is subjected to an ac magnetic field with gradually decreasing amplitude. The ac-demagnetisation allows the sample to explore different energy states and the domain structure in the remanent state is expected to reflect a minimum of energy and therefore is of particular interest.

A copper in-plane ac-demagnetising stage has been designed by Dr Heyderman. It is illustrated schematically in Fig. 3.14. The copper stub described earlier (Fig. 3.13) is used to support the specimen in the stage while the stage is connected to a motor and spins in a magnetic field produced by an external electromagnet. All samples investigated in this work support magnetisation lying in the plane of the film. Thus the external field is applied in the plane of the specimen to ac-demagnetise it. The in-plane ac demagnetising experiment is performed by slowly increasing the external field to the maximum of 8000 Oe before it is slowly decreased to zero while the sample is rapidly rotated.

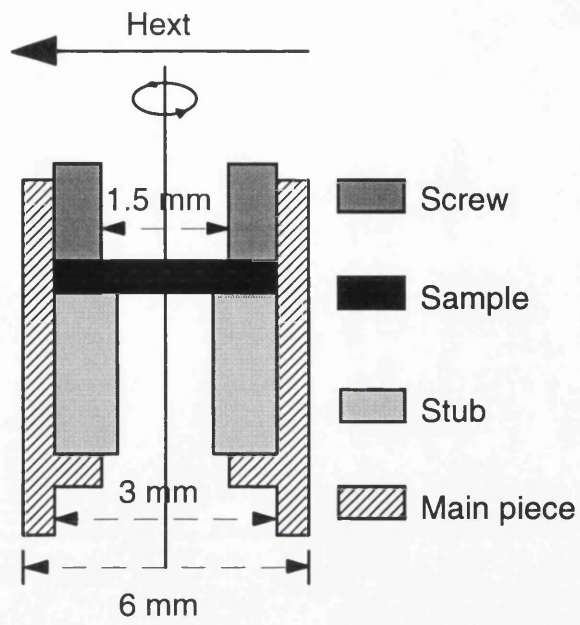


*Fig. 3.14 Schematic diagram of the in-plane ac-demagnetising stage. The sample is secured by the screw.*

## **Chapter 4**

# **Induced anisotropy in permalloy thin film elements by oblique incidence evaporation**

### **4.1 Introduction**

Magnetic anisotropy is an important factor in the determination of magnetic properties of materials. It can be induced by applying an external magnetic field during deposition this defines a favoured direction of the magnetisation (Wilts 1966). Cohen (1961) proposed that another type of anisotropy, which is defined as "oblique anisotropy", can be induced in continuous  $\text{Ni}_{81}\text{Fe}_{19}$  thin films by performing thermal evaporation at oblique angles (Chapter 3). He observed that the shape of the crystal grains is different from that of the film evaporated at normal incidence (Chapter 3) and thus concluded this is responsible for the presence of the oblique anisotropy. In order to discuss this anisotropy, a term "oblique angle" is defined as the angle between the evaporation beam and the direction normal to the surface of a substrate. This term will be used throughout this thesis.

The oblique anisotropy in 30 nm thick continuous permalloy ( $\text{Ni}_{82.5}\text{Fe}_{17.5}$ ) films has been studied. These films are evaporated at  $30^\circ$  and  $80^\circ$  incidence without heating the substrate. Fig. 4.1a is a bright field image recorded from the film evaporated at  $30^\circ$  incidence. The evaporation direction is deduced from the shadow of a piece of debris and indicated by an arrow. Lorentz microscopy is used to characterise the magnetic configuration in the film and it is found that the as-grown and ac-demagnetised states support similar domain structures. This configuration is demonstrated by a Fresnel image in Fig. 4.1b, which is recorded from the ac-demagnetised state of the film. Basically, it comprises large-scaled domains separated by cross-tie walls. The magnetisation is perpendicular to the evaporation beam, indicating the induced easy axis is in this direction.

The permalloy film deposited at  $80^\circ$  incidence is investigated using the Foucault mode of Lorentz microscopy and its domain structure is displayed by a pair of Foucault images in Fig. 4.2a and b. They suggest that the film

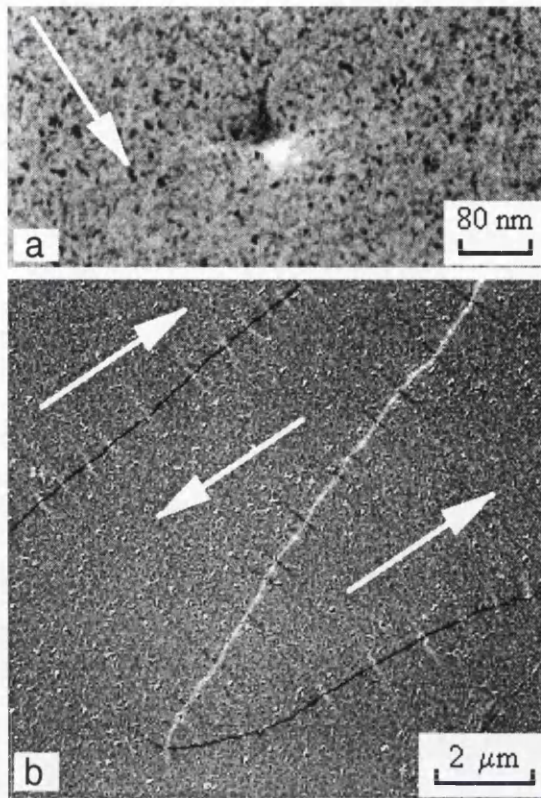


*Fig. 4.1 (a) Crystalline image of the continuous permalloy thin film evaporated at  $30^\circ$  incidence. The arrow indicates the projection of the evaporation beam in the film plane. (b) Fresnel image of the continuous permalloy thin film in the ac-demagnetised state. The arrows indicate the direction of the magnetisation.*

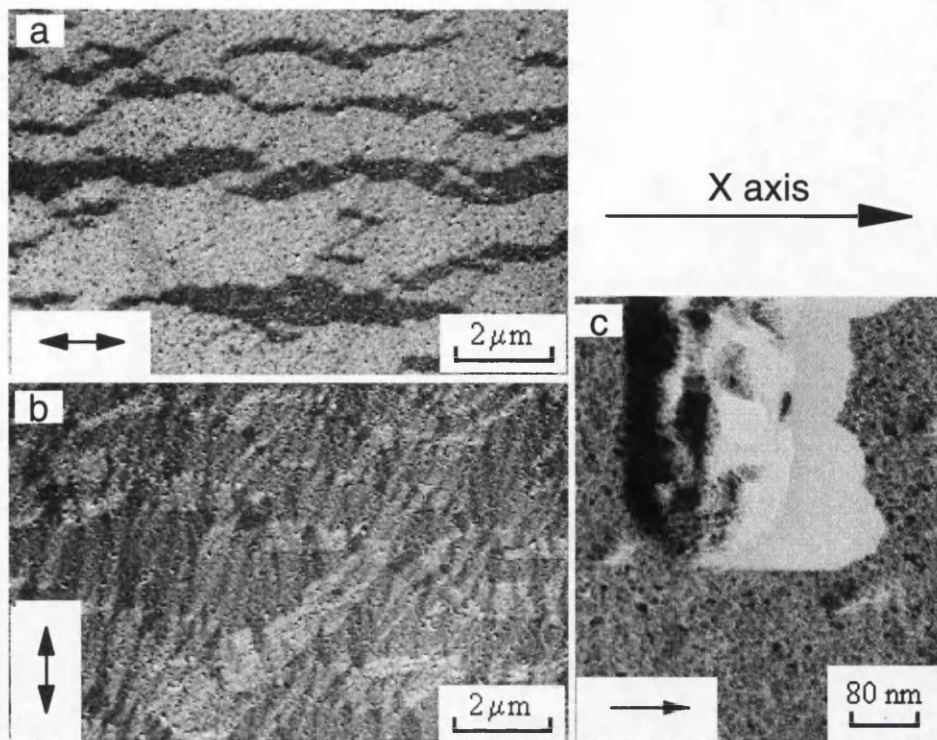


*Fig. 4.2 (a) & (b) Foucault images of the domain structure in the ac-demagnetised state of the continuous permalloy film evaporated at  $80^\circ$  incidence. The arrows indicate the mapping directions. (c) Crystalline image of the specimen. The arrow indicates the projection of the evaporation beam in the film plane.*

supports domains with magnetisation predominantly parallel to the X axis as indicated in the figure. Magnetic ripple is also present, indicating a small degree of divergence in the direction of the magnetisation. The bright field image shown in Fig. 4.2c suggests that the projection of the evaporation beam in the film plane is also parallel to the X axis. Thus, the induced easy axis in the film evaporated at  $80^\circ$  incidence is parallel to the projection of the evaporation beam in the film plane. This is in good agreement with Cohen's work (1961).

The aim of this work is to investigate the induced anisotropy in rectangular permalloy elements evaporated at  $30^\circ$  incidence. This angle was chosen due to problems associated with lift-off operation in the lithography process as discussed in Chapter 3. The elements are defined using patterns AN1 to AN6 and evaporated to a thickness of 25 nm. In order to investigate the effect of the induced anisotropy, geometrically identical elements are fabricated using normal incidence evaporation and studied for comparison. The physical characteristics of the elements are investigated using bright field imaging and electron diffraction techniques (section 4.2). The domain structures of these elements are characterised using the Foucault mode of Lorentz microscopy and drawn schematically in section 4.3. The study of the elements evaporated at normal incidence is presented in section 4.4 whereas the study of the elements evaporated at the oblique incidence is presented in section 4.5 and 4.6. The above studies are performed on the JEOL 200FX CTEM/STEM (Chapter 2) at 200 kV. The ac-demagnetised state of the specimen is obtained utilising the in-plane ac-demagnetising stage (Chapter 3). The major irreversible changes in domain structure are identified by performing in-situ magnetising experiments using the in-situ magnetising stage (Chapter 3). The conclusion of the investigations are drawn in section 4.7.

## **4.2 Physical characteristics of the elements**

### **4.2.1 Elements evaporated at normal incidence**

The electron diffraction pattern of these elements consists of uniform rings, indicating that the elements comprise a polycrystalline structure with randomly orientated grains. Fig. 4.3 is a bright field image recorded from a

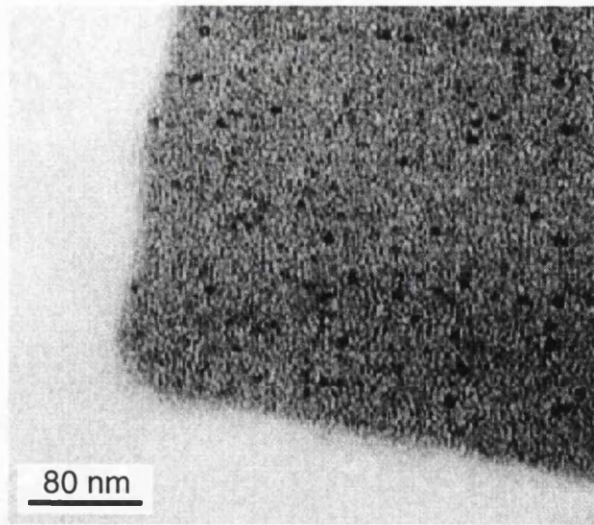


*Fig. 4.3 Bright field image of a thin film element evaporated at the normal incidence.*

corner of an element. The grains are clearly visible and their dimensions are in the range of 5 ~ 10 nm. This image also shows that the element has well defined edges.

#### 4.2.2 Elements evaporated at 30° incidence

The electron diffraction patterns and bright field images of the elements evaporated at 30° incidence are similar to those of the elements evaporated at normal incidence. Furthermore, there is no visible difference in their crystalline structures in the scale at which the imaging is performed. This is different from the study performed by Cohen (1970) as he found that the oblique evaporation results in the formation of crystalline chains or columns depending on incidence angles. A reason may be that our elements are evaporated at a substrate temperature much lower than that used in his experiment (200°C).

#### 4.3 Schematic diagrams of some domain structures

Six types of domain structure are observed in this study. They are demonstrated by schematic diagrams in Fig. 4.4 to Fig. 4.9 and the directions of magnetisation are indicated by arrows. In this chapter,  $V$  represents the total volume of an element while  $V_L$  represents the volume occupied by the component of magnetisation parallel to the long in-plane axis of the element. A term  $Q_L$  is defined as the ratio of  $V_L$  to  $V$ , i.e.  $Q_L = V_L / V$ .

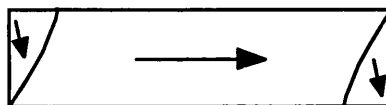


*Fig. 4.4 Schematic diagram of type 1 domain structure. This is a non-solenoidal domain structure.*

Type 1 domain structure has three domains as shown in Fig. 4.4. The central

section is a large domain uniformly magnetised along the long in-plane axis of the element. At either end of the element, a triangular domain occurs. This triangular domain has a component of magnetisation normal to the edge of the element so that  $\mathbf{M} \cdot \mathbf{n} \neq 0$  ( $\mathbf{n}$  represents the unit vector normal to the surface of the element). Therefore, magnetic poles occur on the edges. Type 1 structure is a non-solenoidal domain configuration.

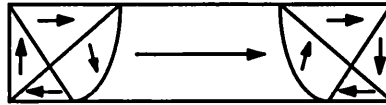


Fig. 4.5 Schematic diagram of type 2 domain structure. This is a non-solenoidal domain structure.

Type 2 domain structure (Fig. 4.5) comprises three sections. The centre of the element is a domain magnetised parallel to the long in-plane axis of the element. At the ends, four domains form a partial flux closure structure and the domain wall separating it from the central section is usually curved, indicating there may be volume magnetic poles due to  $\nabla \cdot \mathbf{M} \neq 0$ . The magnetisation in the end structure is parallel to the nearest edges, i.e.  $\mathbf{M} \cdot \mathbf{n} = 0$ . Thus there are no surface magnetic poles present. Type 2 domain structure is also a non-solenoidal configuration.

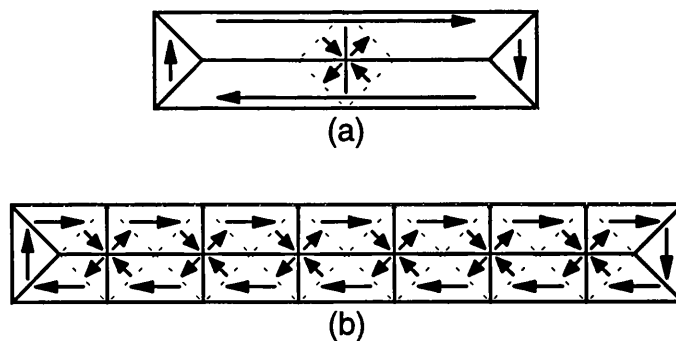
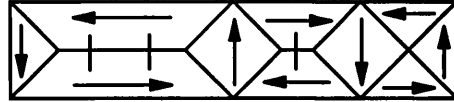


Fig. 4.6 Schematic diagrams of type 3a and 3b domain structures. They are solenoidal domain structures.

Type 3a and type 3b domain structures (Fig. 4.6) are solenoidal. They

support triangular domains at the end of the element magnetised parallel to the edges. In the central section, domains are separated by a cross-tie wall. Therefore, in these configurations  $\mathbf{M} \cdot \mathbf{n} = 0$  so that there are no surface magnetic poles present. Type 3a structure is different from type 3b structure in the number of cross-tie lines present.



*Fig. 4.7 Schematic diagram of type 4 domain structure. It is a solenoidal domain structure.*

Type 4 solenoidal domain structure shown in Fig. 4.7 consists of 4 domains magnetised along the short in-plane axis of the element and 6 domains magnetised along the long in-plane axis of the element. In such a configuration, a domain magnetised along the short in-plane axis and a domain magnetised along the long in-plane axis are always separated by a  $90^\circ$  wall. However, a wall between two domains magnetised along the long in-plane axis is of the cross-tie type. As the magnetisation is always parallel to the nearest edge,  $\mathbf{M} \cdot \mathbf{n} = 0$  so that there are no surface magnetic poles present on the edges.

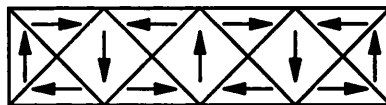


*Fig. 4.8 Schematic diagram of type 5 domain structure. It is a solenoidal domain structure.*

Type 5 domain structure is a solenoidal structure as illustrated by Fig. 4.8. The shape of the domains magnetised along the long in-plane axis is triangular. However, the domains magnetised along the short in-plane axis can be either triangular at the extremities or diamond-shaped in other regions. Therefore, a wall separating a domain magnetised along the long in-

plane axis and a domain magnetised along the short in-plane axis is always of the  $90^\circ$  type. Another characteristic of such domain structure is that the magnetisation is parallel to the edges so that surface magnetic poles do not occur.

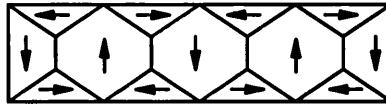


Fig. 4.9 Schematic diagram of type 6 domain structure. It is a solenoidal domain structure.

The type 6 domain structure (Fig. 4.9) supports triangular domains magnetised along the long in-plane axis of the element. The domains magnetised along the short in-plane axis can be both trapezoidal and hexagonal at the end and in the centre of the element respectively. Thus, a wall between two adjacent domains magnetised along the short in-plane axis is always of the  $180^\circ$  type although a wall between a domain magnetised along the short in-plane axis and a domain magnetised along the long in-plane axis is always of the  $90^\circ$  type. Such a configuration is a solenoidal structure and there are no surface magnetic poles present on the edges of the element.

## 4.4 Magnetic study of elements evaporated at normal incidence

### 4.4.1 As-grown state

Foucault imaging of the elements suggests that 2 types of domain structure are supported and they are summarised in Table 4.1. As a number of elements are fabricated for a given ratio of in-plane dimensions  $R$  and they may support different domain structures due to local inhomogeneity, the proportion of each domain structure is given in the last column.

Element	Domain structure	Number of element
AN1 (R = 3.7)	Type 3a	2/8
	Type 2	6/8
AN2 (R = 4.3)	Type 2	15/15
AN3 (R = 4.7)	Type 2	8/8
AN4 (R = 5.5)	Type 2	15/15
AN5 (R = 7.4)	Type 2	10/10
AN6 (R = 8.1)	Type 2	10/10

*Table 4.1 Domain structures supported by the as-grown state of the elements evaporated at normal incidence. A rate m/n means m out of a total of n elements support the particular domain structure stated in the second column of the same row.*

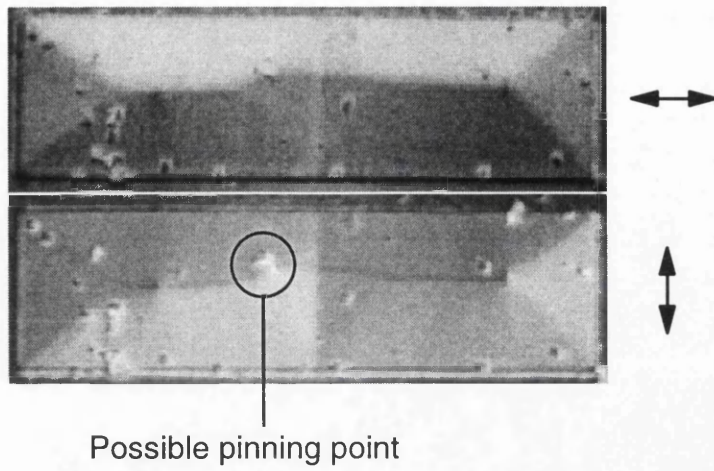
Fig. 4.10 demonstrates a pair of Foucault images recorded from an AN1 element. This is a typical type 3a domain structure and the schematic diagram is shown in Fig. 4.6. However, it is observed that the cross-tie wall is slightly deformed, indicating that there is some local inhomogeneity present. Apparently, there is debris present and a piece of debris is observed in the region where the cross-tie wall is bent. Therefore, it may be a pinning centre.

Fig. 4.11 shows a pair of Foucault images recorded from an AN4 element, which supports type 2 domain structure. Such a domain configuration is also observed in other elements.

As the as-grown state of the element is a unique state determined by the history of the sample, it may not be reproducible. The ac-demagnetised state of the element is a low energy state and the study of it is given in the next section.

#### **4.4.2 Ac-demagnetised state**

The investigation of the ac-demagnetised state of the elements indicates that they support identical domain structures as in the as-grown state (Table 4.1). However, the curved cross-tie wall in type 3a domain structure supported by



*Fig. 4.10 Foucault images of the as-grown state of an AN1 element evaporated at the normal incidence. This is the type 3a solenoidal domain structure.*

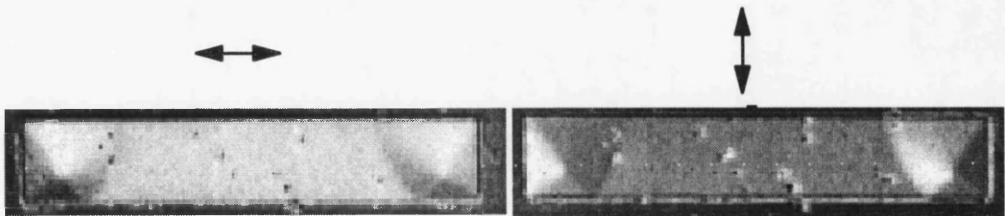


*Fig. 4.11 Foucault images of the as-grown state of an AN4 element evaporated at the normal incidence. This is the type 2 non-solenoidal domain structure.*

the as-grown state of the AN1 element is straight now. This suggests that the local inhomogeneity has been overcome by the ac-demagnetising field. It is also found that the central sections of the elements supporting type 2 domain structure are magnetised along either direction parallel to the long in-plane axis of the element, indicating both configurations are equal-energy states. As type 2 and type 3a structures are supported by the ac-demagnetised states, they are low energy and reproducible domain configurations.

The permalloy used in this study has a low value of magnetocrystalline anisotropy so that the anisotropy energy can be taken as zero. Thus, the energy terms in the element studied in this section are magnetostatic energy and exchange energy. The magnetostatic energy is a result of the presence of magnetic poles. The non-zero divergence of the magnetisation ( $\nabla \cdot \mathbf{M} \neq 0$ ) gives rise to volume magnetic poles while  $\mathbf{M} \cdot \mathbf{n} \neq 0$  gives rise to surface magnetic poles. The exchange energy is determined by the orientation of magnetic moments (Chapter 1) and it is usually associated with the presence of domain walls. A domain structure in an element is a result of the trade off between these energy terms, which is usually called the shape effect.

This shape effect has been the subject of a study for permalloy elements of 60 nm and 20 nm thick (McVitie 1988). For those with R of 4 or less, solenoidal domain structures were observed like those of type 5 for example. Elements with R greater than 4 supported non-solenoidal structures such as the type 2 configuration, which significantly has a much shorter total length of domain wall compared to the type 5 structure. This illustrates the balance between magnetostatic energy and exchange energy.

For an element with small R, solenoidal domain structures are favoured as they reduce magnetostatic energy and the domain wall length is short so that the resultant exchange energy is limited. Previous work conducted by McVitie (1988) and Hefferman (1991a) on permalloy elements with thickness of a few hundred angstroms indicated that R = 4 is approximately the ratio of in-plane dimensions separating the solenoidal structure from the non-solenoidal structure. The AN1 element studied in this section has a R = 3.7. As this value is close to 4, it is reasonable that this element can support both type 2 non-solenoidal structure and type 3a solenoidal structure depending on its history.

The shape effect in elements with different R is demonstrated quantitatively by the measurements of  $Q_L$  (Table 4.2), which are obtained from type 2 domain structure. For type 3a domain structure in the AN1 element,  $Q_L$  is 0.81. It is noticed that  $Q_L$  is always greater than 0.5. This confirms that for these elements, magnetisation parallel to the long in-plane axis of the element is favoured by the shape effect. It is also apparent that  $Q_L$  increases monotonically as R increases, indicating the magnetisation parallel to the long in-plane axis is more favoured by increasingly acicular elements. More detailed discussion on this issue will be given in Section 4.7.

Element	AN1 (R = 3.7)	AN2 (R = 4.3)	AN3 (R = 4.7)	AN4 (R = 5.5)	AN5 (R = 7.4)	AN6 (R = 8.1)
$Q_L$	0.74	0.79	0.83	0.85	0.88	0.90

Table 4.2  $Q_L$  measured from type 2 domain structure of the elements evaporated at normal incident.

#### 4.4.3 In-situ magnetising experiments

Remanent states of these elements are produced by magnetising them in a  $-8000$  Oe field directed parallel to the long in-plane axis and then reducing the field to zero. This is the state from which the in-situ magnetising experiment starts. Initially, the external field  $H_{ext}$  is directed towards the positive direction; while it is increased, domain wall movement and nucleation are observed. In order to identify these major irreversible changes in domain structure, the elements are consistently monitored using the Foucault mode of Lorentz microscopy. Since this study is performed on a group of elements for each given R, it is expected that for different elements there are small differences (usually in the range of 2 to 5 Oe) in the magnitude of the critical field whereby the irreversible changes occur. Therefore, a critical field is given at which the irreversible changes have taken place in at least 80% of the elements with the same R. The net magnetisation parallel to the long in-plane axis of the element is defined as  $M = (V_+ - V_-) / V$  where  $V_+$  and  $V_-$  represent the volumes occupied by

domains which are magnetised along the positive and negative directions respectively.

The Foucault images recorded from the remanent states of the elements indicate that they support type 2 domain structure (Fig. 4.5) and the central domains are magnetised along the negative direction. The net magnetisation in this state is termed  $-M_r$ . As the behaviour of these elements is similar during the in-situ magnetising process, the major irreversible changes in domain structure are shown in Fig. 4.12 by a series of Foucault images recorded from the AN2 element. The principle of such an imaging mode indicates that in an image mapped along the positive direction, bright, grey and dark regions represent domains magnetised parallel, normal and antiparallel to the positive direction respectively. As  $H_{\text{ext}}$  increases, domains with magnetisation parallel to the field direction expand whereas domains with magnetisation antiparallel to the field direction shrink. In addition, the volume of the domains with magnetisation normal to the field direction also increases. Although these elements still support type 2 domain structure, the net magnetisation increases slightly.

A concertina domain structure (Hefferman 1991a) occurs in the AN1, AN2, AN3 and AN4 elements when  $H_{\text{ext}}$  is close to coercivity  $H_c$ , i.e.  $H_{\text{ext}} = H_c - \Delta H = H_{c-}$  where  $\Delta H$  is a small positive field. A schematic diagram of the concertina structure is given Fig. 4.12. As brightness variation is observed in the central section, the magnetisation is no longer uniform there; instead a considerable component of magnetisation has been introduced perpendicular to the long in-plane axis of the element. Thus, the net magnetisation is further increased to a negative value  $-M_{c-}$ . The concertina structure is not observed in the AN5 and AN6 elements during the magnetising process.

Once  $H_{\text{ext}}$  exceeds the coercivity  $H_c$  ( $H_{\text{ext}} = H_c + \Delta H = H_{c+}$ ), the magnetisation in the central section suddenly switches to the positive direction and type 2 domain structure is restored. In the Foucault image mapped along the positive direction, it can be observed that most of the volume of the element is bright, indicating positive magnetisation. The consequence of this switching is that the net magnetisation jumps abruptly to a positive value  $M_{c+}$ .

Further increase of  $H_{\text{ext}}$  from  $H_{c+}$  to 100 Oe results in negligible changes in

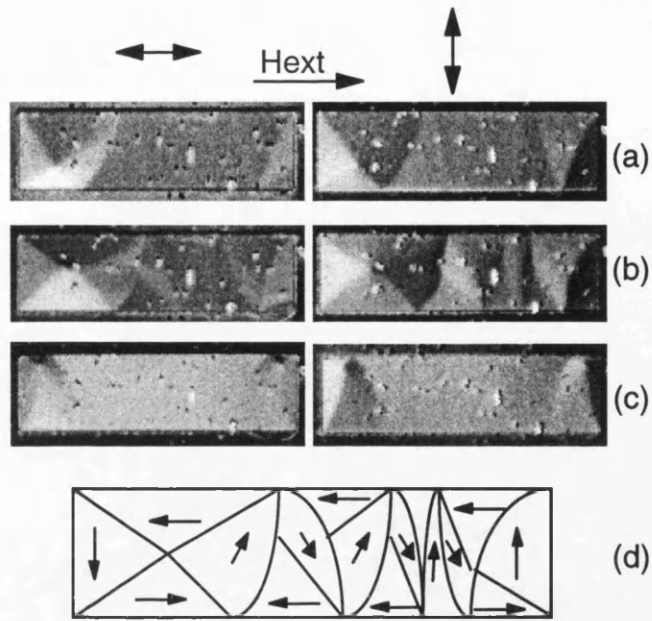


Fig. 4.12 Foucault images showing the irreversible changes in the domain structure of the elements evaporated at normal incidence. (a) Remanent state ( $H_{ext} = 0$ ). (b) Concertina domain structure ( $H_{ext} = H_{c-}$ ). (c) Type 2 domain structure ( $H_{ext} = H_{c+}$ ). (d) Schematic diagram of the concertina domain structure.

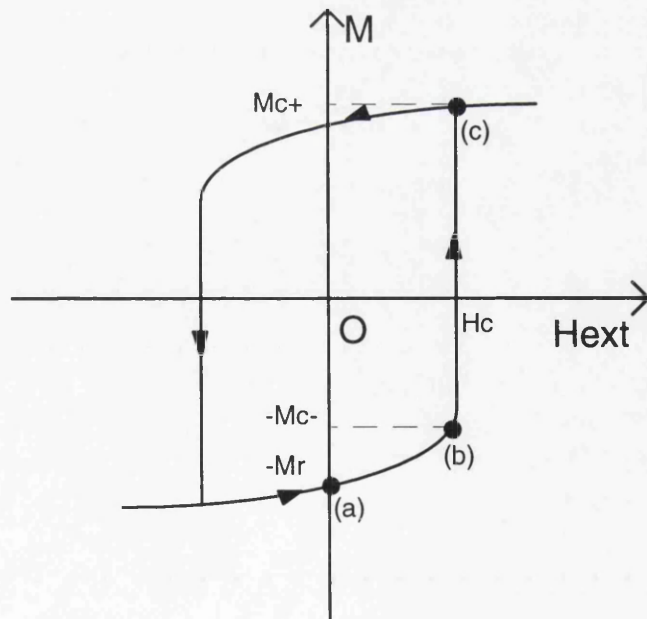


Fig. 4.13 Schematic drawing of the type A hysteresis loop. Points (a), (b) and (c) refer to the magnetic states shown in Fig. 4.12.

domain structure and net magnetisation. The reduction of  $H_{\text{ext}}$  from 100 Oe to 0 results in a reduction of net magnetisation although type 2 domain structure is maintained. The net magnetisation in this state is  $M_r$ .

The above major irreversible changes in domain structure are illustrated by a schematic hysteresis loop shown in Fig. 4.13 and it is termed a type A hysteresis loop. The parameters of the hysteresis loop  $H_c$ ,  $M_r$ ,  $M_{c-}$  and  $M_{c+}$  are different for different elements and summarised in Table 4.3.

	$H_c$ (Oe)	$M_r$	$M_{c-}$	$M_{c+}$
AN1 (R = 3.7)	28	0.62	0.31	0.82
AN2 (R = 4.3)	29	0.63	0.32	0.83
AN3 (R = 4.7)	32	0.73	0.42	0.89
AN4 (R = 5.5)	34	0.74	0.42	0.90
AN5 (R = 7.4)	47	0.82	0.57	0.91
AN6 (R = 8.1)	48	0.84	0.63	0.93

Table 4.3 Parameters of type A hysteresis loops, which are obtained from the elements evaporated at normal incidence.

## 4.5 Magnetic study of AN2, AN4 and AN6 elements evaporated at oblique incidence

In Chapter 3, it has been described that the long in-plane axes of the AN2, AN4 and AN6 elements evaporated at  $30^\circ$  incidence are normal to the evaporation beam. Therefore, according to the studies of the continuous film evaporated at the same oblique angle (section 4.1), an easy axis parallel to the long in-plane axis is induced in the elements.

### 4.5.1 As-grown state

The domain structures supported by the elements are summarised in Table 4.4.

Element	Domain Structure	Number of element
AN2 (R = 4.3)	Type 1	15/15
AN4 (R = 5.5)	Type 1	14/15
	Type 2	1/15
AN6 (R = 8.1)	Type 1	10/10

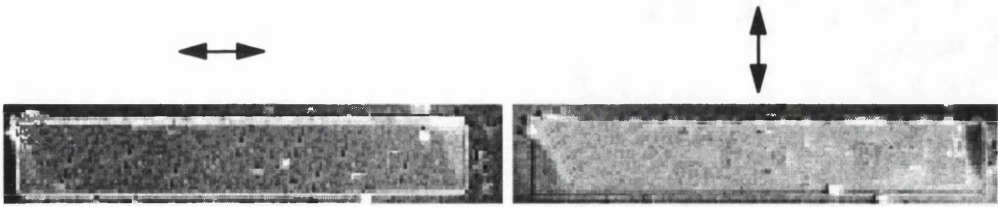
*Table 4.4 Domain structures supported by the as-grown state of the AN2, AN4 and AN6 elements evaporated at oblique incidence. These elements possess an induced easy axis parallel to their long in-plane axis.*

Fig. 4.14 displays a pair of Foucault images of type 1 domain structure recorded from the AN4 element. Brightness variations due to stray field have been observed at the end of the element during the experiment, indicating that there are magnetic poles on the edges of the element. This is why we propose that the magnetisation has a component normal to the surface at the end of the element in the schematic diagram (Fig. 4.4). The type 2 domain structure is supported by only one of the AN4 elements and demonstrated by the Foucault images in Fig. 4.15.

#### 4.5.2 Ac-demagnetised state

The ac-demagnetised state of the elements is the same as the as-grown state. Therefore, both type 1 and type 2 domain structures are stable and reproducible states. Although the AN2, AN4 and AN6 elements evaporated at normal incidence have the same geometry as the elements studied in this section, they support different domain structures. This reflects the effect of the induced anisotropy.

In type 1 domain structure,  $M \cdot n \neq 0$ , i.e. there are surface magnetic poles. The curved domain walls may also result in volume magnetic poles due to  $\nabla \cdot M \neq 0$ . Since the magnetisation in the end domains has a component normal to the direction of the induced easy axis, there is also a energy contribution from the induced anisotropy. Therefore, the total energy of the



*Fig. 4.14 Foucault images of a type 1 domain structure. They are recorded from the as grown state of the AN4 element evaporated at oblique incidence. This element comprises an induced easy along the long in-plane axis of the element.*

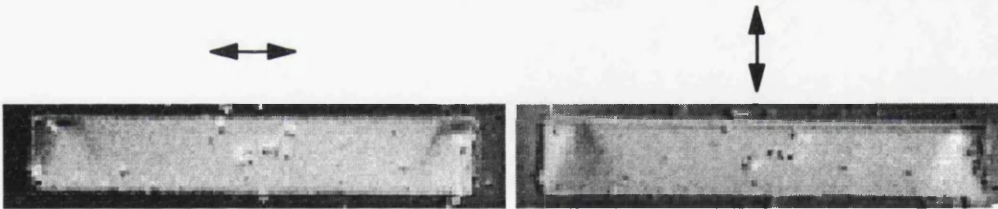


*Fig. 4.15 Foucault images of a type 2 domain structure. They are recorded from the as grown state of the AN4 element evaporated at oblique incidence. This element comprises an induced easy along the long in-plane axis of the element.*

type 1 domain structure is the sum of surface magnetostatic energy, volume magnetostatic energy, exchange energy and anisotropy energy.

In type 2 domain structure supported by the normal incidence elements, the magnetisation is parallel to the edges at the end of the elements. Hence, there is no surface magnetostatic energy contribution. Furthermore, since the elements are evaporated at normal incidence, the anisotropy energy is zero. Therefore, the total energy in the type 2 domain structure is the sum of volume magnetostatic energy and exchange energy.

The length of domain walls in the type 2 structure is longer than in the type 1 structure which may give rise to higher exchange energy and volume magnetostatic energy. Clearly the presence of the induced anisotropy favours the type 1 structure in which there is a large domain magnetised in the easy axis direction with the walls at the end to reduce the volume magnetostatic and exchange energy contributions.

One of the AN4 elements evaporated at the oblique incidence also supports the type 2 domain structure. However, the comparison between Fig. 4.11 and Fig. 4.15 indicates that the volume of the uniformly magnetised section in the centre of the element evaporated at the oblique incidence is larger. Therefore, it is expected that the  $Q_L$  is different and this is also an effect of the induced easy axis.  $Q_L$  is measured from these elements and summarised in Table 4.5. The detailed discussion of  $Q_L$  vs R in terms of shape effect and induced anisotropy will be given in section 4.7.

Element	AN2 (R = 4.3)	AN4 (R = 5.5)	AN6 (R = 8.1)
$Q_L$	0.93*	0.96*, 0.94**	0.98*

\* measured from type 1 domain structure.

\*\* measured from type 2 domain structure.

*Table 4.5  $Q_L$  measured from the ac-demagnetised state of the AN2, AN4 and AN6 elements evaporated at oblique incidence. These elements comprise an induced easy axis parallel to the long in-plane axis.*

### 4.5.3 In-situ magnetising experiment

The in-situ magnetising experiments start with the remanent state produced in the same manner as described in Section 4.4.3. It is observed that only type 1 domain structure (Fig. 4.4) is supported in this state and the net magnetisation is a negative value  $-M_r$ . While the external field is applied, the domain wall movement and magnetisation reversal are observed. The occurrence of the irreversible changes in domain structure is similar in these elements and is illustrated by the Foucault images recorded from the AN2 element in Fig. 4.16.

Initially, the external field is applied antiparallel to the magnetisation in the central section of the elements which has been magnetised along the negative direction. While the field increases, the domain at the end of the element expands slightly although the element still comprises type 1 domain structure. As a result of that, the net magnetisation  $M$  also increases. At  $H_{\text{ext}} = H_{c-}$ , brightness variation due to the deviation of magnetisation from the long in-plane axis direction is present in regions close to the end structure. However, the magnetisation throughout the central section is still reasonably uniform. The concertina structure which was present in the element evaporated at normal incidence (Fig 4.12) is not seen here. This may be due to the fact that the induced easy axis is parallel to the long in-plane axis thus makes the component of magnetisation normal to the easy axis energetically unfavoured. Such a domain structure is demonstrated by the schematic diagram shown in Fig. 4.16 and the net magnetisation in this state is still a negative value  $-M_{c-}$ .

As soon as the external field exceeds  $H_c$ , the magnetisation in the central domain suddenly switches to the positive direction. In the meantime, the shape and the magnetisation of the end domains are also changed as demonstrated by Fig. 4.16c. A consequence of these irreversible changes is that the net magnetisation jumps from the negative value  $-M_{c-}$  to a positive value  $M_{c+}$ .

It is found that the maximum field 100 Oe supplied by the in-situ magnetising stage is not sufficient to saturate the elements as domains are still visible at the end of the element. When the field is removed, the resultant state is also

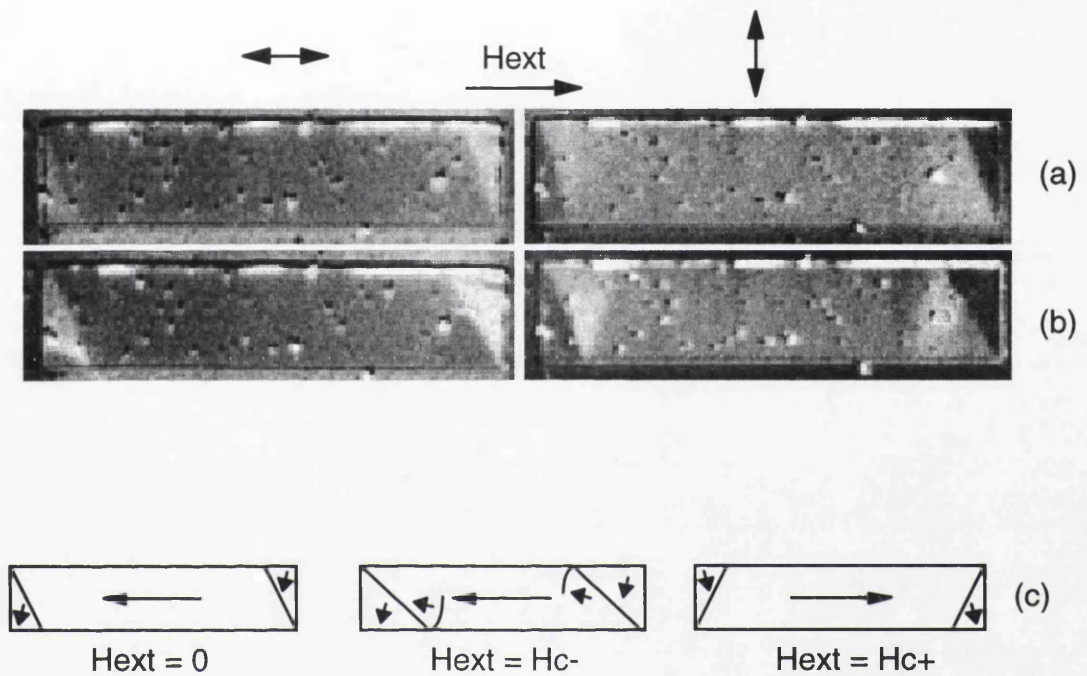


Fig. 4.16 (a) Foucault images showing the remanent state ( $H_{ext} = 0$ ) of the AN2 element evaporated at the oblique incidence. (b) Foucault images showing the domain structure of the AN2 element evaporated at oblique incidence at  $H_{ext} = H_c$ . (c) Schematic diagram demonstrating irreversible changes in domain structure that occurred during the in-situ magnetising process.

type 1 domain structure although the magnetisation in the central section is reversed compared to the initial state. The behaviour of the elements during these in-situ magnetising experiments can also be represented by the type A hysteresis loop shown schematically in Fig. 4.13. The parameters of the hysteresis loop are measured from each element and summarised in Table 4.6.

Element	$H_c$ (Oe)	$M_r$	$M_{c-}$	$M_{c+}$
AN2 (R = 4.3)	53	0.90	0.80	0.93
AN4 (R = 5.5)	58	0.94	0.85	0.95
AN6 (R = 8.1)	82	0.98	0.90	0.98

*Table. 4.6 Hysteresis loop parameters of the AN2, AN4 and AN6 elements evaporated at oblique incidence. These elements possess an induced easy axis parallel to the long in-plane axis.*

## 4.6 Magnetic study of AN1, AN3 and AN5 elements evaporated at oblique incidence

The AN1, AN3 and AN5 elements studied in this section are evaporated with their short in-plane axis normal to the evaporation beam. Therefore, they have an induced easy axis parallel to the short in-plane axis in contrast to the elements studied in the previous section. As a consequence, they possess different magnetic properties which will be investigated in this section.

### 4.6.1 As-grown state

Four types of domain structure are observed in these elements (Table 4.7). Basically, they are solenoidal configurations comprising regularly shaped domains. Foucault images of these domain structures have been recorded and the results are summarised below.

Element	Domain Structure	Number of element
AN1 (R = 3.7)	Type 6	8/8
AN3 (R = 4.7)	Type 5	8/8
AN5 (R = 7.4)	Type 3b	9/10
	Type 4	1/10

*Table 4.7 Domain structures supported in the as-grown state of the AN1, AN3 and AN5 elements evaporated at oblique incidence. They have an induced easy axis parallel to the short in-plane axis of the element.*

The Foucault images of type 3b, type 4, type 5 and type 6 domain structures are given in Fig. 4.17, Fig. 4.18, Fig. 4.19 and Fig. 4.20 respectively. The major features of these domain configurations have been described along with their schematic diagrams in Section 4.3.

#### 4.6.2 Ac-demagnetised state

The Foucault mode of Lorentz microscopy studies of these elements suggest that the AN1 and AN3 elements support the same domain structures as in the as-grown state. However, the AN5 element in the ac-demagnetised state only supports type 3b domain structure. Thus type 3b, type 5 and type 6 domain structures are the reproducible magnetic configurations of these elements whilst type 4 structure may be a result of the unique history of the element.  $Q_L$  is measured from these reproducible structures and summarised in Table 4.8.

Element	AN1 (R = 3.7)	AN3 (R = 4.7)	AN5 (R = 7.4)
$Q_L$	0.31	0.50	0.71

*Table 4.8  $Q_L$  of AN1, AN3 and AN5 elements evaporated at oblique incidence.*

Previous studies have indicated that the major domain structure supported by AN1, AN3 and AN5 elements evaporated at normal incidence is type 2 non-solenoidal structure, which is due to the shape effect. The elements

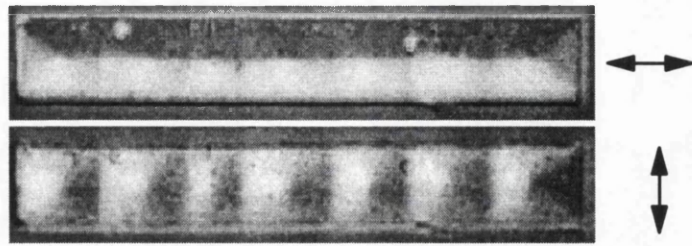


*Fig. 4.17 Foucault images of the type 3b solenoidal domain structure. It is recorded from an AN5 element evaporated at oblique incidence.*

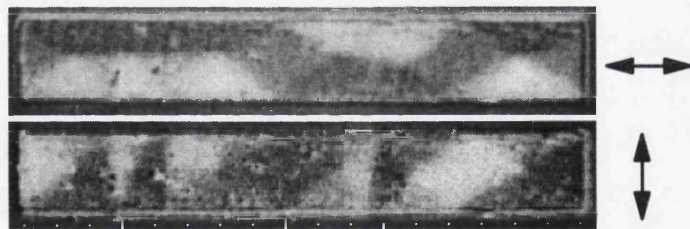


*Fig. 4.18 Foucault images of the type 4 solenoidal domain structure. It is recorded from an AN5 element evaporated at oblique incidence.*

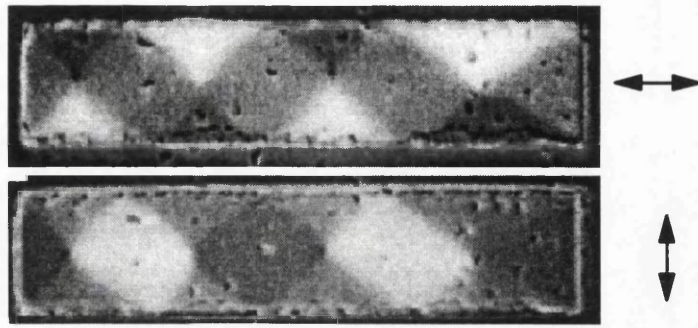


*Fig. 4.19 Foucault images of the type 5 solenoidal domain structure. It is recorded from an AN3 element evaporated at oblique incidence.*

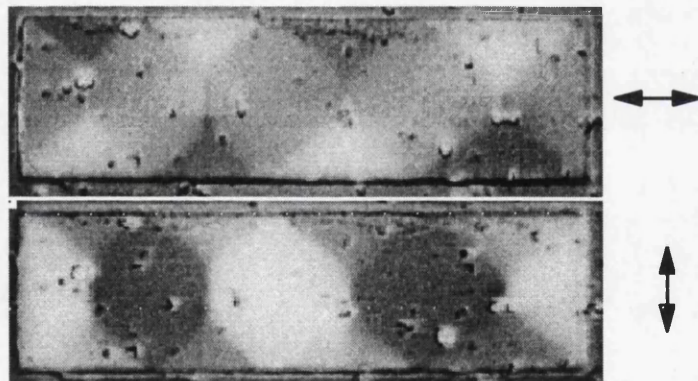


*Fig. 4.20 Foucault images of the type 6 solenoidal domain structure. It is recorded from an AN1 element evaporated at oblique incidence.*

studied in this section have identical geometry to those elements but they support solenoidal domain structures. The probable reason is that there is an extra energy term - anisotropy energy, which also plays an important role. Therefore the final magnetic state of the element is determined by the trade off between the shape effect and the anisotropy. The measurements of  $Q_L$  (Table 4.8) provide important information on the induced anisotropy, which will be extracted in the conclusion section by the comparison of  $Q_L$  between elements evaporated under different conditions.

### **4.6.3 In-situ magnetising experiment**

#### **4.6.3.1 AN1 and AN3 elements**

For the AN1 and AN3 elements evaporated at oblique incidence, this experiment starts from the remanent state, which is produced by applying a  $-8000$  Oe field along the long in-plane axis of the element. The occurrence of irreversible changes in domain configuration in both elements is similar and it is illustrated in Fig. 4.21 by the Foucault images recorded from the AN1 element. The schematic hysteresis loop is drawn in Fig. 4.22. Since the type B and type C loops were observed by Hefferman et al (1991b), this new loop is named the type D loop.

The remanent states are type 6 and 5 domain structures for the AN1 and AN3 elements respectively, which are the same as the structures in their ac-demagnetised state. While the external field is increased to  $100$  Oe, instead of being saturated, both elements comprise type 2 non-solenoidal domain structure (Fig. 4.21a). From this state, the external field is reduced gradually, but there are no significant changes in domain structure so that the net magnetisation is almost unchanged. A solenoidal domain structure is restored as soon as the field is reduced to less than  $H_2$  and this structure is demonstrated by the schematic diagram (Fig. 4.21b). This results in an abrupt reduction in the net magnetisation to  $M_2$ . When the field is removed, the element supports a solenoidal structure (Fig. 4.21c) with a non-zero magnetisation  $M_r$ .

After  $H_{\text{ext}}$  is reduced to zero, the direction of the external field is reversed. As the field is decreased, the solenoidal domain structure is gradually changed

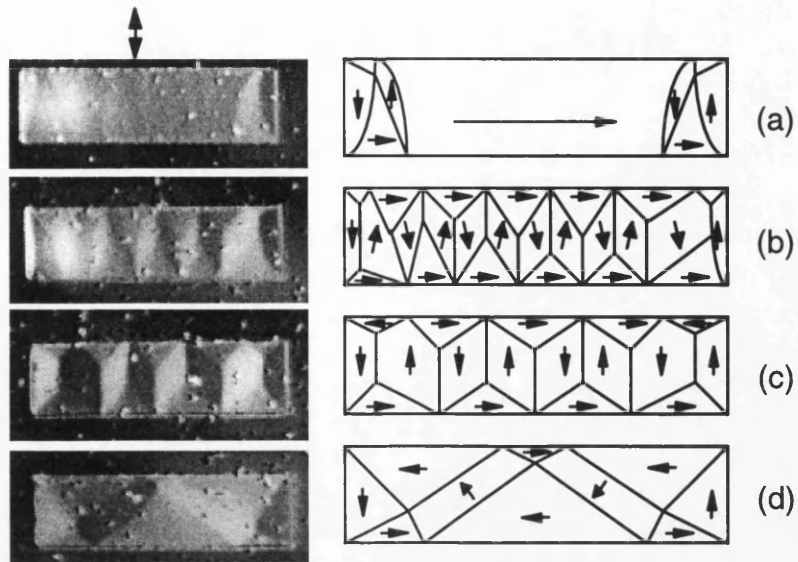


Fig. 4.21 Foucault images recorded from the AN1 element evaporated at oblique incidence during the in-situ magnetising experiment. (a)  $H_{\text{ext}} = 100 \text{ Oe}$ . (b)  $H_{\text{ext}} = H_2 - \Delta H$ . (c)  $H_{\text{ext}} = 0$ . (d)  $H_{\text{ext}} = -H_1 + \Delta H$ . The major irreversible changes can be described by a type D hysteresis loop.

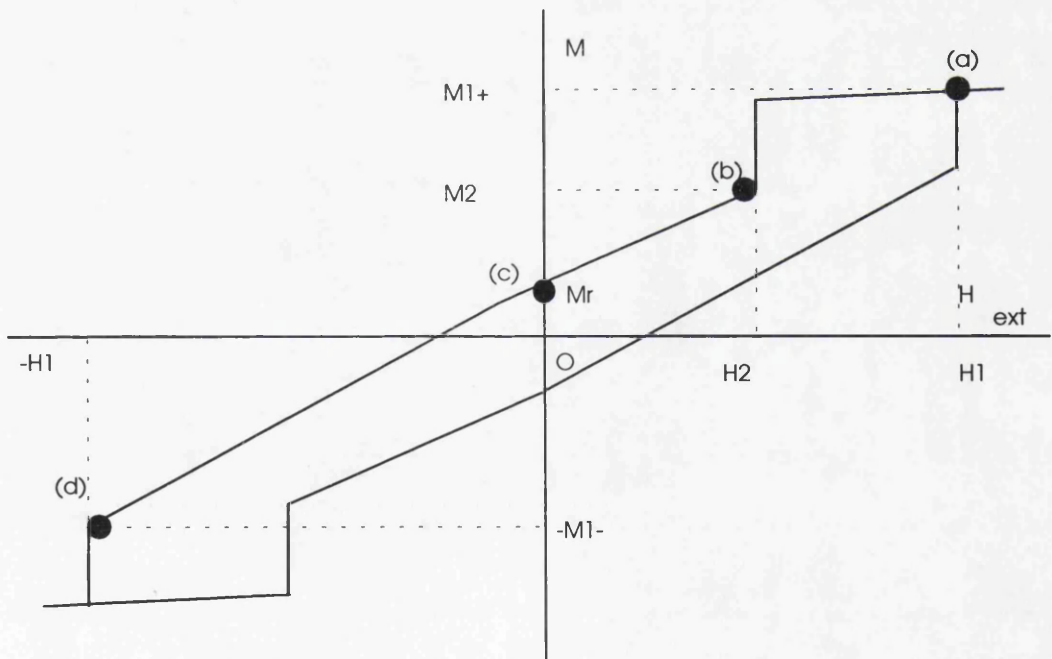


Fig. 4.22 Schematic diagram of a type D hysteresis loop.

to another solenoidal domain structure shown in Fig. 4.21d and the net magnetisation is also decreased to  $-M_{1-}$ . The magnetisation process in this field range consists of lots of small changes in domain structure. Once the field exceeds  $-H_1$ , the type 2 non-solenoidal domain structure occurs with the central section magnetised along the negative direction. In this state, the domain structure is similar to the reversed type 2 domain structure at  $H_{\text{ext}} = 100 \text{ Oe}$  and the net magnetisation is measured to be  $-M_{1+}$ . Further reduction in  $H_{\text{ext}}$  down to  $-100 \text{ Oe}$  does not result in significant changes in domain configuration although the net magnetisation decreases slightly due to expansion of domains magnetised parallel to the external field.

When the external field is increased from this state up to  $100 \text{ Oe}$ , the magnetisation process follows a similar path as shown by the hysteresis loop. The hysteresis loop parameters of these two elements are different and are summarised in Table 4.9.

Element	$H_1$	$H_2$	$M_{1-}$	$M_{1+}$	$M_2$	$M_r$
AN1 (R=3.7)	48	30	0.53	0.79	0.33	0.20
AN3 (R=4.7)	53	20	0.30	0.89	0.25	0.15

*Table 4.9 Hysteresis loop parameters of the AN1 and AN3 elements evaporated at oblique incidence. The induced easy axis in these elements is parallel to the short in-plane axis.*

#### 4.6.3.2 AN5 elements

For the AN5 elements evaporated at oblique incidence, the in-situ magnetising experiment starts from the remanent state. The Foucault mode of Lorentz microscopy suggests that type 2 domain structure (Fig. 4.5) is the only configuration supported by the element.

Starting from the same type of domain structure as that of the AN5 element evaporated at normal incidence, the in-situ magnetising of the AN5 element evaporated at the oblique incidence consists of similar irreversible changes. Thus, it can also be described using a type A hysteresis loop. Table 4.10 summarises the parameters of the hysteresis loop.

Element	$H_c$ (Oe)	$M_r$	$M_c$	$M_{ct}$
AN5 ( $R = 7.4$ )	45	0.82	0.50	0.91

*Table 4.10 Hysteresis loop parameters of the AN5 element evaporated at oblique incidence. The induced easy axis in this element is parallel to the short in-plane axis.*

## 4.7 Comparison and conclusion

The characterisation of the elements evaporated at normal incidence suggests that the shape effect is an important factor in determining domain structure. For the elements with  $R > 4$  (AN2 to AN6), the shape effect results in type 2 non-solenoidal domain structure as a low energy state. For the elements with  $R$  close to 4 (AN1), the shape effect results in both type 3a solenoidal and type 2 non-solenoidal domain structures. In conjunction with McVitie (1988) and Hefferman's work (1991a) on 20 nm and 60 nm thick permalloy elements, it is expected that the shape effect favours solenoidal structures as low energy states for the 25 nm thick permalloy elements with  $R < 4$ . Therefore, 4 is roughly the value of  $R$  determining whether the element supports solenoidal or non-solenoidal domain structures at this thickness.

The study of the continuous thin film evaporated at oblique angles suggests that an easy axis is induced in the element perpendicular to the evaporation beam for  $30^\circ$  incidence evaporation. In the AN2, AN4 and AN6 elements, it is parallel to the long in-plane axis whilst it is parallel to the short in-plane axis in the AN1, AN3 and AN5 elements. For geometrically identical elements, the shape effect is the same. However, as the elements evaporated at the oblique incidence comprise an easy axis, there is an extra term - anisotropy energy - contributing to the total energy so that the final domain structure is the co-effect of the shape and induced anisotropy. As a result of that, they are expected to support different domain structures from the elements evaporated at normal incidence. This has been observed by using the Foucault mode of Lorentz microscopy.

$Q_L$  has been measured from each element in the ac-demagnetised state. By plotting  $Q_L$  vs  $R$  for the elements evaporated under the same condition, the shape effect is demonstrated. Moreover, by comparing the plots of elements with and without an induced easy axis, the effect of the induced anisotropy is extracted. This is demonstrated in Fig. 4.23

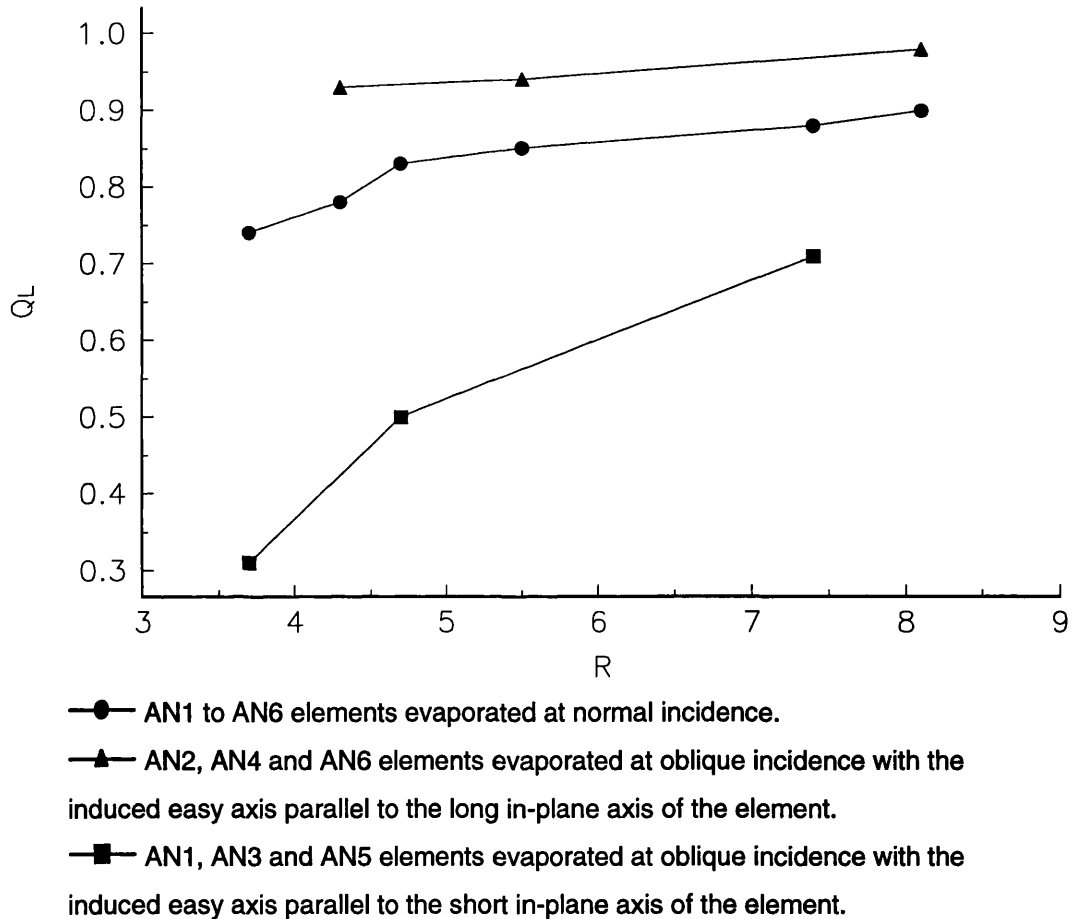
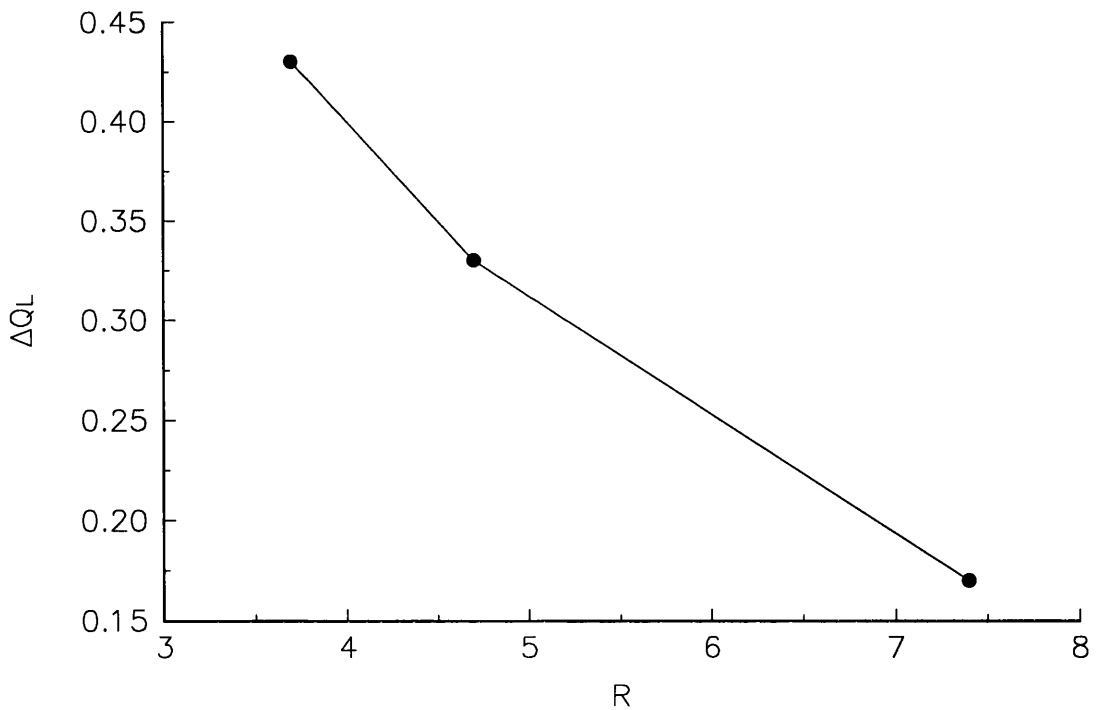


Fig. 4.23 Dependence of  $Q_L$  on  $R$ , reflecting the effect of the shape and the induced anisotropy.

Fig. 4.23 consists of three monotonically increasing curves as  $R$  increases. For the elements evaporated at normal incidence,  $Q_L$  is always  $> 0.5$ , suggesting that the shape effect prefers magnetisation parallel to the long in-plane axis to magnetisation parallel to the short in-plane axis. The induced easy axis in the AN2, AN4 and AN6 elements evaporated at oblique

incidence is parallel to the long in-plane axis, Thus, it favours magnetisation in this direction. This is an effect similar to the shape effect. Thus, in these elements, the induced anisotropy cooperates with the shape effect and increases  $Q_L$ . However, in the AN1, AN3 and AN5 elements, the induced anisotropy favours magnetisation parallel to the short in-plane axis so that it favours the magnetisation  $90^\circ$  from the long in-plane axis. Thus, it competes with the shape effect. As a consequence, the volume occupied by the component of magnetisation parallel to the long in-plane axis is reduced, resulting in the reduction of  $Q_L$ . These expectations are confirmed by Fig. 4.23.

For elements without the induced anisotropy, the total energy  $E_{total}$  consists of magnetostatic energy  $E_{mag}$  and exchange energy  $E_{ex}$  only. For elements with the induced anisotropy, the total energy consists of  $E_{mag} + E_{ex} + E_k$ , where  $E_k$  is the anisotropy energy. A resultant domain structure is a local minimum of the total energy. By comparing  $Q_L$  of the AN1, AN3 and AN5 elements with induced easy axis to those without it, a "balance" between the induced anisotropy and the shape effect is demonstrated.



**Fig. 4.24** Reduction in  $Q_L$  for AN1, AN3 and AN5 elements after inducing the anisotropy.

$\Delta Q_L$  is the difference in  $Q_L$  between AN1, AN3 and AN5 elements with and without the induced anisotropy. Fig. 4.24 shows that for AN1, AN3 and AN5 elements  $\Delta Q_L$  decreases monotonically with increasing R. Since  $\Delta Q_L$  reflects the effect of the extra energy term  $E_k$  while  $E_{total}$  reaches a local minimum, this figure indicates that the importance of the induced anisotropy becomes less for increasingly acicular elements.

The induced anisotropy and the shape of the element also have an effect on the in-situ magnetising process. This is discussed below.

$H_c$  is a key parameter quantifying the magnetic "hardness" of a ferromagnetic sample and its relation with R provides information on how it is affected by the shape effect and induced anisotropy (Fig. 4.25). For the element evaporated at normal incidence, it is noticed that  $H_c$  increases monotonically as R increases, indicating that the element becomes magnetically harder. Significantly, the AN6 elements possess a coercivity of 20 Oe higher than the AN1 elements. This is attributed to the increased importance of the shape effect.

The  $H_c$  vs R curve of the elements with the induced easy axis parallel to the long in-plane axis is also a monotonically increased curve, demonstrating the shape effect. Nevertheless, it is noticed that this curve is always higher than that of the elements without the induced easy axis and the difference in the coercivity of the AN6 elements is 34 Oe, i.e. a 50% increase in coercivity has been obtained. This suggests that the "hardness" of the elements is increased by the induced anisotropy.

The in-situ magnetising experiment performed on the AN5 element with an induced easy axis along the short in-plane axis can also be described using a type A loop. The coercivity of those elements is 45 Oe in contrast to  $H_c = 48$  Oe for the AN5 element evaporated at normal incidence. Thus, the induced anisotropy reduces the coercivity due to the orientation of the easy axis being orthogonal to the direction of magnetisation favoured by the shape effect. However, the reduction in  $H_c$  is only about 7%, which is much less than the increase caused by the induced anisotropy in AN6 elements.

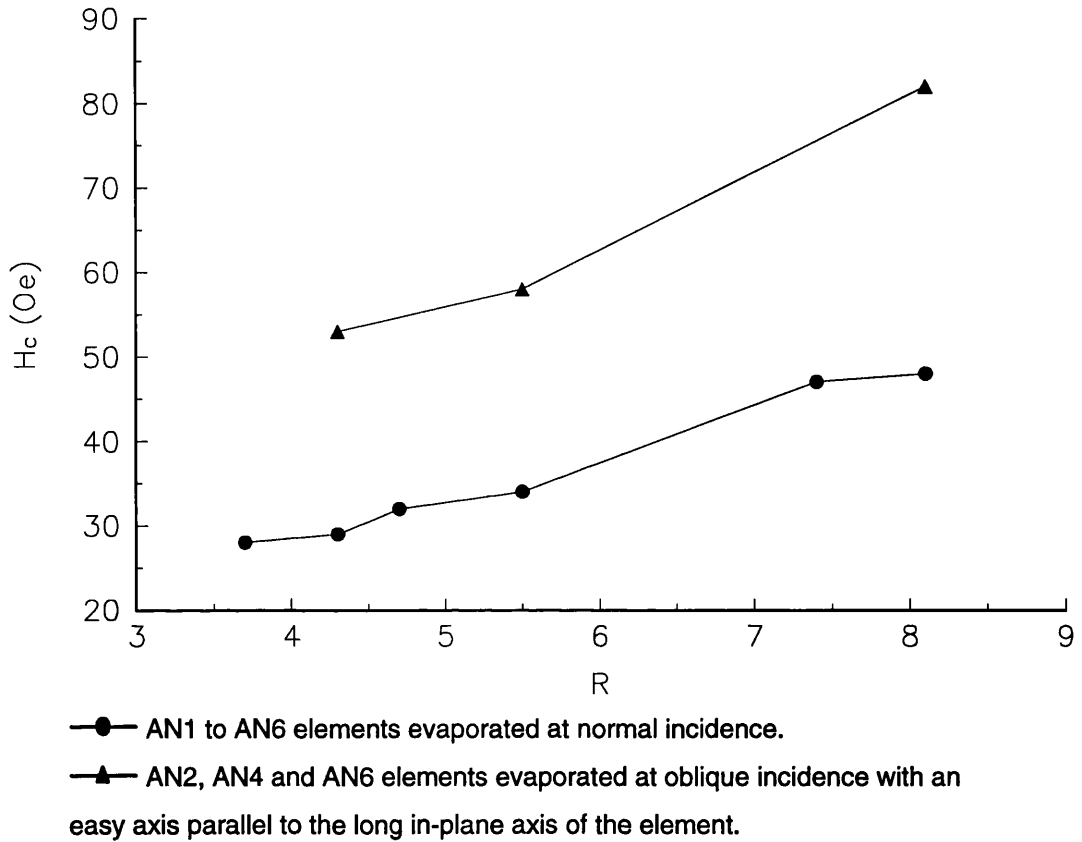


Fig. 4.25 Characterisation of the magnetic hardness of the elements.

For elements evaporated at normal incidence, each stable domain structure in the magnetising process is a minimum energy state of  $E_{\text{mag}} + E_{\text{ex}} + E_{\text{H}}$ , where  $E_{\text{H}}$  is the Zeeman energy (Chapter 1). For the elements with induced anisotropy, the magnetising process is determined by local minimisations of  $E_{\text{mag}} + E_{\text{ex}} + E_{\text{H}} + E_{\text{k}}$ .

The in-situ magnetising experiments show that the effect of  $E_{\text{mag}} + E_{\text{ex}} + E_{\text{H}}$  results in type A loop for the normal incidence elements. For elements with the easy axis parallel to the long in-plane axis, magnetisation in this direction is always favoured by the induced anisotropy. The experiment suggests that the type A loop is also the result of balance among the above energy terms. The AN1 and AN3 elements with the induced easy axis parallel to the short in-plane axis have maximum anisotropy energy when the magnetisation is parallel to the long in-plane axis. Therefore, it is expected that they support a

different hysteresis loop and this has been confirmed by the experiment. For the AN5 element with the induced easy axis parallel to the short in-plane axis, the extra energy term  $E_K$  does not result in a different type of hysteresis loop. This may be due to the fact that the magnitude of  $E_K$  is relatively small comparing to  $E_{\text{mag}} + E_{\text{ex}} + E_H$ .

Despite the fact that type A loops are supported by elements with and without the easy axis parallel to the long-plane axis, some differences are found when details of the loops are considered. These are discussed in terms of shape effect and induced anisotropy in the following few paragraphs.

The relation between the remanent magnetisation  $M_r$  and  $R$  is demonstrated in Fig. 4.26. For the elements evaporated at normal incidence, the remanent magnetisation increases monotonically as  $R$  increases. This is similar to the relation between  $Q_L$  and  $R$  although  $M_r$  is measured in the remanent state whilst  $Q_L$  is measured in ac-demagnetised state. The dependence of the shape effect on  $R$  also results in the increasing of  $M_r$  for the elements evaporated at the oblique incidence as demonstrated by the other curve in Fig. 4.26. It is found that the  $M_r$  vs  $R$  curve of the elements with the induced easy axis parallel to the long in-plane axis is higher than that of the element without the induced anisotropy. This reflects a "cooperative" effect of the induced anisotropy.

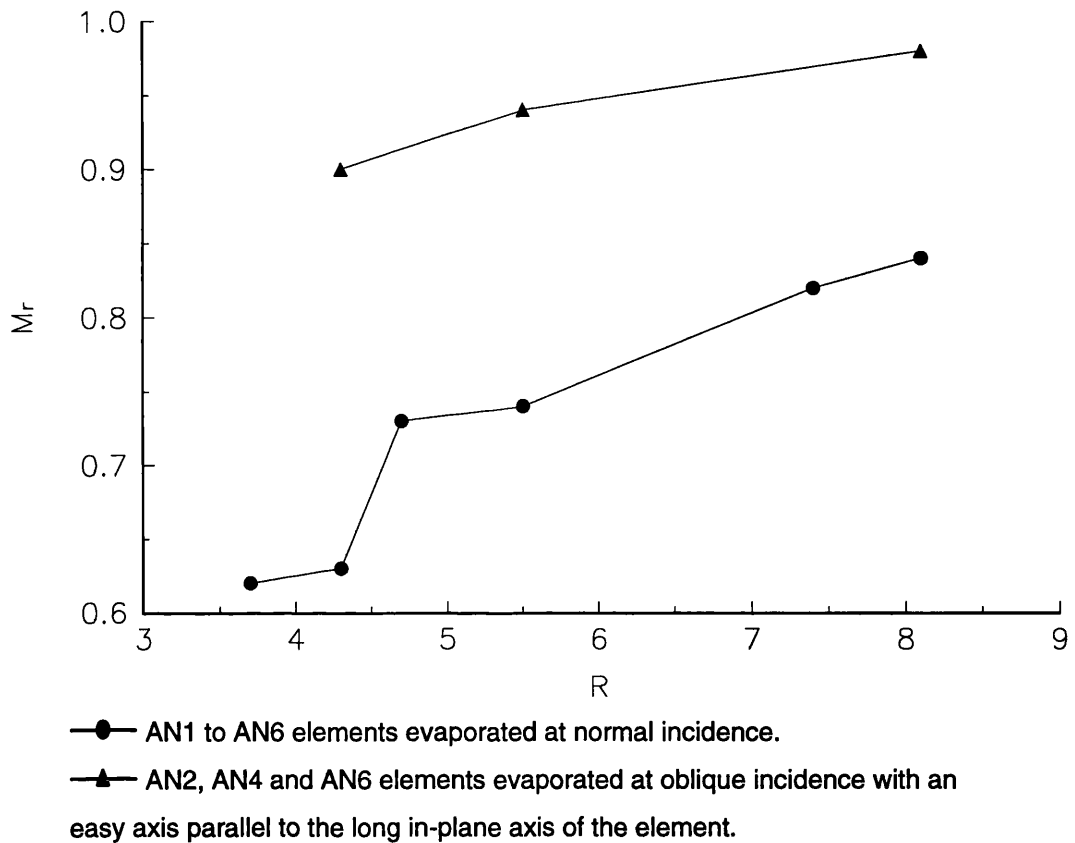
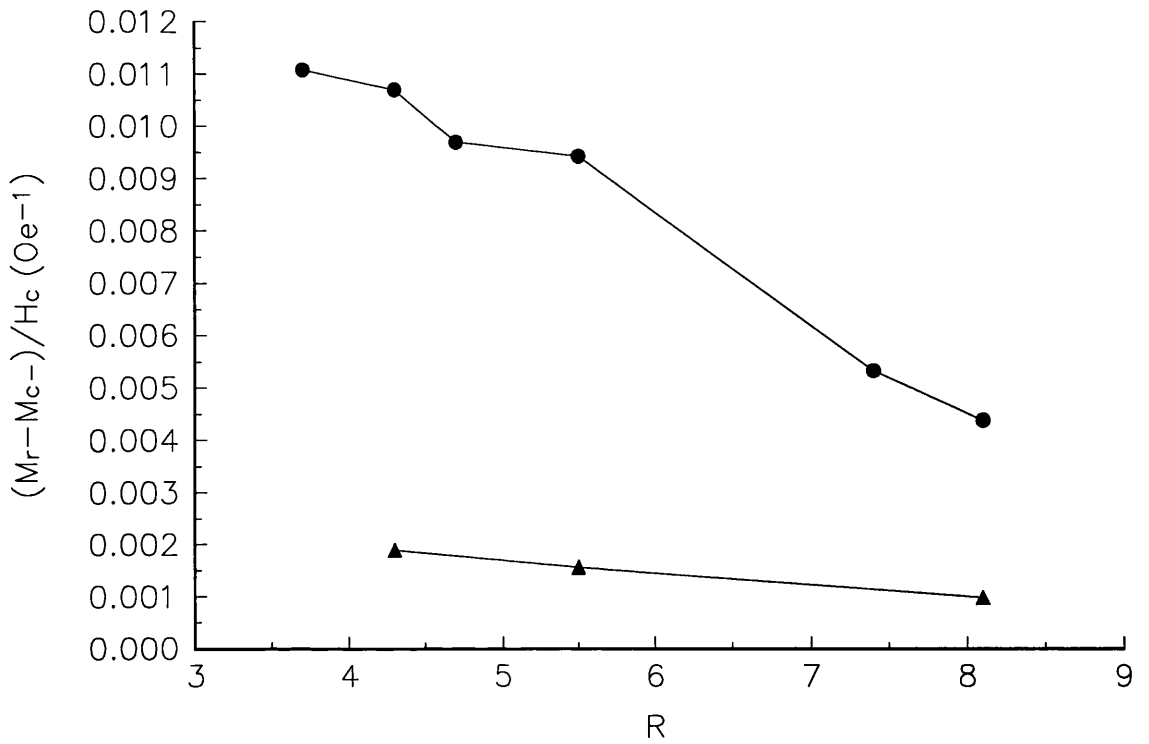


*Fig. 4.26 Dependence of  $M_r$  on  $R$ , demonstrating the effect of the shape and induced anisotropy on hysteresis loops.*

The slope of the loop between  $-H_c$  and  $H_c$  can be quantified by  $(M_r - M_{c-}) / H_c$  and  $(M_{c+} - M_r) / H_c$ . The less these terms are, the more square the hysteresis loop. Hence, their relation to  $R$  shows how shape effect changes the shape of the loop. The plots of  $(M_r - M_{c-}) / H_c$  vs  $R$  and  $(M_{c+} - M_r) / H_c$  vs  $R$  are shown in Fig. 4.27 and Fig. 4.28 respectively. It is observed that for the elements without the induced anisotropy, these two parameters decrease monotonically as  $R$  increases. Therefore, the shape effect causes the hysteresis loop to be more "square" in increasingly acicular elements. For the element with the induced easy axis parallel to the long in-plane axis, the plots also monotonically decrease due to the shape effect. However, compared with the plots of the elements without the induced anisotropy, this curve is lower, indicating that the induced anisotropy increases the "squareness" of the hysteresis loop.



- AN1 to AN6 elements evaporated at normal incidence.
- ▲ AN2, AN4 and AN6 elements evaporated at the oblique incidence which comprise an easy axis parallel to the long in-plane axis of the element.

**Fig. 4.27** Plot of  $(M_r - M_{c-})/H_c$  vs R demonstrating how the hysteresis loops are affected by the shape and the induced anisotropy.

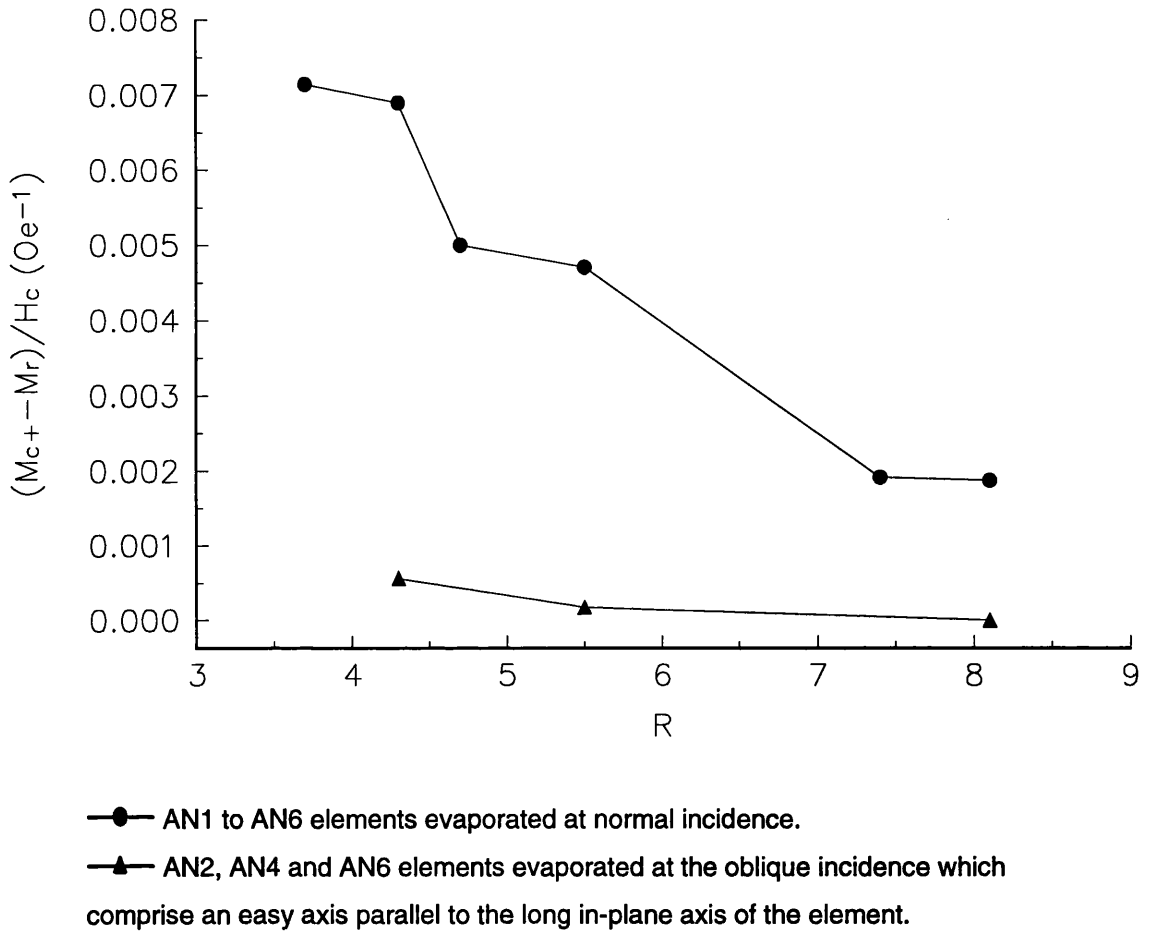


**Fig. 4.28** Plot of  $(M_{c+} - M_r) / H_c$  vs R demonstrating how the hysteresis loops are affected by the shape and the induced anisotropy.

The studies described in this chapter have shown the effect of shape and induced anisotropy in permalloy thin film elements. The explanation of the results are also given in terms of energy minimisation, which provides an insight into the behaviour of the elements.

## **Chapter 5**

# **Characterisation of MFM tips using the MDPC mode of Lorentz microscopy and computer simulation**

### **5.1 Introduction**

An MFM image is formed by detecting the interaction between an MFM tip and the stray field of a magnetic specimen. Thus the image is highly dependent on the magnetic structure of the tip and it is important that this is known and stable if the MFM image is to be interpreted quantitatively. Recently, commercial MFMs have been available, such as the instruments made by TopoMetrix (Loh et al. 1993) and NanoScope (Digital Instruments 1994). Using these instruments, MFM images have been taken from recording media samples and display image contrast with good resolution (< 50 nm). Due to the fact that most of MFM tips are too small in dimension (< 100 nm in the apex region) to be imaged using Kerr or Faraday microscopy (Chapter 2) and opaque for Lorentz microscopy, direct characterisation of their domain structure is still a problem. Thus, the tip-sample interaction is not well understood and quantitative interpretation of the images is limited.

In our collaboration with the group at Manchester Metropolitan University, an MFM has been built (Valera et al. 1995, Valera and Farley 1995) and we are concerned with characterisation of the tip. This MFM uses one-face coated cobalt MFM tips made from Park Scientific Microlevers<sup>TM</sup> (Chapter 3) and high resolution (about 30 nm) domain patterns have been obtained from recording media samples (Chapter 6). This MFM will be called "our MFM" throughout later chapters in this thesis. As the aim of this research is to improve the quantitative aspect of MFM imaging, it is necessary that the tip is characterised both physically and magnetically. This work is accomplished by combining experimental characterisations and computer simulations, which will be detailed in this chapter.

In section 5.2, the fabrication of MFM tips suitable for our MFM is discussed. The MFM tips investigated in this chapter are coated with cobalt film on the whole surface or one face of the pyramid. The physical characteristics of the

tips are first studied using a Philips SEM515 at 30 kV so as to examine the topography of the deposited magnetic film. Then high magnification TEM studies are performed in a JEOL 2000FX CTEM/STEM (Chapter 2) at 200 kV whereby the crystalline structure of the film at the end of the tip and the radius of the apex are investigated (section 5.3). Such studies are essential as those parameters are important in determining the resolution of an MFM (Grütter et al. 1992, Schönenberger and Alvarado 1990, Wadas et al. 1990). Although the magnetic film on the tip is thin enough to be imaged using the CTEM/STEM, the pyramid and the cantilever are too thick so that the tips are effectively opaque for Lorentz electron microscopy. Therefore rather than trying to image the magnetic structure in the film directly it is necessary to examine the stray field, produced by the magnetisation configuration in the tip, which extends beyond the edges of the film. In section 5.4, this stray field is investigated using the MDPC mode of Lorentz electron microscopy performed on an extended VG HB5 STEM at 100 kV (Chapter 2). The tip is magnetised in an 8000 Oe magnetic field directed towards the apex of the tip prior to the MDPC imaging and it is expected that the remanent state of the cobalt thin film on the tip supports a well defined magnetic state.

As the stray field reflects the interior magnetic configuration of the tip, the MDPC images of a uniformly magnetised tip are simulated and compared with the experimental MDPC images. The simulation models and details of calculation will be given in section 5.5 and 5.6. The one-face coated tip and the whole-surface coated tip are simulated in section 5.7 and 5.8 respectively. Image processing allows quantitative information to be extracted from these images and it is accomplished by using DIP (Digital Image Processing) program performed on an IBM PC and by intensity line tracings.

## **5.2 Fabrication of MFM tip**

In Chapter 3, normal and oblique evaporation techniques have been described. Coating the Microlevers<sup>TM</sup> with magnetic thin films using these methods results in whole-surface and one-face coated MFM tips respectively.

Fig. 5.1 is an SEM image recorded from a whole-surface coated tip. It is obvious that the cantilever has been deformed significantly through an angle of  $21.0^\circ \pm 0.5^\circ$ . This may be due to the stress imposed by the evaporated magnetic film.

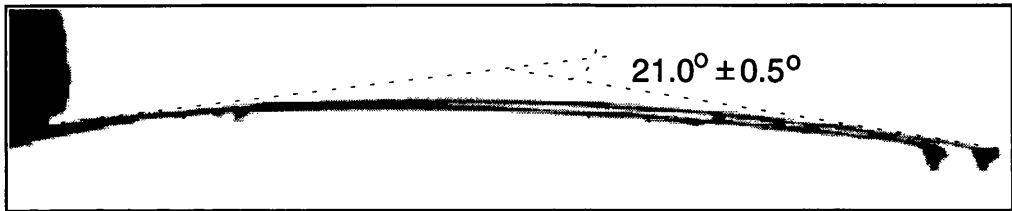


Fig. 5.1 SEM image of the whole-surface coated MFM tip.

In our MFM, a laser interferometric detection system is used to sense the displacement of the tip in the Z direction as a result of the interaction between the tip and samples (Beaumont et al. 1994). Fig. 5.2A illustrates how this system works with a straight cantilever while Fig. 5.2B indicates the unsuitability of a deformed cantilever for this detection system.

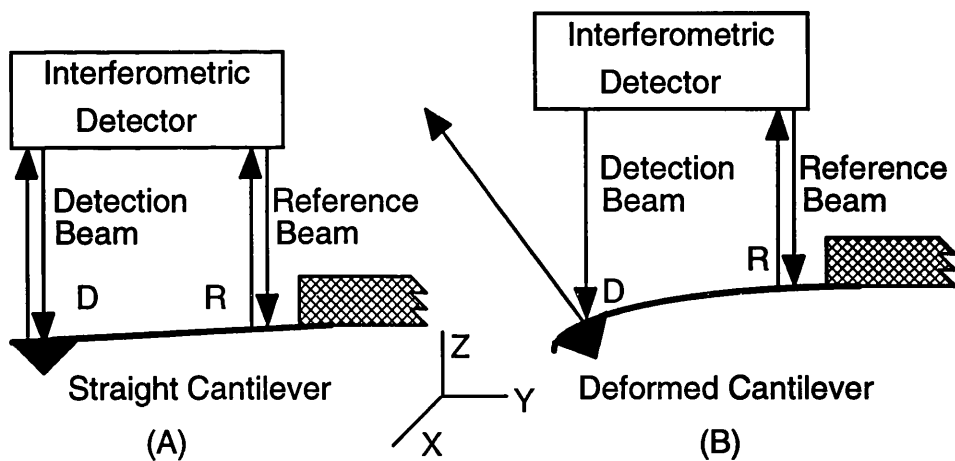


Fig. 5.2 Schematic diagram of the interferometric detection system used in our MFM.

Fig. 5.2 illustrates the static operation mode of an MFM (Chapter 2). One laser beam is focused on a point R while the other one is focused on the

back of the pyramid tip (point D). Since R is far away from the tip (DR is usually longer than 100  $\mu\text{m}$ ), the displacement of R is negligible and therefore the laser beam incident on the cantilever at R is used as a reference beam. The deflected cantilever results in a phase difference between the detection and reference beams. A gold thin film has been coated on the back of the cantilever so that these two laser beams are reflected back into a phase detection system where the displacement at D is measured (Fig. 5.2A). However, when the cantilever is deformed as shown in Fig. 5.2B, the detecting beam is reflected outside of the detector so that the displacement is not detectable. Hence, such a deformed cantilever is not suitable for use in our MFM.

This problem is overcome by coating the Microlevers<sup>TM</sup> with cobalt films at oblique angles (Chapter 3). In this experiment, the cantilever is tilted through an angle of about  $55^\circ$ , i.e. the evaporation beam is normal to one face of the pyramid. SEM imaging of such MFM tips suggests that the cantilever is straight now and this may be due to the increased mobility of evaporated atoms at an oblique incidence angle so that the stress is relieved. A further advantage of doing this is that the magnetic film is limited predominantly to one face of the pyramid, which is beneficial for high resolution MFM imaging (Grütter, 1994). A thin layer of carbon is coated afterwards using thermal evaporation to prevent the sample from electrically charging in electron microscopes.

## **5.3 Experimental study of physical characteristics of tips**

### **5.3.1 CTEM observation of whole-surface coated tip**

Since the physical characteristics of the apex region in the MFM tip are essential in determining the resolution of the MFM imaging, they are of particular interest. Fig. 5.3 is a bright field image recorded from the whole-surface coated tip. Three regions are observed: the central  $\text{Si}_3\text{N}_4$  pyramid, the cobalt thin film and the outermost carbon film. The cobalt film is found to be in good contact with both the  $\text{Si}_3\text{N}_4$  pyramid and carbon film. MFM imaging performed using such tips indicates that consistent imaging conditions have been obtained even after the tips crash on specimens. The thickness of the cobalt film is measured to be  $35 \pm 5$  nm, which is in good

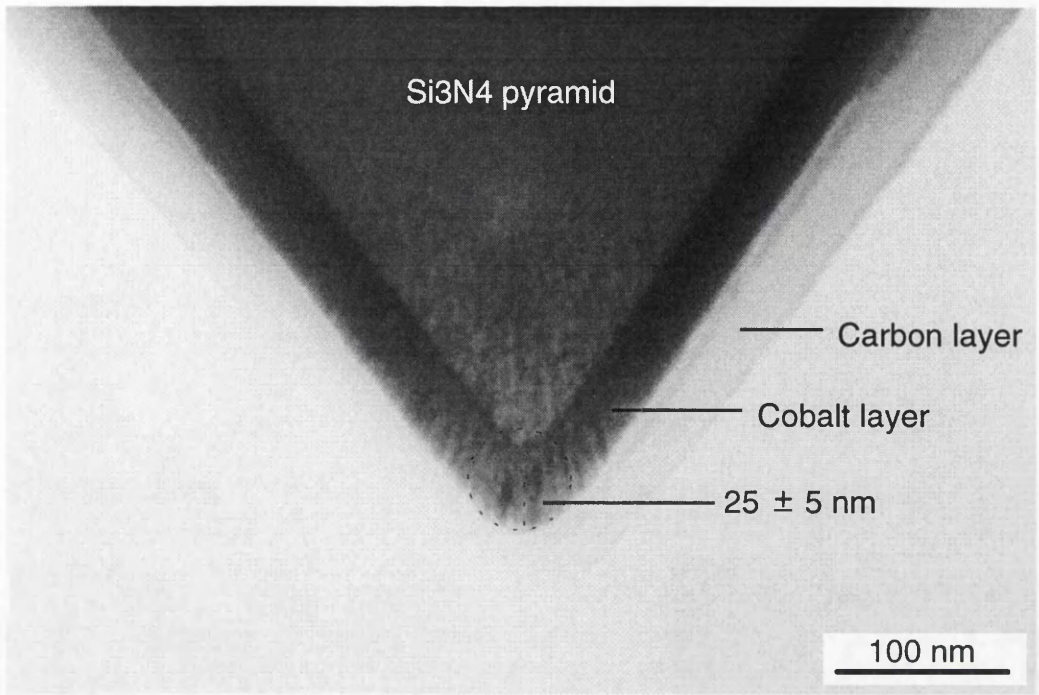


*Fig. 5.3 TEM image of the whole-surface coated cobalt tip.*

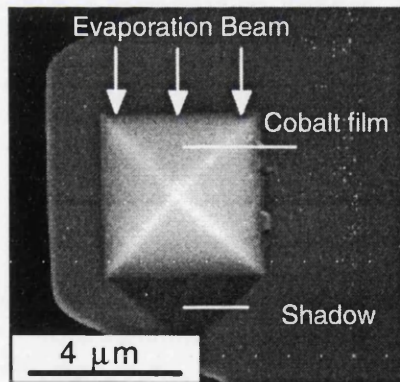


*Fig. 5.4 SEM image of the one-face coated cobalt tip. The tip is viewed from the top of the pyramid.*

agreement with the evaporation design of 35 nm. The radius of curvature of the cobalt film at the apex is measured to be  $25 \pm 5$  nm and this may be a reason why the resolution of our MFM is restricted to about 30 nm.

### **5.3.2 SEM observation of one-face coated cobalt tip**

The top view of the one-face coated tip is shown in Fig. 5.4. In this SEM image made using secondary electrons, the cantilever is imaged as a uniform surface whereas the pyramidal tip is represented by a square region at the end of the cantilever. The bright cross within the square represents the edges of the pyramid and the projection of the evaporated beam on the cantilever plane is indicated by arrows. It can be seen that there is a triangular region on the cantilever next to the edge of the pyramid. This can be explained using the schematic drawing of the set up for the oblique evaporation (Chapter 3). It indicates that the evaporated atoms are partially blocked by the pyramid resulting in an uncoated region on the cantilever. Fig. 5.4 proves directly that the cobalt film is predominately coated on one face of the pyramid and the whole of the cantilever (except for the triangular region). Furthermore, by measuring the dimensions of the triangular shadow and the pyramid, the oblique angle used during the evaporation is calculated to be about  $55^\circ$  which is in good agreement with the evaporation set up. The other SEM image showing the topography of this tip is displayed in Fig. 3.7. In that image, the apex region of the pyramid is found to be almost contamination free although several clusters of debris are observed on the cantilever. Nevertheless, as they are far away from samples during MFM imaging, they have negligible effect.

## **5.4 Experimental MDPC imaging of one-face coated tip**

### **5.4.1 MDPC images of one-face coated tip**

A pair of experimental MDPC images are shown in Fig. 5.5. The contrast in the images due to the stray field reflects the interior domain configuration of the tip and is important in terms of understanding the tip-sample interaction. Since the stray field around the apex region of the tip is essential for MFM imaging, the STEM is set up to image this region so as to reveal details of

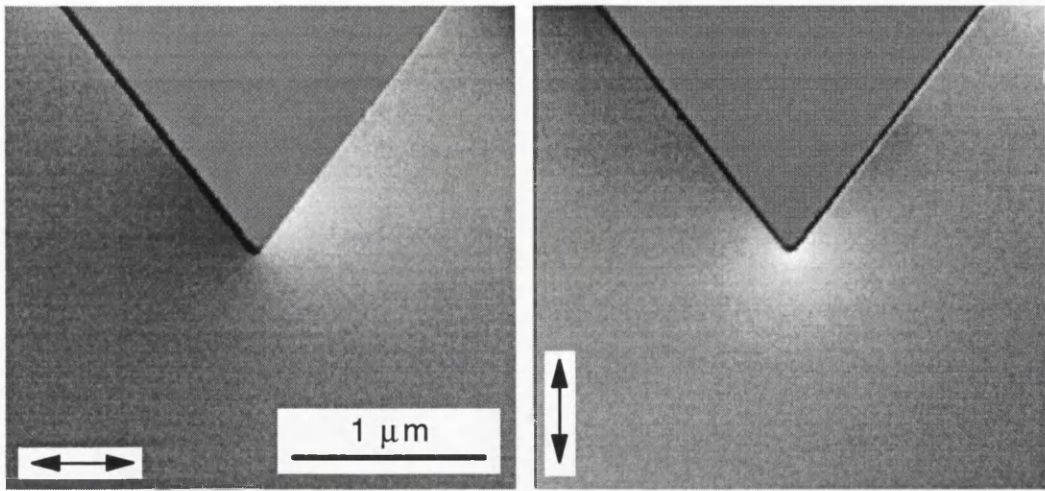


*Fig. 5.5 Experimental MDPC images of the one-face coated tip.*

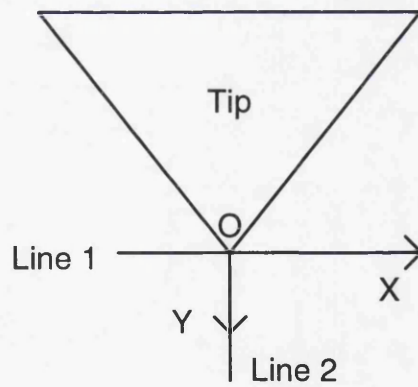


*Fig. 5.6 The coordinate system used in line tracings.*

the stray field. The images suggest that in a region around the end of the tip the configuration of the stray field is qualitatively symmetric about the Y axis which is defined in Fig. 5.6. However, the stray field in other regions is not symmetric. Moreover, the contrast variation is smooth along the edges of a region at the end of the tip, which extends to approximately 0.5  $\mu\text{m}$  from the apex whilst abrupt contrast variations are observed in other regions. They indicate that rather than the whole of the tip, probably only a small volume in the apex is uniformly magnetised.

#### **5.4.2 Analysis of the MDPC images using arrow mapping method**

Two terms "grey level" and "signal level" are used in this thesis when discussing MDPC images. The grey level  $G(X,Y)$  is the brightness of a pixel  $(X,Y)$ . In an 8 bit image (Appendix 1), a grey level of 128 represents zero Lorentz deflection. The signal level  $I(X,Y)$  is proportional to the Lorentz deflection angle and related to the grey level by

$$I(X, Y) = G(X, Y) - 128 \quad (5.1)$$

Therefore, in an MDPC image, the signal levels of two pixels reflect the relative magnitude of the Lorentz deflections. The actual value of the signal level is a function of many parameters of the STEM and acquisition system, e.g. probe current, gain and offset setting of the amplifier etc..

The linearity of the MDPC signal levels to Lorentz deflection angles enables quantitative analysis to be performed and two means are used in this study. The first one uses arrows to demonstrate the stray field and is termed the arrow mapping method. The other one uses the plot of the signal level in the above experimental MDPC images or directly Lorentz deflection angles calculated using simulation models (later sections) against the distance from the apex of the tip to illustrate the decay of the stray field. It is termed the line tracing method.

The basic principle of the arrow mapping is to represent the magnitude and direction of the Lorentz deflection at a point using the length and orientation of an arrow respectively. If we assume that the signal level is  $I_x(X, Y)$  at a

pixel  $(X, Y)$  in an MDPC image mapped along the X direction and it is  $I_x(X, Y)$  in an image mapped along the Y direction at  $(X, Y)$ , the total signal is

$$I(X, Y) = [I_x^2(X, Y) + I_y^2(X, Y)]^{1/2} \quad (5.2)$$

The direction of the stray field is described by the angle  $\theta$  measured from the X axis. This value can be calculated using the following equation

$$\theta(X, Y) = \tan^{-1}[I_y(X, Y) / I_x(X, Y)] \quad (5.3)$$

The DIP program performs the above calculations and plots the arrows. The length of the arrow at  $(X, Y)$  is determined as a linear function of  $I(X, Y)$  and it points to the direction which makes an angle  $\theta(X, Y)$  with the X axis.

The result of the arrow mapping performed on the pairs of experimental MDPC images is given in Fig. 5.7. It confirms that in the region at the end of the tip the stray field is symmetric about the Y axis. Furthermore, the maximum stray field occurs in this region with a strong Y component and decays rapidly as the distance from the tip increases. Some asymmetry in the stray field is observed in regions other than that around the end of the tip. This may be due to the magnetisation across the whole of the tip not being uniform.

### **5.4.3 Analysis of experimental MDPC images using line tracing method**

Line tracing is a method of analysing variation of a quantity along a particular direction. By plotting the magnitude of the MDPC signals or Lorentz deflection angles calculated using the models, the decay of the stray field is demonstrated graphically. Another merit of this method is that it also allows analytical interpretations of data such as curve fitting to be attempted.

The line tracing is performed along the X and Y axes which are defined in Fig. 5.6. Along the X axis, it starts from  $X = -1.30\mu\text{m}$  and finishes at  $X = 1.30\mu\text{m}$ ; this line is defined as line 1. Since the signal level is zero within the tip, line tracing along the Y axis is performed only along the positive Y

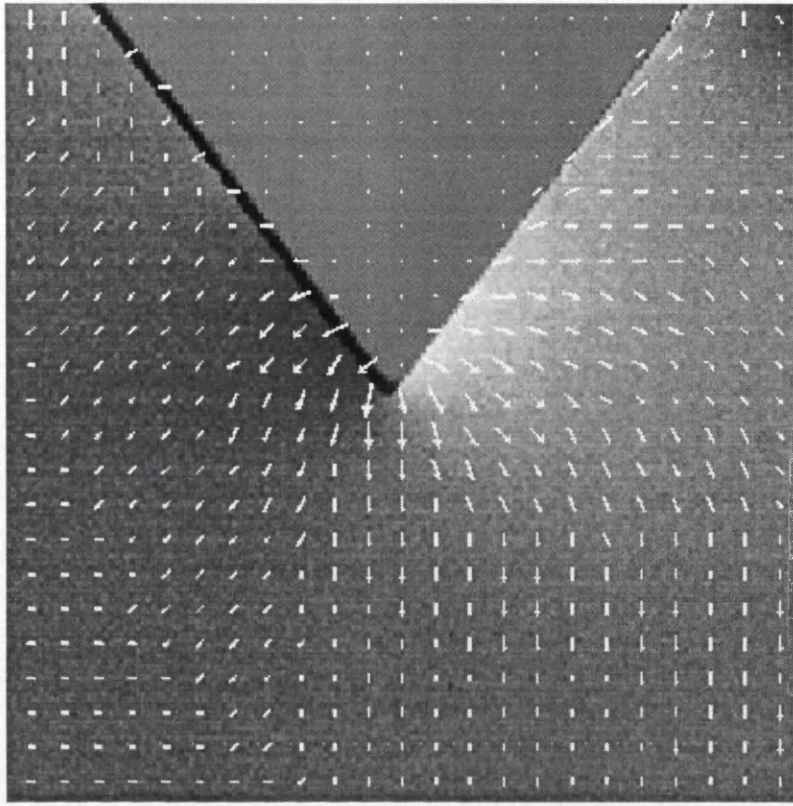


*Fig. 5.7 Arrow mapping result of the experimental MDPC images recorded from the one-face coated cobalt tip.*

axis from the origin (end of the tip) to the bottom border ( $Y = 1.15 \mu\text{m}$ ) and this line is defined as line 2.

The decay of the Y component of the stray field along line 2 is demonstrated in Fig. 5.8. Since the tip is mounted on a spring cantilever which may vibrate under the influence of environment noises, it is very difficult to keep the tip still during the image acquisition which usually takes more than 1 minute to acquire a frame of MDPC image. Thus, all the MDPC images shown in this chapter are acquired without subsequent averaging. The drawback of doing this is that SNR is reduced so that the plot is less smooth.

Curve fittings have been performed using several functions such as exponential function  $Y = ae^{bx}$ , power function  $Y = aX^b$  and polynomial function  $Y = \sum_{i=0}^n a_i X^i$  and indicate that a function in the form of  $I_y(Y) = a - b \ln(Y + c)$  is the best to describe the experiment data. By adjusting a, b and c, the best fit is achieved at  $a = 11.96$ ,  $b = 27.34$  and  $c = 0.026 \mu\text{m}$ . The reason that there is a constant c is that the line tracing starts at  $Y = 0$  which is a singularity point for the logarithm function and we can avoid this problem by introducing c. As an obvious limit of this function,  $I_y(Y)$  becomes negative at  $Y > e^{a/b} - c = Y_c$ , which is not true in the real case. However, since  $Y_c = 1.52 \mu\text{m}$ , the function is valid in the region where the line tracing is performed. The fitted curve is indicated by a dotted line in the figure and in good agreement with the plot of the experiment plot.

A term "decay distance" D is defined as the distance from the origin, where the signal level is 1/e times as high as the highest signal level (at the origin). This term quantifies how rapid the stray field decays. According to the best-fit function for  $I_y(Y)$  described above, D is calculated to be  $0.32 \mu\text{m}$ .

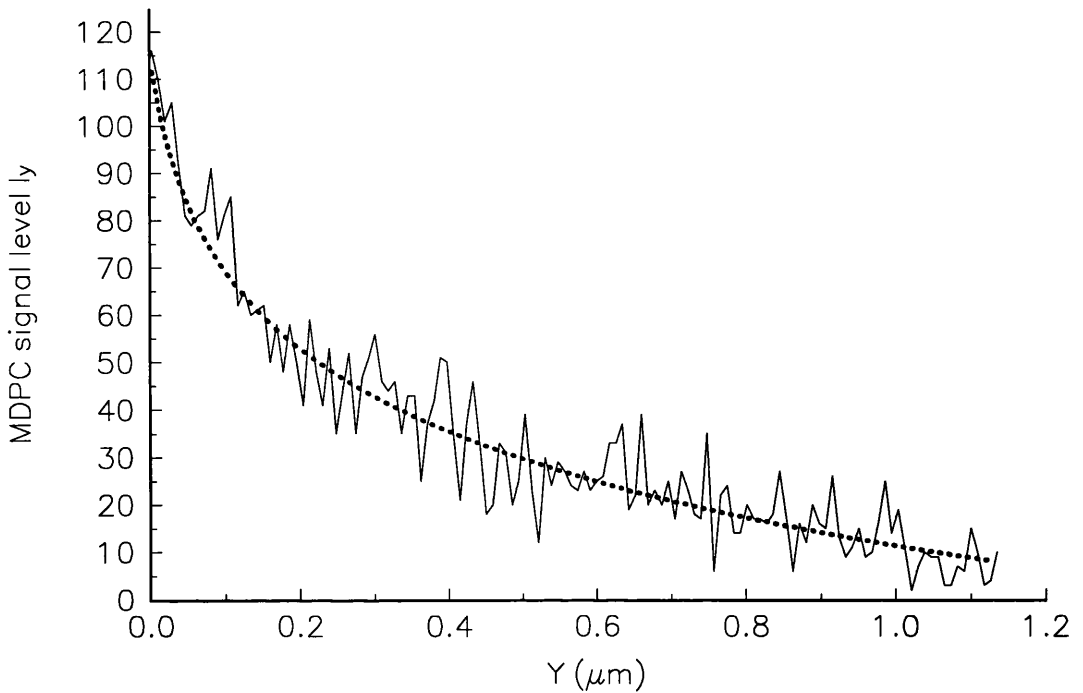


**Fig. 5.8** Line tracing along line 2 in the experimental MDPC image mapped along the Y direction. The dotted line is the fitted curve using  $I_y(Y) = 1196 - 27.34 \ln(Y + 0.026)$ .

The distribution of the Y component of the stray field along line 1  $I_y(x)$  is shown in Fig. 5.9. Curve fittings have been attempted using various functions discussed before for the whole plot and for each half of the plot on either side of the Y axis. Nevertheless, none of them gives a satisfactory result. There are a number of possible explanations. Firstly, the experimental plot comprises significant noise which makes the fitting more difficult. Secondly, it is possible that  $I_y(X)$  can not be approximated to an analytical function due to the complexity of the integral of Lorentz deflection (Chapter 3). Another possibility is that the best-fit function is in a form other than the above functions. Therefore, a curve is drawn manually through the mean points of the zigzag shaped plot. It shows that the stray field decreases monotonically on either side of the Y axis as  $|X|$  increases.

It is apparent that the plot is approximately symmetric about the Y axis between  $X = -0.5 \mu\text{m}$  and  $X = 0.5 \mu\text{m}$  although the whole of the curve is not symmetric. Using this fitted curve, the decay distance  $D$  is measured to be  $0.37 \mu\text{m}$  and  $0.25 \mu\text{m}$  on the right and left hand side of the Y axis respectively.

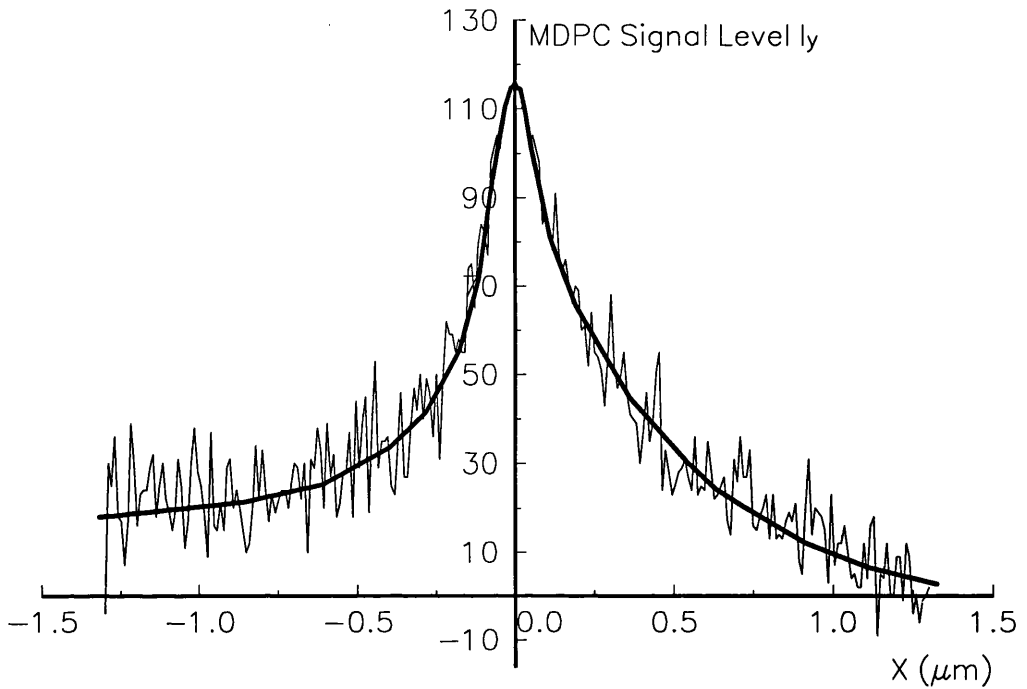


*Fig. 5.9 Line tracing along line 1 in the experimental MDPC image mapped along the Y direction. The fitted curve is indicated by the bold line.*

For the MDPC image mapped along the X direction, the line tracing along line 1 is shown in Fig. 5.10. It is observed that the shape of the plot is slightly irregular and comprises a degree of asymmetry. Furthermore, the SNR is the lowest among the three plots. Therefore, the attempt to fit the plot with the functions was not successful and a curve is drawn manually to show the trend of the stray field. The decay distance on either side of the Y axis is beyond the region of the MDPC imaging thus not given here.

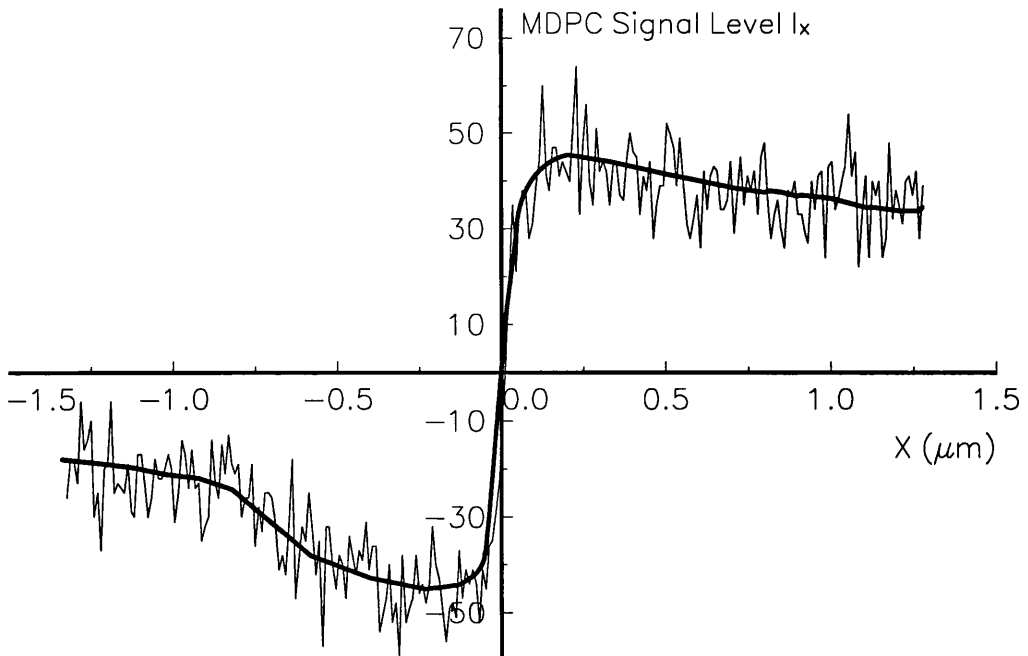


*Fig. 5.10 Line tracing along line 1 in the experimental MDPC image mapped along the X direction. A curve (bold line) is fitted to the line tracing data.*

## 5.5 Models used in computer simulation

### 5.5.1 One-face coated models

Computer modelling is performed to simulate the stray field of an idealised single domain structure in the tip. As the  $\text{Si}_3\text{N}_4$  tip is pyramidal, the magnetic film on one face of the tip is simplified to a triangular plate which is uniformly magnetised. The Z axis is perpendicular to the film and the Y axis is pointing to the apex in the plane of the plate. The orientation of the magnetisation is assumed to be parallel to the Y axis as shown in Fig. 5.11. In this diagram, faces 1 and 2 are the interfaces between the magnetic film and the free space while face 3 is the interface between the magnetic film on the tip and the magnetic film on the cantilever (tip-cantilever interface). The point T represents the apex of the tip whereas the origin of the absolute coordinate system O (section 5.6.2) is set at the centre of the plate. Since the edges of the real tip are equal in length, the edges of the triangular face in the plate are also assumed to be equal in length.

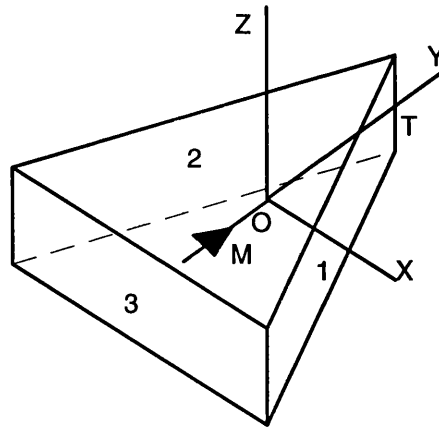


Fig. 5.11 Schematic diagram of the triangular plate with a uniform magnetisation.

The areal density of magnetic poles  $\sigma$  due to the discontinuity of magnetisation on an interface can be calculated using the equation

$$\sigma = \mathbf{M} \cdot \mathbf{n} \quad (5.4)$$

Where  $\mathbf{n}$  is the unit vector which is normal to the interface and points to the outside of the magnetic volume. In Fig. 5.11, the magnetic pole areal densities on the interfaces are

$$\sigma_1 = \sigma_2 = |\mathbf{M}| / 2 \quad (5.5)$$

$$\sigma_3 = -|\mathbf{M}| \quad (5.6)$$

In the above discussion, it is implied that the magnetisation is not continuous on the tip-cantilever interface. Hence this model simulates the one-face coated tip with an isolated triangular magnetic film and is named model 1.

On the other hand, as there is no physical discontinuity between the film on one face of the tip and the film on the cantilever, it is possible that the magnetisation in the tip extends to the film on the cantilever. In this case, the magnetic pole on the tip-cantilever interface may be approximately zero, i.e.

$$\sigma_3 = 0 \quad (5.7)$$

Therefore this model simulates the one-face coated tip with continuous magnetisation and is named model 2.

### **5.5.2 Whole-surface coated tip**

A schematic diagram of the whole-surface coated MFM tip is shown in Fig. 5.12. In this diagram, point T is the apex and plane ABCD is the base of the tip on the cantilever. M is the centre of plane ABCD. The origin of the absolute coordinate system (section 5.6) is set at the middle point of line TM with the Z axis perpendicular to plane TEF. The magnetic films on the tip and their magnetisation are illustrated schematically in plane TGH (Fig. 5.13). The magnetisation is assumed to be in the plane of the films and parallel to the lines GT, ET, HT and FT on the faces of ADT, ABT, BCT and CDT respectively. As a result of the discontinuity of the magnetisation, magnetic poles occur on the 4 interfaces between these films, which are in planes TAC and TBD. Fig. 5.14 is a schematic diagram demonstrating a plane parallel to the base of the tip. In this plane, the 4 interfaces are shown as diagonals. The magnetic pole densities on these faces can be calculated using equation (5.4). Here we still have two models depending on whether there are magnetic poles on the tip-cantilever interfaces or not. Using the same ideas as in the one-face coated models, model 3 and model 4 are developed to simulate the whole-surface coated tip with discontinuous and continuous magnetisation in the tip-cantilever interfaces respectively.

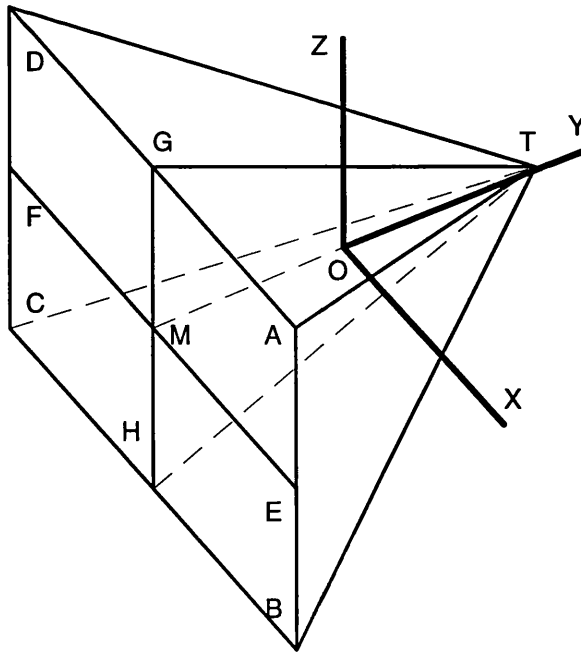


Fig. 5.12 Schematic diagram of a whole-surface coated MFM tip.

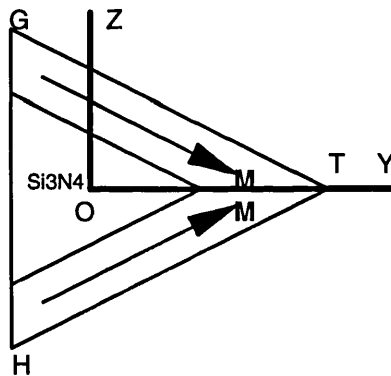


Fig. 5.13 Schematic diagram of plane TGF in the whole-surface coated tip.

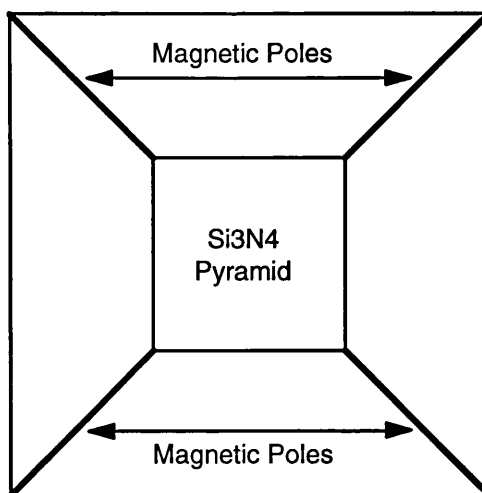


Fig. 5.14 Schematic diagram of a plane parallel to plane ADCB in the whole-surface coated tip.

## 5.6 Details of the simulation

### 5.6.1 Brief description of the simulation

The principle of the MDPC mode of Lorentz microscopy discussed in Chapter 2 indicates that the MDPC signal is a linear function of components of the Lorentz deflection angle  $\beta_L$ . Therefore, the MDPC images of the MFM tips are simulated by calculating the Lorentz deflection angles then converting them to an image format. In this work, the Lorentz deflection angle data are calculated in an  $8 \times 8 \mu\text{m}$  frame which consists of  $256 \times 256$  pixels with the base of the tip on the top border. All the programs are written in FORTRAN 77, compiled and run on an IBM 3090 mainframe computer incorporating the NAG library.

The simulation procedure involves the following three steps and they are detailed in the following sections.

- (1) Calculation of the components of the stray field perpendicular to the electron beam.
- (2) Calculation of the Lorentz deflection angles by integrating electron-field interaction over the electron trajectory.

(3) Conversion of the Lorentz deflection angle data to an image format.

### 5.6.2 Calculation of components of the stray field perpendicular to the electron beam

McVitie (1988) quoted formulae which can be used to calculate the stray field of a uniformly magnetised parallelepiped with magnetic poles on a face. In order to simplify the calculation, in this work the origin of the coordinate system  $S'$  is set at the centre of a charged plane ABCD in Fig. 5.15 where magnetic poles occur.

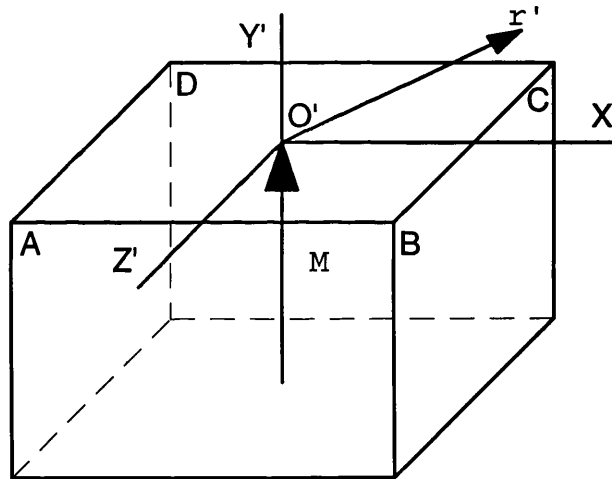


Fig. 5.15 A local coordinate system  $S'$ .

In the models considered, there may be several charged planes. For example there are 3 charged planes in model 1 so that there are 3 coordinate systems in which the stray field  $H'(r')$  of each charged plane is calculated. Therefore,  $S'$  is named the local coordinate system.

The calculation of the areal density of the magnetic poles in each model has been described in section 5.5. It is assumed that the magnetisation  $M$  is  $800 \text{ emu/cm}^3$ , the thickness of the magnetic film is 35 nm and the geometry of

the tip is exactly the same as the specifications of the Microlever<sup>TM</sup> (Chapter 3).

According to the principle of the MDPC technique, the Lorentz deflection angles should be calculated in a coordinate system which only depends on the location and orientation of the MDPC detector. This is the absolute coordinate system S which has been defined for each model in section 5.5. The position vector of a pixel is  $\mathbf{r}$  in S which is usually different from the position vector  $\mathbf{r}'$  of the same pixel in S' unless S and S' are coincident. However, the equations are based on the local coordinate systems. Hence a shifting operation  $\mathbf{T}$  and a rotation operation  $\mathbf{R}$  are performed. By using the shifting operation,  $\mathbf{r}'$  can be calculated from  $\mathbf{r}$  so that  $\mathbf{H}'(\mathbf{r}')$  is calculated in S'. Since the X' and Y' directions in S' are not necessarily parallel to the X and Y directions in S respectively, the  $\mathbf{R}$  operation is performed on  $\mathbf{H}'(\mathbf{r}')$  to obtain the components of  $\mathbf{H}(\mathbf{r})$  in S which are perpendicular to the electron beam.

If we suppose that the position vector of the origin O' of a local coordinate system is  $\mathbf{r}_o$  in S, then the above steps can be described mathematically using the following equations

$$\mathbf{H}'(\mathbf{r}') = \mathbf{H}'[\mathbf{R}(-\eta_1, -\eta_2, -\eta_3)\mathbf{T}(\mathbf{r}_o)\mathbf{r}] \quad (5.8)$$

$$\mathbf{H}(\mathbf{r}) = \mathbf{R}(\eta_1, \eta_2, \eta_3)\mathbf{H}'(\mathbf{r}') \quad (5.9)$$

$$R_1(\eta_1) = \begin{pmatrix} 1 & 0 & 0 \\ 0 & \cos\eta_1 & \sin\eta_1 \\ 0 & -\sin\eta_1 & \cos\eta_1 \end{pmatrix} \quad (5.10)$$

$$R_2(\eta_2) = \begin{pmatrix} \cos\eta_2 & 0 & -\sin\eta_2 \\ 0 & 1 & 0 \\ \sin\eta_2 & 0 & \cos\eta_2 \end{pmatrix} \quad (5.11)$$

$$R_3(\eta_3) = \begin{pmatrix} \cos\eta_3 & \sin\eta_3 & 0 \\ -\sin\eta_3 & \cos\eta_3 & 0 \\ 0 & 0 & 1 \end{pmatrix} \quad (5.12)$$

Where  $\eta_1$ ,  $\eta_2$ , and  $\eta_3$  are the angles through which the coordinate system  $S'$  has to be rotated around its own  $X'$ ,  $Y'$  and  $Z'$  axes respectively so that it can be coincident with  $S$ . After these operations, the stray field of each of the charged planes is calculated in the absolute coordinate system. The total stray field of the tip is then obtained by adding them together.

### 5.6.3 Calculation of Lorentz deflection angles

The Lorentz deflection angle consists of two orthogonal components  $\beta_x(X, Y)$  and  $\beta_y(X, Y)$  and they can be calculated using the equations given in Chapter 2. As the MFM tip is imaged using 100 keV electrons in the experiment, the wavelength  $\lambda$  is 0.0037 nm.

Since the dimension of the simulated object is very small and the fact that the magnetic field decays rapidly with distance, the extension of the stray field in the  $Z$  direction is limited. Therefore,  $Z_1$  and  $Z_2$  are approximated to 6  $\mu\text{m}$  and  $-6 \mu\text{m}$ . The integral is solved using the  $n$ -point Gaussian quadrature numerical method (NAGFLIB 1983, Davis 1967) as specified in the NAG library.

### 5.6.4 Conversion of Lorentz deflection angle data to an image format

The simulated MDPC images are obtained by linearly converting the Lorentz deflection angle data into the 8 bit grey scale image format. A pixel where the Lorentz deflection is zero will have a grey level of 128 while a pixel with the maximum Lorentz deflection angle  $(\beta)_{\text{max}}$  will have a grey level of either 255 or 0 depending on whether the deflection angle is positive or negative. More details of this image format are given in Appendix 1. The equation used to accomplish this conversion is

$$G_x(X, Y) = 128 + \frac{\beta_x(X, Y)}{|\beta_{\text{max}}|} \quad (5.13)$$

$$G_y(X, Y) = 128 + \frac{\beta_y(X, Y)}{|\beta_{\max}|} \quad (5.14)$$

The Lorentz deflection angles are calculated along two orthogonal directions simultaneously. The images mapped along the X and Y directions are converted from the deflection angle data using the same  $|\beta_{\max}|$  which is obtained by means of surveying the Lorentz deflection data of both components using the FORTRAN 77 program shown in Appendix 4.

## 5.7 Simulation of MDPC images using the one-face coated models

### 5.7.1 Simulated MDPC images

The MDPC images simulated using model 1 and model 2 are given in Fig. 5.16 and Fig. 5.17 respectively. As the tip is experimentally opaque to 100 keV electrons, the signal level of the tip region is set to be 0 during the simulation so as to make it consistent with the experiments. It is observed that the stray field configurations of both models are symmetric about the Y axis. Apparently the X component of the Lorentz deflection angle is relatively strong along the edges of the tip whereas the Y component of the deflection is strong at the end of the tip. These characteristics are what we expected from the input and are similar to that of the experimental MDPC images qualitatively. Compared to the MDPC images of model 2, the MDPC images of model 1 comprise higher contrast along the edges, especially in regions close to the tip-cantilever interface. This reflects the effect of the negative poles on the interface.

### 5.7.2 Analysis of the simulated MDPC images using arrow mapping method

Fig. 5.18 and Fig. 5.19 are the arrow mapping results of the MDPC images simulated using model 1 and 2 respectively. The length of the arrows indicates that in both cases the strongest Lorentz deflection occurs at the

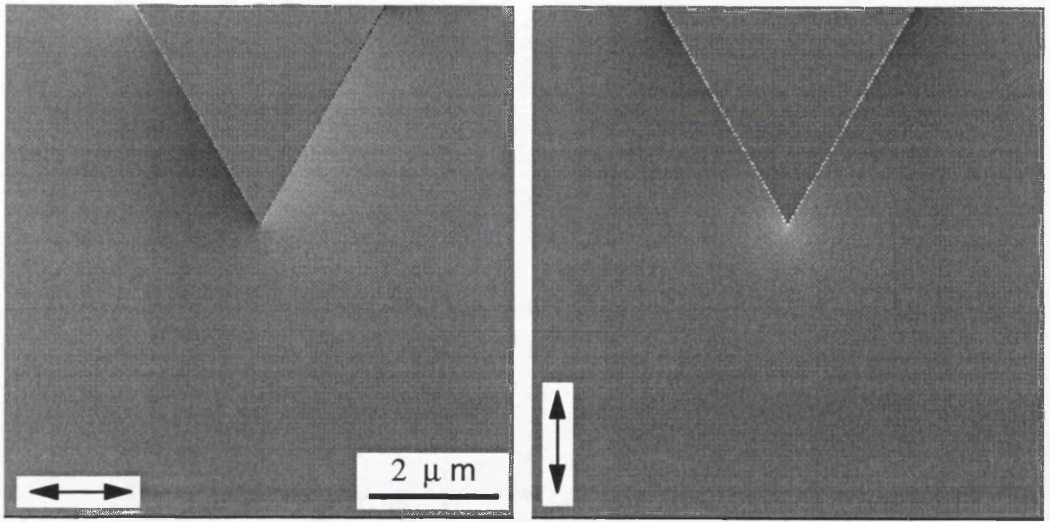


*Fig. 5.16 MDPC images simulated using model 1.*

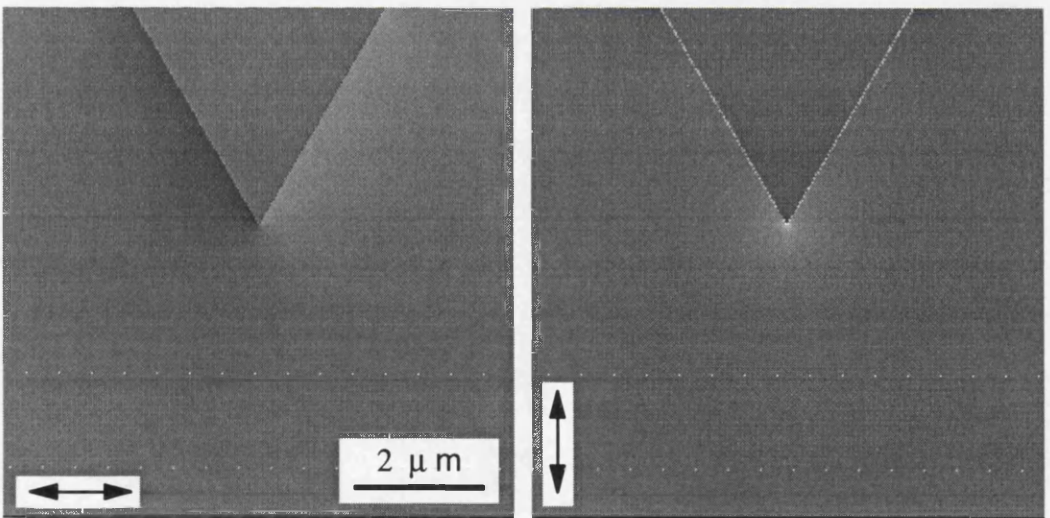


*Fig. 5.17 MDPC images simulated using model 2.*

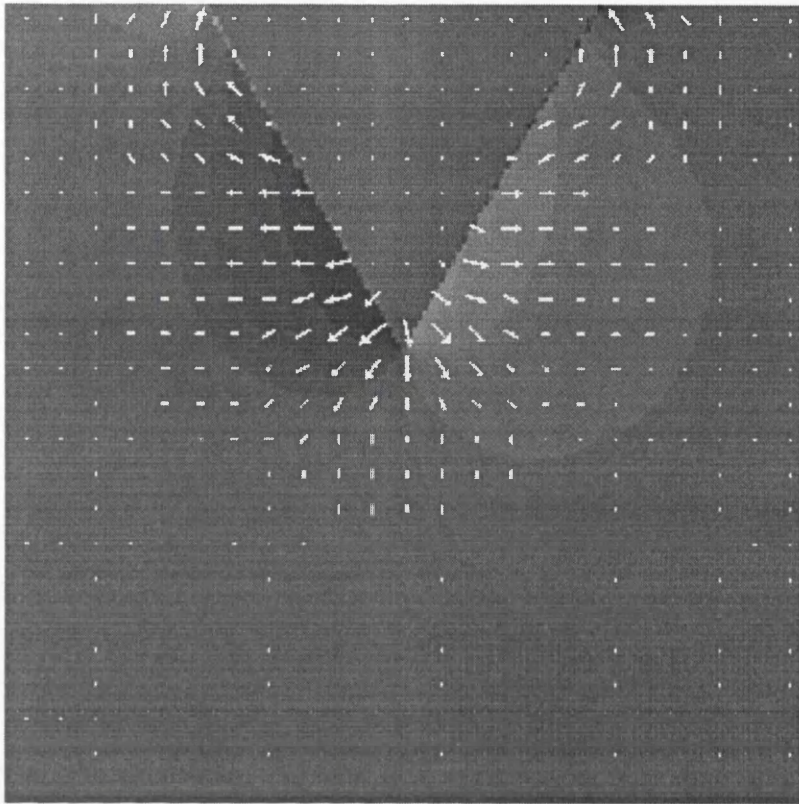


*Fig. 5.18 Arrow mapping of the MDPC images simulated using model 1.*

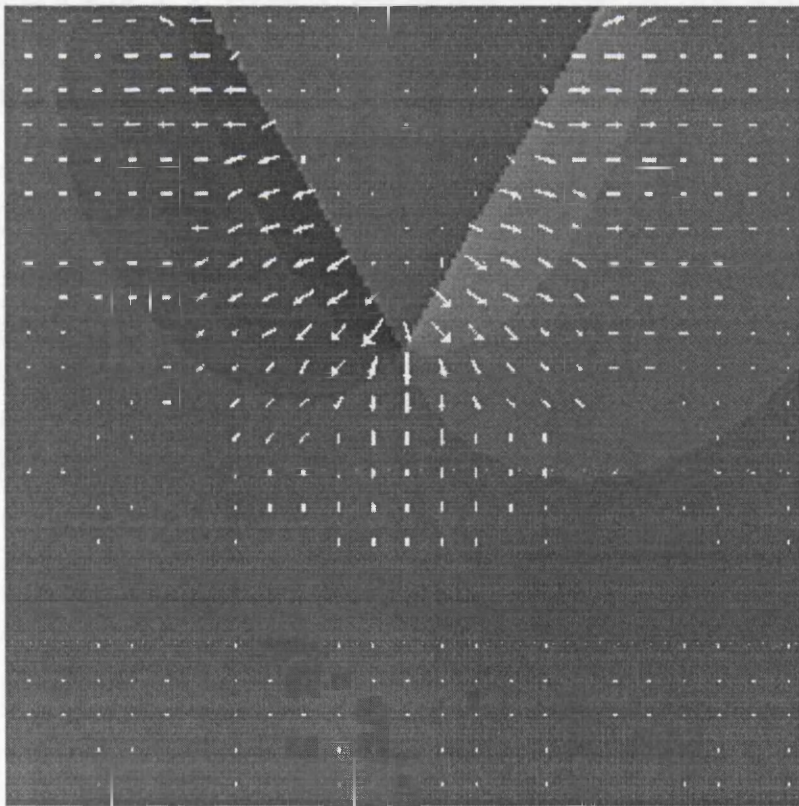


*Fig. 5.19 Arrow mapping of the MDPC images simulated using model 2.*

end of the tip and decays in both the X and Y directions. This is in accordance with the experimental result.

Fig. 5.18 suggests that the stray field is also strong at the corners on the tip-cantilever interface and the stray field forms a flux closure configuration there. This is due to the fact that there are negative poles on the tip-cantilever interface. Another effect of these negative poles is that they reduce the stray field from the positive poles and consequently makes the stray field decay more rapidly than in model 2.

### **5.7.3 Analysis of simulated MDPC images using line tracing method**

In this section, the line tracings are again performed along line 1 and line 2 as defined in Fig. 5.6.

The decay of the Y component of the Lorentz deflection along line 2 are illustrated by Fig. 5.20. Curve fittings of these data have been performed and it is found that the plots can be described by functions in the form of  $\beta_y(Y) = a - b \ln(Y + c)$ . The fitting parameters for each model are given in Table 5.1.

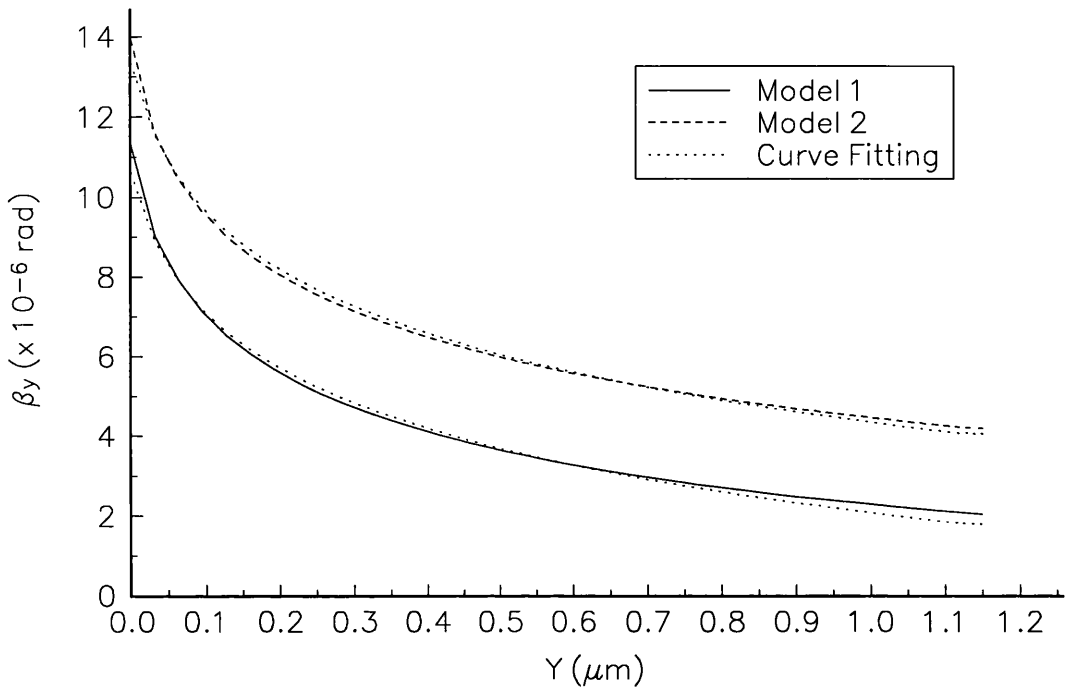


Fig. 5.20 Line tracings along line 2 in the MDPC images simulated using the one-face coated models and curve fittings. These images are mapped along the Y direction.

	a	b	c
Experiment $I_v(Y)$	11.96	27.34	0.026
Model 1 $\beta_v(Y)$	$2.15 \times 10^{-6}$	$2.436 \times 10^{-6}$	0.031
Model 2 $\beta_v(Y)$	$4.43 \times 10^{-6}$	$2.569 \times 10^{-6}$	0.031

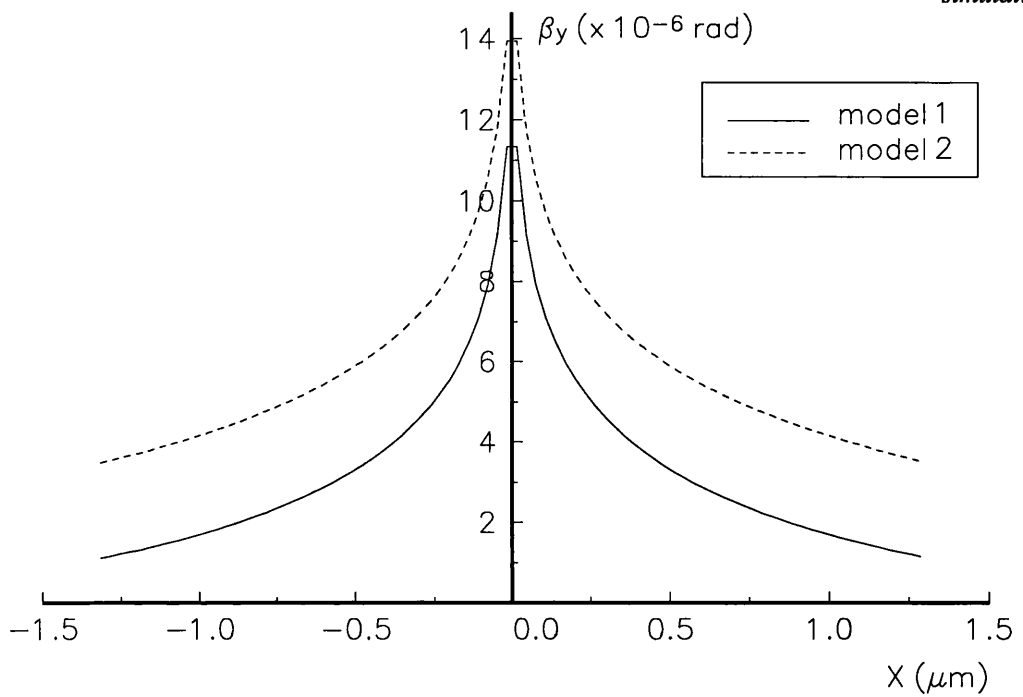
Table 5.1 Parameters of curve fittings. The unit for c is  $\mu\text{m}$ . The unit for a and b is rad.

Fig. 5.20 shows that the fitted curves are almost coincident with the modelling results. This verifies that the curves are good fits of the data. The maximum Lorentz deflections occurred at  $Y = 0$  are  $1.13 \times 10^{-5}$  rad and  $1.39 \times 10^{-5}$  rad for Model 1 and 2 respectively and they decay along the Y axis. The decay distance is measured according to the modelling data and summarised in Table 5.2

	$D_x$ ( $\mu\text{m}$ )	$D_y$ ( $\mu\text{m}$ )
Experiment	0.37 (Right) 0.25 (Left)	0.32
Model 1	0.37	0.36
Model 2	0.70	0.73
Model 3	0.64	0.62
Model 4	0.86	0.78

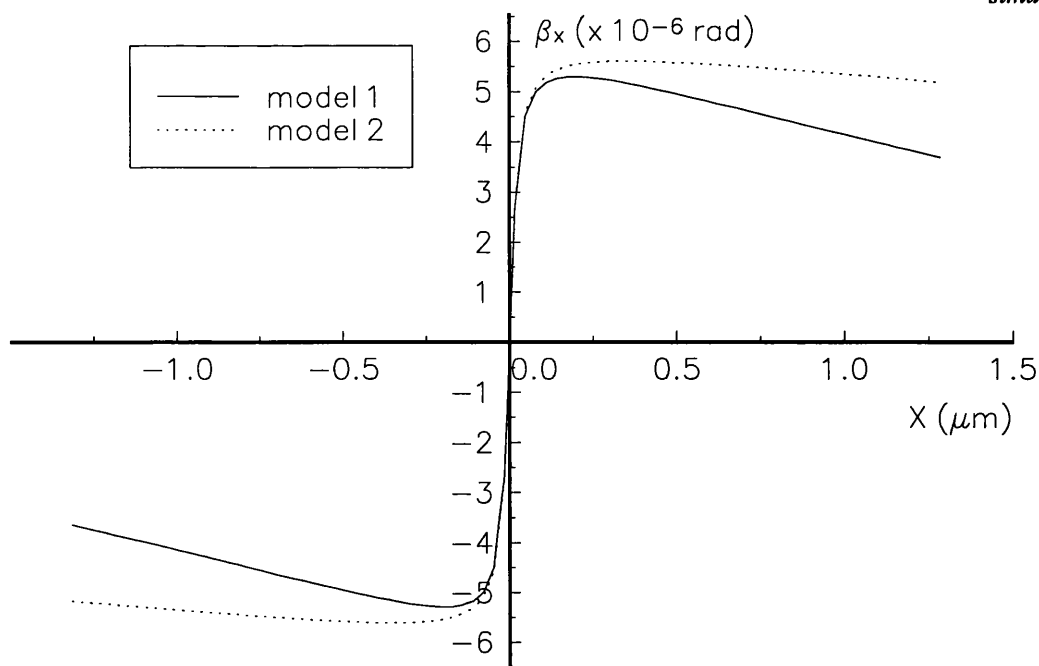
Table 5.2 Parameters measured using line tracing method.  $D_x$  and  $D_y$  represent the decay distances of  $\beta_y$  along line 1 and line 2 respectively.

Fig. 5.21 demonstrates the line tracing results along line 1 in the MDPC images which are mapped along the Y direction. They confirm quantitatively that the Y component of the stray field is symmetric about the Y axis as we expect from the models. They also suggest that the Y component of the stray field of model 2 is always stronger than that of model 1. Although these two curves can not be fitted with the functions, they demonstrate how this component of stray field decays along line 2 and allow decay distance of both models to be measured (Table 5.2).



*Fig. 5.21 Line tracings along line 1 in the MDPC images simulated using the one-face coated models. These images are mapped along the Y direction.*

The line tracing results along line 1 in the MDPC images mapped along the X direction are given in Fig. 5.22. It is obvious that the X component of the Lorentz deflection  $\beta_x$  is anti-symmetric about the Y axis in both models. Since the decay distance is beyond the range of the line tracing, it can not be measured. Nevertheless, the figure indicates that the stray field of model 1 decays more rapidly than that of model 2. The maximum  $\beta_x$  are  $5.29 \times 10^{-6}$  rad and  $5.60 \times 10^{-6}$  rad for model 1 and model 2 respectively.



*Fig. 5.22 Line tracings along line 1 in the MDPC images simulated using the one-face coated models. These images are mapped along the X direction.*

#### 5.7.4 Comparison between experiment and simulations

It has been stated earlier that we are interested in MFM tips which are uniformly magnetised towards the apex and this motivates the computer simulation of the uniformly magnetised tip. By comparing the experiment images with simulated images, we can have an insight into the domain structure in the tip and the stray field it generates. This helps us to understand the tip-sample interaction in MFM imaging.

The computer simulations indicate that for the uniformly magnetised tip the distribution of the Y component of the stray field is symmetric about the Y axis whilst the X component is anti-symmetric. However, the study of the experimental images and line tracings along line 1 suggest that both components of the stray field are asymmetric about the Y axis over the whole of the imaging area, which is different from the modelling results. Therefore, the whole of the tip is not in a single domain state even after application of an 8000 Oe magnetic field. The simulated MDPC images indicate that the

variation of the signal level is smooth along the edges of the tip. In the experimental MDPC images, some abrupt changes in the signal level are observed along the edges. Moreover, these abrupt changes do not occur in places which are symmetric about the Y axis. This suggests that the magnetic pole density  $\sigma$  is not uniform on the edges. Since  $\sigma = \mathbf{M} \cdot \mathbf{n}$  and  $\mathbf{n}$  is constant on a flat surface, the change in  $\sigma$  reflects a non-uniformity in the component of magnetisation normal to the edges. Another possible reason for the sudden changes in signal level is the presence of volume magnetic poles due to non-zero divergence of the magnetisation ( $\nabla \cdot \mathbf{M} \neq 0$ ). Nevertheless, it also leads to the same conclusion that the magnetisation is not uniform in the whole of the tip.

For an MFM tip, it is usually the apex region that dominates the interaction with samples and determines the MFM imaging resolution. Although the whole of the tip does not support uniform magnetisation, some information about the domain structure at the end of the tip can be extracted. As far as the single domain models are concerned, the strongest stray field occurs at the end of the tip, which is the same as the experimental result. Moreover, both the experimental MDPC imaging and the quantitative analysis indicate that a region of about 0.5  $\mu\text{m}$  in radius around the end of the apex comprises the similar stray field distribution as the simulation. As the domain structure at the end of the tip has the most important impact on the stray field in this region, it suggests that the end of the tip may comprise uniform magnetisation. In addition, it is apparent in the experimental MDPC images that no abrupt variation in signal level occurs along the edges of an apex region which extends up to about 0.5  $\mu\text{m}$  from the apex. According to the computer simulation result, this is what we expected from a uniformly magnetised region. Therefore, it confirms that the end of the tip does support uniform magnetisation and the size of such a region is about 0.5  $\mu\text{m}$ .

Since the whole of the tip does not support uniform magnetisation, it would be interesting to know what differences and similarities it makes in terms of the stray field compared to a uniformly magnetised tip which has been simulated using model 1 and model 2. The above comparison has presented some of the major differences to lead us to the conclusions on the domain structure in the tip. More quantitative information on this aspect can be gathered and the impact of the negative poles on the tip-cantilever interface can be found out by studying the line tracing results.

The line tracing of the Y component of the stray field along line 2 suggests that both the experimental data and the modelling data can be described using functions in the form of  $Y = a - b \ln(X + c)$  and the value of the parameters are listed in Table 5.1. It has been pointed out that the curve fitting is performed on the signal level and Lorentz deflection angle for the experiment and simulations respectively. Since the MDPC signal level is a linear function of the Lorentz deflection angle, the modelling data can be scaled linearly according to the fitted curve of the experimental data so that they have the same maximum MDPC signal level (Fig. 5.23). An apparent indication given by the figure is that the Y component of the stray field decays faster in model 1 than in model 2. This is due to the different assumptions used in the modelling. In model 2, only positive poles are assigned along the edges of the tip. Nevertheless, in model 1, extra negative poles are assigned on the tip-cantilever interface. Those negative poles generate stray field which tends to cancel the stray field from the positive poles. This is similar to the case of a monopole and a dipole - the field of the dipole decays more rapidly than the field of the monopole.

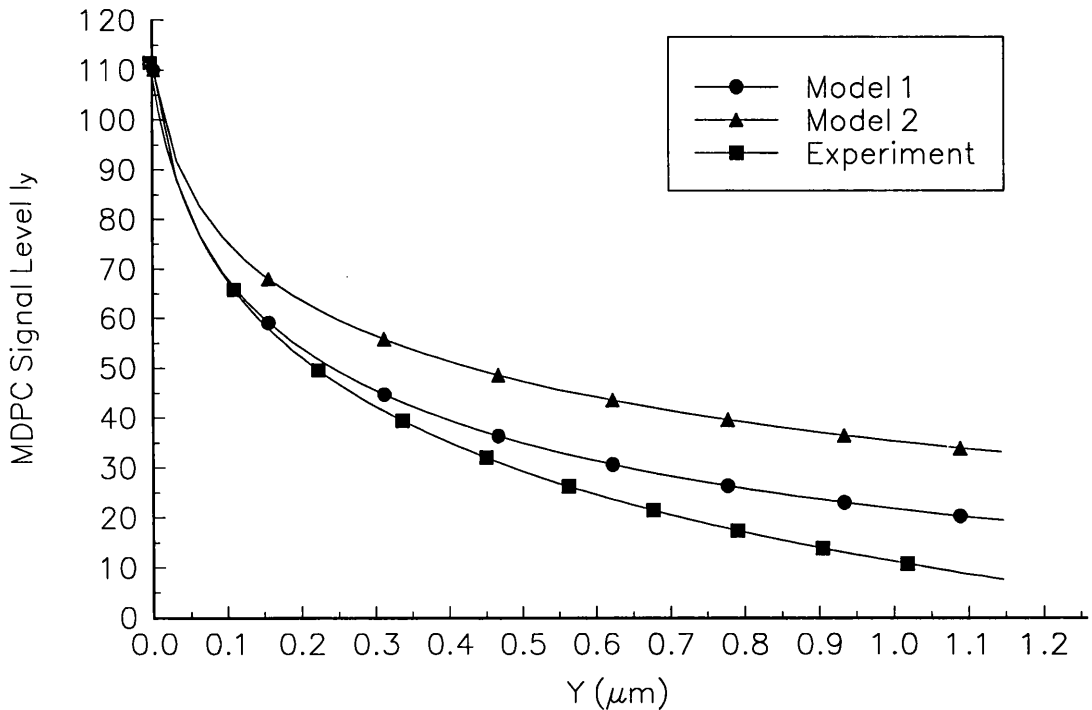


Fig. 5.23 Line tracing of both experimental MDPC images and simulated MDPC images after being re-scaled.

Comparing the simulation with the experiment, we can see that the Y component of the stray field decays even faster than that of model 1. This reflects the effect of the non-uniformity in magnetisation. The non-uniform magnetisation in the tip may result in the presence of both negative and positive magnetic poles. Since magnetic field decays rapidly as the distance from magnetic poles increases, it is predominantly determined by the poles close to the point where it is measured. Therefore, the poles at the end of the tip have a major effect on the stray field distribution along line 2, i.e. as an approximation, the function used for curve fitting may be determined by the domain structure at the end of the tip. Magnetic poles in other regions are farther from the point where the field is measured and thus have a secondary effect on the stray field, i.e. they only finely tune the fitting parameters  $a$ ,  $b$  and  $c$ . Since both the real tip and the models support uniform magnetisation at the end of the apex, the data can be fitted using the same form of function. However, the distribution of poles in other regions is different for each case. As a consequence, the parameters are not identical.

The decay distances have been summarised in Table 5.2 and they confirm the conclusion we have drawn from Fig. 5.22. For the line tracing of the Y component of the stray field along line 1, we did not find an analytical expression. However, by comparing the decay distances, it is found that the experimental data also decays more rapidly than either model and the slowest decay is supported by model 2. This is in agreement with the above discussion.

## **5.8 Simulation of MDPC images using whole-surface coated models**

### **5.8.1 Simulated MDPC images**

It has been discussed in the introduction of this Chapter that the magnetic film can also be coated on the Microlever<sup>TM</sup> using the normal evaporation method and this produces whole-surface coated tips. Since this type of tip is not suitable for use in our MFM as a result of the deformation of the cantilever, it is not imaged using MDPC technique in this work. However, a method will be suggested in Chapter 8 which may overcome this problem.

Thus computer simulations are performed using model 3 and model 4 which have been detailed in section 5.4 to allow comparisons in future.

Qualitatively, the contrast in the MDPC images simulated using both models is symmetric about the Y axes as expected. This is illustrated in Fig. 5.24 by a pair of MDPC images of model 4. They suggest that strong Lorentz deflections occur at the end of the tip as well as along the edges of the tip. Moreover, the equal-deflection rings can be observed in the images radiating from the tip, demonstrating the decay of the stray field.

### **5.8.2 Analysis of MDPC images using arrow mapping method**

The arrow mapping result of the MDPC images simulated using model 3 is given in Fig. 5.25. The length of the arrows indicates that Lorentz deflection is the strongest at the corners on the tip-cantilever interface rather than the end of the apex. This is apparently due to the fact that there are negative poles on the tip-cantilever interfaces. However this is different from the simulation result of model 1 where the strongest deflection occurs at the end of the apex. The arrows appear not to be symmetric in the image although the data indicate that the Lorentz deflection angles are symmetric. This is due to the artefacts of the plotting software.

Fig. 5.26 is the arrow mapping result of model 4. The arrows demonstrate the Lorentz deflection on one side of the Y axis is in a mirror relation to the deflection on the other side of the Y axis. The figure also indicates that the strongest Lorentz deflection occurs at the end of the tip. This is similar to the mapping results of model 1 and model 2 although it is different from the mapping result of model 3. The reason is that there are more magnetic poles on the tip-cantilever interface in model 3 and they make an important contribution to the stray field.

### **5.8.3 Analysis of MDPC images using line tracing method**

The line tracings in these MDPC images are performed along the X and Y axes which are defined in Fig. 5.6. Along the X axis, the line tracing starts from one side of the simulation frame and finishes on the adjacent side.

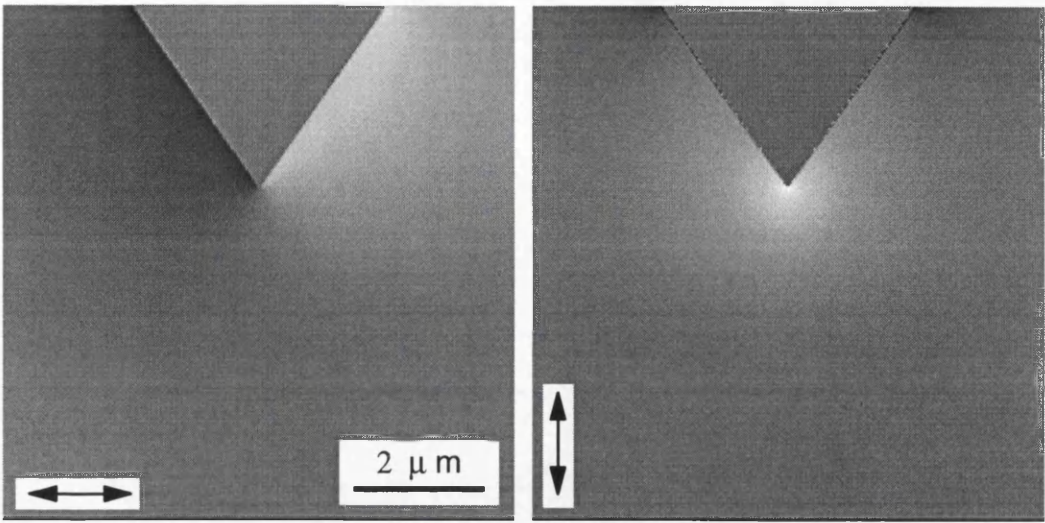


*Fig. 5.24 MDPC images simulated using model 4.*

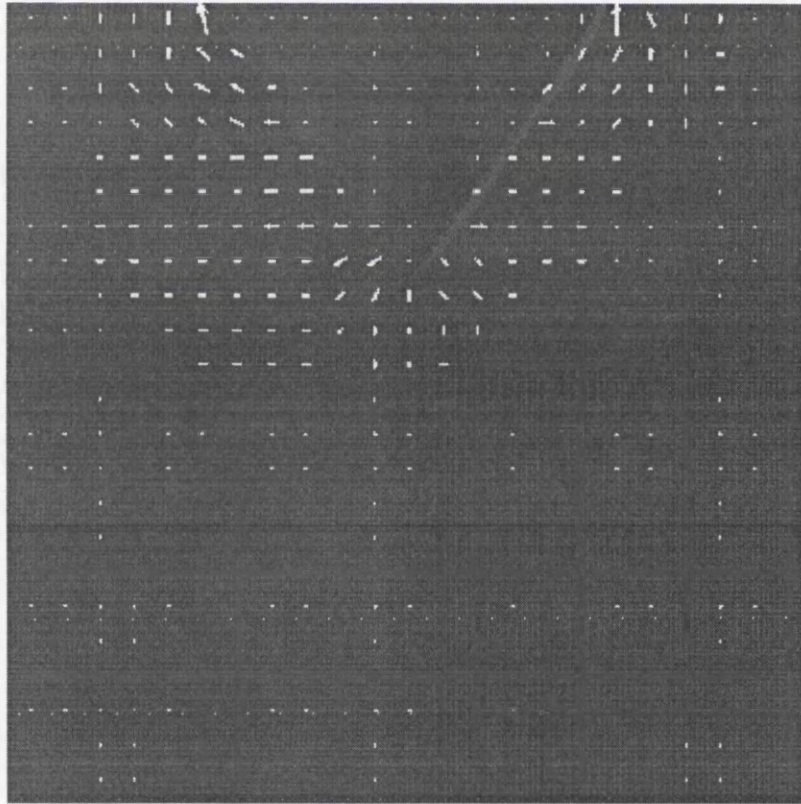


*Fig. 5.25 Arrow mapping result of the MDPC images simulated using model 3.*

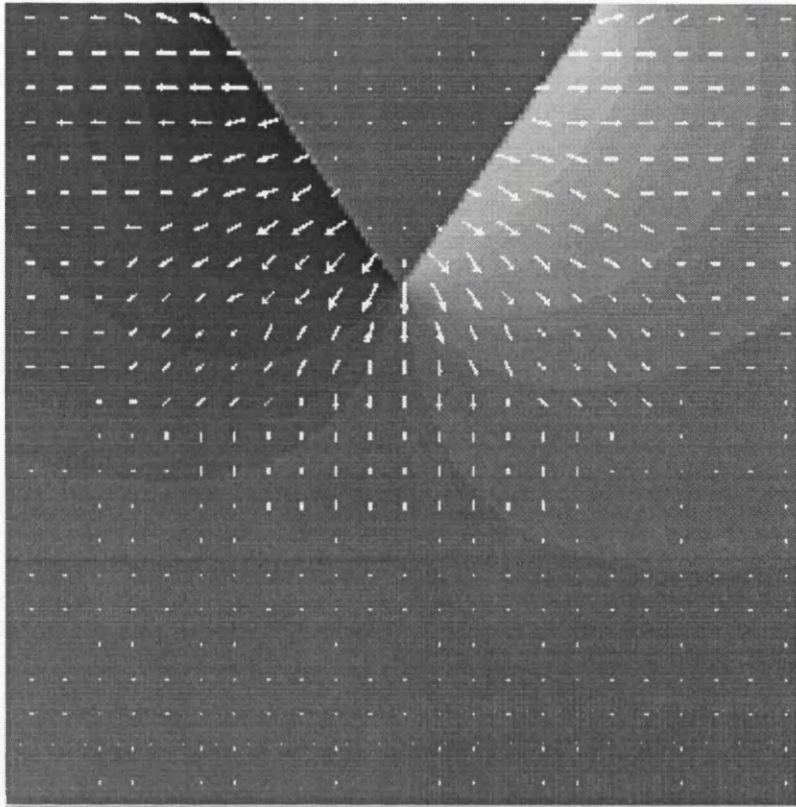


*Fig. 5.26 Arrow mapping result of the MDPC images simulated using model 4.*

Along the Y axis, the line tracing starts from the end of the tip and finishes on the bottom border of the simulation frame.

The decays of the Y component of the MDPC images are demonstrated by the line tracings along the Y axis (Fig. 5.27). Curve fittings have been tried and it is found that the line tracing data cannot be described by functions discussed before. The decay distances are  $0.62\ \mu\text{m}$  and  $0.78\ \mu\text{m}$  for model 3 and model 4 respectively.

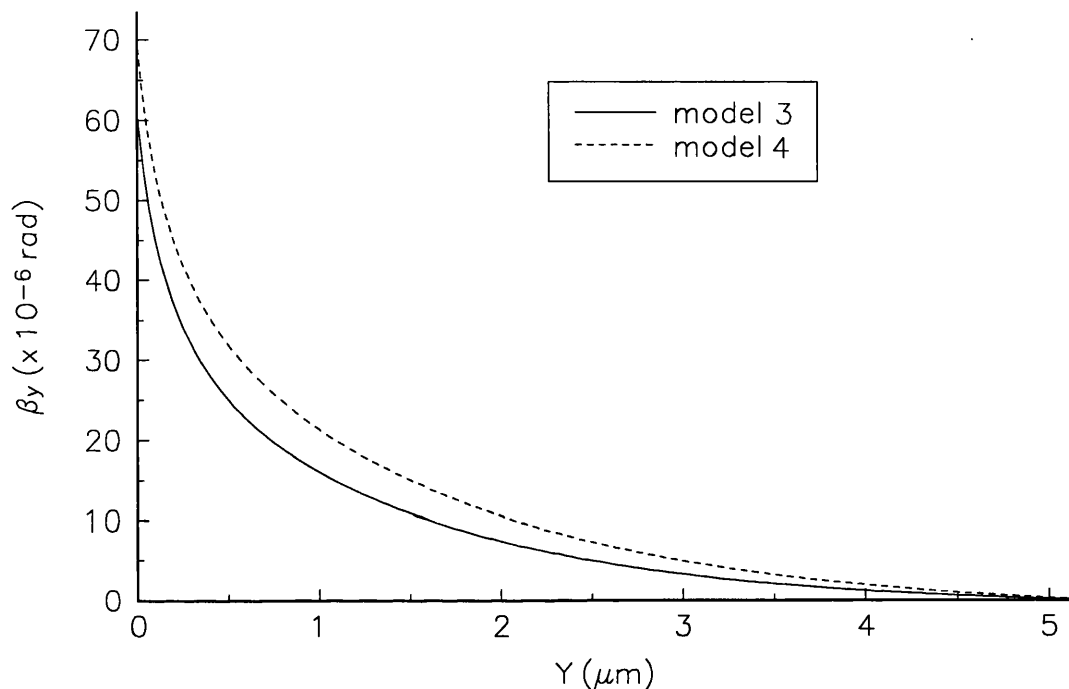


*Fig. 5.27 Line tracings along the Y axes of the MDPC images simulated using the whole-surface coated models. These images are mapped along the Y direction.*

Fig. 5.28 shows the line tracings along the X axes of the MDPC images which are mapped along the Y direction. Basically, they are symmetric about the Y axes with the maximum values at  $Y = 0$ , which are similar to the result of the one-face coated models. Moreover, the line tracing of model 3 is always lower than that of model 4, indicating weaker Lorentz deflection. The maximum Y components of the Lorentz deflection are  $6.04 \times 10^{-5}$  rad and  $6.90 \times 10^{-5}$  rad for model 3 and model 4 respectively. These values decay to  $0.01 \times 10^{-6}$  rad and  $3.73 \times 10^{-6}$  rad respectively at  $Y = 4\ \mu\text{m}$ . The decay

distance is measured to be  $0.64 \mu\text{m}$  for model 3 whereas it is  $0.86 \mu\text{m}$  for model 4.

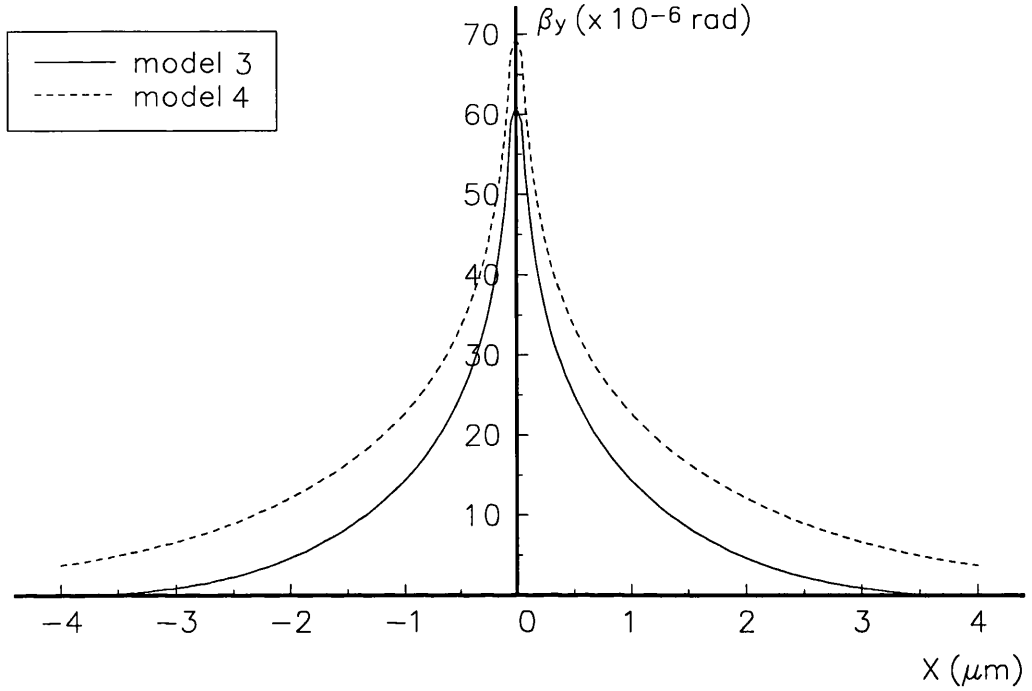


Fig. 5.28 Line tracings along the X axes of the MDPC images simulated using the whole-surface coated models. These images are mapped along the Y direction.

The line tracings along the X axis of both models are shown in Fig. 5.29. It is found that the plot of model 3 is always closer to the X axis than that of model 4, indicating weaker Lorentz deflection. For model 3  $(\beta_x)_{\text{max}}$  is  $2.07 \times 10^{-5}$  rad and decreases to  $5.14 \times 10^{-6}$  rad at  $X = 4 \mu\text{m}$ . For model 4,  $(\beta_x)_{\text{max}}$  is  $2.12 \times 10^{-5}$  rad and decreases to  $9.25 \times 10^{-6}$  rad at  $X = 4 \mu\text{m}$ . Thus,  $\beta_x$  decays more rapidly in model 3 than in model 4 due to the magnetic poles on the tip-cantilever interfaces. Compared to the equivalent one-face coated models, the maximum X components of the Lorentz deflection of the whole-surface coated models are about 4 times larger. This is obviously due to the fact that the whole-surface coated tip comprises more magnetic poles.

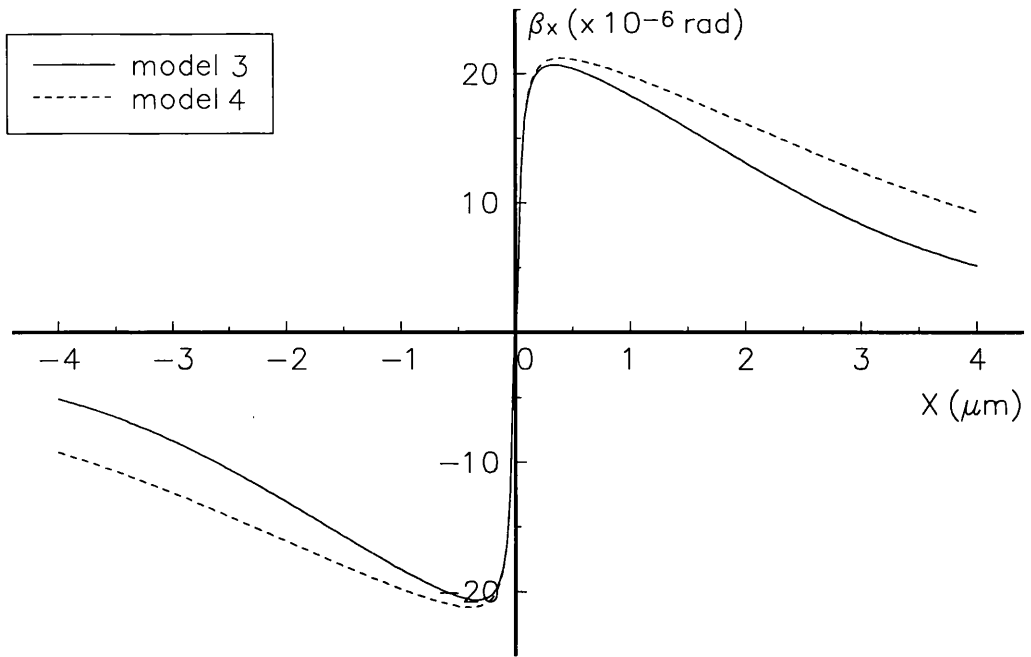


Fig. 5.29 Line tracings along the X axes of the MDPC images simulated using the whole-surface coated models. These images are mapped along the X direction.

#### 5.8.4 Comparison between whole-surface coated models and one-face coated models

Both the one-face coated models and whole-surface coated models support symmetric distribution of stray field about the Y axis, which is in agreement with the input. However, the calculations indicate that the stray field of the whole-surface coated tip is stronger than the stray field of the one-face coated tip, which is due to the fact that the whole-surface coated tip comprises more magnetic poles. Moreover, by comparing the values listed in Table 5.2, it is also noticed that the decay of the stray field of the whole-surface coated tip is slower than that of the one-face coated tip. A consequence of this in terms of MFM imaging is that domain structure of soft magnetic specimens is more likely to be affected by the whole-surface coated tip. Therefore, the one-face coated tip is more suitable for use in the MFM imaging of soft magnetic materials. Another disadvantage of the larger magnetic volume is that it may result in lower MFM resolution as some work in this field has indicated (Grütter et al. 1992). Nevertheless, as the whole-

surface coated tip consists of a larger magnetic volume, it will suffer a stronger deflection force due to tip-sample interaction and thus generate higher MFM signals.

## **5.9 Conclusion**

In this project, both the normal and oblique thermal evaporation techniques have been applied to fabricate MFM tips. SEM studies demonstrate that the curvature of the cantilever caused by the normal evaporation can be overcome by using the oblique thermal evaporation at an oblique angle of about  $55^\circ$ . Although the curvature of the cantilever is a very common problem in the preparation of MFM thin film tips, it has not previously been reported in the literature. The triangular shadow due to the oblique evaporation is observed in the SEM image recorded from the one-face coated tip, which confirms that the cobalt film is predominately coated on one face of the pyramid. By examining the whole-surface coated tip using bright field imaging in the CTEM, the magnetic thin film is found to have good contact with the  $\text{Si}_3\text{N}_4$  pyramid and the thickness of the film is measured to be in good agreement with the experiment design. This suggests that the film on the tip provides good coverage and its thickness can be accurately controlled.

The experimental MDPC studies and computer simulations of the one-face coated tip indicate that the tip does not comprise a uniformly magnetisation throughout the whole volume. However, it appears that uniform magnetisation has been obtained in the apex region and it is the dominant factor in the determination of the stray field at the end of the tip. The decay of the Lorentz deflection angles has been investigated and the decay distances are measured.

The simulations of the whole-surface coated tip indicate that it produces stronger stray field than the one-face coated tip. Since the magnetic volume of the whole-surface coated tip is larger than that of the one-face coated tip and the location of the magnetic poles is different, the distribution of stray field is different. These simulation results will be compared with experimental characterisations in future.

## **Chapter 6**

# **Characterisation of elements simulating thin films on MFM tips**

### **6.1 Introduction**

The one-face coated cobalt tips studied in Chapter 5 have been used in our MFM (Beaumont et al 1994, Valera and Farley 1995). This instrument has been used to image various magnetic specimens and a typical image recorded from a Co/Pt multilayer specimen is displayed in Fig. 6.1. This MFM image suggests the tip is capable of imaging 30 nm magnetic details (Valera et. al. 1995). Occasionally we find that when the tip is used to characterise specimens with strong stray fields, the observed contrast is not as straightforward. Fig. 6.2 is an MFM image acquired from a Co/Pt sample, which displays little magnetic contrast. One possible explanation for this phenomenon is that the domain structure of the tip is perturbed by the field from the specimen. Such a condition is undesirable and MFM images acquired in this way are difficult to interpret. In order to avoid this problem, it is necessary that the behaviour of the tip in magnetic fields is understood and in this chapter we attempt to provide such information.

Since the Microlevers<sup>TM</sup> (Chapter 3) are too thick to be imaged using Lorentz microscopy, permalloy and cobalt thin film elements are fabricated on the Si<sub>3</sub>N<sub>4</sub> membrane substrates (Chapter 3) to simulate magnetic thin films on the one-face coated MFM tips. The evaporation condition used to fabricate the cobalt elements is the same as that used to fabricate the MFM tips which have been studied in the previous chapter. Thus the exchange coupling between grains in the cobalt elements is reduced. The evaporation of the permalloy elements was performed with a relatively faster growth rate thus producing fully exchange coupled grains. More details of the evaporation set up can be found in Chapter 3. These elements allow direct imaging of domain structures in various states to be carried out. Moreover, the dynamic behaviour of these elements can also be investigated by performing in-situ magnetising experiments utilising the in-situ magnetising stage (Chapter 3). The ideas used in designing the SIM1 to SIM4 patterns and the specimen fabrication process have been given in Chapter 3. The physical

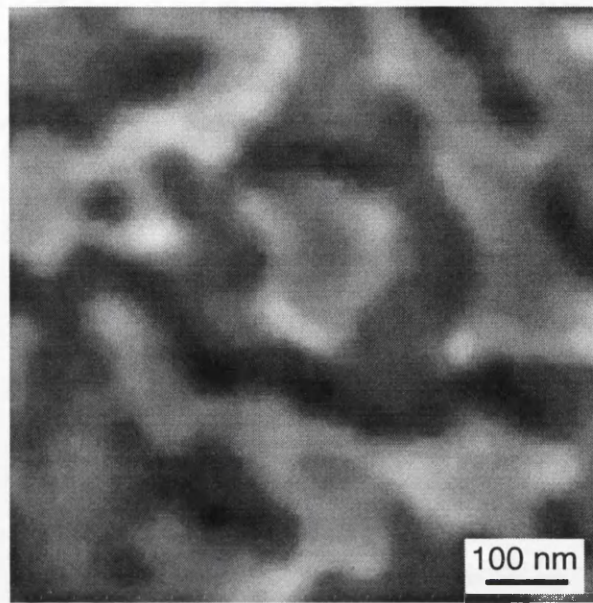


*Fig. 6.1 MFM image of a Co/Pt multilayer specimen acquired with a one-face coated cobalt tip (Courtesy of Dr. A Farley).*

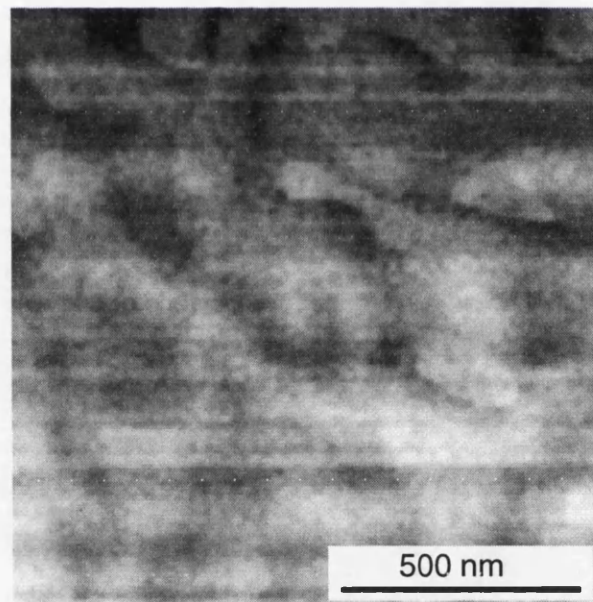


*Fig. 6.2 MFM image of a Co/Pt multilayer specimen acquired with a one-face coated cobalt tip (Courtesy of Dr. A Farley).*

characteristics of the elements are investigated using bright field and electron diffraction modes whereas the magnetic configurations are examined using the Fresnel and Foucault modes of Lorentz microscopy. These studies are performed on the JEOL 2000FX CTEM/STEM (Chapter 2) and the results of the cobalt and permalloy elements are described in section 6.2 and 6.3 respectively.

## **6.2 Cobalt elements**

### **6.2.1 Physical characteristics of elements**

The diffraction pattern shown in Fig. 6.3 comprises diffraction rings and each of them is uniform in brightness. This indicates the elements comprise a randomly oriented polycrystalline structure. Fig. 6.4 is a bright field image taken from the apex region of the SIM1 element. The grain size is measured to be in the range of 5 ~ 10 nm and the radius of the apex is  $30 \pm 5$  nm which is consistent with that of the cobalt film on the MFM tip studied in Chapter 5. Bright field images of other elements confirm that they have the similar grain size and apex sharpness. From these observations, it is apparent that the elements are good representations of the film on the one-face coated MFM tips.

### **6.2.2 Magnetic study of SIM1 element**

#### **6.2.2.1 As-grown state**

The domain structure of the SIM1 element in the as-grown state is studied using the Foucault mode of Lorentz microscopy. As the arrows indicate in Fig. 6.5 the domain configuration is characterised along two orthogonal mapping directions and domains are represented by dark and bright clusters. A fine domain structure is observed and the average width of the domains is measured to about 300 ~ 400 nm. In both components, it is observed that the overall areas of the black and white regions are about equal indicating the net magnetisation of the element is zero. Furthermore no contrast due to stray field is observed around the element, which suggests the magnetisation

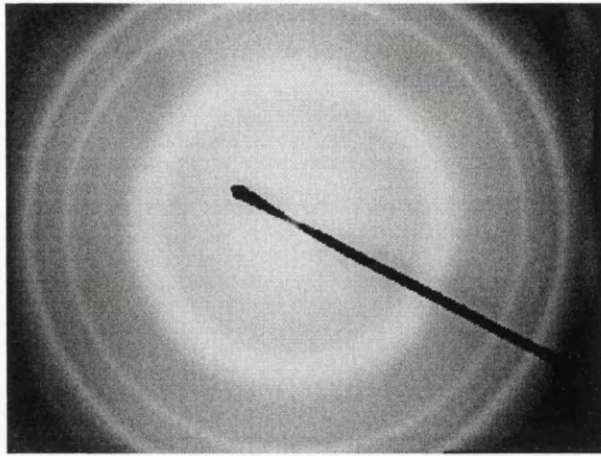


*Fig. 6.3 Electron diffraction pattern of the cobalt elements indicating a polycrystalline structure.*

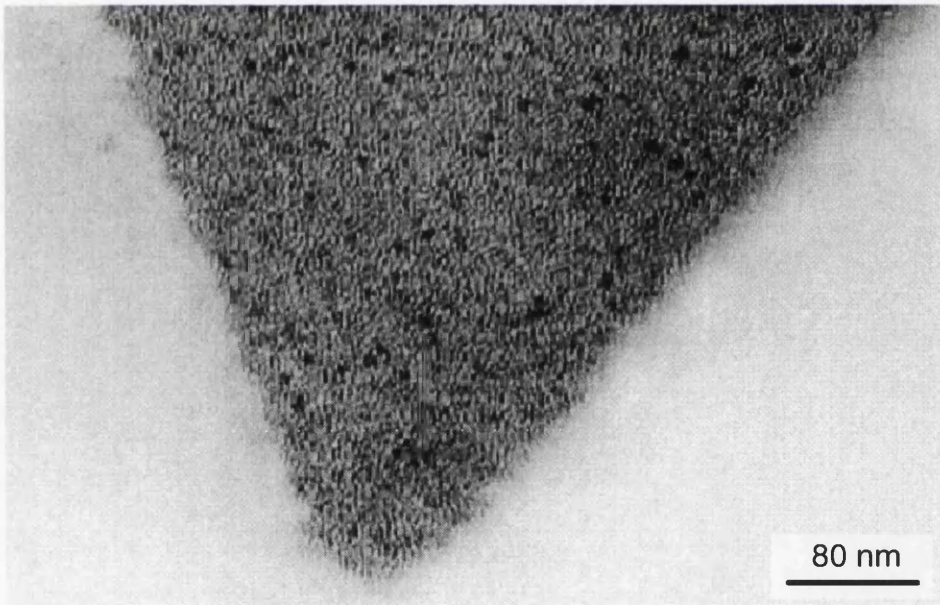


*Fig. 6.4 TEM image of the apex region of the cobalt SIM1 element.*

is approximately parallel to the edges of the element so that the magnetostatic energy associated with surface poles is eliminated. These observations indicate that the small scale domain structure is not strongly influenced by the shape of the element except perhaps only in regions very close to the edges.

### 6.2.2.3 Ac-demagnetised state

The procedure for performing in-plane ac-demagnetising experiments has been described along with the instrumentation in Chapter 3. In general, the resultant domain structure is expected to be a low energy state. The Foucault images of this element is shown in Fig. 6.6. It supports a fairly regular domain structure with a degree of solenoidality due to the shape effect. In the rectangular region, large scale domains are observed containing magnetisation ripple (Craik and Tebble 1965) and the magnetisation is parallel to the nearest edge of the element to reduce the magnetostatic energy. Each of the triangular regions comprises effectively two domains with magnetisations parallel to the nearest edge as indicated by arrows in the figure. These two domains are almost equal in size with a domain wall running towards the apex.

### 6.2.2.4 Remanent state

This remanent state is produced by applying an 8000 Oe external field along the X direction and then decreasing it to zero. The domain structure in this state is again imaged using the Foucault mode as shown in Fig. 6.7. It is observed that the overall structure is rather irregular. The rectangular region comprises a considerable component of magnetisation perpendicular to the applied external field. The magnetisation in regions close to the edges appears to be approximately parallel to the edge thus reducing the magnetostatic energy.

The domain structures of the triangular regions are investigated at higher magnification in order to reveal details. It is noted that their domain structures are very similar. Hence, Foucault images are only recorded from

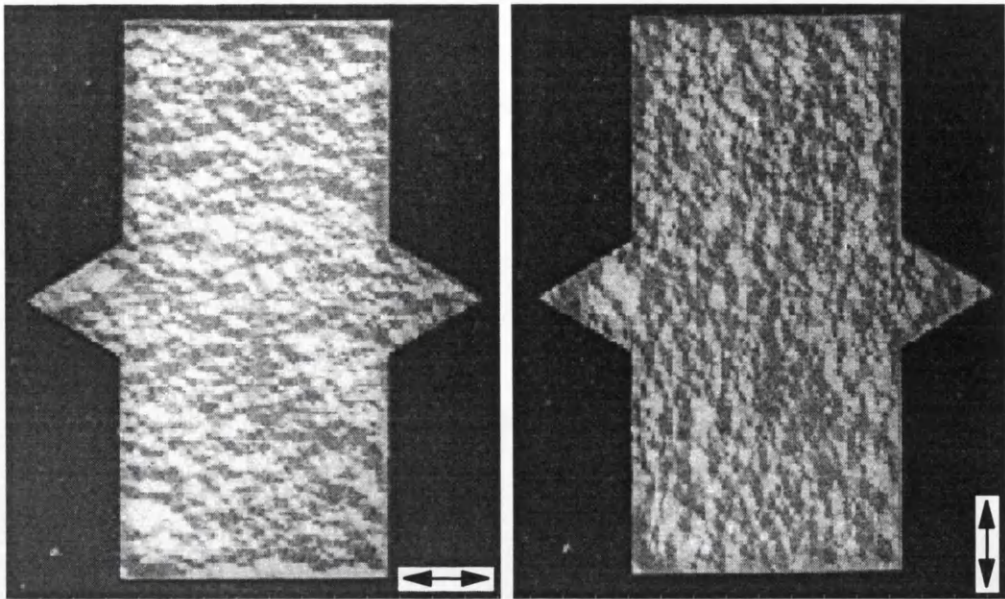


*Fig. 6.5 Foucault images of the cobalt SIM1 element in the as-grown state. The X axis is horizontal while the Y axis is vertical. The length of the edge of the triangular region is 4  $\mu\text{m}$ .*

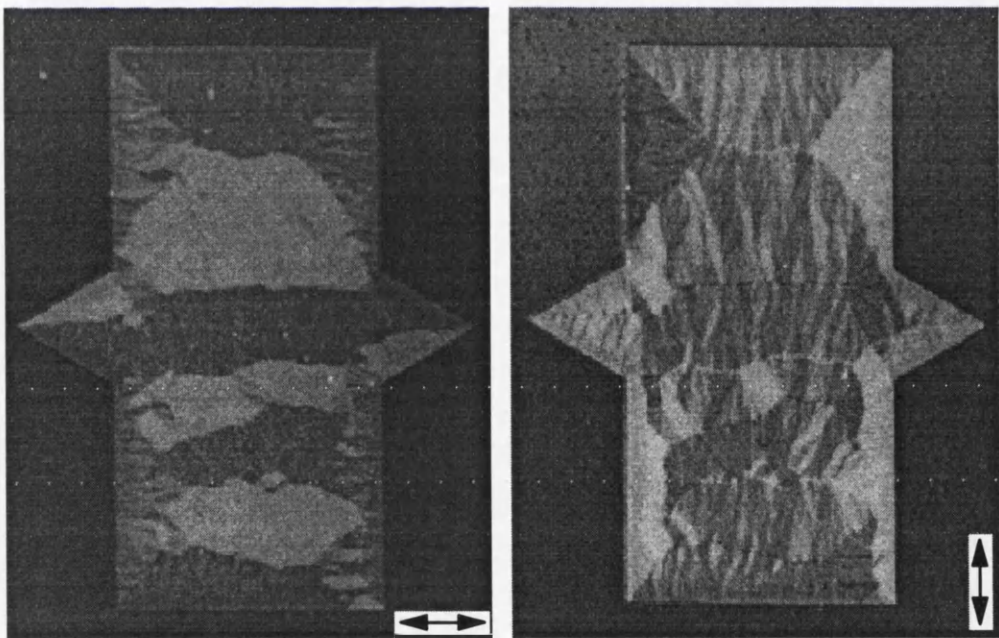


*Fig. 6.6 Foucault images of the cobalt SIM1 element in the ac-demagnetised state. The X axis is horizontal while the Y axis is vertical. The length of the edge of the triangular region is 4  $\mu\text{m}$ .*

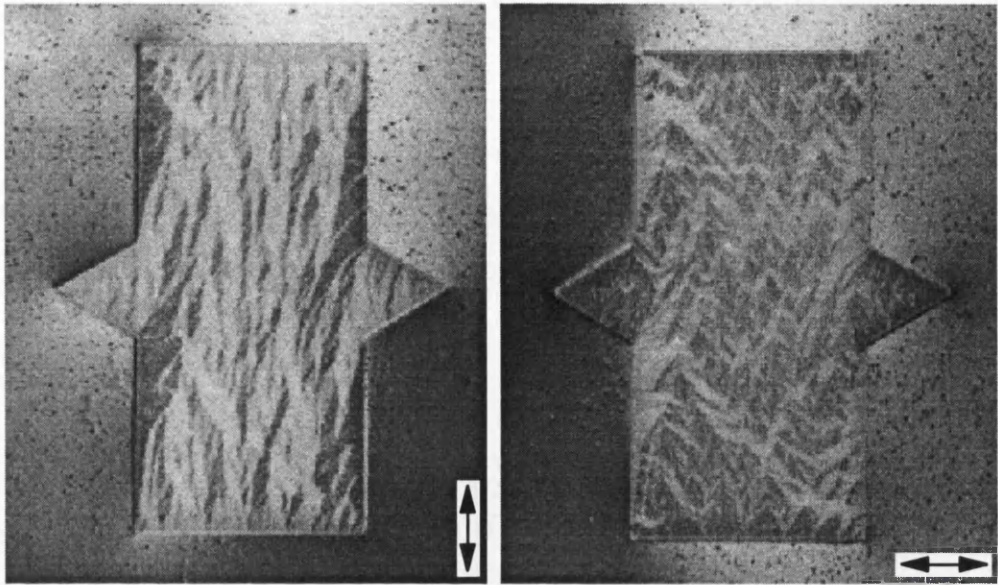


*Fig. 6.7 Foucault images of the cobalt SIM1 element in the remanent state. The X axis is horizontal while the Y axis is vertical. The length of the edge of the triangular region is 4  $\mu\text{m}$ .*

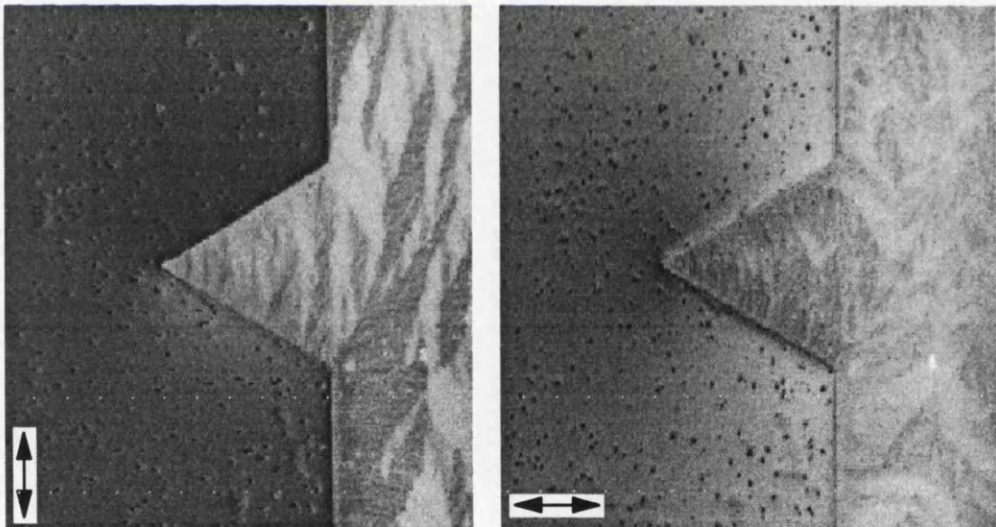


*Fig. 6.8 Foucault images highlighting one of the apex regions of the cobalt SIM1 element in the remanent state. The X axis is horizontal while the Y axis is vertical. The length of the edge of the triangular region is 4  $\mu\text{m}$ .*

one of them and shown in Fig. 6.8. They demonstrate a typical ripple structure with an average direction of the magnetisation pointing to the apex. Apparently, there is little or no ripple in a region of  $500 \pm 20$  nm long at the extremity, which indicates this small volume is indeed uniformly magnetised along the X axis. This is in good agreement with our conclusion on the size of the uniformly magnetised region in the one-face coated cobalt tip, which was drawn from stray field distribution (Chapter 5). Since the magnetisation is discontinuous on the edges, magnetic poles occur and stray field is observed around the apex.

Comparing this domain structure with that in the as-grown and ac-demagnetised states, it is found the magnetisation in the remanent state has more directionality especially in the triangular region. This is the result of the applied magnetising field and causes a part of the apex region to be uniformly magnetised. Again it reflects the reduced exchange coupling between the grains.

#### 6.2.2.5 In-situ magnetising experiment

The in-situ magnetising experiment performed on the SIM1 element starts with the remanent state as it is a reasonably well defined and reproducible state. Moreover, it is also usually the state in which an MFM tip is used to image samples. The whole magnetising process is shown in Fig. 6.9. Since in the Foucault mode imaging any small variation in the magnetic field generated by the in-situ magnetising stage causes instability in the imaging condition, especially when a large external field is applied, the imaging condition has to be reset every time the field is varied. Therefore, the Fresnel imaging mode is used in this experiment to identify main changes in domain structure. In this experiment, we are interested in the domain nucleation process especially in the triangular region of the element since this region represents the magnetic material in the MFM tip close to the sample and its domain structure is the major factor determining the stray field around the end of the tip (Chapter 5). The element is consistently monitored while the external field is gradually increased from 0 to the maximum 100 Oe against the initial magnetisation direction before being decreased to 0.

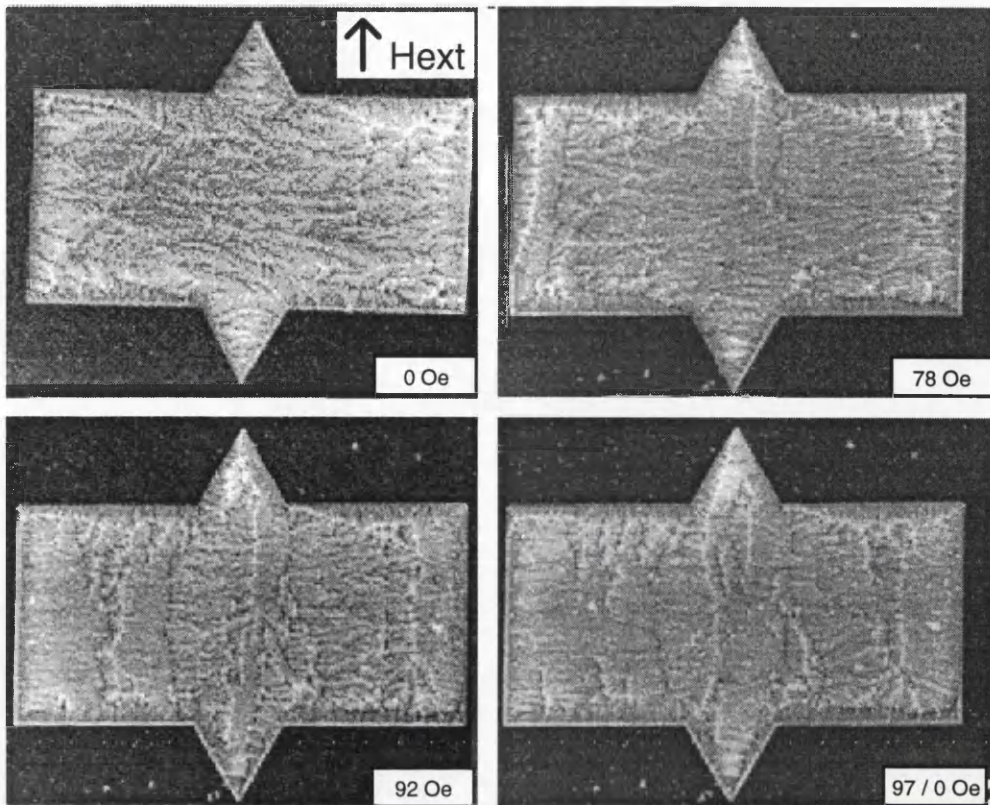


Fig. 6.9 Fresnel images of the cobalt SIM1 element during the in-situ magnetising experiment. The X axis is horizontal while the Y axis is vertical. The length of the edge of the triangular region is  $4 \mu\text{m}$ .

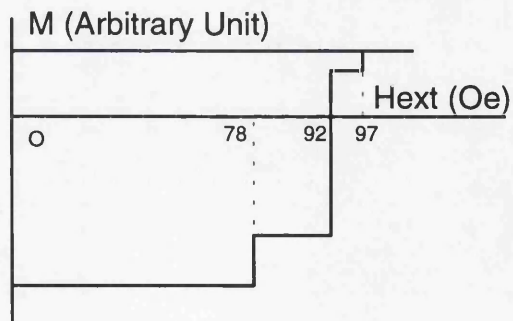


Fig. 6.10 Schematic diagram of a part of hysteresis loop illustrating the in-situ magnetising experiment performed on the cobalt SIM1 element.

During the application of the field, there are three major irreversible changes in the domain structure and they are illustrated schematically in the hysteresis loop (Fig. 6.10). As described earlier in this chapter, the remanent state of the SIM1 element comprises a near uniform magnetisation at the end of the apexes. This domain structure does not change markedly until the external field reaches 78 Oe where a domain wall is nucleated in the top triangular region. This domain wall runs through the triangular region and therefore the magnetisation in the extremity is no longer uniform. Meanwhile, further domain wall nucleation also takes place in the rectangular region although the volume occupied by the nucleated domains is very small in relation to the volume of the element. This domain structure is stable until the external field reaches a value of 92 Oe. At this field many domain walls are generated and the extremity of each triangular region comprises several domains. In this state, the magnetisation in most of the volume has been aligned along the field direction and thus the net magnetisation becomes a positive value. Further domain wall nucleation and movement are observed, mostly in the centre of the element, when the external field reaches 97 Oe. Apparently, the triangular region still does not support a uniform magnetisation not even at the extremities; the rectangular region also supports a multidomain structure. Increasing the external field to 100 Oe does not make any significant changes and this configuration is maintained after the field has been removed.

More domain wall nucleation and motion are expected to occur beyond 100 Oe, but they cannot be observed using this in-situ magnetising stage. Although this is certainly a limitation, the applied field is enough to change the domain structure in the apex region and provides useful information on the stability of the tip's remanent state in an external field.

### **6.2.3 Magnetic study of SIM2 element**

#### **6.2.3.1 As-grown state**

Fig. 6.11 shows the Foucault images taken from the element SIM2. It is apparent the magnetic configuration is very similar to that of the SIM1 element in the as-grown state. However, the average width of the domains is

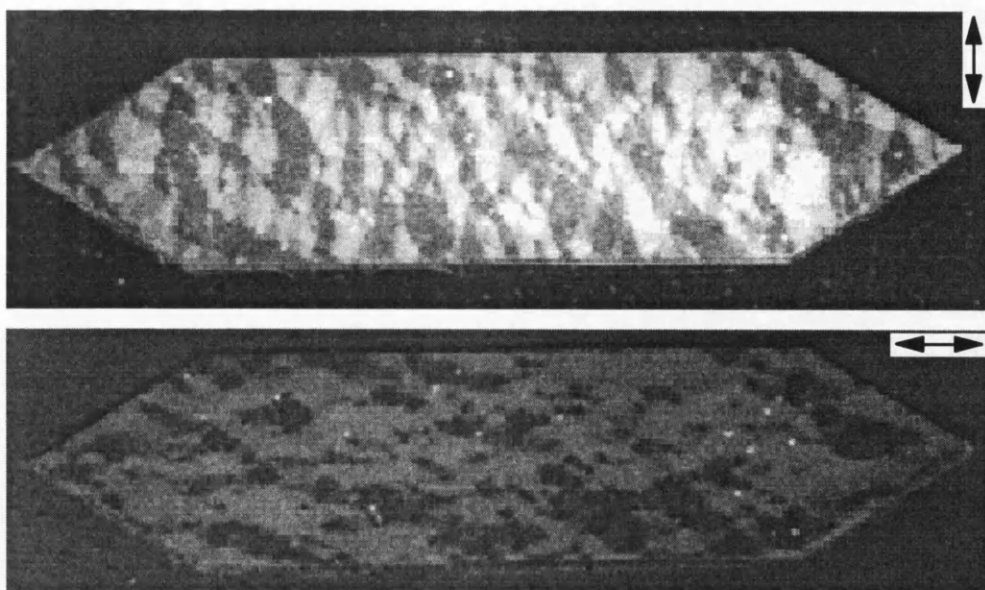


*Fig. 6.11 Foucault images of the cobalt SIM2 element in the as-grown state. The X axis is horizontal while the Y axis is vertical. The length of the edge of the triangular region is 4  $\mu\text{m}$ .*

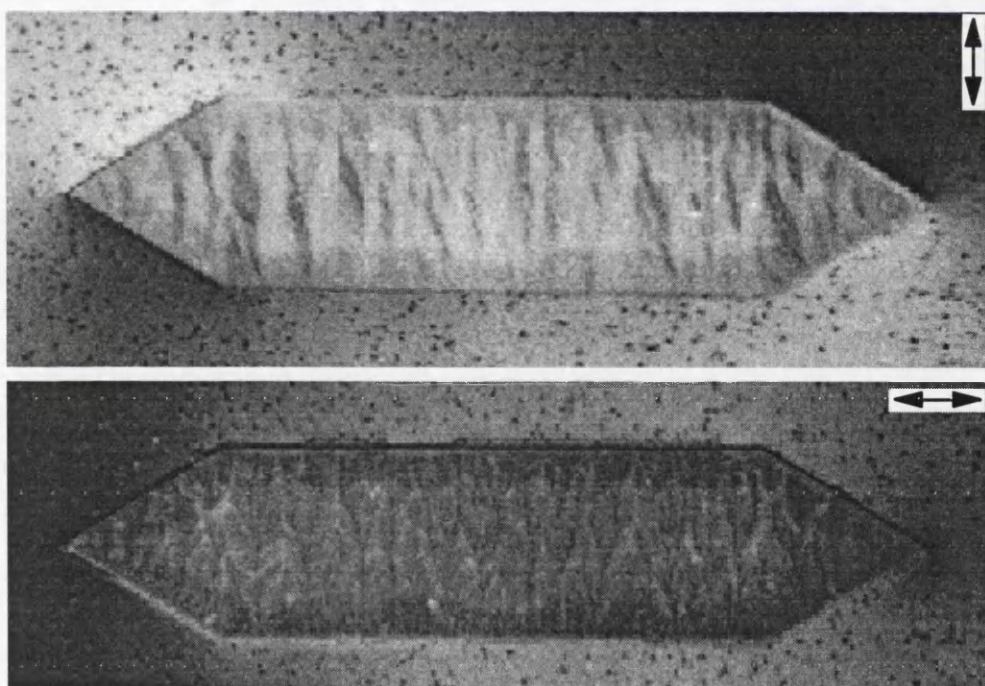


*Fig. 6.12 Foucault images of the cobalt SIM2 element in the ac-demagnetised state. The X axis is horizontal while the Y axis is vertical. The length of the edge of the triangular region is 4  $\mu\text{m}$ .*

measured to be in the range of 400 ~ 500 nm which is wider than that of the SIM1 element in the same state. Moreover, in the SIM2 element, the total area of the bright domains in the image mapped along the X direction is greater than the total area of the dark domains, although they appear almost equal in the image mapped along the Y direction. Thus, there is a net component of magnetisation parallel to the X axis. Although this reflects the fact that the SIM2 element is more acicular, it is quite surprising because of the small scale of the domain structure relative to the size of the element.

### 6.2.3.2 Ac-demagnetised state

The ac-demagnetised state of the SIM4 element is shown in Fig. 6.12. This is a typical ripple structure with the average direction of magnetisation parallel to the length of the element. At the end of the apex region, the ripple becomes negligible indicating a near uniform magnetisation. Thus, magnetic poles occur on the edges due to the discontinuity of the magnetisation. In the image mapped along the Y direction, the stray field around the end of the triangular regions is symmetric and this is qualitatively what is expected from such a nearly uniformly magnetised triangular region.

The fine domain structure in the as-grown state of this element has disappeared although there are still magnetic variations due to the ripple. It is slightly surprising that the ac-demagnetised state supports a near uniform magnetisation distribution rather than one with a flux closure structure. The acicular nature of the element is no doubt a dominant factor in this respect.

### 6.2.3.3 Remanent State

The overall domain structure of the SIM2 element in the remanent state is effectively identical to its ac-demagnetised state. Fig. 6.13 displays the high magnification Foucault images recorded from one apex region. Although brightness variations due to ripple can be observed in most of the volume of the element, the variation is significantly reduced in a region  $500 \pm 20$  nm from the end of the apex. This suggests that the region supports a uniform magnetisation as the SIM1 element does in the same state. Thus, it is

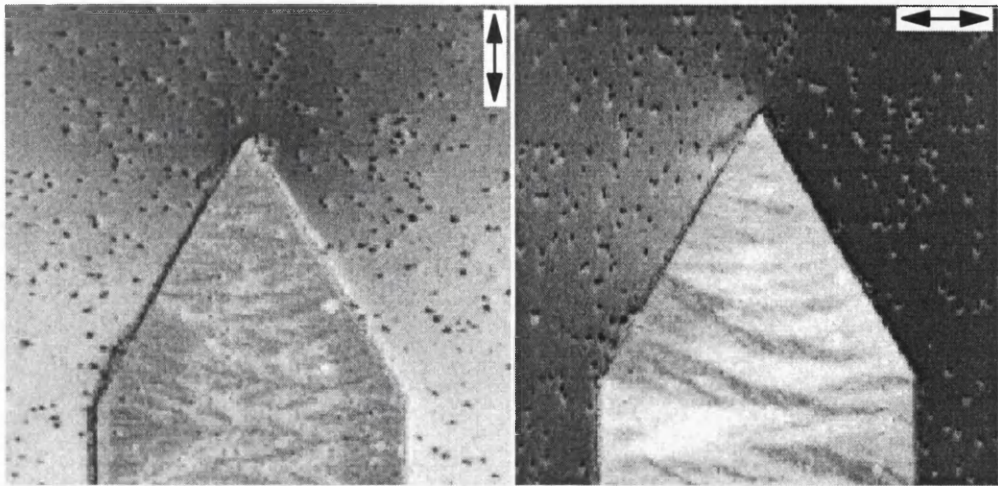


Fig. 6.13 Foucault images of the cobalt SIM2 element in the remanent state. The X axis is horizontal while the Y axis is vertical. The length of the edge of the triangular region is 4  $\mu\text{m}$ .

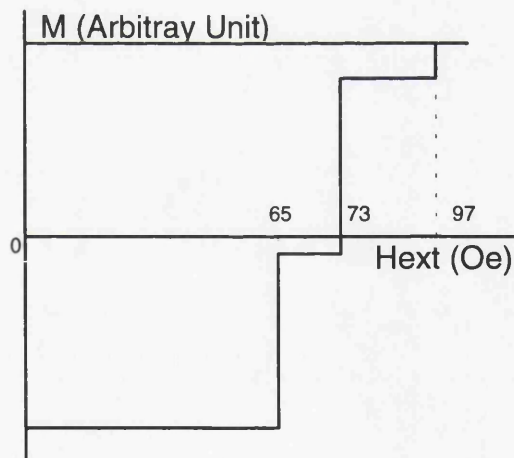


Fig. 6.14 Schematic diagram of a part of hysteresis loop illustrating the in-situ magnetising experiment performed on the cobalt SIM2 element.

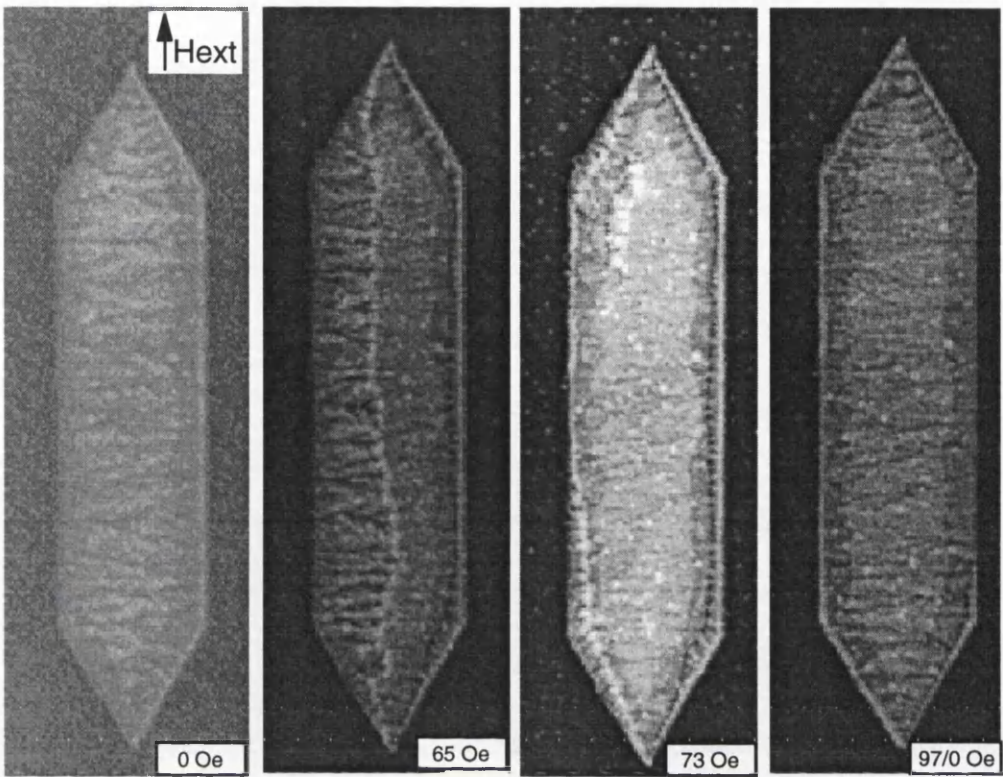
confirmed that the one-face coated cobalt tip does support a near uniform magnetisation at the end of the apex region and its length is about 500 nm.

#### 6.2.3.4 In-situ magnetising experiment

The in-situ magnetising experiment performed on the SIM2 element starts from the remanent state and has 3 main irreversible changes in domain structures within the field range. This process is schematically shown in the hysteresis loop (Fig. 6.14). The domain structure of the element is recorded after each irreversible change happens and is displayed in Fig. 6.15.

The remanent state of the element has been imaged using Foucault imaging and discussed in detail in the previous section. No significant change is observed before the applied external field reaches  $H_{\text{ext}} = 65$  Oe where two domain walls have been generated which run along the length of the element. The element now supports three domains as shown in the schematic diagram (b). Here the central domain is in the direction of the applied field whereas the domains along the edges still maintain antiparallel magnetisation to the external field. In this domain configuration each apex of the element is split into three parts. Increasing the field to 73 Oe results in the third magnetic configuration as the schematic diagram (c) shows. In this state, the two domain walls are driven closer to the edges of the element and the majority volume of the element comprises a magnetisation parallel to the external field. A small "island" domain is observed within the central domain with a magnetisation antiparallel to the direction of the external field. The domains close to the edges also maintain the initial magnetisation direction (antiparallel to  $H_{\text{ext}}$ ) but their volume is very small compared to the nucleated domain. These domain walls are found to be of the cross-tie type. This structure is stable again until the external field reaches 97 Oe, where all the domains with magnetisation antiparallel to the external field has disappeared. Therefore, the element comprises a near uniform magnetisation with ripple present. This domain structure is identical to the remanent state apart from the fact that the average direction of magnetisation is reversed.

In this magnetising process, although the external field is still applied up to

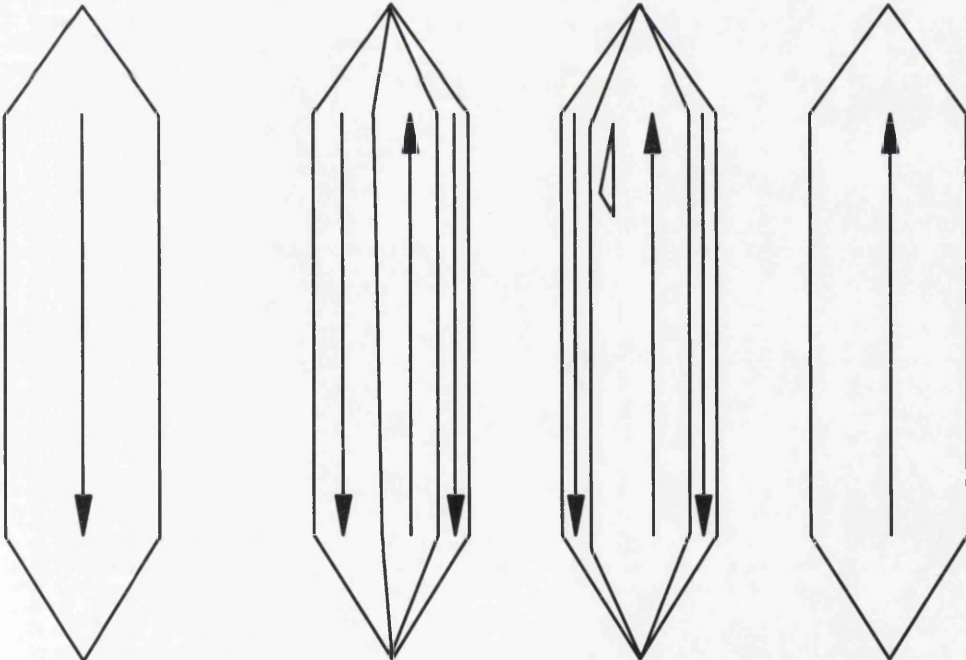


(a)

(b)

(c)

(d)



(a)

(b)

(c)

(d)

*Fig. 6.15 Fresnel images and schematic diagrams of domain structures of the cobalt SIM2 element during the in-situ magnetising experiment. The X axis is horizontal while the Y axis is vertical. The length of the edge of the triangular region is 4  $\mu\text{m}$ .*

100 Oe, it is almost sufficient to saturate the element. Hence, this experiment demonstrates effectively the behaviour of the element during a major hysteresis loop.

## **6.2.4 Magnetic study of SIM3 element**

### **6.2.4.1 As-grown state**

Fig. 6.16 displays the Foucault images of the SIM3 element in the as-grown state. Relatively large scale domains with irregular shapes are observed. The magnetisation in the domains is approximately parallel to the edges of the element and exhibits a degree of flux closure associated with shape effect. No stray field is visible in the images confirming the solenoidality. It is also found that the brightness in the top apex is not uniform, which suggests that this region does not comprise uniform magnetisation.

### **6.2.4.2 Ac-demagnetised state**

The ac-demagnetised state of this element is shown in Fig. 6.17. It is observed that the SIM3 element comprises a "Y" type of domain structure with three equal-sized domains. The magnetisation of each domain is parallel to its nearest edge although some ripple is present indicating a degree of divergence in the direction of magnetisation. Clearly the element possesses a flux closure structure indicating that the shape effect is significant in the formation of the domain structure.

### **6.2.4.3 Remanent state**

This state is produced by applying an 8000 Oe field along the Y axis and decreasing it to zero. The Foucault images of the remanent state are shown in Fig. 6.18. This element contains markedly more significant variations in the magnetisation direction than in the triangular parts of the SIM1 and SIM2 elements in the same state. Although a fairly irregular domain structure is supported by the element, the apex is found to support a near uniform

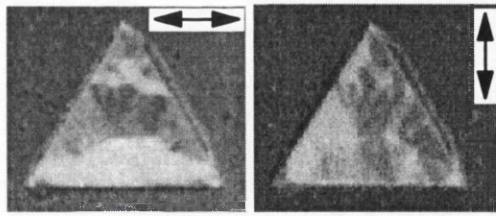


*Fig. 6.16 Foucault images of the cobalt SIM3 element in the as-grown state. The X axis is horizontal while the Y axis is vertical. The length of the edge of the element is 4  $\mu\text{m}$ .*

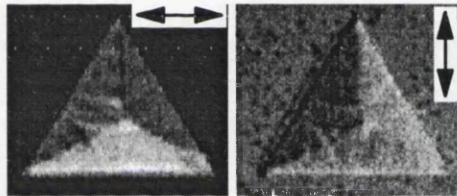


*Fig. 6.17 Foucault images of the cobalt SIM3 element in the ac-demagnetised state. The X axis is horizontal while the Y axis is vertical. The length of the edge of the element is 4  $\mu\text{m}$ .*

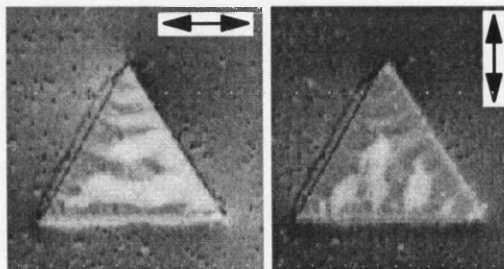


*Fig. 6.18 Foucault images of the cobalt SIM3 element in the remanent state. The X axis is horizontal while the Y axis is vertical. The length of the edge of the element is 4  $\mu\text{m}$ .*

magnetisation in a region of  $350 \pm 20$  nm long. Therefore, stray field is observed around this apex. Comparing the size of the uniformly magnetised regions in the SIM1 and SIM2 elements, the uniformly magnetised region in the SIM3 element is significantly shorter although the mechanism responsible for this difference is not obvious. A narrow domain is observed along the bottom edge of the element in the images mapped along the X direction. This domain has its magnetisation parallel to the edge in order to reduce the magnetostatic energy.

#### 6.2.4.4 In-situ magnetising experiment

This experiment performed on the SIM3 element starts with the remanent state which has been described in the previous section. It is found that the domain structure of the element experiences 2 major irreversible changes in the field range used in the magnetising process as shown in the schematic hysteresis loop of Fig. 6.19. The first irreversible change occurs at  $H_{\text{ext}} = 78$  Oe where a Y-like domain structure is generated. This is effectively a solenoidal configuration although not as simple as in the ac-demagnetised state. In this structure, the top apex where the magnetisation was nearly uniform initially is now split into two domains by a domain wall. This domain structure is stable until the external field reaches 98 Oe where the domain at the left edge of the element increases slightly by movement of the domain wall farther to the right hand side. However this is still a Y-like domain configuration albeit distorted.

As the final domain structure at  $H_{\text{ext}} = 100$  Oe comprises several domains, the element only experiences a small part of the hysteresis loop. Nevertheless, this experiment still demonstrates some major changes in the element as domain nucleation and the reduction in net magnetisation to nearly zero are observed.

### 6.2.5 Magnetic study of SIM4 element

#### 6.2.5.1 As-grown state

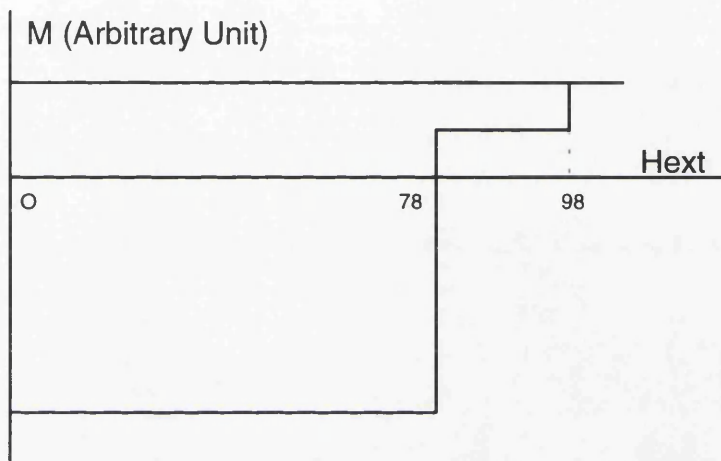
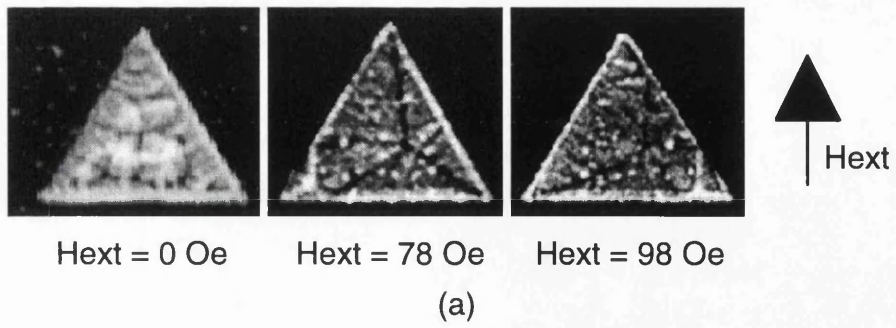


Fig. 6.19 (a) Fresnel images of the cobalt SIM3 element during the in-situ magnetising experiment. The X axis is horizontal while the Y axis is vertical. (b) Schematic diagram of a part of hysteresis loop illustrating the in-situ magnetising experiment. The length of the edge of the element is  $4\ \mu\text{m}$ .

Fig. 6.20 shows the Foucault images recorded from the SIM4 element. It appears that the element comprises a complex domain structure with irregularly shaped domains and the net magnetisation is not zero. The fact that no stray field is observed in either component suggests that the magnetisation of the domains close to the edges is near parallel to these edges.

#### 6.2.5.2 Ac-demagnetised state

The domain structure of the ac-demagnetised state is also investigated using Foucault imaging and demonstrated in Fig. 6.21. The contrast in the images suggests this is an almost symmetric structure about the long diagonal. It consists of a domain with a near uniform magnetisation in the centre of the element surrounded by four domains. The magnetisation in the central domain is parallel to the long diagonal whereas the magnetisations in the four surrounding domains are parallel to their nearest edges so as to form a solenoidal structure. Some variations in brightness are present running across the domain walls in the X direction mapped image. That indicates these domain walls are of the cross-tie type.

#### 6.2.5.3 Remanent state

This state is produced by applying an 8000 Oe field parallel to the long diagonal and gradually reducing it to zero. The Foucault images recorded after application of the field are shown in Fig. 6.22. Some ripple like contrast is observed in both components, which suggests that the element has been predominantly magnetised along the long diagonal. In a region of  $350 \pm 20$  nm long at the end of the apex, ripple is not apparent. Hence the magnetisation in that region is uniform and the configuration of the stray field around the apex confirms this. The length of this region is the same as that in the SIM3 element. A region with reversed magnetisation is observed in the centre of the element and it is not clear why this is so.

#### 6.2.5.4 In-situ magnetising experiment

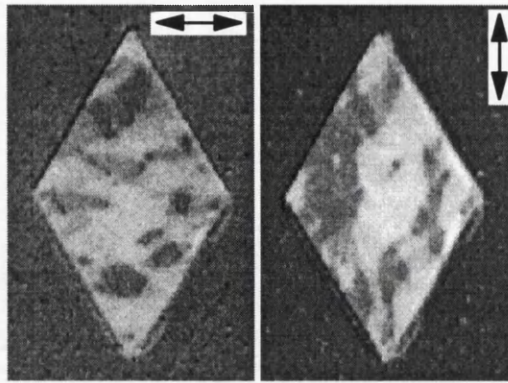


*Fig. 6.20 Foucault images of the cobalt SIM4 element in the as-grown state. The X axis is horizontal while the Y axis is vertical. The length of the edge of the element is 4  $\mu\text{m}$ .*

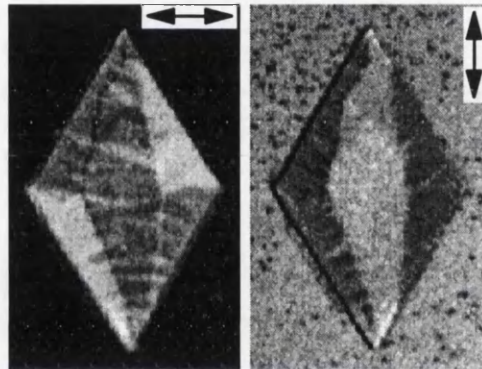


*Fig. 6.21 Foucault images of the cobalt SIM4 element in the ac-demagnetised state. The X axis is horizontal while the Y axis is vertical. The length of the edge of the element is 4  $\mu\text{m}$ .*

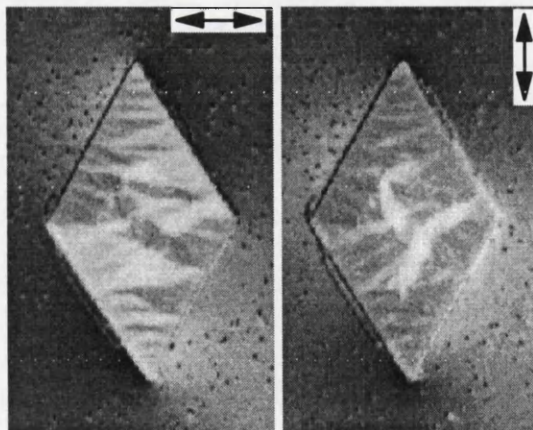


*Fig. 6.22 Foucault images of the cobalt SIM4 element in the remanent state. The X axis is horizontal while the Y axis is vertical. The length of the edge of the element is 4  $\mu\text{m}$ .*

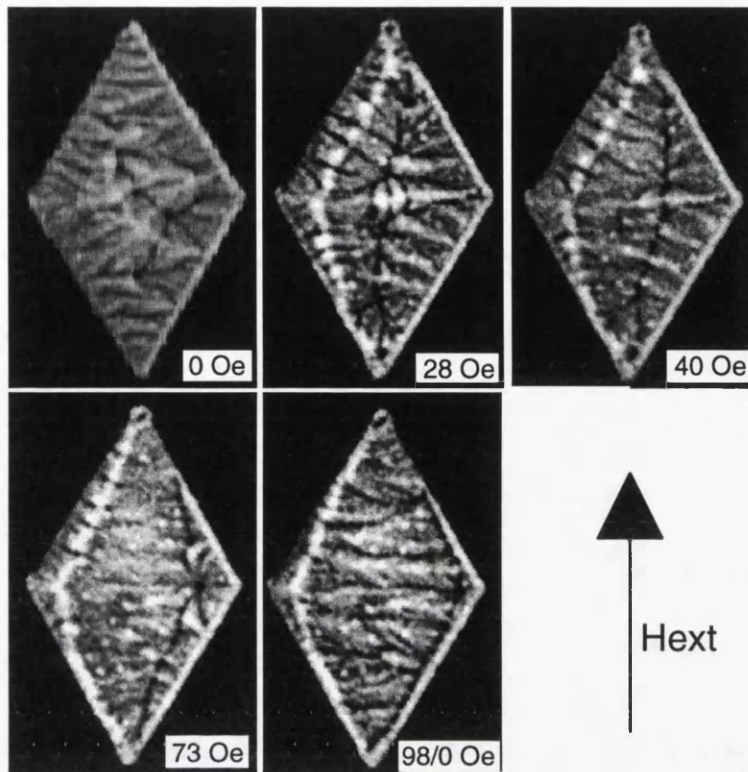


Fig. 6.23 Fresnel images of the cobalt SIM4 element during the in-situ magnetising experiment. The X axis is horizontal while the Y axis is vertical. The length of the edge of the element is 4  $\mu\text{m}$ .

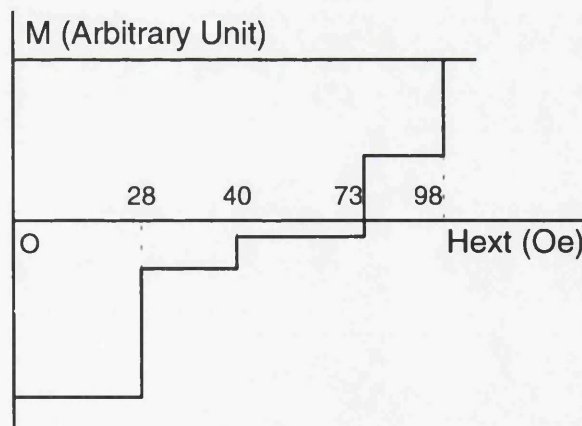


Fig. 6.24 Schematic diagram of a part of hysteresis loop illustrating the in-situ magnetising experiment performed on the cobalt SIM4 element.

A sequence of Fresnel images recorded from the SIM4 element during the in-situ magnetising experiment is shown in Fig. 6.23. This experiment starts from the remanent state and comprises four main irreversible changes in domain structure. A schematic hysteresis loop is also given in Fig. 6.24 to illustrate the process. Initially, the remanent state comprises a near uniform magnetisation antiparallel to the external field. As the external field increases to 28 Oe, a domain is generated in the centre of the element with a magnetisation parallel to  $H_{\text{ext}}$  while the domains at the edges appears to be still antiparallel to the applied field. The walls separating these domains are noted to be of the cross-tie type. Such a domain structure is similar to that in the ac-demagnetised state. This structure is stable until  $H_{\text{ext}}$  reaches 40 Oe, where the cross-tie wall in the centre of the element moves further to the right as this middle domain increases in size. This domain structure does not change until the external field reaches 73 Oe, where the size of the middle domain further increases, driving both of the domain walls closer to the edges of the element. As shown in the schematic hysteresis loop the net magnetisation is now in the direction of the applied field. At  $H_{\text{ext}} = 98$  Oe, the middle domain expands slightly, but the external field is not enough to eliminate the surrounding domains.

## **6.3 Permalloy elements**

### **6.3.1 Physical characteristics of elements**

The electron diffraction pattern and bright field image of these permalloy elements indicate that they also comprise a randomly oriented polycrystalline structure with a grain size of similar dimension to that of the cobalt elements. In addition, the sharpness of the apexes is also identical. Refer to section 6.2.1 for details.

### **6.3.2 Magnetic study of SIM1 element**

#### **6.3.2.1 As-grown state**

The as-grown state of the SIM1 element is shown in Fig. 6.25. It can be observed that the rectangular region of the element comprises a solenoidal domain structure. This is explained due to the dominating influence of the shape effect as the previous study indicated (McVitie 1988) and is consistent with a film in which the grains are fully exchange coupled. Curved domain walls of the cross-tie type are observed in the lower half of the element although the other domain walls are reasonably straight. In the triangular regions the domains are slightly irregular and the walls extend to the apexes. The fact that no stray field is observed suggests the magnetisation is parallel to the edges of the element.

### 6.3.2.2 Ac-demagnetised state

Fig. 6.26 shows a pair of Foucault images recorded in this state. It is obvious that the rectangular region comprises a solenoidal domain structure although the central domain wall parallel to the Y axis is slightly curved. The domain structure of the triangular region on the right hand side is similar to that in the as-grown state while the triangular region on the left hand side contains two equal-sized domains with magnetisation parallel to the edges of this region. Although the overall structure is similar in these two states, the ac-demagnetised state exhibits a more symmetric domain structure than the as-grown state.

### 6.3.2.3 Remanent state

Fig. 6.27 shows a Fresnel image taken from the SIM1 element. In this image, domain walls are represented by bright and dark lines. It is observed that in the rectangular region, the domains form a flux closure structure although they are fairly irregular. In the triangular region on the left hand side of the rectangle, no domain walls are visible suggesting that it is uniformly magnetised. Domain walls are observed in the triangular region on the right hand side, however, most of the volume of the triangular region is still uniformly magnetised.

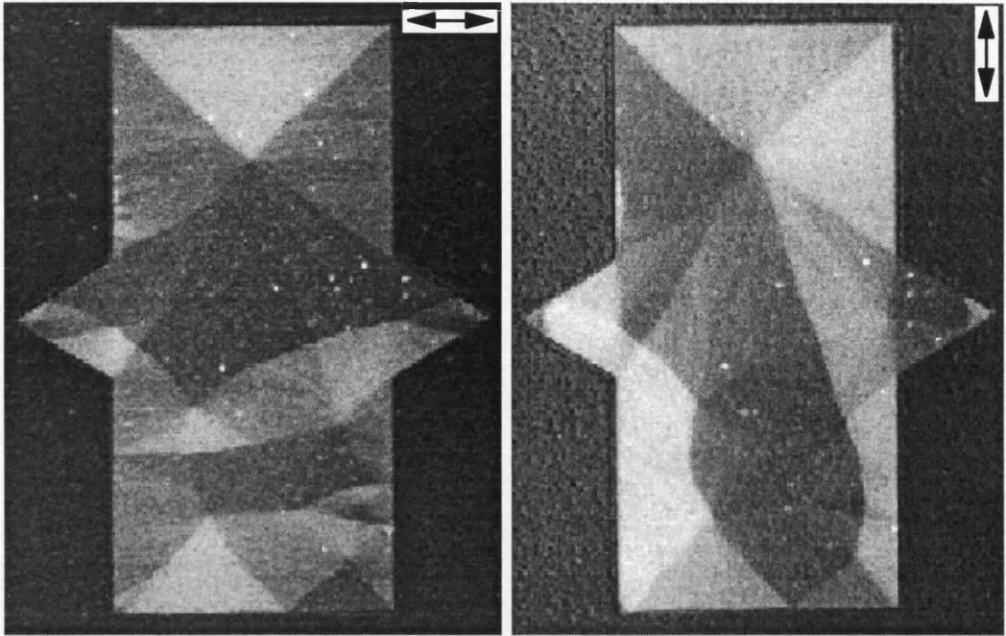


*Fig. 6.25 Foucault images of the permalloy SIM1 element in the as-grown state. The X axis is horizontal while the Y axis is vertical. The length of the edge of the triangular region is 4  $\mu\text{m}$ .*

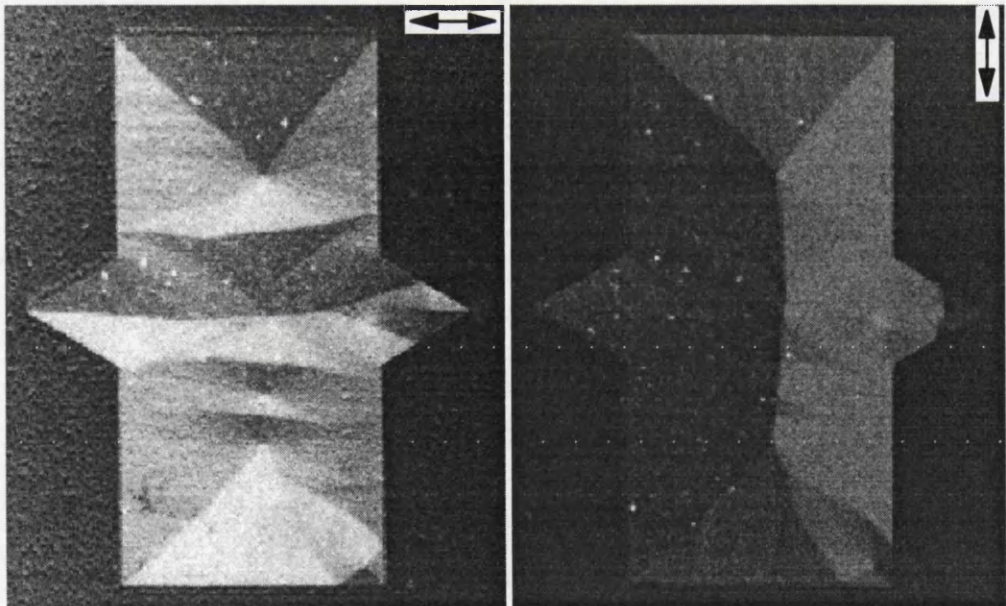


*Fig. 6.26 Foucault images of the permalloy SIM1 element in the ac-demagnetised state. The X axis is horizontal while the Y axis is vertical. The length of the edge of the triangular region is 4  $\mu\text{m}$ .*

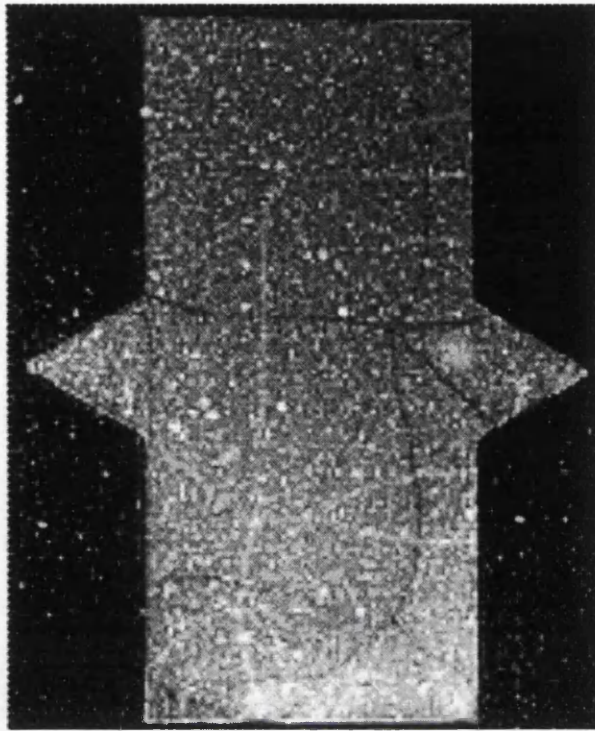


*Fig. 6.27 Fresnel image of the permalloy SIM1 element in the remanent state. The X axis is horizontal while the Y axis is vertical. The length of the edge of the triangular region is 4  $\mu\text{m}$ .*

This structure is significantly different from that of the SIM1 cobalt element in the same state. The reason for this is that the grains in the permalloy element are fully exchange coupled and its domain structure is much more heavily influenced by the shape effect.

#### 6.3.2.4 In-situ magnetising experiment

The in-situ magnetising experiment is performed on the permalloy SIM1 element in the same manner as on the cobalt SIM1 element. The Fresnel images are recorded when irreversible changes in the domain structure occur while  $H_{\text{ext}}$  is varied (Fig. 6.28). Starting from the remanent state which has been imaged in the previous section, many irreversible changes are observed in the field range of 2.5 Oe to 52.5 Oe while the field is increased up to 100 Oe. These changes are represented by domain wall movement and can be observed directly. Changes occur in the rectangular and triangular regions. Whilst the latter is of primary concern, what happens there is affected by the changes occurring in the former region. Therefore, the images demonstrating the changes occurring in the rectangular region are also included. It is found that a single domain is obtained in the triangular region as soon as the field reaches 24 Oe. In such a state, most of the rectangular region has also been magnetised along the field direction although domain walls are observed at the edges perpendicular to the field direction. Increasing the field from this value up to 52.5 Oe does not change the domain configuration although the net magnetisation along the field direction is increased slightly. The edge domain walls are still visible in the rectangular region even at 100 Oe, indicating that the 100 Oe field is not strong enough to generate uniform magnetisation throughout the element.

The domain nucleation process is also studied while the field is decreased from 100 Oe to 0 Oe and 3 major irreversible changes are observed. At 22.5 Oe and 9.5 Oe, the edge domains expand and ripple is observed in the rectangular region. However, the domain structure in the triangular region is unchanged. Domain walls are observed to have nucleated in both apexes simultaneously as soon as the external field reaches 4.5 Oe.

In this magnetising process, it has been observed that even at  $H_{\text{ext}} = 100$  Oe,

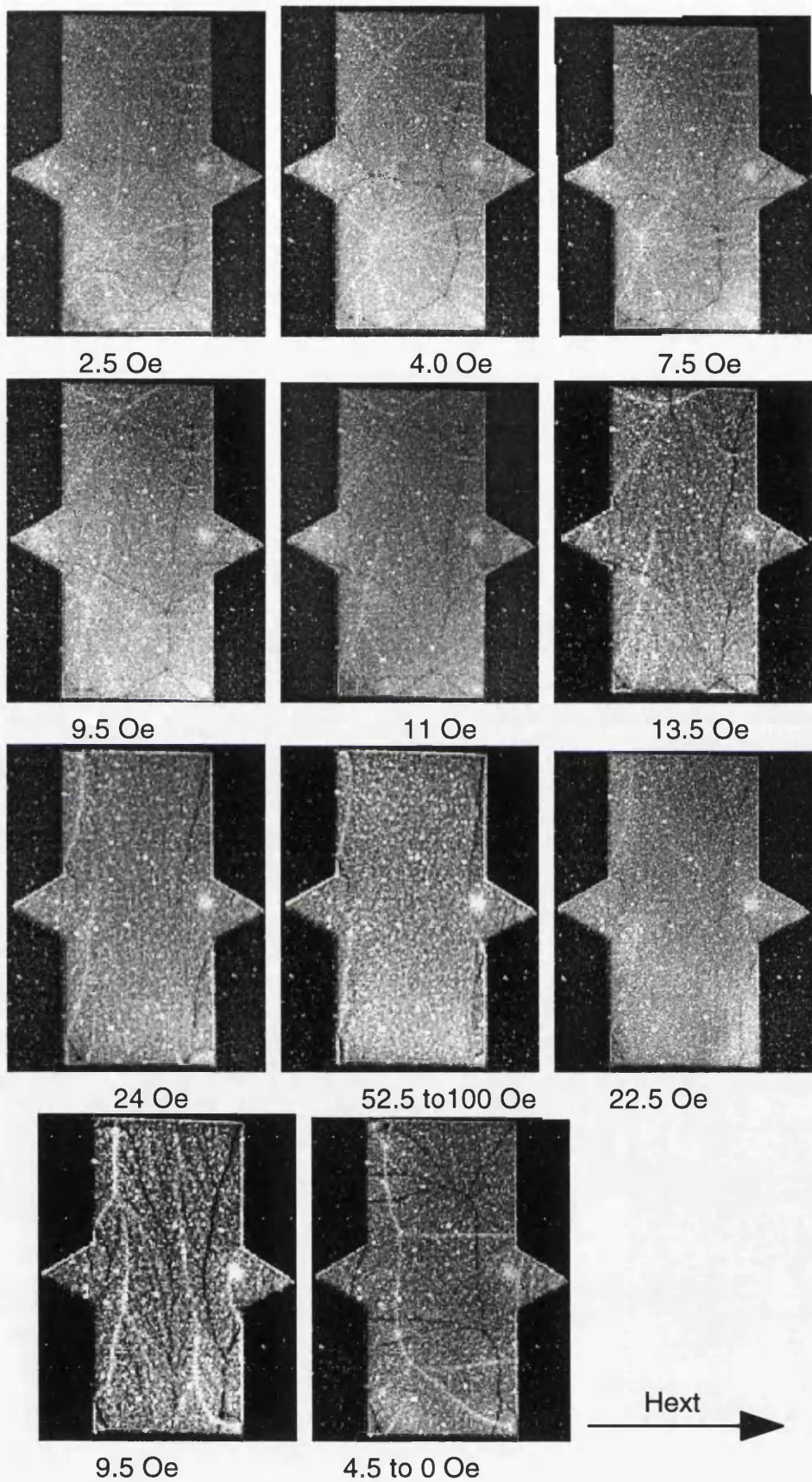


*Fig. 6.28 Fresnel images of the permalloy SIM1 element during the in-situ magnetising experiment.*

the element still possesses some domain walls. The presence of domain walls in the triangular region at zero field and their movements at small fields indicate that in the MFM, such tips may always experience an attractive force. This is in agreement with some experimental studies of permalloy tips (Grütter et al 1991).

### **6.3.3 Magnetic study of SIM2 element**

#### **6.3.3.1 As-grown state**

A pair of Foucault images taken from this element are shown in Fig. 6.29. It can be seen that the central region is predominantly magnetised along the length of the element. At the triangular regions, domain walls are visible running towards the apexes. As no stray field is observed in both components, the magnetisation is found to be parallel to the edges of the element.

#### **6.3.3.2 Ac-demagnetised state**

The Foucault images of the SIM2 element in the ac-demagnetised state are displayed in Fig. 6.30. They suggest that this element supports two equal-sized domains separated by an irregular cross-tie wall. The comparison between this structure with that of the physically identical cobalt SIM2 element in the same state which comprises a nearly uniform magnetisation demonstrates the effect of the full exchange coupling between the grains.

#### **6.3.3.3 Remanent state**

The domain structure of the remanent state is demonstrated by the Foucault images in Fig. 6.31. In the image mapped along the length of the element, almost no brightness variation is observed within the element while considerable contrast due to ripple is present in the Y direction mapped image. This suggests that the element supports a nearly uniform magnetisation parallel to the length. This domain structure is quite similar to

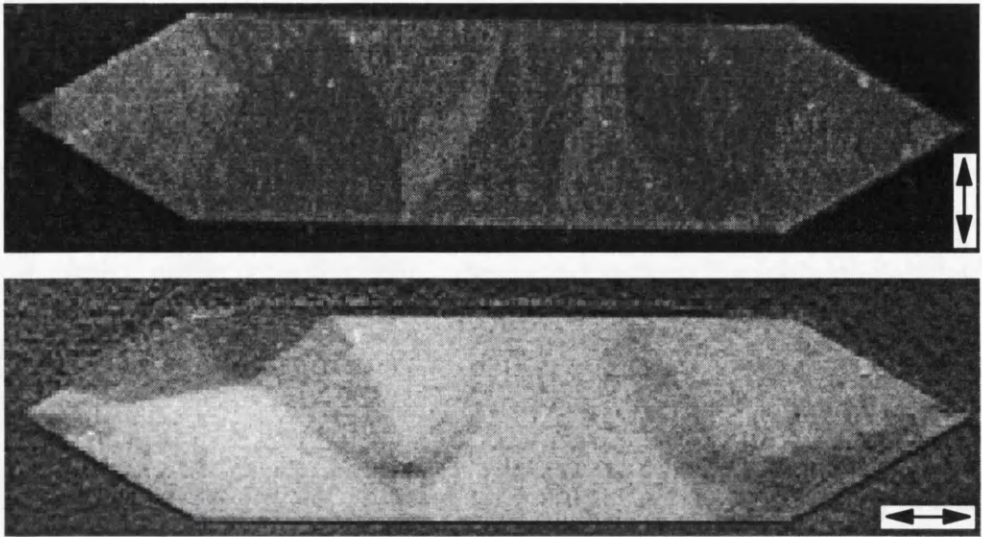


*Fig. 6.29 Foucault images of the permalloy SIM2 element in the as-grown state. The X axis is horizontal while the Y axis is vertical. The length of the edge of the triangular region is 4  $\mu\text{m}$ .*

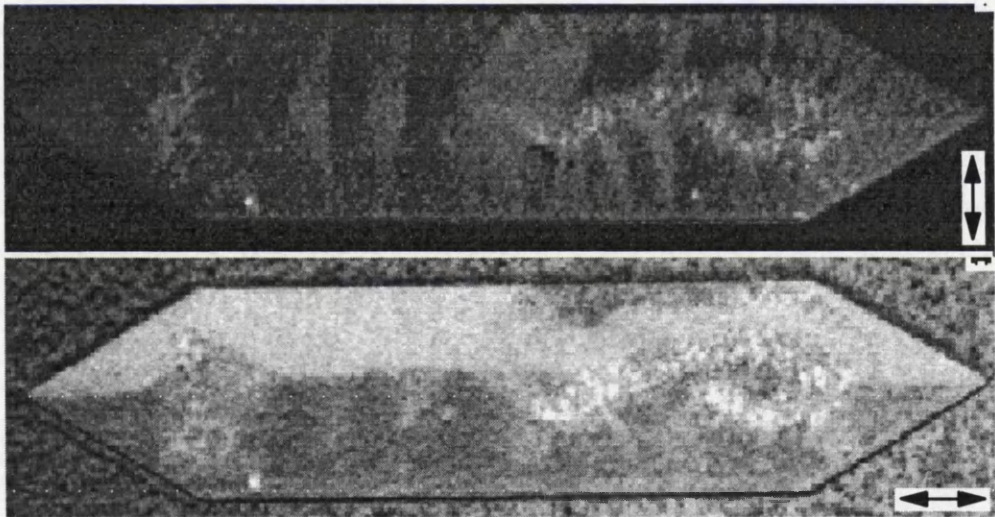


*Fig. 6.30 Foucault images of the permalloy SIM2 element in the ac-demagnetised state. The X axis is horizontal while the Y axis is vertical. The length of the edge of the triangular region is 4  $\mu\text{m}$ .*

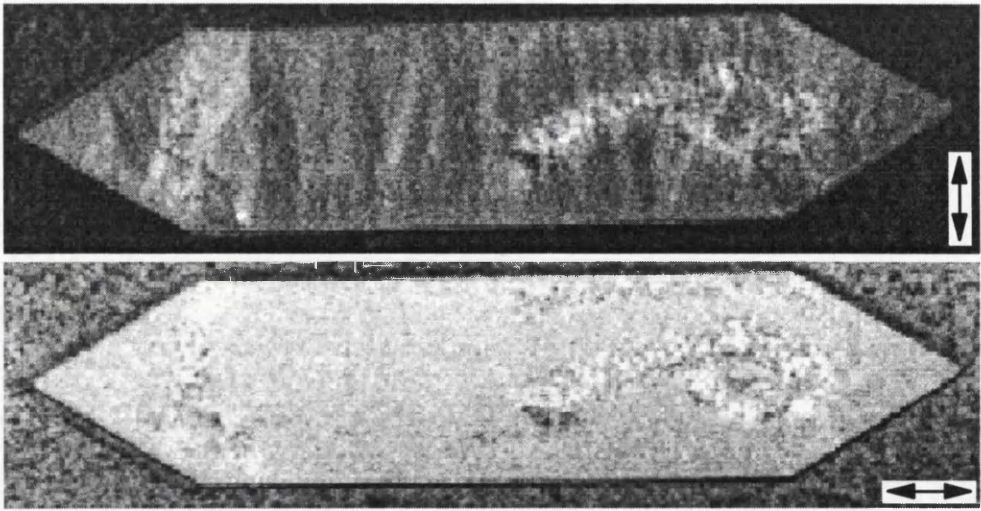


Fig. 6.31 Foucault images of the permalloy SIM2 element in the remanent state. The X axis is horizontal while the Y axis is vertical. The length of the edge of the triangular region is  $4\ \mu\text{m}$ .

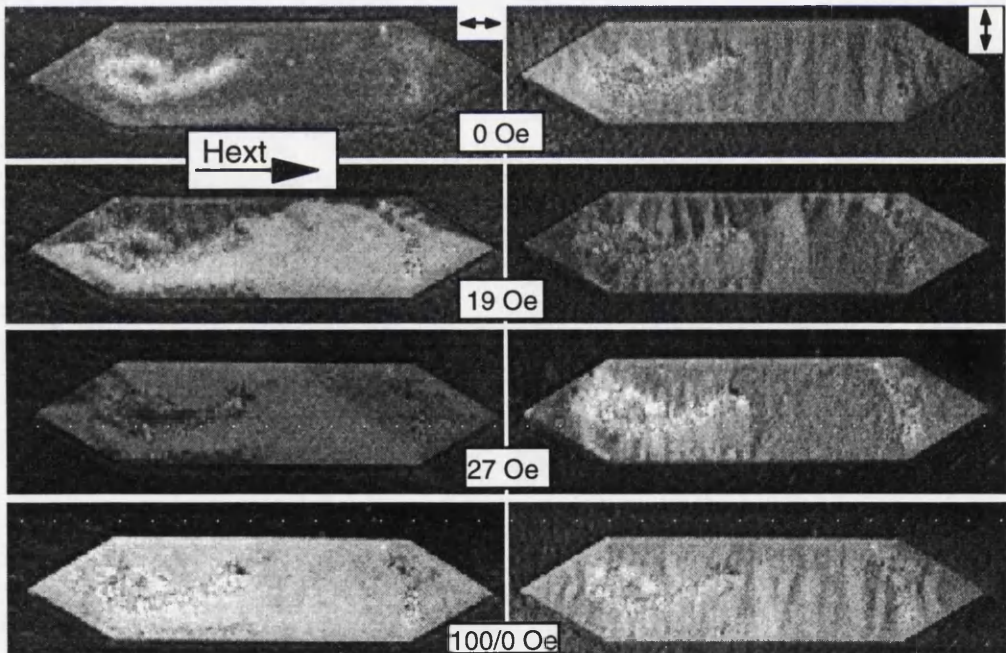


Fig. 6.32 Foucault images of the permalloy SIM2 element during the in-situ magnetising experiment. The X axis is horizontal while the Y axis is vertical. The length of the edge of the triangular region is  $4\ \mu\text{m}$ .

that of the cobalt SIM2 element in the same state.

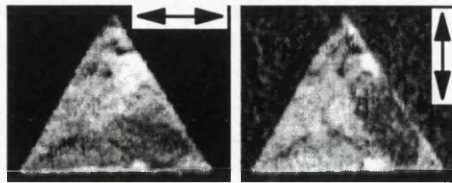
#### 6.3.3.4 In-situ magnetising experiment

Fig. 6.32 displays a sequential Foucault images while the external field is increased from 0 to 100 Oe against the initial magnetisation of the element. Since all the main irreversible changes in domain structure occur at low fields, they are investigated utilising Foucault imaging. It has been described in the previous section that the remanent state of this element contains a near uniform magnetisation. When the field is increased to 19 Oe, a large scale domain is generated along the element which occupies a volume more than half of the element and the apexes no longer support uniform magnetisation. On increasing the field to 27 Oe, the antiparallel domain is further reduced by the nucleation of domains along the top edge of the element. Here the right hand apex appears uniformly magnetised. The antiparallel domain is completely removed at 100 Oe so that the element supports a ripple structure with the average direction of magnetisation parallel to the field. Reduction of the field from  $H_{\text{ext}} = 100$  Oe down to 0 does not change the domain structure.

#### 6.3.4 Magnetic study of SIM3 element

The Foucault images of the SIM3 element in the as-grown, ac-demagnetised and remanent states are displayed in Fig. 6.33, Fig. 6.34 and Fig. 6.35 respectively. Basically, the as-grown and remanent states support complex domain structures with irregularly shaped domains. However, the ac-demagnetised state supports a "Y" type solenoidal domain structure. The fact that no stray field is observed in any state suggests that each comprises flux closures. In the ac-demagnetised state the ripple present in the cobalt SIM3 element is not seen in the permalloy SIM3 element, which demonstrates the full exchange coupling between the permalloy grains.

In-situ magnetising experiments were carried out at the end of the project. After completing the in-situ magnetising experiments on the SIM1 and SIM2 elements, the specimen was damaged. Thus in-situ magnetising



*Fig. 6.33 Foucault images of the permalloy SIM3 element in the as-grown state. The X axis is horizontal while the Y axis is vertical. The length of the edge of the element is 4  $\mu\text{m}$ .*

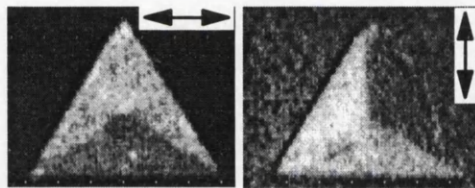


*Fig. 6.34 Foucault images of the permalloy SIM3 element in the ac-demagnetised state. The X axis is horizontal while the Y axis is vertical. The length of the edge of the element is 4  $\mu\text{m}$ .*

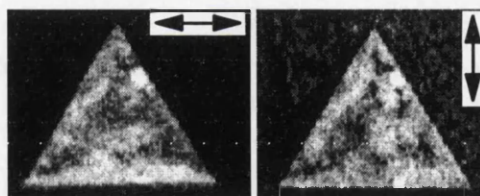


*Fig. 6.35 Foucault images of the permalloy SIM3 element in the remanent state. The X axis is horizontal while the Y axis is vertical. The length of the edge of the element is 4  $\mu\text{m}$ .*

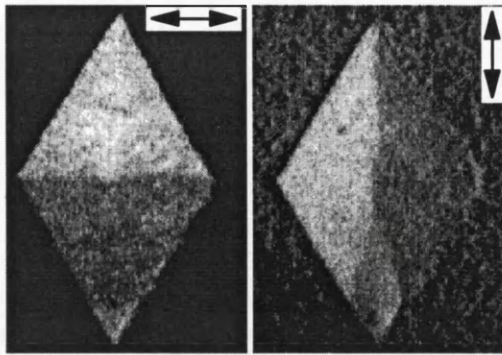


*Fig. 6.36 Foucault images of the permalloy SIM4 element in the as-grown state. The X axis is horizontal while the Y axis is vertical. The length of the edge of the element is 4  $\mu\text{m}$ .*

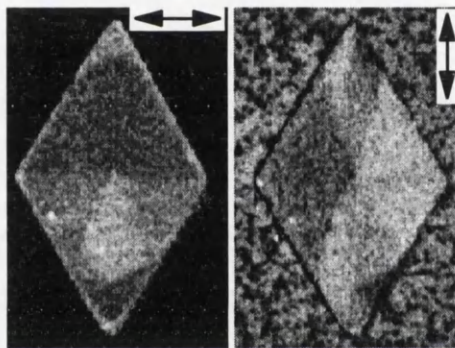


*Fig. 6.37 Foucault images of the permalloy SIM4 element in the ac-demagnetised state. The X axis is horizontal while the Y axis is vertical. The length of the edge of the element is 4  $\mu\text{m}$ .*

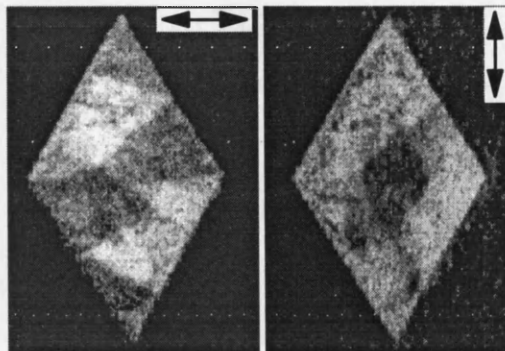


*Fig. 6.38 Foucault images of the permalloy SIM4 permalloy element in the remanent state. The X axis is horizontal while the Y axis is vertical. The length of the edge of the element is 4  $\mu\text{m}$ .*

experiments are not performed on either the SIM3 or SIM4 element.

### **6.3.5 Magnetic study of SIM4 element**

The Foucault images of the SIM4 element in the as-grown, ac-demagnetised and remanent states are displayed in Fig. 6.36, Fig. 6.37 and Fig. 6.38 respectively. It is noted that the as-grown and ac-demagnetised states support domain structures with a degree of regularity. Although some large scale domains with magnetisation parallel to the edges are present, the domain structure in the apexes are rather irregular. The remanent state of the element comprises a complex magnetic configuration with irregular domains. The magnetisation in the remanent state seems to have a considerable component parallel to the Y axis. This is similar to the domain structure of the cobalt SIM4 element in the same state although the domains in this case are somewhat larger.

## **6.4 Conclusion and discussion**

The investigations of the cobalt thin film elements in the as-grown and ac-demagnetised states suggest that the triangular regions of these elements do not support a single domain structure. However, by applying an 8000 Oe external field to the specimen then decreasing it to zero, a uniform magnetisation can be obtained in a small region at the end of the apexes. Comparing the length of these regions in different elements with the length of the uniformly magnetised region in the one-face coated cobalt tip, it is found that the SIM1 and SIM2 elements are the best representations of the film on the tip. As the domain structure in this remanent state is well defined and relatively simple, it is suitable for use in MFM imaging so that the acquired MFM images may be interpreted quantitatively. This information has been applied to the MFM imaging and our colleagues in Manchester Metropolitan University use the remanent state of the one-face coated cobalt MFM tip to image samples. The high quality MFM image shown in Fig. 6.1 is a good example of such a set up. The drawback of this uniformly magnetised region is that it results in relatively strong stray field and this may influence the domain structure of samples during MFM imaging.

The behaviour of the cobalt elements in external fields is investigated by performing in-situ magnetising experiments. It indicates that the magnetisation at the end of the apex region is no longer uniform when the external field exceeds certain critical values. For the SIM1 and SIM2 elements, the critical value is in the range of 60 ~ 80 Oe. Such results give us an insight into the stability of the domain structure in the one-face coated cobalt MFM tip in the stray field of specimens.

The observations of the domain structure of the permalloy elements suggest that the apex regions of the elements usually support multidomain structures. Thus the tip-specimen interaction is more complex, which makes the quantitative interpretation of an MFM image acquired by a one-face coated permalloy tip more difficult. Nevertheless, as it does not comprise a uniformly magnetised region, its stray field will be weaker than that of the cobalt tip. Thus, it is especially useful in the MFM imaging of soft magnetic specimens.

The in-situ magnetising experiments performed on the permalloy elements indicate that their domain structures can be changed easily with a weak field. Thus, while a one-face coated permalloy tip is scanning over a specimen, the domain structure in the tip may be frequently switched to align with the stray field of the specimen. This results in that the tip always experiencing an attractive force and it may also be useful in MFM imaging.

It is observed that the domain structure of the cobalt elements is different from that of the equivalent permalloy elements. This may be due to two facts. Firstly, cobalt supports a strong uniaxial anisotropy with  $K_{u1} = 4.1 \times 10^5 \text{ J/m}^3$  (Jiles 1991) whereas permalloy has negligible anisotropy. The anisotropy helps the cobalt element to be magnetised when a field is applied parallel to the easy axis. However, since not all the easy axes are aligned perfectly along one direction, the distribution of the easy axes in the cobalt grains gives rise to significant ripple. Secondly, the permalloy elements are fabricated with an evaporated rate of 0.1 nm/s and the previous studies indicate that an element evaporated at such a rate possesses fully exchange coupled grains. By using a slow evaporation rate, 0.04 nm/s, while fabricating cobalt elements, the exchange coupling between the cobalt grains is reduced (Wong et. al. 1992). As a result of that, the magnetisation of each

cobalt grain is more independent of that of the neighbouring grains and this makes the shape effect less important than in the permalloy elements.

The separation of the effects of these two factors on domain structure requires comparison with other cobalt elements fabricated at the same evaporation rate as that used to fabricate the permalloy elements. By comparing the domain structures of these cobalt elements with that of the cobalt elements studied in this chapter, the effect of the reduced exchange coupling can be deduced. Hefferman (1991) had fabricated some 17 nm and 60 nm rectangular cobalt elements using an evaporation rate 0.1 nm/s. He observed that the remanent states of these elements were solenoidal domain structures with ripple present. This contrasts with the near uniform domain structures observed from the cobalt elements in this chapter, so it is apparent that the reduced exchange coupling is the dominant parameter in the determination of the near uniform magnetisation distribution.

## Chapter 7

### Characterisation of other types of MFM tip

#### 7.1 Introduction

Magnetic Force Microscope (MFM) is established as a member of the family of scanning probe microscopy techniques and it is destined to play an important role in the imaging of the surface stray field distribution of thin film and bulk magnetic materials on nanometre scale. The basic principle and instrumentation of an MFM have been given in chapter 2. The evolution of the MFM tip from bulk tip (Martin and Wickramasinghe 1987), thin film tip (Grütter et. al. 1991) to the state of the art needle tip (Fischer et. al. 1993) is also discussed there. Some work in this area has indicated that the radius of the apex, the magnetic properties and the volume of the magnetic material on a tip are the most direct factors determining the performance of the MFM and they are summarised by Grütter et al (1992). In this chapter, initial characterisations of Nanoprobe™ and needle tips are presented in section 7.2 and 7.3 respectively.

The instruments used in this work are Philips SEM515, JEOL 2000FX and VG HB5 (Chapter 2). The physical properties of the tips are studied using the bright field and secondary electron imaging techniques. The magnetic characterisations are performed using the Foucault and MDPC modes of Lorentz microscopy whereby the distribution of stray field is investigated.

#### 7.2 Investigation of Nanoprobe™ thin film tip

##### 7.2.1 Tip fabrication

The Nanoprobe™ tip is etched in n-type doped single crystal silicon (Grütter et. al. 1990, Wolter et. al. 1991). Nanoprobe™ thin film tips are fabricated by sputtering a 50 nm thick CoCr film on the whole surface of the non-magnetic Nanoprobe™ tip without an applied magnetic field. The tip investigated in this section is supplied by Dr. Ken Babcock of Digital Instruments Inc. at

Santa Barbara. More details of the process can be found in Babcock's work (1994).

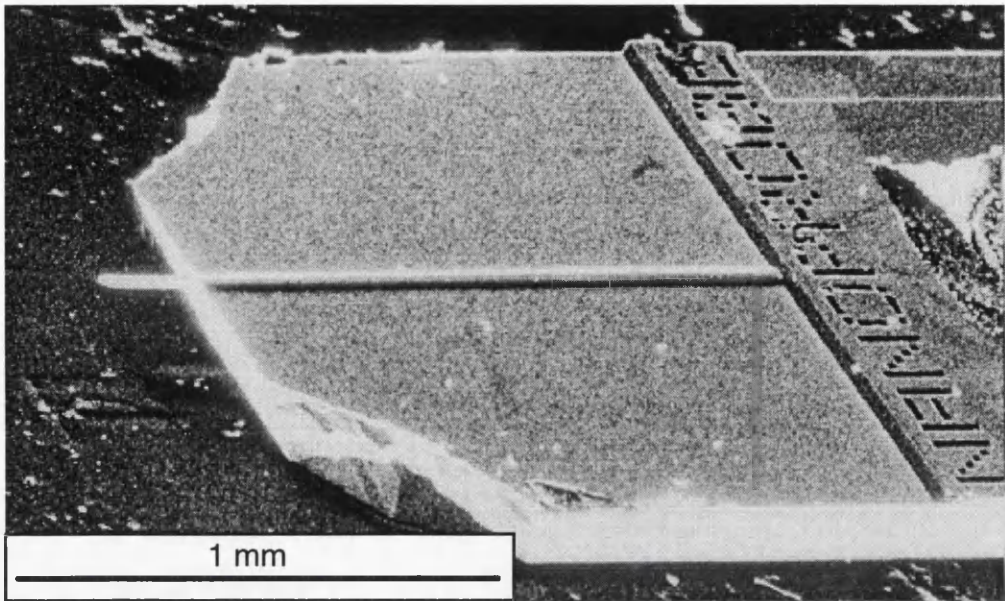
## 7.2.2 Physical characteristics

Fig. 7.1 is an SEM image of the Nanoprobe™ tip, illustrating the cantilever and the substrate. As the tip is very small compared to the silicon substrate and the image is recorded to illustrate the overview of the whole of the piece, the tip is not visible in this image. The length of the cantilever is measured to be about 220  $\mu\text{m}$ . The topography of the tip is displayed in Fig. 7.2, indicating that the tip is particularly sharpened at the end. The interior angle of the apex is about  $60^\circ$  and the height of the Nanoprobe™ tip is about 15  $\mu\text{m}$ . A schematic diagram is given in Fig. 7.3 to demonstrate the overview and size of the Nanoprobe™ tip. Although most of the tip is opaque to 200 kV electrons in the TEM, the apex is thin enough to be imaged and a bright field image is recorded (Fig. 7.4). In this image, the radius of the tip is measured to be about 20 nm. Another SEM image of the Nanoprobe™ tip recorded at a lower magnification is displayed in Fig. 7.5. It suggests that the cantilever is just slightly deformed after sputtering. Subsequent MFM imaging suggests that it is suitable for use in our MFM which comprises an interferometric detecting system (Valera et al 1995a and 1995b).

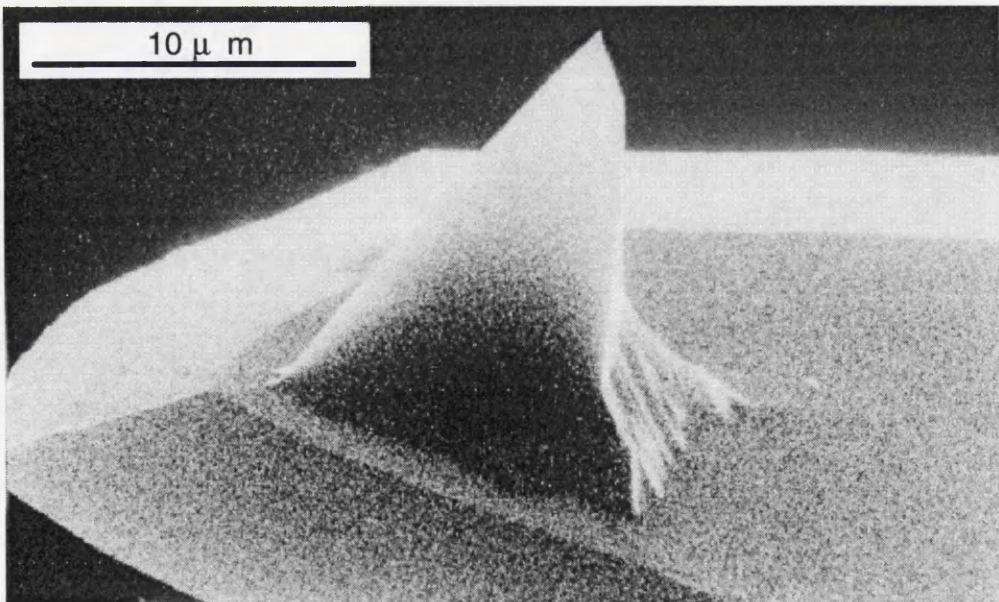
## 7.2.3 Magnetic study of as-grown state

Fig. 7.6 shows Foucault images of the tip in the as-grown state, where the stray field is mapped along two orthogonal directions as the arrows indicated. Considerable abrupt contrast variation is observed in both components in places at the end of the tip as well as along the edges. Therefore the configuration of the stray field is not well defined, which indicates that the magnetisation in the tip is not uniform. A consequence of that is the interaction between the tip and samples becomes complicated and an MFM image acquired by a Nanoprobe™ tip in such a state virtually can not be interpreted quantitatively.

## 7.2.4 Magnetic study of remanent state



*Fig. 7.1 SEM image of a Nanoprobe™.*



*Fig. 7.2 SEM image of a Nanoprobe™ MFM tip, highlighting the tip region.*

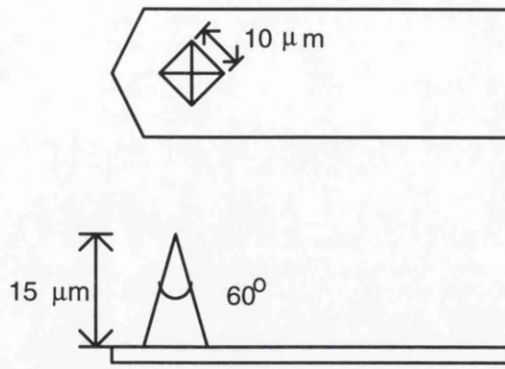


Fig. 7.3 Schematic diagram of the Nanoprobe™ MFM tip.

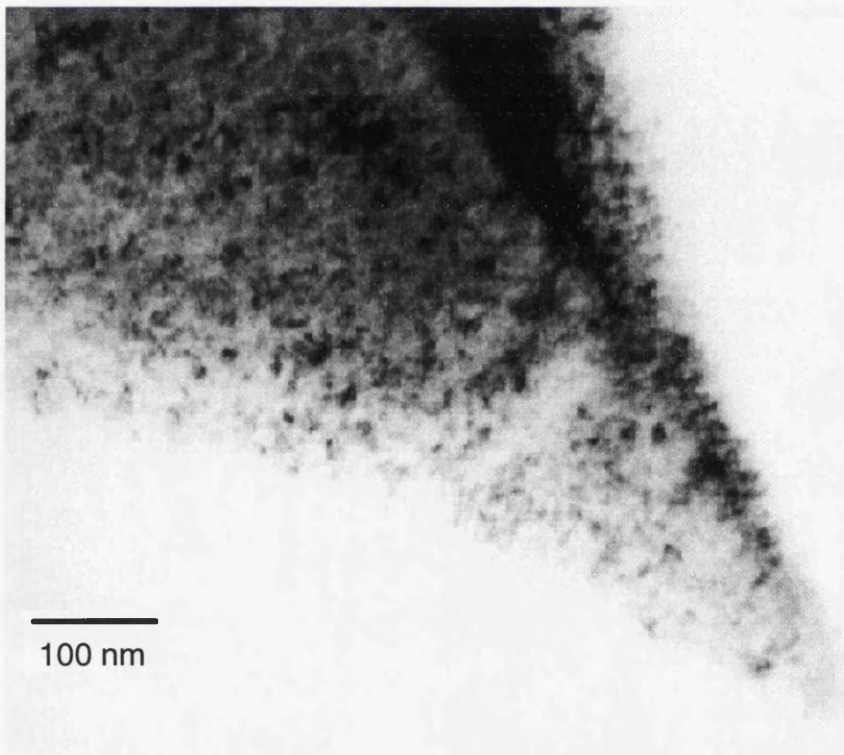


Fig. 7.4 High magnification TEM image showing crystalline structure of the Nanoprobe™ MFM tip at the apex.

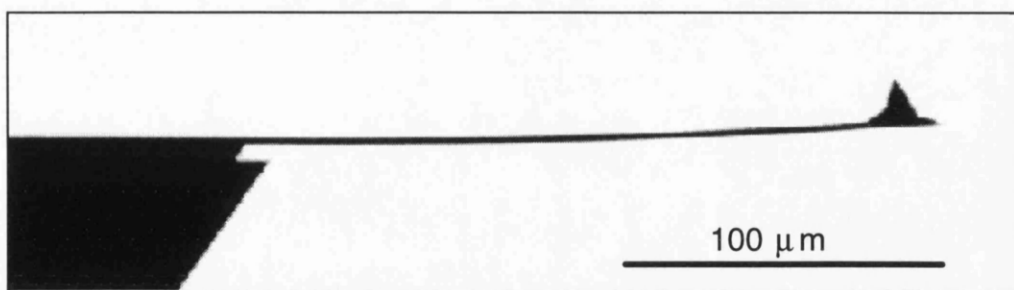


Fig. 7.5 TEM image of a Nanoprobe™ MFM tip and cantilever.

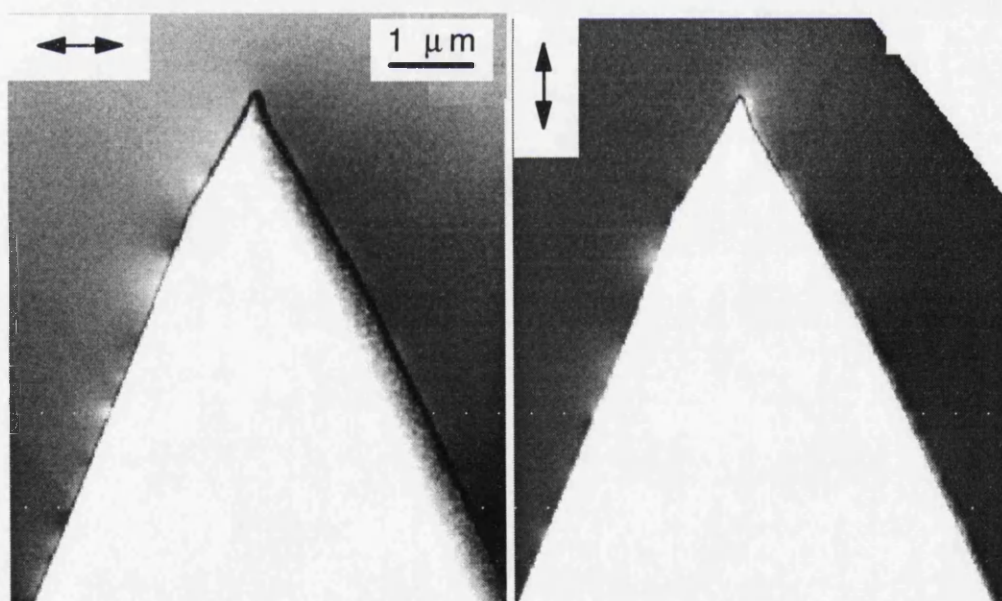
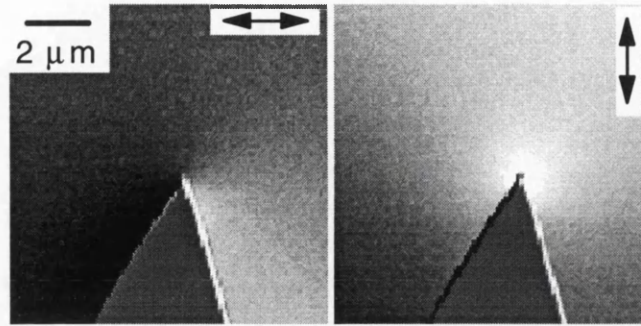


Fig. 7.6 Foucault images of a Nanoprobe™ MFM tip in as-grown state.



*Fig. 7.7 DPC images of the Nanoprobe™ MFM tip in remanent state.*

The remanent state of the tip is produced by applying an 8000 Oe field directed towards the apex. The MDPC mode of Lorentz microscopy is used to investigate the stray field distribution around the tip and it is demonstrated in Fig. 7.7. As the tip is opaque to 100 keV electrons, it has zero contribution to the final MDPC images so that the tip region is grey (Chapter 3). It is apparent that the brightness in this pair of images is symmetric about the central line of the tip and strong Lorentz deflection occurs at the end of the tip, which is to be expected from a uniformly magnetised tip. Therefore, it appears that the remanent state of the Nanoprobe™ tip supports uniform magnetisation near the apex.

## 7.3 Investigation of the needle tips

### 7.3.1 Tip fabrication

Electron beam induced deposition (EBID) of carbonous or metallic materials out of a vapour of organic or metal-organic components in SEMs is well known in microelectronics (Koops et al 1988). In our work, an ISI M7 SEM is used in spot mode to grow carbon "contamination" needles on the apex of the Park Scientific Microlever™. The tip is prepared by Dr M Rührig at Twente University in Enschede. An acceleration voltage of 15 kV and a magnification of 40K are used during the growth process, resulting in a growth rate of about 20 nm/min. The needle MFM tip is obtained by coating a 20 nm thick  $\text{Co}_{80}\text{Ni}_{20}$  film on one side of the needle utilising thermal evaporation without applied magnetic field. Fig. 7.8 illustrates the set up of the evaporation. As the needle has a high aspect ratio, the CoNi film on it favours a single domain structure with the magnetisation pointing to the apex of the needle due to shape effect. More details of the fabrication can be found elsewhere (Rührig et al 1994).

### 7.3.2 Characterisation of the needle tip

The physical characteristics of the needle tips are investigated using the bright field mode of TEM imaging (Fig. 7.9). It can be observed that the needle is grown on the top of the apex and it is very small compared to the

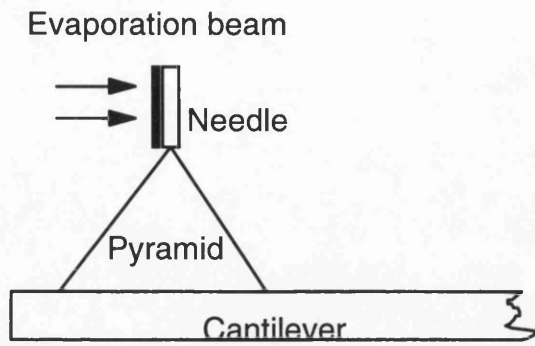


*Fig. 7.8 Schematic diagram showing the set up for the evaporation of needle MFM tips.*

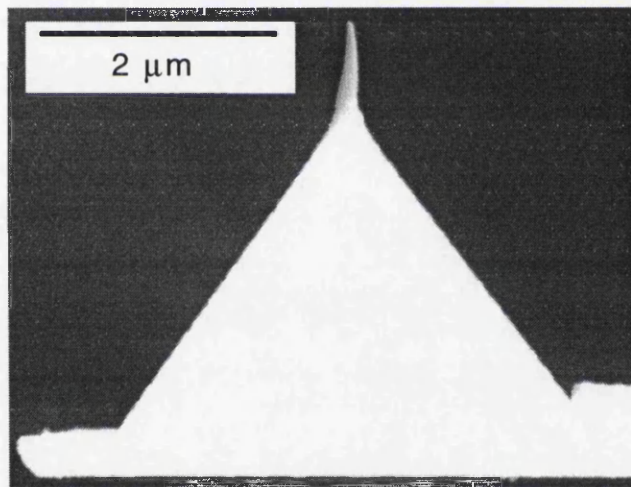


*Fig. 7.9 TEM image of the needle MFM tip.*

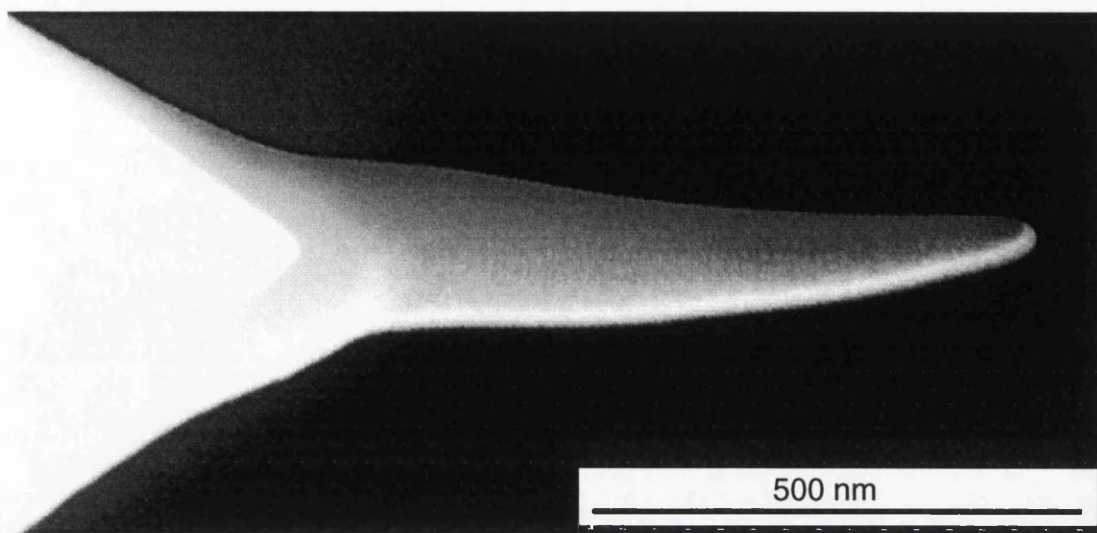


*Fig. 7.10 High magnification TEM image of the needle MFM tip.*

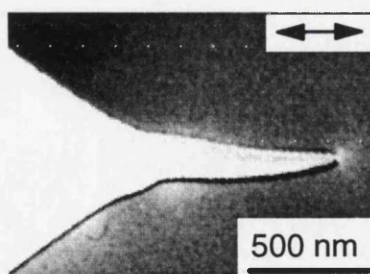


*Fig. 7.11 Foucault image of the needle MFM tip. The arrow indicates the mapping direction.*

size of the pyramid. In another bright field image recorded at a higher magnification (Fig. 7.10), the needle is found not to be completely uniform in shape and orientation. The length of the needle is about 750 nm and the radius of the needle apex is about 10 nm.

The as-grown state of the needle tip is also characterised. The Foucault image displayed in Fig. 7.11 is mapped along the long axis of the needle and demonstrates that the stray field is restricted in a region at the end of the tip. Brightness variations are also observed at the junction between the needle and the pyramid, indicating a multidomain configuration. However, that region is about 750 nm away from the needle apex so that it would have a negligible effect on MFM imaging. Since no significant contrast variation is observed along the edges of the needle, the needle may support a uniform magnetisation which is what we expected due to the shape effect.

## 7.4 Conclusion

The characterisations of the MFM tips presented in this chapter are preliminary as the work was carried out at the end of the project. However, some of the main physical features and magnetic properties of the tips are characterised, which provide very useful information on the application of the tips to MFM imaging.

The Nanoprobe<sup>TM</sup> tip is based on silicon cantilevers. The magnetic thin film is coated on the whole surface of the tip and the whole of the cantilever using sputtering technique. It is found that the cantilever is stiff enough to maintain its straightness after sputtering. This enables MFM images to be acquired using whole-surface coated tip in our MFM. Hence, a relatively strong tip-sample interaction can be achieved due to its large magnetic volume (comparing to one face coated tips). Nevertheless, the whole-surface coated tip also has a strong stray field, which might change the magnetisation of imaged samples. Therefore, the Nanoprobe<sup>TM</sup> is useful for the MFM imaging of hard magnetic samples with weak stray field. The bright field image of the tip also indicates that the radius of the tip is about 20nm. Thus, it may be applied for MFM imaging with a resolution on a similar scale. The magnetic investigation of the tip suggests that a well defined domain structure may be

obtained in the remanent state. Therefore, it is a good candidate for quantitative MFM imaging.

The needle tip has a high aspect ratio so that the shape effect is very strong and it tends to align the magnetisation in the direction pointing to the apex of the needle. As a result of that, the as-grown state may support uniform magnetisation. This helps the subsequent magnetising process, which is usually performed before MFM imaging to achieve a well defined domain structure in the tip. Another benefit provided by this shape effect is that it may result in a high coercivity (Chapter 4) to help the tip maintain the uniform magnetisation during MFM imaging so that consistent image acquisition conditions may be established and maintained. Thus it may be used in the imaging of samples with strong stray field. The needle tip is the sharpest one among the Microlever<sup>TM</sup>, Nanoprobe<sup>TM</sup> and needle MFM tips so that it is the best candidate for high resolution MFM imaging.

## Chapter 8

### Conclusion and Future Work

#### 8.1 Conclusion

The work described in this thesis focuses on characterisations of thin film MFM tips and related structures. The MFM tip studied in Chapter 5 has been used to reveal 30 nm magnetic domain details in Co/Pt multilayer (Valera et al 1995). The major conclusions of the work presented in Chapter 4 to Chapter 7 are outlined below.

The shape effect and anisotropy induced by oblique incidence evaporation in permalloy thin film elements (25 nm thick) are investigated in Chapter 4. The ratio  $R$  of in-plane dimensions of those elements varies from 3.7 to 8.1. For the elements evaporated at the normal incidence, the trade off between exchange energy and magnetostatic energy is an important factor in the determination of domain structures. This is usually called shape effect. The study indicates that elements with  $R$  greater than 4 support the type 2 nonsolenoidal domain structure as the reproducible magnetic state. Nevertheless the elements with  $R = 3.7$  support both the type 3a solenoidal and type 2 nonsolenoidal domain structures. Major changes in domain structures in in-situ magnetising experiments with the external field applied parallel to the long in-plane axis of the elements are identified using the Foucault mode of Lorentz Microscopy. It is found that the changes can be described by a type A hysteresis loop although complete saturation of the magnetisation was not achieved due to the fact that a limited field (up to 100 Oe) can be applied using the in-situ magnetising stage. A comparison of coercivities suggests that the elements with higher  $R$  are magnetically harder than the elements with lower  $R$ . Table 4.3 summarises the major parameters of the hysteresis loops.

At the  $30^\circ$  incidence, the induced easy axis in permalloy films is normal to the evaporation beam. This easy axis gives rise to an extra energy term - anisotropy energy and significantly affects the domain structure of the elements. For the elements with the induced easy axis parallel to the long in-

plane axis, the magnetisation parallel to this axis is favoured so as to reduce the anisotropy energy. The type 1 non-solenoidal domain structure is found to be the reproducible magnetic configuration, which is different from our observations of the elements evaporated at normal incidence. However, the in-situ magnetising experiments suggest that the major irreversible changes in domain structure can also be described using the type A hysteresis loop. The coercivity (Table 4.6) has been increased by the induced anisotropy so that the element is harder than the equivalent element evaporated at the normal incidence. The anisotropy also results in higher remanent magnetisation and a more square hysteresis loop. These results reflect a cooperation between the shape effect and the induced anisotropy.

In the case of elements with the induced easy axis parallel to the short in-plane axis, magnetisation parallel to the short in-plane axis is favoured by the induced anisotropy. The type 5 and type 6 solenoidal domain structures are observed, which comprise significant components of magnetisation parallel to the short in-plane axis. Moreover, the major irreversible changes in domain structures are described using the type D hysteresis loop in contrast to the type A loop. This reflects the competition between the shape effect and the induced anisotropy.

In Chapter 5, the cobalt thin film MFM tip made from Park Scientific Microlever™ is characterised by performing electron microscopy and computer simulation. For the whole-surface coated tip made by evaporating cobalt film at normal incidence, the bright field imaging shows that the film has good contact with the pyramid and the radius at the apex region is 25 nm. However, such a tip is not suitable for our MFM, which comprises an interferometric detection system, due to the fact that the cantilever has been deformed. This problem is overcome by evaporating the cobalt film at 55° incidence, i.e. one face of the pyramid is normal to the evaporation beam. SEM imaging indicates that the cantilever is straight and the film is coated predominantly on this face as well as the whole of the cantilever. Since the one-face coated tip comprises less magnetic volume than the whole-surface coated tip, it is expected to be more useful for high resolution MFM imaging.

The MDPC mode of Lorentz microscopy performed on the one face coated tip demonstrates a fairly symmetric distribution of the stray field around the apex of the tip and some abrupt brightness variations along the edges of the

tip. Line-tracing analysis suggests that the component of the stray field perpendicular to the cantilever surface can be described using a logarithm function with a shift in the origin of the coordinate system. The comparison between the experimental and simulated MDPC images of the one-face coated tip suggests that only the apex region of the tip is uniformly magnetised although in general the experimental images appear to be slightly different from the simulated ones of a uniformly magnetised tip. This may be due to the fact that the magnetisation in other regions is not uniform. The computer modelling of the whole-surface coated tip is also performed so that they can be compared with experimental work in future.

When a magnetic thin film is evaporated on the tip, the cantilever is also coated. The magnetic structure of the film on the cantilever may give rise to stray field. At the end of the tip, which is typically more than 3  $\mu\text{m}$  distance from the cantilever, the stray field may still be dominated by the magnetic film on the tip since magnetic field decays with distance. In regions close to the cantilever, the DPC contrast is the sum of stray field from both the tip and cantilever. Further investigations are necessary to separate these two effects.

Cobalt and permalloy thin film elements have been fabricated on the  $\text{Si}_3\text{N}_4$  membrane substrates to simulate the magnetic film on the one-face coated MFM tip (Chapter 6). Each of the patterns used in this study (SIM1 to SIM4) comprises two triangular regions in the extremities whose geometry is identical to one face of the pyramid on the Microlever<sup>TM</sup>. The cobalt elements are evaporated at the same evaporation rate as the MFM tips studied in Chapter 5. The permalloy elements are evaporated at a more rapid rate (0.1 nm/s). Previous work (Wong 1992) suggests that the crystalline grains in the permalloy elements are fully exchange coupled and exchange coupling between the cobalt grains is reduced. The characterisations indicate that the cobalt elements support domain structures with more uniformity in magnetisation than the permalloy elements in the remanent state. The work carried out by Hefferman (1991) suggested that cobalt elements with fully exchange coupled grains supported a similar domain structure to the permalloy elements studied in this work. Therefore, the reduced exchange coupling is responsible for the differences. The remanent state of the cobalt elements supports a uniformly magnetised region at the end of the triangular

apex, which is in excellent agreement with the characterisation of the one-face coated MFM tip (Chapter 5).

The irreversible changes in domain structure are identified by performing in-situ magnetising experiment. It is found that the fields required to initiate changes in domain structures in the cobalt elements are higher than in the permalloy elements. These critical fields whereby the major domain structure changes occur in the triangular region are summarised in Table 8.1. This indicates that domain structure in a permalloy MFM tip is less stable and more likely to be affected by the stray field of the specimen. The irreversible changes in the cobalt elements occur at higher magnetic field so that cobalt MFM tip can be used to image specimens with a relative high stray field.

Element	Critical Field (Oe)
Cobalt SIM1	78
Cobalt SIM2	65
Cobalt SIM3	78
Cobalt SIM4	28
Permalloy SIM1	24
Permalloy SIM2	19

*Table 8.1 Critical external fields where irreversible changes in domain structure occur.*

In chapter 7, initial characterisations of the Nanoprobe™ MFM tip and needle MFM tip are performed. The radius of the Nanoprobe™ MFM tip is found to be about 20 nm. MDPC imaging of the Nanoprobe™ MFM tip suggests that in the remanent state, the stray field at the end of the apex is similar to that of a uniformly magnetised tip. Hence, it is useful for quantitative MFM imaging. The needle MFM tip has an apex radius of about 10 nm so that it is the sharpest among the three types of MFM tip studied in this thesis. The needle tip also has a high ratio of dimensions so that the magnetisation is more likely to be uniform due to a strong shape effect. The magnetic imaging of this tip indicates that stray field is very localised around the apex. Although these are just preliminary studies, the results have indicated that these two

types of tips are good candidates for quantitative MFM imaging with high resolution. The disadvantages of the needle tips include that they are fragile and can not be batch fabricated at present. The reproducibility of the needle geometry is also much less than the batch fabricated tips.

## 8.2 Future work

In this section we outline possible future work.

1. The anisotropy induced by  $80^\circ$  oblique incidence in thin film elements was not studied due to a lift-off problem in the lithography process. Khamsehpour et al (1995) have demonstrated that a dry-etching technique is capable of fabricating permalloy thin film elements possessing similar micromagnetic properties to those produced by lift-off. Therefore, it can be used to define elements without problems associated with the lift-off process.

2. The method used to obtain a uniformly magnetised region at the end of the cobalt thin film MFM tip is to slow down the evaporation rate and introduce impurity atoms between grains to reduced the exchange coupling. A disadvantage of doing this is that the magnetic moment of the tip is reduced and this may affect the resolution of MFM imaging. The work described in chapter 4 has indicated that an easy axis can be induced in magnetic thin films by oblique evaporation and it helps the alignment of the magnetisation along the easy axis. Therefore, evaporation of magnetic films onto the tip at an oblique angle to a face of the pyramid can be investigated.

3. Evaporation of magnetic film in a magnetic field can also induce an easy axis in magnetic thin films. Therefore, the MFM tip can be evaporated in a field directed along the apex of the tip so that the easy axis is in this direction to help achieve uniform magnetisation.

4. The whole-surface coated Microlever<sup>TM</sup> MFM tips is fabricated using thermal evaporation. However, the cantilever is deformed by the stress imposed by the evaporated film so that it is not suitable for our MFM. As increased mobility of evaporated atoms may reduce the stress, increase of the substrate temperature during the deposition may be helpful.

5. Since the MFM tip studied in chapter 5 consists of grains with reduced exchange coupling, MDPC images of MFM tips with decoupled or partially decoupled grains can be simulated using micromagnetics models. These models incorporate all magnetic energy contributions, i.e. exchange energy, magnetostatic energy, anisotropy energy and Zeeman energy. Therefore the effect of exchange coupling between grains can be investigated.

6. As a further development of the model described in chapter 5, the volume of the uniformly magnetised region at the end of the apex can be varied to reflect the real situation, which was observed in chapter 6 and corresponded to  $\sim 0.5 \mu\text{m}$  from the end. The simulated MDPC images can then be compared with the experimental MDPC images in order to determine the effect of grains farther away from the apex region on the stray field.

## **Appendix 1**

### **Conversion of 16 bit grey scale image to 8 bit grey scale image**

Grey Scale pixel values represent a level of grains or brightness, ranging from completely black to completely white. This class is sometimes referred to as "monochrome." In an 8-bit grey scale image, a pixel with a value of 0 is completely black, and a pixel with a value of 255 is completely white. A value of 128 represents a grey colour exactly halfway between black and white (medium-grey), and a pixel value of 64 has a grey colour halfway between medium-grey and black.

8-bit grey scale format is the most common format in use. Intensity value of a pixel is represented with 8-bit integers, providing 256 (0 - 255) levels of grey. In a 16-bit grey scale format image, intensity value of a pixel is represented with 16-bit integers, providing 65,536 levels of grey.

Due to the fact that there is a difference in the number of byte per pixel, the converting procedure involves two steps. Firstly, the range of the grey scales is reduced from the maximum of [-32767, 32767] to [0, 255] but the image still bears 16 bits format. This is achieved by dividing the grey scale value with a constant which is chosen depending of the highest grey scale. For example, if the highest grey scale is 1020, then the constant may be chosen as 4. By doing this, the second byte of each pixel is set to zero and all the grey scale information is contained in the first byte. In the second step, the second byte is removed from each pixel so that the 8 bits format is obtained.

There has already been some commercial software which can accomplish the above task automatically, such as Digital Micrograph for Macintosh and IMPDEV for IBM RISC6000 workstation. The shortcoming of these automatic process is that they can only process one image per time and the constant may various from one image to another. This is not suitable for the processing of the MDPC images as that will change the relative scale of the two orthogonal mapped MDPC images so that they can not be mapped using DIP program.

In this work, the following procedure is developed and it is suitable for the quantitative analysis detailed in Chapter 5.

- (1) Both of the two orthogonal mapped MDPC images are surveyed and the highest grey scale  $G_{\max}$  is found.
- (2) The constant is worked out as  $G_{\max} / 255$ .
- (3) Both images are divided by this constant so that the grey scale range is reduced to  $[0, 255]$ .
- (4) The 8 bits images are obtained by simply change the format of the images.

## **Appendix 2**

### **BASIC program used to display electron beam lithography patterns**

This program is written in BASIC language to display patterns of the electron beam lithography so as to assist the pattern design. It has been tested in IBM PC with SVGA monitor. As soon as the program is executed, it will prompt

Pattern file = ?

on the monitor and the pattern will be displayed after a valid pattern file is given.

```
DIM x(200, 2), y(200, 2)
SCREEN 12
col = 12
displayx = 600
displayy = 440
sem = 4096
ratiox = sem / displayx
ratioy = sem / displayy
REM - Input data file -
INPUT "Pattern file="; f$
CLS
OPEN f$ FOR INPUT AS #1
100 n = n + 1
INPUT #1, x(n, 1), y(n, 1), x(n, 2), y(n, 2)
    IF x(n,1)=0 AND y(n,1)=0 AND x(n,2)=0 AND y(n,2)=0 THEN
                                                GOTO 200
GOTO 100
200 CLOSE #1

REM ---- Draw frame ----
REM ---- Draw patterns ----
LINE (0, 0)-(600, 440), col, B
```

```
i = 0
300 i = i + 1
IF i >= n THEN END
REM ---- find rectangle command line ----
  IF x(i,1) = 0 AND x(i,2) = 1 AND y(i,2) = 0 THEN i=i + 1
REM ---- find triangle command line -----
  IF x(i,1)=0 AND y(i,1)=10 AND x(i,2)=0 AND y(i,2)=0 THEN
    i = i + 1
    GOSUB triangle
    GOSUB delay
    GOTO 300
  END IF
REM ---- default rectangle ----
  GOSUB rectangle
  GOSUB delay
  GOTO 300
END
```

rectangle:

```
  GOSUB scale
  LINE (x1, y1)-(x2, y2), col, B
  RETURN
```

triangle:

```
  GOSUB scale
  LINE (x1, y1)-(x2, y2), col, B
  x3 = x1
  y3 = y1
  x4 = x2
  y4 = y2
  i = i + 1
  GOSUB scale
  LINE (x1, y1)-(x2, y2), col, B
  LINE (x4, y4)-(x2, y1), col
  LINE (x3, y4)-(x1, y1), col
  RETURN
```

*Appendix 2 BASIC program used to display electron beam lithography patterns*

scale:

```
x1 = INT(x(i, 1) / ratiox)
y1 = INT(y(i, 1) / ratioy)
x2 = INT(x(i, 2) / ratiox)
y2 = INT(y(i, 2) / ratioy)
RETURN
```

delay:

```
FOR de = 1 TO 5000
NEXT de
RETURN
```

## **Appendix 3**

### **BASIC program used to display results of electron beam lithography**

This is a program written in BASIC language to display results of the electron beam lithography. It require 2 files:

(1) A controlling file which tell the computer the exposure order and magnification of each patterns.

The format of the controlling files is

```
MAGNIFICATION1 PATTERN1
MAGNIFICATION2 PATTERN2
..                ..
0                 0
```

(2) A position file which tells the computer the position of each patterns.

When the program has been executed, it will prompt

control file=?

position file=?

do you want to see grid (Y/N)?

As soon as these questions are answered, it will display the result on the screen. Here is the program.

```
CLS
DIM x(200, 2), y(200, 2)
SCREEN 12
k = 3
col = 12
```

```
colb = 7
display = 460
sem = 4096
membrane = .12
REM -frame size at 5K -
fx = .03
fy = .022
mf = 5000

grid = display / 12

REM -input magnification and order control files -
INPUT "control file="; c$
REM - Input position file -
INPUT "position file="; p$
INPUT "do you want to see grid(Y/N)"; g$
CLS
REM - Draw membrane border -
LINE (0, 0)-(460, 460), colb, B
IF g$ = "Y" OR g$ = "y" OR g$ = "YES" OR g$ = "yes" THEN
  FOR d = 0 TO 460 STEP grid
    LINE (0, d)-(460, d), colb
    LINE (d, 0)-(d, 460), colb
  NEXT d
END IF

OPEN c$ FOR INPUT AS #1
OPEN p$ FOR INPUT AS #3

REM - Input control data -
150 k = k + 1
INPUT #1, m, f$
IF m = 0 THEN GOTO 900

REM - input pattern data -
OPEN f$ FOR INPUT AS #k
n = 0
```

*Appendix 3 BASIC program used to display results of electron beam lithography*

```
100 n = n + 1
INPUT #k, x(n, 1), y(n, 1), x(n, 2), y(n, 2)
  IF x(n, 1) = 0 AND y(n, 1) = 0 AND x(n, 2) = 0 AND y(n,
      2) = 0 THEN GOTO 200

GOTO 100
200 CLOSE #k

REM - Input position data -
INPUT #3, xp, yp, t1, t2, t3

REM - calculate frame sizw at magnification of m -
lx = fx * mf / m
ly = fy * mf / m

REM - Draw patterns -
i = 0
300 i = i + 1
IF i >= n THEN GOTO 150
REM - find rectangle command line -
IF x(i, 1) = 0 AND x(i, 2) = 1 AND y(i, 2) = 0 THEN i = i
      + 1
REM - find triangle command line -
  IF x(i, 1) = 0 AND y(i, 1) = 10 AND x(i, 2) = 0 AND y(i,
      2) = 0 THEN

    i = i + 1
    GOSUB triangle
    GOSUB delay
    GOTO 300
  END IF
REM - default rectangle -
  GOSUB rectangle
  GOSUB delay
  GOTO 300

GOTO 150

900 CLOSE #1
CLOSE #3
```

END

rectangle:

```
GOSUB shift1
GOSUB scale1
GOSUB shift2
GOSUB scale2
LINE (x1, y1)-(x2, y2), col, B
RETURN
```

triangle:

```
GOSUB shift1
GOSUB scale1
GOSUB shift2
GOSUB scale2
LINE (x1, y1)-(x2, y2), col, B
x3 = x1
y3 = y1
x4 = x2
y4 = y2
i = i + 1
GOSUB shift1
GOSUB scale1
GOSUB shift2
GOSUB scale2
LINE (x1, y1)-(x2, y2), col, B
LINE (x4, y4)-(x2, y1), col
LINE (x3, y4)-(x1, y1), col
RETURN
```

shift1:

```
x(i, 1) = x(i, 1) - 2048
y(i, 1) = 2048 - y(i, 1)
x(i, 2) = x(i, 2) - 2048
y(i, 2) = 2048 - y(i, 2)
RETURN
```

scale1:

*Appendix 3 BASIC program used to display results of electron beam lithography*

```
x1 = x(i, 1) * lx / 4096
y1 = y(i, 1) * ly / 4096
x2 = x(i, 2) * lx / 4096
y2 = y(i, 2) * ly / 4096
RETURN
```

shift2:

```
x1 = x1 + xp
y1 = y1 + yp
x2 = x2 + xp
y2 = y2 + yp
RETURN
```

scale2:

```
x1 = INT(x1 * display / membrane)
y1 = INT(display - y1 * display / membrane)
x2 = INT(x2 * display / membrane)
y2 = INT(display - y2 * display / membrane)
RETURN
```

delay:

```
FOR de = 1 TO 5000
NEXT de
RETURN
```

## **Appendix 4**

### **FORTRAN 77 program converting Lorentz deflection angle data to 8-bit grey scale raw data format image**

The following program has been successfully compiled and executed in an IBM 3090 mainframe computer and a RISC 6000 workstation.

```
C Channel 10 is X deflection angle files input
C Channel 11 is Y deflection angle files input
C Channel 12 is X IAX format file output
C Channel 13 is Y IAX format file output
      DOUBLE PRECISION X(256,256),Y(256,256),MAX
      INTEGER RX,RY,A(256,256),B(256,256)
      RX=256
C RX is the number of pixels in the x direction
      RY=256
C RY is the number of pixels in the y direction
      MAX=0.0
C-- Read data files and find the maximum. -
      DO 500 J=1,RY
        DO 550 I=1,RX
          READ (10,100) X(I,J)
          READ (11,100) Y(I,J)
550 CONTINUE
500 CONTINUE
C --- Find Max ---
      DO 400 J=1,RY
        DO 450 I=129,RX
          IF (DABS(X(I,J)).GT.MAX) MAX=DABS(X(I,J))
          IF (DABS(Y(I,J)).GT.MAX) MAX=DABS(Y(I,J))
450 CONTINUE
400 CONTINUE
C --- Range data to 2-254.--
      DO 20 J=1,RY
        DO 30 I=1,RX
          A(I,J)=INT(126.0*X(I,J)/MAX+128)
```

*Appendix 4 FORTRAN 77 program converting Lorentz deflection angle data to 8-bit grey scale raw data format image*

```
        B(I,J)=INT(126.0*Y(I,J)/MAX+128)
30    CONTINUE
20    CONTINUE
C --- Write IAX1 format image files. -
      DO 60 J=1,RY
        WRITE (12) (CHAR(A(I,J)), I=1,256)
        WRITE (13) (CHAR(B(I,J)), I=1,256)
60    CONTINUE
100  FORMAT(D15.8)
      END
```

## References

### Chapter 1

- Barkhausen H, 1919, Phys. Z., 20, P 401.
- Bitter F, 1931, Phys. Rev., 38, P 1903.
- Bitter F, 1932, Phys. Rev., 41, P 507.
- Bloch F, 1932, Z. Physik, 74, P 295.
- Dirac P A M, 1929, Proc. Roy. Soc., A123, P 714.
- Hamos L V and Thiessen P A, 1932, Z. Physik., 71, P 442.
- Heisenberg W, 1928, Z. Phys., 49, P 619.
- Huber E E, Smith D O and Goodenough J G, 1958, J Appl. Phys., 29, P 294.
- Hubert A, 1969, Phys. Stat. Sol., 32, P 519.
- Kosinski R, 1977, Acta Physica Polonica, A51, P 647.
- LaBonte A E, 1969, J. Appl. Phys., 39, P 855.
- Landau L and Lifshitz E, 1935, Physik. Z. Sowjetunion, 8, P 153.
- Li Z Z, 1985, Principle of Solid State Physics, High Education Pub. Hou., China, P 74.
- Lifshitz E, 1944, J. Phys. USSR, 8, P 337.
- Middelhoek S, 1963, J. Appl. Phys., 34, P 1054.
- Neel L, 1955, Compt. Rend., 421, P 533.
- Warburg E, 1881, Ann. Physik, 13, P 141.
- Weiss P, 1907, J. Phys. 6, P 661.
- Weiss P, 1948, Phys. Rev. 74, P 1493.

### Chapter 2

- Aharonov Y and Bohm D, 1959, Phys. Rev. 115, P 485.
- Allenspach R, 1994, Physics World, 3, P 44.
- Argyle B E and Herman D A, 1986, IEEE Trans. Mag., Mag., 22, P 722.
- Bitter F, 1931, Phys. Rev., 38, P 1903.
- Chapman J N, Batson P E, Waddell E M and Ferrier R P, 1978, Ultramicrosc., 3, P 203.
- Chapman J N, McFadyen I R and McVitie S, 1990, IEEE Trans. Mag., 26 (5), P 1506.
- Chapman J N, 1984, J. Phys. D: Appl. Phys., 17, P 623.
- Chikazumi S, 1964, Physics of Magnetism, John Wiley & Sons, Inc..

- Clegg W W, Heyes N A E, Hill E W and Wright C D, 1990, *J. Mag. Mag. Mat.*, 83, P 535.
- Dekkers N H and Lang H de, 1974, *Optik*, 41, P 452.
- Dillion J F, 1958, *J. Appl. Phys.*, 29, P 1286.
- Fischer P B, Wei M S and Chou S Y, 1993, *J. Vac. Sci. Technol.*, B 11 (6), P 2570.
- Grütter P, Mamin H J and Rugar D, 1992, *Magnetic force microscopy. Springer Series in Surface Science 28. Scanning Tunnelling Microscopy II.* (ed. Wiesendanger R and Güntherodt H J, P 151-207. Springer, Berlin.
- Grütter P, Meyer E, Heinzelmann, Rosenthaler L, Hidber H R and Güntherodt H -J, 1988, *J. Vac. Sci. Technol.*, A (6), P 279.
- Grütter P, Rugar D, Mamin H J, Castillo G, Lin C J, McFadyen I R, Valetta R M, Wolter O, Bayer T and Greschner J, 1991, *J. Appl. Phys.*, 69, P 5883.
- Hale M E, Fuller H W and Rubinstein H, 1959, *J. Appl. Phys.*, 30, P 789.
- Hartmann U, 1987, *Appl. Phys. Letts.*, 51, P 374.
- Hefferman S J, Chapman J N and McVitie S, 1991, *J. Magn. Magn. Mater.*, 95, P 76.
- Herman D A, Argyle B E and Petek B, 1987, *J. Appl. Phys.*, 61, P 4200.
- Iijima T and Yasuda K, 1988, *Jap. J. Appl. Phys.*, 27, P 1546.
- Jakubovics J P, 1975, *Electron Microscopy in Materials Science, Vol. 4,* (ed) U. Valdre and E. Ruedl (Bussels Commission of the European Communities) P 130.
- Jakubovics J P, 1978, *Phil. Mag.*, 37, P 76.
- Koike K and Hayakawa K, 1984, *Appl. Phys. Lett.*, 45, P 585.
- Martin Y and Wickramasinghe H K, 1987, *Appl. Phys. Lett.*, 50, P 1455.
- McVitie S and Hartmann U, 1991, 49th Annual Meeting of the Electron Microscopy Society of America, P 770.
- Porthun S, Rührig M and Lodder J C, 1994, 'Magnetic force microscopy on thin film magnetic recording media', *Force in scanning probe microscopy, NATO ASI Series E: Applied Sciences*, Edited by Güntherodt H J et al.
- Rave W, Schafer R and Hubert A, 1987, *J. Mag. Mag. Mater.*, 65, P 7.
- Rave W and Hubert A, 1990, *IEEE Trans. Mag.*, 26, P 2813.
- Robert B W and Bean C P, 1954, *Phys. Rev.*, 96, P 1494.
- Rugar D, Mamin H J, Guethner P, Lambert S E, Stern J E, McFadyen I and Yogi T, 1990, *J. Appl. Phys.*, 68, P 1169.
- Rührig M, Bartsch W, Vieth M and Hubert A, 1990, *IEEE Trans. Mag.*, 26,

P 2807.

- Saenz J J Garcia N, Grütter P, Meyer E, Heinzelmann H, Wiesendanger R, Tosenthaler L, Hidber H R and Güntherodt, 1987, J. Appl. Phys., 62, P 4293.
- Schmidt F, Rave W and Hubert A, 1985, IEEE Trans. Mag., 21 (5), P 1596.
- Schönenberger C and Alvarado S F, 1990, Z. Phys. B 80, P 373.
- Tonomura A, 1993, IEEE Trans. Mag., 29 (6), P 2488.
- Tsuno K and Taoka T, 1983, J. Appl. Phys., 22, P 1047.
- Valera M S, Farley A N, Hoon, S R, Zhou L, McVitie S and Chapman J N, 1995, Apply. Phys. Lett., 67, (17), P 2566
- Wadas A and Grütter P, 1989, Phys. Rev., B 39, P 12013.
- Wadas A and Guntherodt H J, 1990, Phys. Lett., 146, P 277.

### Chapter 3

- Fredkin D R, Koehler T R, 1990, IEEE Trans. Mag. MAG-26, P1518.
- Hefferman S J, Chapman J N and McVitie S, 1991, J. Magn. Magn. Mat., 95, P 76.
- Huijjer E and Watson J K, 1979, J. Appl. Phys., 50 (3), P 2149.
- Kittel C, 1946, Phys. Rev., 70, P 965.
- Lo D S, Cosimini G J, Zierhut L G, Dean R H and Paul M C, 1985, IEEE Trans Mag. MAG-21, P 1776.
- Mackie S, Ph.D. Thesis, 1984, University of Glasgow.
- McVitie S and Chapman J N, 1988, IEEE Trans. Mag. MAG-24, P 1778.
- McVitie S, 1988, PhD thesis, University of Glasgow.
- Rührig M, Porthum S and Lodder J C, 1994, Rev. Sci. Instr., 65 (10), P 3224.
- Schmidts H F and Kronmüller H, 1994, J. Magn. Magn. Mater., 129, P 361.
- Tsang C, Fontana R E, Lin T, Heim D E, Speriosu V S, Gurney B A and Williams M L, 1994, IEEE Trans. Mag. 30 (6), P 1994.
- Wong H Y, Chapman J N, McVitie S and Hefferman S J, 1992, J. Magn. Magn. Mater. 104, P 329.

### Chapter 4

- Cohen M S, 1961, J. Appl. Phys. 32, 87S.

- Cohen M S, 1970, Handbook of Thin Film Technology, Edited by Maissel L I and Glang R, McGraw - Hill book Company, P 17 - 6.
- Hefferman S J, 1991a, PhD thesis, University of Glasgow, P 74.
- Hefferman S J, Chapman J N and McVitie S, 1991b, J. Magn. Magn. Mater., 95, P 76.
- McVitie S, 1988, PhD thesis, University of Glasgow.
- Wilts C H, 1966, *Basic Problems in Thin Film Physics*, (eds) Niedermayer R and Mayer H, Vandenhoeck and Ruprecht, Goettingen.

## Chapter 5

- Beaumont S, Farley A N and Valera M S, 1994, J. De Phys., Proc. 13th Int. Congress Electron Microscopy.
- Davis P J and Rabinowitz P, 1967, Numerical Integration, Blaisdell Pub. Comp..
- Digital Instruments, 1994, Nanovations, 1(1), P 3.
- Grütter P, 1994, MSA Bulletin, Vol. 24, No. 1, P 416.
- Grütter P, Mamin H J and Rugar D, 1992, Magnetic force microscopy. Springer Series in Surface Science 28, Scanning Tunnelling Microscopy II, ed. Wiesendanger R and Güntherodt H J, Springer, Berlin.
- Loh K G, Jobe R and Christie, 1993, Technical Notes, Advances in Scanning Probe Microscope Technology, No. 2-1093-002.
- McVitie S, 1988, PhD thesis, Department of Physics & Astronomy, University of Glasgow.
- NAGFLIB, 1983, 1593/0: Mk10: 8th February, D01-Quadrature, D01BAF, P 1.
- Schönenberger S and Alvarado S F, 1990, Z. Phys. B 80, P 373.
- Valera M S, Farley A N, Hoon S R, Zhou L, McVitie S and Chapman J N, 1995, Appl. Phys. Lett., 67, (17), P 2566.
- Valera M S and Farley A N, 1995, A high performance magnetic force microscope, submitted to Measurement Science and Technology.
- Wadas A and Guntherodt H J, 1990, Phys. Lett., 146, P 277.

## Chapter 6

- Beaumont S, Farley A N and Valera M S, 1994, J. De Phys., Proc. 13th Int. Congress Electron Microscopy.
- Craik D J and Tebble R S, 1965, Ferromagnetism and Ferromagnetic

- Domains, ed. Wohlfarth E P, North-Holland Publishing Company - Amsterdam, P 201.
- Grütter P, Rugar D, Mamin H J, Castillo G, Lin C J, McFadyen I R, Valletta R M, Wolter O, Bayer T and Greschner J, 1991, *J. Appl. Phys.*, 69, P 5883.
  - Hefferman S J, 1991, PhD thesis, The University of Glasgow.
  - Jiles D, 1991, *Introduction to Magnetism and Magnetic Materials*, Chapman and Hall.
  - McVitie S, 1988, PhD thesis, University of Glasgow, UK.
  - Valera M S, Farley A N, Hoon S R, Zhou L, McVitie S and Chapman J N, 1995, *Appl. Phys. Lett.*, 67, (17), P 2566.
  - Valera M S and Farley A N, 1995, A high performance magnetic force microscope, Submitted to *Measurement Science and Technology*.
  - Wong H, McVitie S and Chapman J N, 1992, *J. Magn. Magn. Mater.*, 104, P 329.

## Chapter 7

- Babcock K, Elings V, Dugas and Loper S, 1994, *IEEE Trans. MAG.*, 30 (6), P 4503.
- Fischer P B, Wei M S and Chou S Y, 1993, *J. Vac. Sci. Technol.*, 1993, B 11 (6), P 2570.
- Grütter P, Rugar D, Mamin H J, Castillo G, Lambert S E, Lin C J, Valletta R M, Wolter O, Bayer T and Greschner, 1990, *Appl. Phys. Lett.*, 57 (17), P 1820.
- Grütter P, Rugar D, Mamin H J, Castillo G, Lin C J, McFadyen I R, Valletta R M, Wolter O, Bayer T and Greschner J, 1991, *J. Appl. Phys.*, 69, P 5883.
- Grütter P, Mamin H J and Rugar D, 1992, *Magnetic Force Microscopy*, Spring Series in Surface Science 28, *Scanning Tunnelling Microscopy II*, ed. Wiesendanger R and Güntherodt H J, Berlin.
- Koops H W, Weiel R, Kern D P and Bum T H, 1988, *J. Vac. Sci. Technol.*, B 6, P 477.
- Martin Y and Wickramasinghe H K, 1987, *Appl. Phys. Lett.*, 50, P 1455.
- Rührig M, Porthun S and Lodder J C, 1994, *Rev Sci. Instr.*
- Valera M S, Farley A N, Hoon S R, Zhou L, McVitie S and Chapman J N, 1995a, *Appl. Phys. Lett.*, 67, (17), P 2566.
- Valera M S and Farley A N, 1995b, *Developments in magnetic force*

microscopy instrumentation, submitted to Measurement Science and Technology.

- Wolter O, Bayer T and Greschner J, 1991, J. Vac. Sci. Technol., B 9 (2), P 1353.

## **Chapter 8**

- Valera M S, Farley A N, Hoon S R, Zhou L, McVitie S and Chapman J N, 1995, Appl. Phys. Lett., 67, (17), P 2566.
- Hefferman S J, 1991, PhD thesis, The University of Glasgow.
- Khamsehpour B, Wilkinson C D W and Chapman J N, 1995, Appl. Phys. Lett., 67, (21), P 3194.
- Wong H, McVitie S and Chapman J N, 1992, J. Magn. Magn. Mater., 104, P 329.

